Homogénéisation non linéaire des matériaux poreux monocristallins: Modélisation, implémentation numérique et applications au fluage et à la fatigue

Mbiakop Armel

HAL Id: tel-01235253
https://pastel.hal.science/tel-01235253

Submitted on 29 Nov 2015

Thèse présentée pour l'obtention du titre de

DOCTEUR DE L'ÉCOLE POLYTECHNIQUE

Spécialité : Mécanique

par

ARMEL MBIAKOP

Sujet de thèse

Homogénéisation non linéaire des matériaux poreux monocristallins: Modélisation, implémentation numérique et applications au fluage et à la fatigue

Nonlinear homogenization in porous creeping single crystals: Modeling, numerical implementation and applications to fracture and fatigue

M. Renald BRENNER	*Rapporteur*
M. Vincent MONCHIET	*Rapporteur*
M. Jacques BESSON	*Examinateur*
M. Jean-Baptiste LEBLOND	*Examinateur*
M. Eric MAIRE	*Examinateur*
M. Jean Jacques MARIGO	*Examinateur*
M. Thomas PARDOEN	*Examinateur*
M. Andrei CONSTANTINESCU	*Directeur de thèse*
M. Kostas DANAS	*Codirecteur de thèse*

"La modestie est au mérite ce que les ombres sont aux figures dans un tableau : elle lui donne force et relief", Jean de La Bruyère

À mes parents.

Acknowledgments

ABSTRACT

Nonlinear homogenization in porous creeping single crystals: Modeling, numerical implementation and applications to fracture and fatigue

Armel Mbiakop

Advisers: Professor Andrei Constantinescu / Professor Kostas Danas

This study is concerned with the development of a rate-dependent constitutive model for porous single crystals with arbitrary crystal structure containing general ellipsoidal voids. The proposed model, called modified variational model (MVAR), is based on the nonlinear variational homogenization method, which makes use of a linear comparison porous single crystal material to estimate the response of the nonlinear porous single crystal. Thus, the main objective of this work is to propose a general constitutive model that accounts for the evolution of the microstructure and hence the induced anisotropy resulting when the initially anisotropic porous single crystal is subjected to finite deformations.

Furthermore, periodic finite element simulations are used in order to validate the MVAR for a large number of parameters including cubic (FCC, BCC) and hexagonal (HCP) crystal anisotropy, various creep exponents (i.e., nonlinearity), several stress triaxiality ratios, Lode angle, general void shapes and orientations and various porosity levels. The MVAR model is found to be in good agreement with the finite element results for all cases considered in this study. The model is then used in a predictive manner to investigate the complex response of porous single crystals in several cases with strong coupling between the anisotropy of the crystal and the (morphological) anisotropy induced by the shape and orientation of the voids. In addition, an innovate way of calibrating the MVAR with just two adjustable parameters is depicted in the rate-independent context so that an excellent agreement related to simulation results is obtained. Moreover, a porous Tresca model is derived by an original approach starting from the novel porous single crystal model and considering the limiting case on infinite number of slip systems which leads to the Tresca criterion.

Finally, the above-mentioned results are then extended to account for the evolution of microstructure when the material is subjected to finite deformations.

RÉSUMÉ

Homogénéisation non linéaire des matériaux poreux monocristallins:
Modélisation, implémentation numérique et applications au fluage et à la fatigue

Armel Mbiakop

Directeurs de thèse: Professeur Andrei Constantinescu / Professeur Kostas Danas

Ce travail de thèse porte sur le développement d'un modèle constitutif viscoplastique pour monocristaux poreux à structure cristalline arbitraire et microstructures ellipsoidales. Le modèle proposé, appelé modèle variationel modifié (MVAR), est basé sur la méthode d'homogénisation variationelle non linéaire, qui utilise un composite linéaire de comparaison pour estimer la réponse non linéaire du monocristal poreux. Par conséquent, l'objectif principal de cette étude est de proposer un modèle constitutif général prenant en compte l'évolution de la microstructure et l'anisotropie induite quand le monocristal poreux est sollicité en déformations finies.

En outre, des simulations EF périodiques sont utilisées pour valider le MVAR pour un grand nombre de paramètres incluant l'anisotropie cristalline cubique (FCC, BCC) et hexagonale (HCP), plusieurs exposants de fluage (i.e. nonlinéarité), différentes triaxialités, angles de Lode, formes et orientations de pores et plusieurs niveaux de porosité. Le MVAR est en bon accord avec les résultats EF pour tous les cas considérés dans cette étude. Il est ensuite utilisé pour investiguer la réponse mécanique complexe des monocristaux poreux sous differentes conditions avec notammant le très fort couplage entre l'anisotropie cristalline et l'anisotropie morphologique induite par la forme et l'orientation des pores. De plus, une approche nouvelle de calibration avec seulement deux paramètres ajustables est proposée de maniére à obtenir un excellent accord entre modèle et simulations. Par ailleurs, un modèle de Tresca poreux est dérivé par le biais d'une approche originale se servant du modèle pour monocristaux poreux et considérant le cas limite d'un nombre infini de systèmes de glissements (qui conduit au critère de Tresca).

Enfin, les différents résultats sus-mentionnés sont étendus afin de prendre en compte l'évolution de la microstructure quand le matériau est sollicité en déformations finies.

Contents

Chapter 1

Introduction

This study deals with the estimation of the constitutive behavior of composite materials and precisely porous single crystals. A composite material can be defined as a heterogeneous material consisting of multiple materials, denoted phases, with different properties. In addition, a porous single crystal is a specific type of two-phase composite material that consists of voids (pores/cavities) and a surrounding single crystal matrix. Such random distribution of voids (i.e microstructure) are found in a large range of materials, including metals or ceramics. For instance, Requena et al. [2014] analyzed the formation of damage during deformation of a DP sample steel using a tomograph (see Fig. 1.1). By looking onto a plane parallel to the load direction, they have in particular observed that some cavities were already present before straining the sample, i.e. $\varepsilon_{loc} = 0$. In principle, numerical computation techniques like "finite element" or Fourier transform algorithms can be used to determine the local behavior of the material when the exact shape and location of the pores in the material are known. Nonetheless, the only available information is in general the volume concentration and, possibly, the two-point probability distribution function of the voids. Moreover, the element size used in a finite element algorithm should be smaller than the size of the microstructure, which in turn is several orders of magnitude smaller than the size of the macroscopic material. Then, the computation would be extremely time-consuming. Consequently, it is useful to develop theoretical approaches to estimate the effective behavior of these materials in a more efficient way.

As already explained, the typical size of the inhomogeneities in the heterogeneous material (microscopic length scale) is much smaller than the size of the of the specimen and the scale of variation of the loading conditions (macroscopic length scale). Thus, a heterogeneous material can be described as a homogeneous material on the

Figure 1.1: Tomograph images showing development of damage in a DP steel, looking onto a plane parallel to the load direction. Three tensile deformation conditions a-c are displayed, where the darker regions correspond to cavities.

macroscale, with so-called "effective properties" that depend on the distribution and the properties of the phases, i.e. the microstructure. In the large majority of practical applications, the microstructure can be characterized only in terms of statistical partial information, since it appears very complex to be fully described in details. The "homogenization" methods provided suitable frameworks to estimate the constitutive behavior of composite materials by making use of the available statistical information about their microstructure. Indeed, a goal of these methods is to link the macroscopic with the microscopic scale in the most efficient manner by including as much information as it is available about the microstructure of the material.

Furthermore, in many theoretical contributions, the microstructure of composite materials is taken to be periodic. This hypothesis presents the advantage to reduce the problem of estimating the effective behavior of the composite to a computation of a single unit-cell provided that the phases are described by strictly convex potentials. Then, the solution is valid in the entire material's volume, except in some "boundary layer" close to its exterior surface. On the other hand, even if most materials of interest consist of random microstructures, it is well known that a random porous material and a periodic material exhibit similar effective behavior either in the case where the distribution of voids is complex enough (adequate for large porosity) or in the limiting case where the porosity is small enough. In these cases, the effective properties of the periodic composite are independent of the prescribed periodic boundary conditions (Gilormini and Michel [1998]). Moreover, for statistically uniform media, it is usual to make an "ergodic" hypothesis that local configurations occur over any one specimen

with the frequency with which they occur over a single neighborhood in an ensemble of specimens. Under this assumption ensemble averages may be replaced by volume averages and therefore the effective behavior of the random composite may be defined over a given volume.

In the context of linear elastic composites, numerous approaches exist to estimate their effective behavior. To begin with, in the pioneering works of Voigt [1889], Reus [1929], simpler rigorous bounds for the effective mechanical properties of random composites were proposed by assuming uniform strain and stress fields over the composite, respectively. In addition, Hershey [1954], Kroner [1958] introduce the self-consistent (SC) approximation for elastic polycrystals. This estimate has been further extended by Budiansky [1965], Hill [1965] to other elastic composites. On the other hand, in his famous contribution, Eshelby [1957] provided the exact solution of the problem of an ellipsoidal inclusion in an infinite, isotropic and elastic matrix. Moreover, Hashin [1962] has provided the exact solution of the hydrostatic effective behavior of composite sphere (CSA) or composite cylinder (CCA) assemblages. Hashin and Shtrikman [1962a,b, 1963] proposed a variational principle that improved significantly the Voigt [1889], Reus [1929] bounds by assuming that the constituent phases are uniformly distributed in the composite. Then, in several contributions, Willis [1977, 1978, 1991] generalized these variational principles by involving two-point statistics information of the composite and thus improved estimates for more general anisotropic microstructure and "particulate" composites. Furthermore, Ponte Castañeda and Willis [1995] built variational approximations for "particulate" composites, accounting possible difference between the shape of the microstructure (voids or inclusions) and the shape of the spatial distribution functions. It is useful to precise that some other approximations like Mori and Tanaka [1973] can generate tensors of effective moduli that don't exhibit necessary symmetry requirements. The estimates that would be used in the present study (Ponte Castañeda and Willis [1995]) are free from such issues due to their variational character.

Moreover, several studies have proposed methods in order to address as well the question of the effective behavior of nonlinear composites. For instance, in an earlier contribution, Taylor [1938] presented simple "Voigt type" bounds in the context of polycrystals. Still in the context of elastoplastic polycrystals, Hutchinson [1976], Berveiller and Zaoui [1979] proposed several schemes inspired by the incre-

mental self-consistent approach developed by Hill [1965]. An extension of the Hashin and Shtrikman [1962a,b, 1963] bounds to the case of nonlinear composites has been introduced by Talbot and Willis [1985] who used a "linear homogeneous comparison material". In addition, Ponte Castañeda [1991b] proposed a more general class of non-linear homogenization methods. These methods, so-called "variational approaches", make use of suitably designed variational principle of a chosen "linear comparison composite" (LCC) with the same microstructure as the nonlinear composite. Further, Suquet [1995] noticed that the optimal linearization in the variational bound of Ponte Castañeda [1991b] is given by the "secant" moduli evaluated at the second moments of the local fields in each phase in the LCC.

While the "variational" method is quite general and delivers a rigorous bound, it tends to give overly stiff predictions at high triaxialities and small porosities. However, this limitation has been removed, at least for isotropic matrix systems, in works by Danas and Ponte Castañeda [2009a,b], making use of the more accurate "second-order" linear comparison homogenization method of Ponte Castañeda [2002a,b]. This method makes used of the generalized-secant moduli of the phases that depend on both the first and the second moments of the local fields. More recently, Ponte Castañeda [2012] developed a novel strategy based on the use of incremental homogenization (Bensoussan et al. [1978], Braides and Lukkassen [2000]). In particular, for porous isotropic matrix subjected to purely hydrostatic loadings, the so-called "ITVAR" bound agrees precisely with the exact results of Leblond et al. [1994] and Idiart [2007] for composite-sphere and sequentially laminated microstructures, demonstrating that the new incremental HS bounds are optimal for at least this particular type of loading. In addition, Danas and Aravas [2012] the modified variational model (MVAR) through simple modifications of the earlier variational homogenization method. These modifications allow for very accurate predictions of the macroscopic response and microstructure evolution of porous materials subjected to general three-dimensional loading conditions at both low and high stress triaxialities, as is the case in the SOM model. Moreover, the MVAR model is more suitable for numerical implementation than the other variational type models (SOM or ITVAR). Indeed, it is for instance more stable and faster numerically than the SOM model since it involves only the evaluation of one-dimensional elliptic integrals of the Eshelby-type, contrary to the SOM model that requires, in the more general case, the numerical evaluation of two-dimensional (surface) integrals which

become singular at large void elongations.

In addition to the nonlinear homogenization methods described previously, some others micromechanical models for porous materials have been developed. More precisely, in the specific case of dilute concentration of voids, a lot of studies, for instance Mc Clintock [1968], Rice and Tracey [1969], Fleck and Hutchinson [1986] may be mentioned. These studies use of a stream function technique, which is mainly applied to problems in two-dimensions or three-dimensions provided that certain symmetries are preserved in the problem (e.g., spheroidal voids and axisymmetric loading conditions aligned with the void symmetry axis). So, such procedure introduces an important limitation since the extension to general three dimensional microstructures and loadings is not straightforward. Moreover, following the contribution of Rice and Tracey [1969], Gurson [1977] proposed a famous model for non-dilute porous solids with ideally-plastic isotropic matrix phase by making use of the exact solution for a shell (spherical or cylindrical cavity) subjected to hydrostatic loading, together with a uniform, purely, deviatoric field. This model, so-called "limit analysis approach" was further calibrated by Tvergaard and Needleman [1984] and used in the context of isotropic matrix with spheroidal (see for instance Gologanu and Leblond [1993], Leblond et al. [1994], Monchiet et al. [2007]) or ellipsoidal voids (Madou and Leblond [2012a,b]).

Far fewer results have been obtained for rate-(in)dependent anisotropic matrix systems, generally based on a phenomenological Hill-type matrix (see Benzerga et al. [2004], Monchiet et al. [2008a], Keralavarma et al. [2011]). The case of porous single crystals have only been studied through discrete dislocations dynamic by (Huang et al. [2007], Hussein et al. [2008], Segurado and Llorca [2010], Huang et al. [2012]) and molecular dynamics at smaller scales (Traiviratana et al. [2008], Zhao et al. [2009], Tang et al. [2010a,b]), or using finite element simulations (Yerra et al. [2010], Ha and Kim [2010]). Such anisotropic matrix systems have known slip directions and contain usually a small volume fraction of impurities. When these material systems are subjected to external loads impurities fail or decohere leading to the creation of pores, which in turn evolve in size, shape and orientation (Srivastava and Needleman [2012]). This complex evolution of microstructure together with the evolution of the rate-dependent matrix anisotropy is critical in the prediction of the eventual fracture of the specimen under monotonic and cyclic loading conditions. As an illustration, the

Fig. 1.2 in Srivastava et al. [2012] presents SEM (scanning electron microscopy) images showing evolution of damage in the gauge region of the specimens creep tested at 982°C/248MPa. Then these authors, through experimental observations at high enough temperatures on tensile specimens, showed that the growth of initially present processing induced voids in a nickel based single crystal superalloy as well as in standard polycrystals played a significant role in limiting creep life.

Figure 1.2: images showing evolution of damage in the gauge region of the specimens creep tested at at 982°C/248MPa. (c) A $h = 3.18$mm thick specimen after $75h$. (d) A $h = 3.18$mm thick specimen after creep rupture. The loading direction is ld.

Nevertheless, there have been only a handful of models for porous single crystals which deal with special void geometries, loading conditions and slip system orientations. Such studies involve the study of cylindrical voids with circular cross-section in a rigid-ideally plastic face-centered cubic (FCC) single crystals using slip line theory (Kysar et al. [2005], Gan et al. [2006], Gan and Kysar [2007]), the study two-dimensional "out of plane" cylindrical voids with circular cross-section subjected to anti-plane loadings (Idiart and Ponte Castañeda [2007]) and that of spherical voids (Han et al. [2013], Paux et al. [2015]). While each one of these studies has its own significant contribution to the understanding of the effective response of porous single crystals none of them is general enough in the sense of arbitrary void shapes and orientations and general loading conditions.

Furthermore, viscoplastic porous single crystals, which is the main topic of this work, can undergo finite deformations. Therefore, their microstructure is expected to evolve in time during the deformation process. In this regard, the scope of the present work is to develop a three-dimensional model based on the MVAR method that is able to deal with arbitrary crystal anisotropy, arbitrary ellipsoidal void shapes at any

given orientation and general loading conditions. The above-mentioned homogenization methodologies will be completed with a framework allowing the characterization of the evolution of microstructure on average terms. More precisely, the determination of "average shape" and "average orientation" of voids will be made by using the macroscopic and the phase average strain-rates delivered by the "modified variational" homogenization method. Then, the question of the strong coupling between the anisotropy of the crystal and the (morphological) anisotropy induced by the shape and orientation of the voids will be investigated.

In the following, a brief description of the chapters of this study is proposed. Consequently, the next chapter (Chapter 2) is concerned with the theoretical aspects of this work. Then, we first define the concept of effective behavior of a porous single crystal subjected to general loading conditions. In order to proceed to specific estimates for the effective behavior of the porous single crystal, it is necessary to specify first the microstructure and the local constitutive behavior of the phases. The phases are described here by a power-law viscoplastic stress potential (or dissipation potential), whereas the microstructure is considered to be "particulate". Next, we provide homogenization estimates for "particulate" porous single crystals, whose phases are described by linearly viscous constitutive laws. For this class of composites, use is made of the Willis [1978] estimates (Ponte Castañeda and Willis [1995]) to obtain expressions for their effective behavior, as well as the corresponding phase average and second moments of the fields. Moreover, we make use of the "modified variational" approach (Danas and Aravas [2012]) to provide estimates of the effective behavior of nonlinear (or viscoplastic) porous single crystals. This variational method is based on the concept of linear comparison composite (LCC), which has the same microstructure than the nonlinear one. On the other hand, since the porous single crystals are in general subjected to finite deformations, their microstructure evolves-on average-to ellipsoidal voids in time with different shape and orientation. Thus, using the estimation of the phase average fields, we have presented the relevant evolution laws for the internal microstructural variables used to describe the volume fraction, shape and orientation of the voids, based on the studies of Ponte Castañeda and Zaidman [1994], Danas and Aravas [2012]. Finally, the aforementioned analysis is specialized for the case of porous media with ideally-plastic matrix phase.

Chapter 3 proposes a brief description of numerous previous porous materials mod-

els. Firstly, in order to make an historical overview, we start with a review of porous isotropic materials, more precisely "Gurson type models", which result from limit analysis as well as "variational type estimates". In this regard then, the famous Gurson [1977] model, which makes use of the exact solution for a shell (spherical or cylindrical cavity) under hydrostatic loadings to obtain estimates for the effective behavior of solids with ideally-plastic matrix phase with isotropic or transversely isotropic distributions of porosity, is described. This model has been extended by (Tvergaard and Needleman [1984], Tvergaard [1990]) to incorporate coalescence, in a so-called GTN model. In addition, we describe some other model which use the limit analysis framework. For instance, the Flandi and Leblond [2005a] model addressed the more general case of viscoplastic porous materials. They consider a spheroidal shell containing a confocal spheroidal void. Monchiet et al. [2014] also derive a new expression of the macroscopic yield function for a rigid ideal-plastic von Mises matrix containing spheroidal cavities, by considering Eshelby-like velocity fields (Eshelby [1957]). Or Madou and Leblond [2012a] who proposed a limit-analysis based model for general (non spheroidal) ellipsoidal cavities, through approximate homogenization of some representative elementary porous cell. On the other hand, in addition to the Gurson-like limit analysis kinematic approach, general constitutive models for porous ductile solid using a nonlinear homogenization variational structure have also been described. Thus, we start with pioneering studies of Ponte Castañeda [1991a], Kailasam and Ponte Castañeda [1998] for viscoplastic composites, which are based on the definition of linear comparison composites as proper linearization of the nonlinear ones. However, it has been shown by Ponte Castañeda [1991b], Michel and Suquet [1992] that this porous Von Mises estimates, so-called variational ("VAR") models, are overly stiff at high stress triaxiality loadings. Consequently we presented several contributions made to remedy to this issue, more specifically the SOM estimate (Ponte Castañeda [2002a,b], Danas and Ponte Castañeda [2009a]), the iterated variational estimate (Ponte Castañeda [2012], Agoras and Ponte Castañeda [2013]) or the MVAR model (Danas and Aravas [2012]) that has inspired a part of the present study. Next, we make a quick recall of some porous anisotropic matrix models with phenomenological Hill-type matrix (Benzerga and Besson [2001], Monchiet et al. [2008a], Keralavarma et al. [2011]). Finally we describe previous contributions in the context of single crystals comprising voids. This description include the study of cylindrical

voids with circular cross-section in a rigid-ideally plastic face-centered cubic (FCC) single crystals using slip line theory (Kysar et al. [2005], Gan et al. [2006], Gan and Kysar [2007]), the study two-dimensional "out of plane" cylindrical voids with circular cross-section subjected to anti-plane loadings (Idiart and Ponte Castañeda [2007]), or more recently yield functions for rate-independent single crystals containing spherical voids (Han et al. [2013], Paux et al. [2015]).

Chapter 4 proposes the numerical evaluation of the effective behavior of rate-dependent porous single crystals. Then, we have make use of numerical periodic homogenization technique, more precisely the analyze of a periodic porous material considering a unit-cell that contains a given distribution of voids.

In Chapter 5, one starts a series of chapters that are related with the application of the above mentioned methods in the context of viscoplastic porous single crystals. Specifically, this chapter deals with the estimation of the instantaneous behavior of rate-dependent porous single crystals consisting of cylindrical pores aligned in the $3-$direction and distributed randomly in the plane $1-2$, that are subjected to plane-strain loading conditions. Moreover, the voids have general elliptical cross-sections. The "MVAR" estimates proposed in this study are validated with full field FE calculations of single- and multi-void periodic unit-cells described in Chapter 4. Finally, a wide range of parameters describing the number and orientation of the slip systems (i.e., crystal anisotropy), the creep exponent (i.e., nonlinearity) of the matrix crystal, the porosity and the void shapes and orientations.

Chapter 6 is the extension of Chapter 5 to the instantaneous effective behavior of porous single crystals consisting of spherical or ellipsoidal voids that are subjected to general loading conditions. The "MVAR" estimates are compared with FE computations for a large range of parameters including non linearity (creep exponent), crystal anisotropy (FCC, BCC, HCP), microstructure anisotropy and general loading conditions. The complex coupling between crystal anisotropy and void shape and orientation is in particular studied, as well as the specific features exhibited by the hydrostatic response of the material. Finally, in the special case of spherical voids embedded in an ideally plastic crystal (i.e. $n \longrightarrow \infty$), the MVAR is compared with Han et al. [2013], Paux et al. [2015] models presented in Chapter 3.

Next, in Chapter 7, we consider the particular context of infinite number of slip systems which exhibits the same critical resolved shear stress CRSS. Thus, in this

limiting case, we develop a three-dimensional MVAR porous Tresca model that is able to deal with arbitrary ellipsoidal void shapes and general loading conditions. Such model is then validated through FE computations described in Chapter 4 and compared with Cazacu et al. [2014b,a] models.

Chapter 8 is a natural continuation of Chapter 6 in the context of finite deformations. More specifically, in this chapter we make use of the results developed in the preceding chapter 3 to estimate the evolution of the microstructure and the effective behavior in the porous single crystal subjected to general loading conditions. The "MVAR" estimates are then proposed for several crystal structures.

Finally Chapter 9 proposes a brief summary of the main findings of the present study as well as some prospects for future works. Some of them are started in the appendix (see Chapter A).

List of publications resulting from this dissertation work

1. Mbiakop A., Constantinescu A., Danas K., 2015, On void shape effects of periodic elasto-plastic materials subjected to cyclic loading, *European Journal of Mechanics A/Solids* 49, 481–499.

2. Mbiakop A., Constantinescu A., Danas K., 2015, A model for porous single crystals with cylindrical voids of elliptical cross-section, *International Journal of Solids and Stuctures* 64–65, 100–119.

3. Mbiakop A., Constantinescu A., Danas K., 2015, An analytical model for porous single crystals with ellipsoidal voids, *Journal of the Mechanics and Physics of Solids* 84, 436–467.

4. Mbiakop A., Constantinescu A., Danas K., 2015, A homogenization based yield criterion for a plastic Tresca material with ellipsoidal voids (submitted).

5. Mbiakop A., Lopez-Pamies O., Danas K., 2015, Analytical iterated variational bounds for hydrostatic behavior of porous viscoplastic materials containing ellipsoidal voids (in preparation).

6. Mbiakop A., Constantinescu A., Danas K., 2015, A model for porous single crystals with general ellipsoidal voids and microstructure evolution (in preparation).

Chapter 2

Theory

The subject of this chapter is to characterize the "effective behavior" of two-phase viscoplastic composites, and particularly of rate-dependent porous single crystals with "particulate" microstructures. The approach used accounts microstructure evolution, that is induced by the finite changes in geometry which result from the applied loading conditions. The main goal of the present work is to build constitutive models for viscoplastic porous single crystals that are able to include:

- the effects of the anisotropy of matrix behavior on void growth through crystal plasticity,

- the nonlinear response of the porous medium,

- microstructural information, such as the volume fraction, the average shape and orientation of the voids,

- the evolution of microstructure,

- development of instabilities.

In addition, these models require to be simple enough to be easily implemented into finite element codes.

In the context of this chapter, the nonlinear "variational" approach developed by (Ponte Castañeda [1991a]), together with the "modified variational" approach of (Danas and Aravas [2012]) will be used. The principal idea of this theory is the construction of convenient variational principles that make use of a "linear comparison composite" (LCC). Then, the theory discussed in the following will be applied to estimate the effective behavior and microstructure evolution in viscoplastic porous single crystals subjected to general loading conditions.

However, at this point, it is important to note that we make use of the hypothesis

of separation of length scales which implies that size of the voids (microstructure) is much smaller than the size of the single crystal and the variation of the loading conditions at the level of the single crystal. Thus, three different length scales can be introduce in the problem:

- the microscopic length scale ℓ, which characterizes the typical size of the inhomogeneities in the heterogeneous material defining the microstructure;

- the macroscopic length scale L, which characterizes the size of the specimen;

- the mesoscopic length scale l, which characterizes the size of regions within the heterogeneous material where the microstructure is essentially (statistically) uniform.

The "separation of length scales" is commonly introduced when a heterogeneous material can be seen as a homogeneous material in the macroscopic scale with some effective properties. The three length scales defined above are such that

$$\ell \ll l \ll L \tag{2.1}$$

Moreover the RVE, first introduced by Hill (Hill [1963]), is defined as the region in the material where the microstructure is considered to be statistically uniform.

2.1 Effective behavior of porous single crystals

In the following, we consider an RVE Ω of a two-phase heterogeneous medium with each phase occupying a sub-domain $\Omega^{(r)}$ ($r = 1, 2$). The notation $\langle \cdot \rangle$ and $\langle \cdot \rangle^{(r)}$ would define volume averages over the RVE (Ω) and the phase r ($\Omega^{(r)}$), respectively.

2.1.1 Effective response

In the present, the convex stress potentials $U^{(r)}$ characterize the local behavior of the phases, such that the local behavior of the composite $U(\mathbf{x}\,\boldsymbol{\sigma})$ is written as:

$$U(\mathbf{x}, \boldsymbol{\sigma}) = \sum_{r=1}^{2} \chi^{(r)}(\mathbf{x}) U^{(r)}(\boldsymbol{\sigma}) \tag{2.2}$$

where the indicator (or distribution) functions $\chi^{(r)}$ denote the distribution of the phases (and thus the microstructure) in the current configuration, such that

$$\chi^{(r)}(\mathbf{x}) = \begin{cases} 1, & \text{if} \quad \mathbf{x} \in \Omega^{(r)}, \\ 0, & \text{otherwise} \end{cases} \tag{2.3}$$

In the context of this study, more precisely for random materials, the distribution functions $\chi^{(r)}$ are generally unknown or known partially (volume fractions, two-point correlation functions) and they can only be defined in terms of $n-$point statistics. Consequently, the local constitutive behavior of the composite and the phases can be expressed through the relation between the Cauchy stress $\boldsymbol{\sigma}$ and the Eulerian strain-rate $\boldsymbol{D}$,

$$\boldsymbol{D}(\mathbf{x}) = \frac{\partial U(\mathbf{x}, \boldsymbol{\sigma})}{\partial \boldsymbol{\sigma}}, \quad \forall \mathbf{x} \in \Omega \quad \text{and} \quad \boldsymbol{D}^{(r)} = \frac{\partial U^{(r)}(\boldsymbol{\sigma})}{\partial \boldsymbol{\sigma}}, \quad r = 1, 2 \qquad (2.4)$$

In these relations, the strain-rate $\boldsymbol{D}(\mathbf{x})$ is the symmetric part of the velocity gradient $\boldsymbol{L} = \nabla \mathbf{v}$ written in classical notation as $\boldsymbol{D} = \left[\nabla \mathbf{v} + (\nabla \mathbf{v})^T \right] / 2$, whereas, for later use, we may also introduce the corresponding spin tensor $\boldsymbol{\Omega}(\mathbf{x})$ as the skew-symmetric part of this velocity gradient such that $\boldsymbol{\Omega} = \left[\nabla \mathbf{v} - (\nabla \mathbf{v})^T \right] / 2$. Moreover, it is useful to define the following local constitutive function

$$\mathbf{S}_t(\mathbf{x}) = \frac{\partial \boldsymbol{D}(\mathbf{x})}{\partial \boldsymbol{\sigma}(\mathbf{x})} = \frac{\partial^2 U(\mathbf{x}, \boldsymbol{\sigma})}{\partial \boldsymbol{\sigma} \partial \boldsymbol{\sigma}}, \quad \forall \mathbf{x} \in \Omega, \qquad \mathbf{S}_t^{(r)} = \frac{\partial \boldsymbol{D}^{(r)}}{\partial \boldsymbol{\sigma}^{(r)}} = \frac{\partial^2 U^{(r)}(\boldsymbol{\sigma})}{\partial \boldsymbol{\sigma} \partial \boldsymbol{\sigma}}, \quad r = 1, 2$$
$$(2.5)$$

with $\mathbf{S}_t$ denoting a fourth-order tensor with both the minor and major symmetries and is used to describe the incremental response of the heterogeneous medium and the phases at a given instant. Under the hypotheses of statistical uniformity and the aforementioned separation of length scales, the effective stress potential $\tilde{U}$ of the two-phase heterogeneous medium is defined as (Hill [1963], Hutchinson [1976]):

$$\widetilde{U}(\overline{\boldsymbol{\sigma}}) = \min_{\boldsymbol{\sigma} \in S(\overline{\boldsymbol{\sigma}})} \langle U(\mathbf{x}, \boldsymbol{\sigma}) \rangle = \sum_{r=1}^{2} c^{(r)} \min_{\boldsymbol{\sigma} \in S(\overline{\boldsymbol{\sigma}})} \langle U^{(r)}(\boldsymbol{\sigma}) \rangle^{(r)}, \qquad (2.6)$$

where

$$S(\overline{\boldsymbol{\sigma}}) = \{ \boldsymbol{\sigma}, \operatorname{div} \boldsymbol{\sigma} = 0 \quad \text{in} \quad \Omega, \langle \boldsymbol{\sigma} \rangle = \overline{\boldsymbol{\sigma}} \} \qquad (2.7)$$

is the set of statically admissible stresses, compatible with the applied average stress $\overline{\boldsymbol{\sigma}}$. In addition, the quantities $c(r) = \langle \chi^{(r)} \rangle$ represent the volume fractions of the given phases and thus they satisfy the identity $\sum_{r=1}^{2} c^{(r)} = 1$. In analogy to the local constitutive behavior provided in relation (2.4), and by making use of Hill's lemma (Hill [1963]), the instantaneous relation between the average Cauchy stress, $\overline{\boldsymbol{\sigma}} = \langle \boldsymbol{\sigma} \rangle$, and the average Eulerian strain-rate, $\overline{\boldsymbol{D}} = \langle \boldsymbol{D} \rangle$, is given by

$$\overline{\boldsymbol{D}} = \frac{\partial \widetilde{U}}{\partial \overline{\boldsymbol{\sigma}}}(\overline{\boldsymbol{\sigma}}). \qquad (2.8)$$

This expression is a constitutive law for the two-phase material at each instant in time, provided if the microstructure is known. Furthermore, as precise in the introduction, the materials considered here can undergo finite deformations, and consequently their microstructure is expected to evolve in time. Thus, their effective behavior will change in time due to the changes in the microstructure. This evolution of the microstructure needs to be described for a full treatment of the problem. Such expressions will be given in a later section.

On the other hand, the above-described analysis can also be made in the context of a dissipation potential $W^{(r)}(\boldsymbol{D})$, which is dual (by means of the Legendre-Fenchel transform) to the stress potential $U^{(r)}(\boldsymbol{\sigma})$ and is given by

$$W^{(r)}(\boldsymbol{D}) = \max_{\boldsymbol{\sigma}} \left\{ \boldsymbol{\sigma} \cdot \boldsymbol{D} - U^{(r)}(\boldsymbol{\sigma}) \right\}, \quad r = 1, 2 \tag{2.9}$$

with

$$\boldsymbol{\sigma}^{(r)} = \frac{\partial W^{(r)}(\boldsymbol{D})}{\partial \boldsymbol{D}}, \quad r = 1, 2 \tag{2.10}$$

The effective behavior can then be defined in terms of the effective dissipation potential by

$$\widetilde{W}(\overline{\boldsymbol{D}}) = \min_{\boldsymbol{D} \in \mathcal{K}(\overline{\boldsymbol{D}})} \langle W(\mathbf{x}, \boldsymbol{D}) \rangle = \sum_{r=1}^{2} c^{(r)} \min_{\boldsymbol{D} \in \mathcal{K}(\overline{\boldsymbol{D}})} \langle W^{(r)}(\boldsymbol{D}) \rangle^{(r)}, \tag{2.11}$$

where $\mathcal{K}(\overline{\boldsymbol{D}})$ is the set of kinematically admissible strain-rate fields given by

$$\mathcal{K}(\overline{\boldsymbol{D}}) = \left\{ \boldsymbol{D} | \text{there is v where} \quad \boldsymbol{D} = \frac{1}{2} \left[\nabla \mathbf{v} + (\nabla \mathbf{v})^T \right] \quad \text{in} \quad \Omega, \quad \mathbf{v} = \overline{\boldsymbol{L}} \mathbf{x} \quad \text{on} \quad \partial\Omega \right\}, \tag{2.12}$$

Here, $\overline{L}$ is the macroscopic velocity gradient, while the macroscopic strain-rate $\overline{\boldsymbol{D}}$ and spin $\overline{\Omega}$ are given by

$$\overline{\boldsymbol{D}} = \frac{1}{2} \left[\overline{\boldsymbol{L}} + \overline{\boldsymbol{L}}^T \right], \quad \overline{\Omega} = \frac{1}{2} \left[\overline{\boldsymbol{L}} - \overline{\boldsymbol{L}}^T \right] \tag{2.13}$$

Furthermore, the effective constitutive behavior of the material is given by

$$\overline{\boldsymbol{\sigma}} = \frac{\partial \widetilde{W}}{\partial \overline{\boldsymbol{D}}} (\overline{\boldsymbol{D}}). \tag{2.14}$$

This description for the effective behavior of a heterogeneous material in terms of $\widetilde{W}$ is equivalent to the one described in relation (2.6) in terms of the effective stress potential $\widetilde{U}$. In the present work, where the focus is on porous materials, it is convenient to

make use of the effective stress potential $\widetilde{U}$ instead of the dissipation potential $\widetilde{W}$, and consequently no explicit results will be given for $\widetilde{W}$ in the rest of the text.

To summarize, the problem of estimating the effective behavior of two-phase non-linear composites is equivalent to that of estimating the function $\widetilde{U}$ in relation (2.6). Nevertheless, computing these functions exactly is an extremely difficult task, which would require, in general, an intensive full-field numerical simulation assuming that the exact location of the phases in the RVE is known. However, in most of the cases, the microstructure is not fully deterministic, and thus, the exact location of the phases in the RVE is not known. For this reason, in this work, we will make use of a variational homogenization technique to be discussed in the following sections.

Let us now use the general framework seen previously, that described the material behavior to any two-phase heterogeneous medium, for the special case of a two-phase porous medium, which is the main subject of this work. In order to achieve this goal, we consider the RVE Ω to be a two-phase porous medium with each phase occupying a sub-domain $\Omega^{(r)}(r = 1, 2)$. The vacuous phase is identified with phase 2 and the non-vacuous phase (i.e., matrix phase) is denoted as phase 1. In the following, the brackets $\langle \cdot \rangle$ and $\langle \cdot \rangle^{(r)}$ would define volume averages over the RVE (Ω) and the phase r ($\Omega^{(r)}$), respectively. According definitions (2.4), the local behavior of the matrix phase is characterized by an anisotropic, convex stress potential $U_1 \equiv U$, such that the corresponding Cauchy stress $\boldsymbol{\sigma}$ and the Eulerian strain-rate $\boldsymbol{D}$ are related by

$$\boldsymbol{D} = \frac{\partial U}{\partial \boldsymbol{\sigma}}(\boldsymbol{\sigma}), \tag{2.15}$$

with the stress potential of the porous phase U_2 is equal to zero. So, from the definition (2.6), it comes that the effective stress potential $\widetilde{U}$ for a porous medium can be reduced to

$$\widetilde{U}(\overline{\boldsymbol{\sigma}}) = (1 - f) \min_{\boldsymbol{\sigma} \in S(\overline{\boldsymbol{\sigma}})} \langle U(\boldsymbol{\sigma}) \rangle^{(1)}, \tag{2.16}$$

where $f = c^{(2)}$ and $1 - f = c^{(1)}$ denote the volume fractions of the porous (i.e., porosity) and the matrix phases, respectively and

$$S(\overline{\boldsymbol{\sigma}}) = \left\{ \boldsymbol{\sigma}, \mathrm{div}\boldsymbol{\sigma} = 0 \quad \text{in} \quad \Omega, \boldsymbol{\sigma}\mathbf{n} = 0 \quad \text{on} \quad \partial\Omega^{(2)}, \langle \boldsymbol{\sigma} \rangle = \overline{\boldsymbol{\sigma}} \right\}, \tag{2.17}$$

is the set of statically admissible stresses that are compatible with the average stress $\overline{\boldsymbol{\sigma}}$ and zero tractions on the surface of the voids. The effective constitutive relation

between the average Cauchy stress, $\overline{\boldsymbol{\sigma}} = \langle \boldsymbol{\sigma} \rangle$, and the average Eulerian strain-rate, $\overline{\boldsymbol{D}} = \langle \boldsymbol{D} \rangle$ is given by relation (2.8).

Practically, the estimation of the effective stress potential $\widetilde{U}$ expressed as (2.16) for a nonlinear porous material requires further information about the distribution of the phases in the RVE. Thus, in the next part, we will define the appropriate microstructures for the class of porous materials to be considered here.

2.1.2 Microstructures

Generally, the physical properties of a random composite material vary with position $\mathbf{x}$ and from sample to sample. Thus, in order to determine completely the location of the phases and hence the microstructure, it is important to specify the functions $\chi^{(r)}(x)$ for all $\mathbf{x}$ in Ω. Nevertheless, in most of the cases of random composites, this is not possible and consequently the description of such materials can be carried out making use of $n-$point correlation functions (n finite integer number). Moreover, these random systems can be considered to be statistically uniform, which implies that the $n-$point correlation functions are insensitive to translations. For these media, it is usual to make an assumption of ergodic type, which yields that local configurations occur every any one specimen with the frequency with which they occur over a single neighborhood in an ensemble of specimens. Consequently, we can be replace ensemble averages by volume averages, and hence the one-point statistics simply give information about the volume fraction of the phases. As an example, the porosity was defined previously in terms of the distribution functions by $f = \langle \chi^{(2)} \rangle$.

Moreover, the $n-$point ($n \geq 2$) statistics give information about the relative position of the phases in Ω. In this study, we will use homogenization methods (Hashin and Shtrikman [1963], Willis [1977], Ponte Castañeda and Willis [1995]) that involve information up to two-point statistics, even if there exist approach that make use of three-point statistics (Beran [1965], Kroner [1977], Milton [1982]), which are more or less complicated and will not be used here. In this regard, following previous work of Willis [1977], we consider a "particulate" microstructure which is a generalization of the Eshelby [1957] dilute microstructure in the nondilute regime. More specifically, we consider a "particulate" porous material consisting of ellipsoidal voids aligned at a certain direction, whereas the distribution function, which is also taken to be ellip-

soidal in shape, provides information about the distribution of the centers of the pores. For simplicity, one will also consider that the shape and orientation of the distribution function is identical to the shape and orientation of the voids themselves (see Danas and Ponte Castañeda [2009a]). Nevertheless, this analysis can be readily extended to distribution of a different shape and orientation than the voids (Ponte Castañeda and Willis [1995], Kailasam and Ponte Castañeda [1998]). Thus, as shown in fig. 2.1, the internal variables characterizing the state of the microstructure are:

- The porosity or volume fraction of the voids $f = V_2/V$, where $V = V_1 + V_2$ is the total volume, with V_1 and V_2 being the volume occupied by the matrix and the vacuous phase, respectively.

- The two aspect ratios $w_1 = a_3/a_1$, $w_2 = a_3/a_2$ ($w_3 = 1$) with $2a_i$ ($i = 1, 2, 3$) denoting the lengths of the principal axes of the representative elliptical void.

- The orientation unit vectors $\mathbf{n}^{(i)}$ ($i = 1, 2, 3$), defining an orthonormal basis set, which coincides with the principal axes of the representative ellipsoidal void.

The above set of the microstructural variables can then be denoted by the set

$$s_\alpha = \left\{ f, w_1, w_2, \mathbf{n}^{(1)}, \mathbf{n}^{(2)}, \mathbf{n}^{(3)} \right\} \tag{2.18}$$

Figure 2.1: Representative ellipsoidal voids embedded in a crystal matrix.

In addition, the shape and orientation of the voids, as well as the shape and orientation of the two-point correlation function can be completely characterized by a symmetric second-order tensor $\mathbf{Z}$ which is given in terms of the two aspect ratios and the three orientation vectors shown in Fig. 2.1, such that

$$\mathbf{Z} = w_1 \mathbf{n}^{(1)} \times \mathbf{n}^{(1)} + w_2 \mathbf{n}^{(2)} \times \mathbf{n}^{(2)} + \mathbf{n}^{(3)} \times \mathbf{n}^{(3)}, \quad \det(\mathbf{Z}) = w_1 w_2. \tag{2.19}$$

Furthermore, it is useful to explore other types of particulate microstructures, which can be derived easily by appropriate specialization of the aforementioned variables s_α (Budiansky et al. [1982]). In this regard, the following cases can be considered:

– $a_1 \to 0$ or $a_2 \to 0$ or $a_3 \to 0$. Thus, if the porosity f remains finite, laminated microstructure is recovered (or alternatively a "porous sandwich"), whereas if $f \to 0$, a porous material with penny-shaped cracks is formed and thus the notion of density of cracks needs to be introduced.

– $a_1 \to \infty$ or $a_2 \to \infty$ or $a_3 \to \infty$. Thus, if the porosity $f \to 0$, a porous material with infinitely thin needles is generated, whereas if f remains finite, the cylindrical microstructure is recovered.

The last particular situation (cylindrical microstructure) is a main case of interest since it can describe two-dimensional (2D) porous single crystals containing polydisperse cylindrical voids aligned with the x_3−axis. In this context, the voids are randomly and uniformly distributed in for instance the transverse plane $x_1 — x_2$. This material is subjected to plane-strain loading in the x_3−direction. In this regard, as shown in Fig. 2.2, the internal variables characterizing the state of the microstructure becomes:

· The porosity or volume fraction of the voids f.

· The aspect ratio $w = a_2/a_1$, with $2a_i$ ($i = 1, 2$) denoting the lengths of the principal axes of the representative elliptical void, in the plane $1 − 2$. The cases $w = 1$ and $w \neq 1$ correspond to voids with circular and elliptical cross-sections, respectively.

· The in-plane orientation unit vectors $\mathbf{n}^{(i)}$ ($i = 1, 2$), defining an orthonormal basis set, which coincides with the principal axes of the representative elliptical void. As a consequence of the 2D representation of the microstructure the two orientation vectors $\mathbf{n}^{(i)}$ can be easily parameterized in terms of a single Euler angle, ψ,

$$\mathbf{n}^{(1)} = \cos\psi\,\mathbf{e}_1 + \sin\psi\,\mathbf{e}_2, \quad \mathbf{n}^{(2)} = -\sin\psi\,\mathbf{e}_1 + \cos\psi\,\mathbf{e}_2 \tag{2.20}$$

The above set of the microstructural variables s_α can then be reduced by the set $s_\alpha = \{f, w, \psi\}$.

Figure 2.2: Representative elliptical cross-section voids embedded in a crystal matrix.

Then, to conclude, the set of the above-mentioned microstructural variables s_α

provide a general three-dimensional description of a particulate porous material. It is evident that in the more general case, where the aspect ratios and the orientation of the ellipsoidal voids are such that $w_1 \neq w_2 \neq 1$ and $\mathbf{n}^{(i)} \neq \mathbf{e}^{(i)}$, the initially anisotropic single crystal becomes highly anisotropic and estimating its overall response appears as a huge challenge. However, linear and nonlinear homogenization methods have been developed in the recent years that are capable of providing estimates and bounds for the effective behavior of such particulate composites. In the following sections, use of these techniques will be made to obtain estimates for crystalline viscoplastic porous media.

2.1.3   Gauge surface

For later use, it is convenient to define here the notion of the gauge surface. Gauge surfaces are equipotential surfaces which have a physical importance in the present analysis as they characterize the domain of statically admissible stresses and are analogous to the yield surfaces in rate-independent plasticity.

Using the homogeneity of the stress potential (2.31) for single crystal matrix together with the general definition of the effective stress behavior (2.16), one can show that the effective stress potential $\widetilde{U}$ is also homogeneous of degree $n + 1$ in $\overline{\boldsymbol{\sigma}}$.

Therefore, it is convenient to introduce the so-called gauge surface P_n (the subscript being used to denote the dependence on the creep exponent n) as in Leblond et al. [1994]. More precisely, it is sufficient to study only one of the equi-potential surfaces $\left\{ \overline{\boldsymbol{\sigma}}, \widetilde{U}(\overline{\boldsymbol{\sigma}}) = const \right\}$ i.e., the so-called gauge surface P_n of the porous material. For instance, in the case of slip systems with identical CRSS τ_0 and reference slip-rate $\dot{\gamma}_0$, one can define the equi-potential surfaces

$$P_n \equiv \left\{ \overline{\boldsymbol{\Sigma}}, \ \widetilde{U}(\overline{\boldsymbol{\Sigma}}, s_\alpha) = \frac{\dot{\gamma}_0 \tau_0^{-n}}{n+1} \right\}. \tag{2.21}$$

The associated gauge factor Γ_n are defined as

$$\widetilde{U}(\overline{\boldsymbol{\sigma}}; s_\alpha) = \frac{\gamma_0 \tau_0}{n+1} \left(\frac{\left| \Gamma_n(\overline{\boldsymbol{\sigma}}; \boldsymbol{\mu}^{(s)}; s_\alpha) \right|}{\tau_0} \right)^{n+1}, \tag{2.22}$$

Then, the gauge function $\widetilde{\Phi}_n$ provides the equation for the gauge surface via the expression

$$\overline{\boldsymbol{\Sigma}} \in P_n \iff \widetilde{\Phi}_n(\overline{\boldsymbol{\Sigma}}, s_\alpha) = (n+1)\widetilde{U}(\overline{\boldsymbol{\Sigma}}, s_\alpha) - \dot{\gamma}_0 \tau_0^{-n} = 0. \tag{2.23}$$

The subscript n has been used to indicate that the gauge function depends explicitly on the creep exponent of the single crystal matrix. The above definitions of the gauge surface and gauge function are analogous to the well known yield function and yield surface in the context of rate-independant plasticity ($n \to \infty$).

The gauge factor Γ_n is homogeneous of degree one in $\overline{\boldsymbol{\sigma}}$, and therefore $\overline{\boldsymbol{\Sigma}}$ is homogeneous of degree zero in $\overline{\boldsymbol{\sigma}}$.

The subscript n has been used to indicate that the gauge function depends explicitly on the nonlinear exponent of the matrix phase. The above definitions of the gauge surface and the gauge function are analogous to the corresponding well known notions of the yield function and the yield surface in the context of ideal-plasticity. Such discussion is made in the following subsection, where the case of ideal-plasticity is particularly studied.

Using the previous definitions, we can redefine the stress triaxiality X_Σ in terms of $\overline{\boldsymbol{\Sigma}}$ as

$$X_\Sigma = \frac{\overline{\Sigma}_m}{\overline{\Sigma}_{eq}}, \quad \overline{\Sigma}_{eq} = \sqrt{3\overline{\boldsymbol{\Sigma}}^d \cdot \overline{\boldsymbol{\Sigma}}^d / 2} \quad, \overline{\Sigma}_m = \overline{\Sigma}_{ii}/3, i = 1, 2, 3, \tag{2.24}$$

where $\overline{\Sigma}_m$ and $\overline{\Sigma}_{eq}$ denote the mean and equivalent part of $\overline{\boldsymbol{\Sigma}}$.

On the other hand, it comes from definition (2.8) and (2.22) that

$$\overline{\boldsymbol{D}} = \gamma_0 \left(\frac{\Gamma_n(\overline{\boldsymbol{\sigma}}; \boldsymbol{\mu}^{(s)}; s_\alpha)}{\tau_0} \right)^n \frac{\partial \Gamma_n(\overline{\boldsymbol{\sigma}}; \boldsymbol{\mu}^{(s)}; s_\alpha)}{\partial \overline{\boldsymbol{\sigma}}} \tag{2.25}$$

2.2 Local constitutive behavior of single crystals

In order to proceed to specific results for nonlinear porous media, we need to define the constitutive relation that describes the local behavior of the matrix phase.

2.2.1 Constitutive behavior of the constituents

Let us consider a reference single crystal which undergoes viscoplastic deformation on a set of K preferred crystallographic slip systems. At this stage, for simplicity in the homogenization procedure elasticity effects are neglected. Then, these systems are characterized by the second-order Schmid tensors $\boldsymbol{\mu}^{(s)}$ ($\forall s = 1, ..., K$) given by

$$\boldsymbol{\mu}^{(s)} = \frac{1}{2} \left(\mathbf{m}^{(s)} \otimes \mathbf{s}^{(s)} + \mathbf{s}^{(s)} \otimes \mathbf{m}^{(s)} \right), \tag{2.26}$$

with $\mathbf{m}^{(s)}$ and $\mathbf{s}^{(s)}$ denoting the unit vectors normal to the slip plane and along the slip direction in the sth system, respectively.

When the crystal is subjected to a stress $\boldsymbol{\sigma}$, the resolved shear stress acting on the sth slip system is given by the Schmid law

$$\tau^{(s)} = \boldsymbol{\sigma} \cdot \boldsymbol{\mu}^{(s)}, \tag{2.27}$$

while the strain-rate $\boldsymbol{D}$ in the crystal is assumed to be given by the superposition of the slip-rates of each slip system, i.e. $\boldsymbol{D} = \sum_{s=1}^{K} \dot{\gamma}^{(s)} \boldsymbol{\mu}^{(s)}$. The slip-rate $\dot{\gamma}^{(s)}$ is assumed to depend on the resolved shear stress $\tau^{(s)}$, via a slip potential $\Psi^{(s)}$ in such a way that

$$\dot{\gamma}^{(s)} = \frac{\partial \Psi^{(s)}}{\partial \tau^{(s)}}(\tau^{(s)}). \tag{2.28}$$

The slip potentials $\Psi^{(s)}$ are assumed to be convex, incompressible and expressed via the power-law form

$$\Psi^{(s)}(\tau) = \frac{\dot{\gamma}_0^{(s)} \tau_0^{(s)}}{n+1} \left(\frac{|\tau|}{\tau_0^{(s)}} \right)^{n+1}, \tag{2.29}$$

where $n \geq 1$, $\dot{\gamma}_0^{(s)}$ and $\tau_0^{(s)}$ denote the creep exponent, the reference slip-rate and the reference flow stress (also denoted critical resolved shear stress CRSS) of the sth slip system, respectively. In addition, let us notice that the limiting values of the exponent, $n = 1$ and $n \to \infty$ correspond to linear viscoelasticity and rate-independent perfect plasticity, respectively. In this connection, it is recalled that, even though the slip potentials $\Psi^{(s)}$ are not differentiable in the perfect crystal plasticity case, it is still possible to relate $\dot{\gamma}^{(s)}$ and $\tau^{(s)}$ via the subdifferential of convex analysis.

An alternative and equivalent way to write down $\tau^{(s)}$ in equation (2.27) is by use of the fourth-order "Schmid" projection tensors $\mathbf{E}^{(s)}$ (see DeBotton and Ponte Castañeda [1995]), such that

$$\left| \tau^{(s)} \right| = \sqrt{\frac{\boldsymbol{\sigma} \cdot \mathbf{E}^{(s)} \cdot \boldsymbol{\sigma}}{2}}, \quad \mathbf{E}^{(s)} = 2\boldsymbol{\mu}^{(s)} \otimes \boldsymbol{\mu}^{(s)} \quad \forall s = 1, K. \tag{2.30}$$

Adding up the potentials of all the slip systems we obtain the constitutive behavior of the matrix phase, characterized by the viscoplastic stress potential U such that

$$U(\boldsymbol{\sigma}) = \sum_{s=1}^{K} \Psi^{(s)}(\tau^{(s)}) = \sum_{s=1}^{K} \frac{\dot{\gamma}_0^{(s)} \tau_0^{(s)}}{n+1} \left(\frac{|\tau^{(s)}|}{\tau_0^{(s)}} \right)^{n+1}. \tag{2.31}$$

Obviously, in this last expression, U is a homogeneous function of degree $n + 1$ in the stress $\boldsymbol{\sigma}$.

The corresponding Cauchy stress $\boldsymbol{\sigma}$ and the Eulerian strain-rate $\boldsymbol{D}$ in the matrix are related through the constitutive relation

$$\boldsymbol{D} = \frac{\partial U}{\partial \boldsymbol{\sigma}}\left(\boldsymbol{\sigma}\right). \tag{2.32}$$

2.2.2 The limit of infinite number of slip systems

The purpose of this section is to establish a connection between stress potentials corresponding to the case of infinite number of slip systems (i.e., $K \to \infty$) and purely isotropic stress potentials. The results of this section will be used in section 2.4.4 to obtain accurate estimates of the porous single crystal in the case of purely hydrostatic loading conditions.

In view of this scope, we choose to study the special, albeit very useful case of K equiangular slip systems (system equally partitioned in 3D space) with identical CRSS and reference slip-rate such that

$$\tau_0^{(s)} = \tau_0, \, \dot{\gamma}_0^{(s)} = \dot{\gamma}_0, \quad \forall s = 1, K. \tag{2.33}$$

This analysis will be shown to be of critical importance in the following sections.

If one considers a triaxial loading state such that the three stresses are aligned with the fixed laboratory axes, the stress tensor can be written as

$$\boldsymbol{\sigma} = \sigma_m\{1, 1, 1\} + \frac{2\sigma_{eq}}{3}\left\{\cos\theta, -\cos\left(\theta + \frac{\pi}{3}\right), -\cos\left(\theta - \frac{\pi}{3}\right)\right\} \tag{2.34}$$

where $\sigma_{eq} = \sqrt{3\,s_{ij}\,s_{ij}/2}$, $\sigma_m = \sigma_{kk}/3$ and $cos(\theta) = 27\det(s_{ij})/2\sigma_{eq}^3$ denote the equivalent Von Mises stress, the hydrostatic stress and the Lode angle, respectively, while **s** is the stress deviator. By introducing this relation in equation (2.31) in the limit $K \longrightarrow \infty$, the viscoplastic stress potential U becomes isotropic and its numerical computation leads to the following isotropic potential (see details in appendix 2.7)

$$\lim_{K \to \infty} U(\boldsymbol{\sigma}) = \frac{\beta_n}{n+1}\left(\sigma_{eq}\,g_\theta\right)^{n+1} \lim_{K \to \infty}\left(\dot{\gamma}_0\tau_0^{-n}\,K\right). \tag{2.35}$$

Here, g_θ is a periodic function of θ with period $\pi/3$ (i.e., $g_0 = g_{\pi/3}$) while β_n is a monotonically decreasing function of the exponent n. These functions were obtained numerically (see details in appendix 2.7) and fitted with simple analytical expressions, such that

$$g_\theta \cong \left(\cos\left(\theta - \frac{\pi}{3}\right)\right)^{n+1}, \qquad \beta_n \cong \frac{4}{25}\,6^{-\frac{n}{2}}. \tag{2.36}$$

Next, by introducing σ_0 and $\dot{\epsilon}_0$ as the reference strain-rate and isotropic flow stress of an isotropic material, respectively, one can set

$$\beta_n \lim_{K \to \infty} \left(\dot{\gamma}_0 \tau_0^{-n} K \right) = \dot{\epsilon}_0 \sigma_0^{-n}. \tag{2.37}$$

This implies that the infinite-slip-system stress potential $\lim_{K \to \infty} U(\boldsymbol{\sigma})$ in equation (2.35) leads to a Lode-dependent isotropic stress potential of the form

$$U_\theta(\boldsymbol{\sigma}) = \frac{\dot{\epsilon}_0 \sigma_0^{-n}}{n+1} \left(\sigma_{eq} \, g_\theta \right)^{n+1}. \tag{2.38}$$

As already noted in the beginning of this section, this last result will be very useful in obtaining accurate results for the purely hydrostatic response of porous single crystals (see section 2.4.4) by appropriate use of exact results that exist in the context of porous materials with purely isotropic matrix phase (such as the one in equation(2.38)) and hydrostatic stress loading states.

2.2.3 Porous media with ideally-plastic matrix phase: General expressions

In this subsection, a special case of the above mentioned viscoplastic behavior is the one of ideal-plasticity obtained by letting $n \to \infty$ or $m \to 0$. From relation (2.31), it follows directly that the stress potential of the matrix phase is defined in the ideally-plastic limit as

$$U(\boldsymbol{\sigma}) = \begin{cases} 0, & \text{if} \quad \left| \tau^{(s)} \right| / \tau_0^{(s)} \leq 1 \quad \forall s = 1, ..., K, \\ \infty, & \text{otherwise,} \end{cases} \tag{2.39}$$

which implies that the yield function can be expressed as

$$\Phi(\boldsymbol{\sigma}) = \max_{s=1,K} \left\{ \left| \tau^{(s)} \right| - \tau_0^{(s)} \right\} \tag{2.40}$$

such that the yield surface is given by $\Phi(\boldsymbol{\sigma}) = 0$.

Now, making use of definition (2.22) in the ideally-plastic limit, the effective stress potential $\widetilde{U}$ of the porous medium becomes

$$\widetilde{U}(\overline{\boldsymbol{\sigma}}; s_\alpha) = \begin{cases} 0, & \text{if} \quad \Gamma_\infty(\overline{\boldsymbol{\sigma}}; \boldsymbol{\mu}^{(s)}; s_\alpha)/\tau_0 \leq 1, \\ \infty, & \text{otherwise,} \end{cases} \tag{2.41}$$

where we have assumed that that all slip systems have the same reference flow stress $\tau_0^{(s)} = \tau_0, \forall s = 1, .., K$.

This relation implies that the equation describing the yield locus is

$$\Gamma_\infty(\overline{\boldsymbol{\sigma}}; \boldsymbol{\mu}^{(s)}; s_\alpha) = \tau_0 \tag{2.42}$$

Furthermore, using the last criterion together with definition (2.21), it is readily derived that

$$\overline{\boldsymbol{\Sigma}} = \frac{\overline{\boldsymbol{\sigma}}}{\tau_0}, \tag{2.43}$$

in the limit as $n \to \infty$. Then, it follows from (2.23), that, in the ideally-plastic limit, the gauge function may be expressed as

$$\widetilde{\Phi}_\infty(\overline{\boldsymbol{\Sigma}}; \boldsymbol{\mu}^{(s)}; s_\alpha) = \Gamma_\infty(\overline{\boldsymbol{\Sigma}}; \boldsymbol{\mu}^{(s)}; s_\alpha) - 1 = \Gamma_\infty(\frac{\overline{\boldsymbol{\sigma}}}{\tau_0}; \boldsymbol{\mu}^{(s)}; s_\alpha) - 1 = \widetilde{\Phi}_\infty(\frac{\overline{\boldsymbol{\sigma}}}{\tau_0}; \boldsymbol{\mu}^{(s)}; s_\alpha), \tag{2.44}$$

so that $\widetilde{\Phi}_\infty(\overline{\boldsymbol{\Sigma}})$ defines the corresponding gauge surface

$$P_\infty \equiv \left\{ \overline{\boldsymbol{\Sigma}}, \quad \Gamma_\infty(\overline{\boldsymbol{\Sigma}}; \boldsymbol{\mu}^{(s)}; s_\alpha) = 1 \right\} \tag{2.45}$$

In the following, it is convenient to define the yield criterion in terms of the macroscopic stress $\overline{\boldsymbol{\sigma}}$. This can be easily extracted from (2.44) by making use of the fact that Γ_∞ is a positively homogeneous function of degree one in its arguments, such that

$$\widetilde{\Phi}(\overline{\boldsymbol{\sigma}}; \boldsymbol{\mu}_{(k)}; s_\alpha) = \tau_0 \widetilde{\Phi}_\infty(\overline{\boldsymbol{\sigma}}; \boldsymbol{\mu}^{(s)}; s_\alpha) = \tau_0 \Gamma_\infty(\overline{\boldsymbol{\sigma}}/\tau_0; \boldsymbol{\mu}^{(s)}; s_\alpha) - \tau_0 = \Gamma_\infty(\overline{\boldsymbol{\sigma}}; \boldsymbol{\mu}^{(s)}; s_\alpha) - \tau_0 \tag{2.46}$$

Thus, $\widetilde{\Phi}(\overline{\boldsymbol{\sigma}}) = 0$ is the equation describing the yield surface

$$P \equiv \left\{ \overline{\boldsymbol{\sigma}}, \quad \Gamma_\infty(\overline{\boldsymbol{\sigma}}; \boldsymbol{\mu}^{(s)}; s_\alpha) = \tau_0 \right\} \tag{2.47}$$

which is nothing else but an homothetic expansion by a factor of τ_0 of the gauge surface P_∞. In other words, the locus of the points in P_∞ can simply be constructed by normalizing the locus of points in P by τ_0.

Consequently, it follows from (2.46) that the corresponding macroscopic strain-rate $\overline{\boldsymbol{D}}$ is defined by

$$\overline{\boldsymbol{D}} = \dot{\Lambda} \frac{\partial \widetilde{\Phi}}{\partial \overline{\boldsymbol{\sigma}}} = \dot{\Lambda} \frac{\partial \Gamma_\infty(\overline{\boldsymbol{\sigma}}; \boldsymbol{\mu}^{(s)}; s_\alpha)}{\partial \overline{\boldsymbol{\sigma}}} \tag{2.48}$$

where $\dot{\Lambda}$ is a positive parameter, known as the plastic multiplier and determined by the consistency condition $\dot{\widetilde{\Phi}}$.

In turn, the consistency condition provides information about the incremental response of the porous material and, by making use of the fact that $\widetilde{\Phi}$ is an isotropic function of its arguments, one finds that

$$\dot{\widetilde{\Phi}} = \frac{\partial \widetilde{\Phi}}{\partial \overline{\boldsymbol{\sigma}}} \overset{\triangledown}{\overline{\boldsymbol{\sigma}}} + \frac{\partial \widetilde{\Phi}}{\partial \boldsymbol{\mu}^{(s)}} \overset{\triangledown}{\boldsymbol{\mu}}^{(s)} + \frac{\partial \widetilde{\Phi}}{\partial s_\alpha} \overset{\triangledown}{s}_\alpha = 0. \tag{2.49}$$

In this expression, the symbol $\overset{\triangledown}{()}$ denotes the Jaumann rate of a given quantity, while

$$\overset{\triangledown}{s}_\alpha = \left\{ \dot{f}, \dot{w}_1, \dot{w}_2, \overset{\triangledown}{\mathbf{n}}^{(1)}, \overset{\triangledown}{\mathbf{n}}^{(2)}, \overset{\triangledown}{\mathbf{n}}^{(3)} \right\}. \tag{2.50}$$

In all the previous relations, the "dot" symbols has been used to denote the time derivatives.

2.3 Linear viscous behavior

As already discussed, we will make use of the "variational" nonlinear homogenization method (Ponte Castañeda [1991a]) to estimate the effective behavior of the viscoplastic porous single crystal. Due to the fact that these nonlinear methods use available results for linearly viscous porous media, it is useful here to recall briefly certain relations for linear composites. Thus, this section concerns the determination of the effective behavior of linearly viscous, two-phase composites, which are specialized later to linearly viscous porous media. It is worth noting here that the linearly viscous is analogous to the linear elastic material.

More precisely, we consider a linearly viscous composite consisting of a matrix phase identified with the label 1, and an inclusion phase identified with label 2. Then, let these phases be described by quadratic stress potentials of the form

$$U^{(r)}(\boldsymbol{\sigma}) = \frac{1}{2}\boldsymbol{\sigma}(\mathbf{x}) \cdot \mathbf{S}^{(r)}\boldsymbol{\sigma}(\mathbf{x}), \quad r = 1, 2, \quad \forall \mathbf{x} \in \Omega^{(r)}, \tag{2.51}$$

where $\mathbf{S}^{(r)}$ are fourth-order, positive-definite, tensors that possess both major and minor symmetries. The corresponding stress-strain-rate relation of such materials is linear and reads

$$\boldsymbol{D}^{(r)} = \frac{\partial U^{(r)}(\boldsymbol{\sigma})}{\partial \boldsymbol{\sigma}} = \mathbf{S}^{(r)}\boldsymbol{\sigma}^{(r)}, \quad r = 1, 2, \tag{2.52}$$

which is similar to the relation

$$\boldsymbol{\sigma}^{(r)} = \mathbf{L}^{(r)}\boldsymbol{D}^{(r)}, \quad r = 1, 2, \tag{2.53}$$

where $\mathbf{L}^{(r)} = \left(\mathbf{S}^{(r)}\right)^{-1}$ denoting the viscous modulus tensor of the phases, which has both major and minor symmetries. These last relations specify completely the local behavior of the phases in the two-phase medium.

Due to the linearity of the problem, the corresponding instantaneous effective stress potential $\widetilde{U}$ of the two-phase linear composite is also of a quadratic form and can be written as

$$\widetilde{U}(\boldsymbol{\sigma}) = \frac{1}{2}\overline{\boldsymbol{\sigma}} \cdot \widetilde{\mathbf{S}}\,\overline{\boldsymbol{\sigma}}, \tag{2.54}$$

with $\widetilde{\mathbf{S}}$ being a fourth-order symmetric (both minor and major symmetries) tensor denoting the effective viscous compliance tensor of the composite. Following definition (2.8), the resulting relation between the average stress and strain-rate is given by

$$\overline{\boldsymbol{D}} = \frac{\partial \widetilde{U}(\overline{\boldsymbol{\sigma}})}{\partial \overline{\boldsymbol{\sigma}}} = \widetilde{\mathbf{S}}\,\overline{\boldsymbol{\sigma}}, \tag{2.55}$$

or equivalently

$$\overline{\boldsymbol{\sigma}} = \widetilde{\mathbf{L}}\,\overline{\boldsymbol{D}}, \tag{2.56}$$

where $\widetilde{\mathbf{L}} = \left(\widetilde{\mathbf{S}}\right)^{-1}$ denoting the effective viscous modulus tensor of the composite. For the case of two-phase particulate composites, where the inclusions and their distribution function have the same ellipsoidal shape and orientation, as discussed in subsection 2.1.2, the effective viscous compliance and modulus tensors, $\widetilde{\mathbf{S}}$ and $\widetilde{\mathbf{L}}$, are given by (Ponte Castañeda and Willis [1995])

$$\widetilde{\mathbf{S}} = \mathbf{S}^{(1)} + c^{(2)}\left[c^{(1)}\mathbf{Q} + \left(\mathbf{S}^{(2)} - \mathbf{S}^{(1)}\right)^{-1}\right]^{-1} \tag{2.57}$$

and

$$\widetilde{\mathbf{L}} = \mathbf{L}^{(1)} + c^{(2)}\left[c^{(1)}\mathbf{P} + \left(\mathbf{L}^{(2)} - \mathbf{L}^{(1)}\right)^{-1}\right]^{-1}. \tag{2.58}$$

In these expressions, $c^{(r)}$ denote the volume fractions of the phases ($r = 1$ for the matrix and $r = 2$ for the inclusions). In addition, the fourth-order microstructural tensors $\mathbf{Q}$ and $\mathbf{P}$ are related to the Eshelby (Eshelby [1957]) and Hill (Hill [1963]) polarization tensor and contain information about the shape and orientation of the inclusions and their distribution function, given by (Willis [1978])

$$\mathbf{Q} = \frac{1}{4\pi \det(\boldsymbol{Z})}\int_{|\xi|=1}\hat{\mathbf{H}}(\xi)\left|\boldsymbol{Z}^{-1}\xi\right|^{-3}dS, \quad \text{with} \quad \hat{\mathbf{H}} = \mathbf{L}^{(1)} - \mathbf{L}^{(1)}\mathbf{H}\mathbf{L}^{(1)}, \tag{2.59}$$

and

$$\mathbf{P} = \frac{1}{4\pi \det(\boldsymbol{Z})}\int_{|\xi|=1}\mathbf{H}(\xi)\left|\boldsymbol{Z}^{-1}\xi\right|^{-3}dS \tag{2.60}$$

In these relations, the tensor $\boldsymbol{Z}$ is given by relation (2.19) and is used to characterize the instantaneous shape and orientation of the inclusions and their distribution function in this context of particulate microstructures. Moreover, $\mathbf{H}_{(ij)(kl)} = \left(\mathbf{L}^{(1)}_{iakb}\xi_a\xi_b\right)^{-1}\xi_j\xi_l|_{(ij)(kl)}$, where the brackets denote symmetrization with respect to the corresponding indices, while ξ is a unit vector. Then, it follows from (2.59) and (2.60) that the $\mathbf{Q}$ and the $\mathbf{P}$ tensor are related through

$$\mathbf{Q} = \mathbf{L}^{(1)} - \mathbf{L}^{(1)}\mathbf{P}\mathbf{L}^{(1)}, \quad \text{with} \quad \int_{|\xi|=1}\left|\boldsymbol{Z}^{-1}\xi\right|^{-3}dS = 4\pi\det(\boldsymbol{Z}). \qquad (2.61)$$

It is important to precise that both expressions (2.57) and (2.58) for $\widetilde{\mathbf{S}}$ and $\widetilde{\mathbf{L}}$, respectively, are equivalent and either of them can be used for the estimation of the instantaneous effective behavior of the linear two-phase medium. In addition, it should be mentioned that the above Willis estimates for $\widetilde{\mathbf{S}}$ (or $\widetilde{\mathbf{L}}$)) lead to uniform fields in the inclusion phase (Willis [1978]), which is consistent with the work of Eshelby (Eshelby [1957]) in the dilute case. Moreover, the Willis estimates are exact for dilute composites. On the other hand, for non-dilute media, the fields within the inclusions are generally non-uniform, even if as shown by (Bornert et al. [1996]), this "non-uniformity" is negligible provided that the inclusions are not in close proximity to each other, precisely, their volume fraction is lower compared to the one of the matrix phase. This observation should be take into account when the application of homogenization techniques is done for composites consisting of high concentrations of particles or voids. Nevertheless, because this work focuss on porous media with low to moderate concentrations of voids, the Willis procedure is expected to be sufficiently.

Furthermore, the homogenization theory is is also capable of generating estimates for other stress and strain-rate quantities such as the first and second moments of the phase fields, in addition to give a description of the instantaneous effective behavior of linearly viscous two-phase materials in terms of macroscopic measures as seen previously. In the present work, the interest is mainly on the first moments of the phase fields, precisely the average stress $\overline{\boldsymbol{\sigma}}^{(r)} = \langle\boldsymbol{\sigma}\rangle^{(r)}$, the average strain-rate $\overline{\boldsymbol{D}}^{(r)} = \langle\boldsymbol{D}\rangle^{(r)}$ and the spin $\overline{\boldsymbol{\Omega}}^{(r)} = \langle\boldsymbol{\Omega}\rangle^{(r)}$ in each phase. It should be noted that the phase average strain-rate $\overline{\boldsymbol{D}}^{(r)}$ and spin $\overline{\boldsymbol{\Omega}}^{(r)}$ tensors are the symmetric and skew-symmetric parts of the phase average velocity gradient. However, in addition to the first moments, expressions can also be derived for the second-moments of the stress and strain-rate fields, which will be presented in the following.

Then, in the case of linear, two-phase materials, the estimation of the average stress and strain-rate fields is given in terms of stress and strain-rate concentration tensors by (Hill [1963]).

$$\overline{\boldsymbol{\sigma}}^{(r)} = \mathbf{B}^{(r)}\overline{\boldsymbol{\sigma}}, \quad \overline{\boldsymbol{D}}^{(r)} = \mathbf{A}^{(r)}\overline{\boldsymbol{D}}, \quad r = 1, 2, \tag{2.62}$$

with $\mathbf{B}^{(r)}$ and $\mathbf{A}^{(r)}$ denoting the fourth-order tensors which exhibit minor symmetry (but not necessarily major symmetry). However, the phase average stresses and strain-rates are related to the macroscopic stress and strain-rate tensor by

$$\overline{\boldsymbol{\sigma}} = \sum_{r=1}^{2} c^{(r)}\overline{\boldsymbol{\sigma}}^{(r)}, \quad \overline{\boldsymbol{D}} = \sum_{r=1}^{2} c^{(r)}\overline{\boldsymbol{D}}^{(r)}, \tag{2.63}$$

Consequently, the stress and strain-rate concentration tensors $\mathbf{B}^{(r)}$ and $\mathbf{A}^{(r)}$ may respect the identities

$$\sum_{r=1}^{2} c^{(r)}\mathbf{B}^{(r)} = \mathbf{I}, \quad \sum_{r=1}^{2} c^{(r)}\mathbf{A}^{(r)} = \mathbf{I}. \tag{2.64}$$

Moreover, by averaging the local constitutive equations (2.53) and (2.52), we obtain as relations for the phase average stress $\overline{\boldsymbol{\sigma}}^{(r)}$ and strain-rates $\overline{\boldsymbol{D}}^{(r)}$,

$$\overline{\boldsymbol{\sigma}}^{(r)} = \mathbf{L}^{(r)}\overline{\boldsymbol{D}}^{(r)}, \quad \overline{\boldsymbol{D}}^{(r)} = \mathbf{S}^{(r)}\overline{\boldsymbol{\sigma}}^{(r)}, \quad r = 1, 2, \tag{2.65}$$

By combining relations (2.62) and (2.65), we can deduce the following relations for the macroscopic strain-rate and stress:

$$\overline{\boldsymbol{\sigma}} = \left\{\sum_{r=1}^{2} c^{(r)}\mathbf{L}^{(r)}\mathbf{A}^{(r)}\right\}\overline{\boldsymbol{D}}, \quad \overline{\boldsymbol{D}} = \left\{\sum_{r=1}^{2} c^{(r)}\mathbf{S}^{(r)}\mathbf{B}^{(r)}\right\}\overline{\boldsymbol{\sigma}}. \tag{2.66}$$

The last relation together with expressions (2.55) and (2.56) gives the relation between the effective viscous compliance and modulus tensors, $\widetilde{\mathbf{S}}$ and $\widetilde{\mathbf{L}}$, and strain-rate concentration tensors $\mathbf{B}^{(r)}$ and $\mathbf{A}^{(r)}$, respectively, such as

$$\widetilde{\mathbf{L}} = \sum_{r=1}^{2} c^{(r)}\mathbf{L}^{(r)}\mathbf{A}^{(r)}, \quad \widetilde{\mathbf{S}} = \sum_{r=1}^{2} c^{(r)}\mathbf{S}^{(r)}\mathbf{B}^{(r)}. \tag{2.67}$$

Using the equation (2.64), the concentration tensors $\mathbf{A}^{(r)}$ and $\mathbf{B}^{(r)}$ can be written in terms of $\widetilde{\mathbf{L}}$ and $\widetilde{\mathbf{S}}$, respectively, by

$$c^{(2)}\mathbf{B}^{(2)} = \left[\mathbf{S}^{(2)} - \mathbf{S}^{(1)}\right]^{-1}\left[\widetilde{\mathbf{S}} - \mathbf{S}^{(1)}\right], \qquad c^{(1)}\mathbf{B}^{(1)} = \mathbf{I} - c^{(2)}\mathbf{B}^{(2)},$$

$$c^{(2)}\mathbf{A}^{(2)} = \left[\mathbf{L}^{(2)} - \mathbf{L}^{(1)}\right]^{-1}\left[\widetilde{\mathbf{L}} - \mathbf{L}^{(1)}\right], \qquad c^{(1)}\mathbf{A}^{(1)} = \mathbf{I} - c^{(2)}\mathbf{A}^{(2)}. \tag{2.68}$$

In the other hand, the evaluation of the average spin tensors $\overline{\boldsymbol{\Omega}}^{(r)}$ in each phase can be evaluated (Ponte Castañeda [1997], Kailasam and Ponte Castañeda [1998]) as

$$\overline{\boldsymbol{\Omega}}^{(r)} = \overline{\boldsymbol{\Omega}} - \mathbf{C}^{(r)}\overline{\boldsymbol{D}}, \quad \text{for} \quad r = 1, 2, \tag{2.69}$$

where $\mathbf{C}^{(r)}$ denote fourth order tensors that are are skew-symmetric in the first two indices and symmetric in the last two, and $\overline{\boldsymbol{\Omega}}$ is the macroscopic spin tensor which is applied externally in the problem.

Moreover, this macroscopic spin tensor can be related to phase average spin tensors $\overline{\boldsymbol{\Omega}}^{(r)}$ via

$$\overline{\boldsymbol{\Omega}} = \sum_{r=1}^{2} c^{(r)}\overline{\boldsymbol{\Omega}}^{(r)}. \tag{2.70}$$

Thus we should have for the spin concentration tensors

$$\sum_{r=1}^{2} c^{(r)}\mathbf{C}^{(r)} = 0. \tag{2.71}$$

By combining the last equations with results of (Ponte Castañeda [1997]), it is possible to write the spin concentration tensors as functions of strain-rate (or equivalently stress) concentration tensors, such as

$$\mathbf{C}^{(2)} = c^{(1)}\boldsymbol{\Pi}\left(\mathbf{L}^{(2)} - \mathbf{L}^{(1)}\right)\mathbf{A}^{(2)}, \quad c^{(1)}\mathbf{C}^{(1)} = -c^{(2)}\mathbf{C}^{(2)}, \tag{2.72}$$

with $\boldsymbol{\Pi}$ a microstructural tensor related to the $\mathbf{Q}$ tensor (2.61) via

$$\boldsymbol{\Pi} = \frac{1}{4\pi \det(\boldsymbol{Z})} \int_{|\xi|=1} \check{\mathbf{H}}(\xi) \left|\boldsymbol{Z}^{-1}\xi\right|^{-3} dS, \quad \text{with} \quad \check{\mathbf{H}}_{ijkl} = \left(\mathbf{L}^{(1)}_{iakb}\xi_a\xi_b\right)^{-1}\xi_j\xi_l|_{[ij](kl)}. \tag{2.73}$$

Here, the simple brackets indicate the symmetric part of the last two indices, while the square brackets denote the skew-symmetric part of the first two indices. Furthermore, as given in the relation (2.19), the second order tensor $\boldsymbol{Z}$ is used to define the instantaneous shape and orientation of the inclusions.

Moreover, after the phase average fields, it is also useful to see how to get the second moments of the stress and the strain-rate fields. Thus, recalling equations (2.6) and (2.54), and using the definition (2.51) for stress potentials, we can write

$$\frac{1}{2}\overline{\boldsymbol{\sigma}}\,\widetilde{\mathbf{S}}\,\overline{\boldsymbol{\sigma}} = \sum_{r=1}^{2} c^{(r)}\langle\frac{1}{2}\boldsymbol{\sigma}(\mathbf{x})\cdot\mathbf{S}^{(r)}\boldsymbol{\sigma}(\mathbf{x})\rangle^{(r)}, \quad \forall \mathbf{x} \in \Omega^{(r)}. \tag{2.74}$$

In addition, the second moments of the stress fields in the linear material can be evaluated by considering the partial derivative with respect to the compliance tensors $\mathbf{S}^{(r)}$ (Idiart and Ponte Castañeda [2007]), such as

$$\langle \boldsymbol{\sigma}(\mathbf{x}) \otimes \boldsymbol{\sigma}(\mathbf{x}) \rangle^{(r)} = \frac{1}{c^{(r)}} \overline{\boldsymbol{\sigma}} \frac{\partial \widetilde{\mathbf{S}}}{\partial \mathbf{S}^{(r)}} \overline{\boldsymbol{\sigma}}, \quad \forall \mathbf{x} \in \Omega^{(r)}. \tag{2.75}$$

Furthermore, if the fields in any of the phases are uniform, i.e. $\boldsymbol{\sigma}(\mathbf{x}) = \overline{\boldsymbol{\sigma}}^{(r)}$ for all $\mathbf{x}$ in $\Omega^{(r)}$, then $\langle \boldsymbol{\sigma} \otimes \boldsymbol{\sigma} \rangle^{(r)} = \overline{\boldsymbol{\sigma}}^{(r)} \otimes \overline{\boldsymbol{\sigma}}^{(r)}$.

As already seen previously, the (Willis [1978]) and (Ponte Castañeda and Willis [1995]) estimates for particulate microstructures result in uniform fields in the inclusion phase. Based on this observation, the fluctuations in the inclusion phases are zero, i.e.,

$$\langle \boldsymbol{\sigma} \otimes \boldsymbol{\sigma} \rangle^{(2)} - \overline{\boldsymbol{\sigma}}^{(2)} \otimes \overline{\boldsymbol{\sigma}}^{(2)} = 0 \quad \text{or} \quad \boldsymbol{\sigma}(\mathbf{x}) = \overline{\boldsymbol{\sigma}}^{(2)} \quad \forall \mathbf{x} \in \Omega^{(2)}. \tag{2.76}$$

By using the Legendre-Fenchel transform, equivalent expressions can also be deduced for the strain-rate fluctuations, more precisely

$$\frac{1}{2} \overline{\boldsymbol{D}} \widetilde{\mathbf{L}} \, \overline{\boldsymbol{D}} = \sum_{r=1}^{2} c^{(r)} \langle \frac{1}{2} \boldsymbol{D}(\mathbf{x}) \cdot \mathbf{L}^{(r)} \boldsymbol{D}(\mathbf{x}) \rangle^{(r)}, \quad \forall \mathbf{x} \in \Omega^{(r)}. \tag{2.77}$$

Moreover, the second moments of the strain fields in the linear material can be evaluated by considering the partial derivative with respect to the modulus tensors $\mathbf{L}^{(r)}$, such as

$$\langle \boldsymbol{D}(\mathbf{x}) \otimes \boldsymbol{D}(\mathbf{x}) \rangle^{(r)} = \frac{1}{c^{(r)}} \overline{\boldsymbol{D}} \frac{\partial \widetilde{\mathbf{L}}}{\partial \mathbf{L}^{(r)}} \overline{\boldsymbol{D}}, \quad \forall \mathbf{x} \in \Omega^{(r)}. \tag{2.78}$$

As previously, the corresponding strain-rate fluctuations in the inclusion phases are zero, i.e.,

$$\langle \boldsymbol{D} \otimes \boldsymbol{D} \rangle^{(2)} - \overline{\boldsymbol{D}}^{(2)} \otimes \overline{\boldsymbol{D}}^{(2)} = 0 \quad \text{or} \quad \boldsymbol{D}(\mathbf{x}) = \overline{\boldsymbol{D}}^{(2)} \quad \forall \mathbf{x} \in \Omega^{(2)}. \tag{2.79}$$

Due to the same reason, the average spin $\boldsymbol{\Omega}^{(2)}$ in the inclusion phase is also uniform, and consequently

$$\boldsymbol{\Omega}(\mathbf{x}) = \overline{\boldsymbol{\Omega}}^{(2)} \quad \forall \mathbf{x} \in \Omega^{(2)}. \tag{2.80}$$

In the following subsection, we specialize the previous results for the particular case of linearly viscous porous media.

2.3.1 Linear viscous porous media

In this subsection, we will consider a linear composite consisting of a matrix phase denoted with the label 1, and a vacuous phase denoted with label 2. The behavior of the matrix phase is described by a quadratic stress potential $U^{(1)} \equiv U$ defined by

$$U(\boldsymbol{\sigma}) = \frac{1}{2}\boldsymbol{\sigma} \cdot \mathbf{S}\,\boldsymbol{\sigma}, \quad \forall \mathbf{x} \in \Omega^{(1)}. \tag{2.81}$$

Here, $\mathbf{S}$ and $\mathbf{L}$ are the viscous compliance and modulus tensors of the matrix phase, respectively. Moreover, the modulus tensor $\mathbf{L}^{(2)}$ of the porous phase has zero eigenvalues, and its viscoplastic stress potential is $U^{(2)} = 0$. Thus, the instantaneous effective stress potential of the porous material is given by relation (2.54), i.e.

$$\widetilde{U}(\overline{\boldsymbol{\sigma}}) = \frac{1}{2}\overline{\boldsymbol{\sigma}} \cdot \widetilde{\mathbf{S}}\,\overline{\boldsymbol{\sigma}}, \tag{2.82}$$

with $\widetilde{\mathbf{S}}$ and $\widetilde{\mathbf{L}} = \widetilde{\mathbf{S}}^{-1}$ denoting the effective viscous compliance and modulus tensors of the porous medium, respectively. These tensors exhibit both minor and major symmetries. Furthermore, the constitutive macroscopic law for the linearly viscous porous medium is given by (2.55) and (2.56),

$$\overline{\boldsymbol{D}} = \widetilde{\mathbf{S}}\,\overline{\boldsymbol{\sigma}}, \quad \overline{\boldsymbol{\sigma}} = \widetilde{\mathbf{L}}\,\overline{\boldsymbol{D}} \tag{2.83}$$

By setting $\mathbf{L}^{(2)} = 0$ in equations (2.57) and (2.58), we can determine the effective tensors $\widetilde{\mathbf{S}}$ and $\widetilde{\mathbf{L}}$. In this connection, we get

$$\widetilde{\mathbf{L}} = \mathbf{L} + f\left[(1-f)\,\mathbf{P} - \mathbf{M}\right]^{-1}, \tag{2.84}$$

and

$$\widetilde{\mathbf{S}} = \mathbf{S} + \frac{f}{1-f}\mathbf{Q}^{-1}, \tag{2.85}$$

where $f \equiv c^{(2)}$ is the porosity, i.e. the volume fraction of the voids. Consequently, the volume fraction of the matrix phase $c^{(1)} = 1 - f$. The relations (2.59) and (2.60) give the microstructural tensors $\mathbf{Q}$ and $\mathbf{P}$, which characterize the instantaneous shape and orientation of the voids and their distribution function.

The corresponding strain-rate and stress concentration tensors $\mathbf{A}^{(r)}$ and $\mathbf{B}^{(r)}$, respectively, given by relation (2.68) simplify to

$$(1-f)\,\mathbf{B}^{(1)} = \mathbf{I}, \quad \mathbf{B}^{(2)} = 0, \quad (1-f)\,\mathbf{A}^{(1)} = \mathbf{S}\,\widetilde{\mathbf{S}}^{-1}, \quad f\mathbf{A}^{(2)} = \mathbf{I} - \mathbf{S}\,\widetilde{\mathbf{S}}^{-1}. \tag{2.86}$$

By combining this result with relation (2.62), we get

$$(1 - f)\,\overline{\boldsymbol{\sigma}}^{(1)} = \overline{\boldsymbol{\sigma}}, \quad \overline{\boldsymbol{\sigma}}^{(2)} = 0. \tag{2.87}$$

It is interesting to notice that this result is in agrement with the fact that for all $\mathbf{x}$ in $\Omega^{(2)}$, the stress in the voids is zero. Moreover, it comes from relations (2.62) and (2.86) that the phase average strain-rate in the matrix and the vacuous phase can be written as

$$\overline{\boldsymbol{D}}^{(1)} = \mathbf{A}^{(1)}\,\overline{\boldsymbol{D}} = \frac{1}{1-f}\mathbf{S}\,\widetilde{\mathbf{S}}^{-1}\,\overline{\boldsymbol{D}} \tag{2.88}$$

$$\overline{\boldsymbol{D}}^{(2)} = \mathbf{A}^{(2)}\,\overline{\boldsymbol{D}} = \frac{1}{f}\left(\mathbf{I} - \mathbf{S}\,\widetilde{\mathbf{S}}^{-1}\right)\overline{\boldsymbol{D}}. \tag{2.89}$$

Another way to write these equations, by using also definitions (2.83) and (2.86) is

$$\overline{\boldsymbol{D}}^{(1)} = \frac{1}{1-f}\mathbf{S}\,\overline{\boldsymbol{\sigma}} \tag{2.90}$$

$$\overline{\boldsymbol{D}}^{(2)} = \frac{1}{f}\left(\widetilde{\mathbf{S}} - \mathbf{S}\right)\overline{\boldsymbol{\sigma}} = \frac{1}{1-f}\mathbf{Q}^{-1}\overline{\boldsymbol{\sigma}}. \tag{2.91}$$

In addition, the phase average spin in the inclusion phase is obtained by relation (2.69), more precisely

$$\overline{\boldsymbol{\Omega}}^{(2)} = \overline{\boldsymbol{\Omega}} - \mathbf{C}^{(2)}\overline{\boldsymbol{D}}, \tag{2.92}$$

where $\mathbf{C}^{(2)}$ is given by (2.72), with $\mathbf{L}^{(2)} = 0$, i.e

$$\mathbf{C}^{(2)} = (f - 1)\,\boldsymbol{\Pi}\,\mathbf{S}^{-1}\,\mathbf{A}^{(2)} = \frac{1-f}{f}\boldsymbol{\Pi}\left(\widetilde{\mathbf{S}}^{-1} - \mathbf{S}^{-1}\right). \tag{2.93}$$

Furthermore, as defined in (2.73), the fourth-order microstructural tensor $\boldsymbol{\Pi}$ is skew-symmetric with respect to the first two indices, and symmetric with respect to the last two ones. Finally, by substituting (2.93) in (2.92) and by made use of (2.83) and (2.84), we obtain

$$\overline{\boldsymbol{\Omega}}^{(2)} = \overline{\boldsymbol{\Omega}} + (1 - f)\,\boldsymbol{\Pi}\,\mathbf{S}^{-1}\,\overline{\boldsymbol{D}}^{(2)} = \overline{\boldsymbol{\Omega}} + \boldsymbol{\Pi}\,\mathbf{S}^{-1}\,\mathbf{Q}^{-1}\overline{\boldsymbol{\sigma}}. \tag{2.94}$$

2.3.2   Partial summary

In this section, we presented several constitutive relations for two-phase, linearly viscous particulate media. We have defined the instantaneous effective behavior of the material and it has been shown that both the macroscopic properties as well as the

phase average fields can be completely defined in terms of the effective viscous compliance tensor $\widetilde{\mathbf{S}}$ (or equivalently the effective viscous modulus tensor $\widetilde{\mathbf{L}}$) of the composite material. These general results for two-phase materials have been specialized to porous media, which is the main subject of this work. It is worth mentioning at this point that in the sequel use will be made of nonlinear homogenization techniques to predict the instantaneous effective behavior of nonlinear porous media. These nonlinear methods make use of results for linear composites and thus the previous results will be very important in the sections to follow.

2.4 Homogenization of porous single crystal

2.4.1 The variational method

As previously mentioned, we will make use of the general nonlinear homogenization methods developed by Ponte Castañeda [1991a, 2002a], which are based on the construction of a linear comparison composite (LCC) with the same microstructure as the nonlinear composite. More precisely, the different phases of the LCC are determined through well defined linearizations of the given nonlinear phases by making use of a suitably designed variational principle. The corresponding phases of the LCC are characterized in general by quadratic stress potentials of the form

$$U_L^{(r)}(\boldsymbol{\sigma}, \mathbf{S}^{(r)}) = \frac{1}{2}\boldsymbol{\sigma}(\mathbf{x}) \cdot \mathbf{S}^{(r)} \cdot \boldsymbol{\sigma}(\mathbf{x}), \quad r = 1, 2, \quad \forall \mathbf{x} \in \Omega^{(r)}, \tag{2.95}$$

where $\mathbf{S}^{(r)}$ serves to denote the fourth-order symmetric compliance tensor. In addition, as proposed by Ponte Castañeda [1991a, 2002a], "corrector" functions $v^{(r)}$ can be defined as the optimal difference between the quadratic stress potentials and the actual nonlinear ones $U^{(r)}$ defined in (2.31), via

$$v^{(r)}(\mathbf{S}^{(r)}) = \sup_{\widehat{\boldsymbol{\sigma}}^{(r)}} \left(U_L^{(r)}(\widehat{\boldsymbol{\sigma}}, \mathbf{S}^{(r)}) - U^{(r)}(\widehat{\boldsymbol{\sigma}}) \right). \tag{2.96}$$

Here, $\widehat{\boldsymbol{\sigma}}^{(r)}$ are assumed to be constant second-order tensors. For simplicity in notation, we precise that $\widehat{\boldsymbol{\sigma}}^{(r)}$ is the field that attains the "sup" operator in (2.96).

In the following, using (2.95) and (2.96), one can show that the effective energy function (2.16) can be approximated (Ponte Castañeda [1991a, 2002a]) via the expres-

sion

$$\widetilde{U}_{var}(\overline{\boldsymbol{\sigma}}) = \sup_{\mathbf{S}^{(r)}(x)} \left(\widetilde{U}_L(\overline{\boldsymbol{\sigma}}, \mathbf{S}^{(r)}) - \sum_{r=1}^{2} c^{(r)} v^{(r)}(\mathbf{S}^{(r)}) \right), \tag{2.97}$$

where $c^{(r)}$ is the volume fraction of the phase r. It is interesting to note that equation (2.97) is a lower bound of the effective energy $\widetilde{U}(\overline{\boldsymbol{\sigma}})$. Nonetheless, the goal of the present work is to provide an estimate of $\widetilde{U}(\overline{\boldsymbol{\sigma}})$ and not a bound, thus, the optimization conditions on $\mathbf{S}^{(r)}$ will be further relaxed next.

2.4.2   Definition of a linear comparison composite (LCC)

In this section, we will choose approximate compliance tensors $\mathbf{S}^{(r)}$ that will allow us to get closed form (semi-analytical) estimates for $\widetilde{U}(\overline{\boldsymbol{\sigma}})$. The difficulty in the choice $\mathbf{S}^{(r)}$ lies in two first points. First, $\mathbf{S}^{(r)}$ do not need to be constant per phase (see Herve and Zaoui [1993]). While such a choice would lead to move accurate estimates, in general, one would have to resolve the fully numerical optimization of the problem, thus making it implicit and thus untractable in reals applications. The second point is that one can choose piecewise constant $\mathbf{S}^{(r)}$ but in general form (see deBotton and Ponte Castañeda [1995], Idiart and Ponte Castañeda [2007]). This choice again leads to a convex but sub-differentiable optimization problem for $\widetilde{U}(\overline{\boldsymbol{\sigma}})$ as a function of $\mathbf{S}^{(r)}$ and thus one has to again resolve the fully numerical optimization procedures (except in special cases as in Idiart and Ponte Castañeda [2007]). For this reason, in the present work, we choose not only piecewise constant $\mathbf{S}^{(r)}$, but also of a special form which is motivated by the viscoplastic stress potential U in the linear case $n = 1$. Thus following (2.31), the viscoplastic potential related to a linear single crystal can be written as

$$U_L(\boldsymbol{\sigma}) = \sum_{s=1}^{K} \frac{\dot{\gamma}_0^{(s)}}{2\tau_0^{(s)}} \left(\tau^{(s)} \right)^2 = \frac{1}{2} \boldsymbol{\sigma} \cdot \mathbf{S} \cdot \boldsymbol{\sigma}. \tag{2.98}$$

Using this relation, we can then rewrite the symmetric, fourth-order, compliance tensor of the LCC as

$$\mathbf{S} = \sum_{s=1}^{K} \frac{1}{2\lambda^{(s)}} \mathbf{E}^{(s)} + \sum_{s=1}^{K} \frac{1}{2\rho^{(s)}} \mathbf{F}^{(s)} + \frac{1}{3\kappa} \mathbf{J}, \tag{2.99}$$

with

$$\mathbf{E}^{(s)} = 2\boldsymbol{\mu}^{(s)} \otimes \boldsymbol{\mu}^{(s)}, \ \mathbf{F}^{(s)} = \mathbf{K} - \mathbf{E}^{(s)}, \ \forall s = 1, K. \tag{2.100}$$

Here $\mathbf{K}$ denotes the fourth-order shear projection tensor whereas $\mathbf{J}$ denotes the fourth-order hydrostatic projection tensor. Thus, $\forall s = 1, K, \left(\mathbf{E}^{(s)}, \mathbf{F}^{(s)}, \mathbf{J} \right)$ form a fourth

order tensor basis [1]. In addition, $\boldsymbol{\mu}^{(s)}$ is the Schmid tensor (2.26) associated to the sth slip system and the bulk modulus $\kappa \to \infty$ (incompressible matrix), $\rho^{(s)} \to \infty$.

Using the generalized Hashin-Shtrikman estimates (Hashin and Shtrikman [1963]) of Willis (Willis [1977]) which are known to be quite accurate for porous random systems, up to moderate concentrations of pores, we write

$$\widetilde{U}_L(\overline{\boldsymbol{\sigma}}) = \frac{1}{2(1-f)}\overline{\boldsymbol{\sigma}} \cdot \left(\sum_{s=1}^{K} \frac{1}{2\lambda^{(s)}}\mathbf{E}^{(s)} + f\mathbf{S}^*\right) \cdot \overline{\boldsymbol{\sigma}}, \tag{2.101}$$

where

$$\mathbf{S}^* = \lim_{\rho^{(s)},\kappa \to \infty} \mathbf{Q}^{-1} - \sum_{s=1}^{K} \frac{1}{2\lambda^{(s)}}\mathbf{E}^{(s)}. \tag{2.102}$$

In this relation, $\mathbf{Q}$ is a microstructural tensor related to the Eshelby tensor (Eshelby [1957]), and is defined as $\mathbf{Q} = \mathbf{S}^{-1} - \mathbf{S}^{-1}\mathbf{P}\mathbf{S}^{-1}$, with $\mathbf{P}$ being the Eshelby tensor. Indeed, for an ellipsoidal void embedded in a matrix, if we denote w_1, w_2 as the aspect ratios and $\mathbf{n}^{(i)}$ ($i = 1, 2, 3$) as the orientation unit vectors (see fig 2.1), the Eshelby tensor $\mathbf{P}$ is expressed as

$$\mathbf{P}_{ijkl} = \frac{1}{4\pi \det \boldsymbol{Z}} \int_{|\xi|=1} \frac{\left(\left(\mathbf{S}^{-1}\right)_{iakb}\xi_a\xi_b\right)^{-1}\xi_j\xi_l|_{(ij)(kl)}}{\left|\boldsymbol{Z}^{-1}\cdot\xi\right|^3}dS \tag{2.103}$$

which brackets $(ij)(kl)$ denote symmetrization with respect to the corresponding indices, $\xi = \{\sin\phi\cos\theta, \sin\phi\sin\theta, \cos\phi\}$ is the position vector and $\boldsymbol{Z}$ the shape tensor expressed as

$$\boldsymbol{Z} = w_1\,\mathbf{n}^{(1)} \otimes \mathbf{n}^{(1)} + w_2\,\mathbf{n}^{(2)} \otimes \mathbf{n}^{(2)} + \mathbf{n}^{(3)} \otimes \mathbf{n}^{(3)}. \tag{2.104}$$

It is recalled here that w_1, w_2 and $\mathbf{n}^{(i)}$ have been defined in the context of Fig. 2.1.

At this point it is important to note that after the limit of $\rho^{(s)} \to \infty$ and $\kappa \to \infty$ are considered in (2.102) the $\mathbf{Q}$ tensor is compressible due to the presence of the voids in the matrix. These limits need to be taken during the evaluation of $\mathbf{Q}$ in (2.102$_2$). If instead the limit is taken before the evaluation of $\mathbf{Q}$ the term $\left(\mathbf{S}^{-1}\right)_{iakb}\xi_a\xi_b$ in (2.103) becomes singular.

The computation of $\mathbf{Q}$ in the above expressions is critical for the optimization problem (2.97). Due to the extremely complicated dependence of $\mathbf{Q}$ on $\lambda^{(s)}$, the optimization problem for the estimation of the effective response in equation (2.97) has to be carried out numerically, except in the special case where we let $\lambda^{(s)} \to \lambda$ for

---

[1] $\forall s = 1, K \; \mathbf{F}^{(s)} \cdot \mathbf{F}^{(s)} = \mathbf{F}^{(s)}, \; \mathbf{E}^{(s)} \cdot \mathbf{E}^{(s)} = \mathbf{E}^{(s)}, \; \mathbf{E}^{(s)} \cdot \mathbf{F}^{(s)} = \mathbf{F}^{(s)} \cdot \mathbf{E}^{(s)} = 0$

all $s = 1, K$. This simplifies tremendously the evaluation of the $\mathbf{Q}$ tensor and allows for approximations as is discussed in the following section.

More specifically, one can write

$$\lim_{\lambda^{(s)} \to \lambda} \mathbf{S}^* \left(\lambda^{(s)} \right) = \frac{1}{\lambda} \widehat{\mathbf{S}}^*, \tag{2.105}$$

where $\widehat{\mathbf{S}}^*$ is given by (c.f. (2.102))

$$\widehat{\mathbf{S}}^* = \widehat{\mathbf{Q}}^{-1} - \sum_{s=1}^{K} \frac{1}{2} \mathbf{E}^{(s)}, \quad \widehat{\mathbf{Q}} = \lim_{\widehat{\rho} \to \infty} \lim_{\widehat{\kappa} \to \infty} \left[\boldsymbol{\mathcal{S}}^{-1} - \boldsymbol{\mathcal{S}}^{-1} \widehat{\mathbf{P}} \, \boldsymbol{\mathcal{S}}^{-1} \right], \tag{2.106}$$

with $\boldsymbol{\mathcal{S}}$ being a reduced version of the $\mathbf{S}$ tensor defined in equation 2.99, and reads

$$\boldsymbol{\mathcal{S}} = \sum_{s=1}^{K} \frac{1}{2} \mathbf{E}^{(s)} + \frac{1}{2\widehat{\rho}} \sum_{s=1}^{K} \mathbf{F}^{(s)} + \frac{1}{3\widehat{\kappa}} \mathbf{J}, \qquad \forall s = 1, K. \tag{2.107}$$

In turn, $\widehat{\mathbf{P}}$ is a microstructural tensor related to the Eshelby tensor (Eshelby [1957]) and is given by (Willis [1977])

$$\widehat{\mathbf{P}}_{ijkl} = \frac{1}{4\pi \det \boldsymbol{Z}} \int_{|\xi|=1} \frac{\left(\boldsymbol{\mathcal{S}}_{iakb}^{-1} \xi_a \xi_b \right)^{-1} \xi_j \xi_l |_{(ij)(kl)}}{\left| \boldsymbol{Z}^{-1} \cdot \xi \right|^3} dS. \tag{2.108}$$

The brackets $(ij)(kl)$ denote symmetrization with respect to the corresponding indices, ξ is a unit three-dimensional vector and $\boldsymbol{Z}$ is a second-order tensor serving to describe the shape and orientation of the voids, i.e.,

$$\boldsymbol{Z} = w_1 \, \mathbf{n}^{(1)} \otimes \mathbf{n}^{(1)} + w_2 \, \mathbf{n}^{(2)} \otimes \mathbf{n}^{(2)} + \mathbf{n}^{(3)} \otimes \mathbf{n}^{(3)}. \tag{2.109}$$

It is very important to stress at this point that the tensors $\widehat{\mathbf{Q}}$ and consequently $\widehat{\mathbf{S}}^*$ in the above expression are independent of λ (see relevant discussion in Danas [2008] and Danas and Ponte Castañeda [2009a]). This property will allow to carry out analytically the optimization problem (2.97) to be discussed in detail in the next section.

2.4.3 Variational estimate for porous single crystal

Using the above definition (2.99) and the estimate (2.101), one can rewrite the non-linear effective potential $\widetilde{U}$, defined in (2.97) as

$$\widetilde{U}_{var} \left(\overline{\boldsymbol{\sigma}} \right) = \max_{\lambda^{(s)} \geq 0} \left(\widetilde{U}_L \left(\overline{\boldsymbol{\sigma}} \right) - (1 - f) \sum_{s=1}^{K} v^{(s)} \left(\lambda^{(s)} \right) \right). \tag{2.110}$$

For $n > 1$, the corrector function for a single slip system can be expressed analytically (deBotton and Ponte Castañeda [1995], Idiart and Ponte Castañeda [2007]) as

$$v(\lambda^{(s)}) = \sup_{\widehat{\boldsymbol{\sigma}}} \sum_{s=1}^{K} \left[\Psi_L^{(s)} \left(\widehat{\tau}^{(s)}, \lambda^{(s)} \right) - \Psi^{(s)} \left(\widehat{\tau}^{(s)} \right) \right]$$

$$\leq \sum_{s=1}^{K} \sup_{\widehat{\tau}^{(s)}} \left[\frac{1}{2\lambda^{(s)}} \left(\widehat{\tau}^{(s)} \right)^2 - \frac{\dot{\gamma}_0^{(s)} \tau_0^{(s)}}{n+1} \left(\frac{\left| \widehat{\tau}^{(s)} \right|}{\tau_0^{(s)}} \right)^{n+1} \right]$$

$$= \frac{n-1}{n+1} \frac{\dot{\gamma}_0^{(s)} \tau_0^{(s)}}{2} \left(\frac{\tau_0^{(s)}}{\lambda^{(s)} \dot{\gamma}_0^{(s)}} \right)^{\frac{n+1}{n-1}}. \tag{2.111}$$

The global optimization problem in (2.110) is a non-trivial one, mainly because of the extremely complicated dependence of the $\mathbf{Q}$ tensor (see (2.102)) on $\lambda^{(s)}$, and in general, it must be carried out numerically. However, we introduce at this point the approximation

$$\mathbf{S}^* \left(\lambda^{(s)} \right) \cong \frac{1}{K} \sum_{s=1}^{K} \frac{1}{\lambda^{(s)}} \widehat{\mathbf{S}}^*, \tag{2.112}$$

where $\widehat{\mathbf{S}}^*$ is given by (2.106). This last expression (2.112) is identically true for $\lambda^{(s)} = \lambda, \forall s = 1, K$ while being a relatively good approximation in the neighborhood of $\lambda^{(i)} \simeq \lambda^{(j)}, \forall i, j = 1, K$. The choice (2.112) allows for a fully analytical resolution of the optimization procedure (2.110) and thus to a fully analytical model.

Consequently, the relation (2.112) together with equations (2.101), (2.110) and (2.111) lead to

$$\widetilde{U}_{var} \left(\overline{\boldsymbol{\sigma}} \right) = \max_{\lambda^{(s)} \geq 0} \left[\sum_{s=1}^{K} \left\{ \frac{1}{1-f} \frac{1}{2\lambda^{(s)}} \left(\left(\overline{\tau}^{(s)} \right)^2 + \frac{f}{K} \overline{\boldsymbol{\sigma}} \cdot \widehat{\mathbf{S}}^* \cdot \overline{\boldsymbol{\sigma}} \right) \right\} \right.$$

$$\left. - (1-f) \sum_{s=1}^{K} \frac{n-1}{n+1} \frac{\dot{\gamma}_0^{(s)} \tau_0^{(s)}}{2} \left(\frac{\tau_0^{(s)}}{\lambda^{(s)} \dot{\gamma}_0^{(s)}} \right)^{\frac{(n+1)}{(n-1)}} \right]. \tag{2.113}$$

Following Han et al. [2013], we interchange the maximization with the summation in (2.113) to get

$$\frac{1}{2\lambda^{(s)}} = \frac{\dot{\gamma}_0^{(s)}}{2\tau_0^{(s)}} \left\{ \frac{\left(\overline{\tau}^{(s)} \right)^2 + \frac{f}{K} \overline{\boldsymbol{\sigma}} \cdot \widehat{\mathbf{S}}^* \cdot \overline{\boldsymbol{\sigma}}}{\left(\tau_0^{(s)} \right)^2 (1-f)^2} \right\}^{(n-1)/2} \tag{2.114}$$

This interchange will preserve the discrete character of the slip-system response in the rate-independent limit and for $f = 0$.

Finally, substitution of (2.114) to (2.110) gives the variational estimate of the effective stress potential of the crystalline porous material

$$\widetilde{U}_{var}\left(\overline{\boldsymbol{\sigma}}\right) = (1 - f) \sum_{s=1}^{K} \frac{\dot{\gamma}_0^{(s)} \tau_0^{(s)}}{n + 1} \left(\frac{\left|\widetilde{\tau}^{(s)}\right|}{\tau_0^{(s)} (1 - f)} \right)^{n+1}, \quad \widetilde{\tau}^{(s)} = \sqrt{\left(\overline{\tau}^{(s)}\right)^2 + \frac{f}{K} \overline{\boldsymbol{\sigma}} \cdot \widehat{\mathbf{S}}^* \cdot \overline{\boldsymbol{\sigma}}}, \tag{2.115}$$

which can also be written as

$$\widetilde{U}_{var}\left(\overline{\boldsymbol{\sigma}}\right) = (1 - f) \sum_{s=1}^{K} \frac{\dot{\gamma}_0^{(s)} \tau_0^{(s)}}{n + 1} \left(\frac{\sqrt{\overline{\boldsymbol{\sigma}} \cdot \widehat{\mathbf{S}}^{var,(s)} \cdot \overline{\boldsymbol{\sigma}}}}{\tau_0^{(s)} (1 - f)} \right)^{n+1}, \tag{2.116}$$

with

$$\widehat{\mathbf{S}}^{var,(s)} = \frac{1}{2} \mathbf{E}^{(s)} + \frac{f}{K} \widehat{\mathbf{S}}^*, \forall s = 1, K. \tag{2.117}$$

It is recalled that $\widehat{\mathbf{S}}^*$ is given by equation (2.106).

2.4.4 Correction of the hydrostatic point

It is well known from Ponte Castañeda [1991b] and Michel and Suquet [1992]) that in the case of isotropic matrix and hydrostatic loadings the variational estimates are overly stiff. This is also the case in the present work, i.e. the estimate (2.116) for $\widetilde{U}_{var}$ is very stiff when compared to numerical unit-cell calculations (performed in the present study and described in the following section). A way to remedy this overly stiff response is to use exact results that are available in the context of porous materials with isotropic matrix phases such as those derived in equation (2.38).

In this regard, the goal of this section is to propose a correction to the $\widetilde{U}_{var}$ estimate (2.116) in the limit of purely hydrostatic loadings. Unfortunately, in the present case of anisotropic crystal plasticity no simple analytical solution is available in the purely hydrostatic limit. Nevertheless, one can insist that the estimate (2.116) must recover the result of an isotropic spherical porous shell (or equivalently a composite sphere assemblage (CSA) microstructure) in the limit of infinite equiangular slip systems ($K \to \infty$), spherical voids and hydrostatic loadings. The reason is that in that theoretical limit, the response becomes fully isotropic, with a matrix phase described by a stress potential of the form (2.38).

Specifically, it has recently been shown by Benallal [2015] that the purely hydrostatic response of a spherical porous shell whose matrix phase is described by a stress

potential of the form (2.38) is identical to that of a porous spherical shell with a J$_2$-type matrix phase and is given by the closed form expression (Hashin [1962], Gurson [1977], Leblond et al. [1994], Danas et al. [2008b])

$$\widetilde{U}_{iso}(\overline{\boldsymbol{\sigma}}) = \frac{\dot{\epsilon}_0\,\widetilde{\sigma}_h}{n+1}\left(\frac{3\,\overline{\sigma}_m}{2\,\widetilde{\sigma}_h}\right)^{n+1}, \quad \frac{\widetilde{\sigma}_h}{\sigma_0} = n\left(f^{-1/n}-1\right), \tag{2.118}$$

where σ_0 and $\dot{\epsilon}_0$ denote the reference strain-rate and the isotropic flow stress of the isotropic matrix. This result is valid for isotropic potentials such as the one in equation (2.38) corresponding to infinite number of slip systems.

Next, motivated by similar work on isotropic matrix systems (Danas and Aravas [2012] but see also Danas et al. [2008a] and Danas et al. [2008b]), we replace $\widehat{\mathbf{S}}^{var,(s)}$ with $\widehat{\mathbf{S}}^{mvar,(s)}$ in (2.116), to get

$$\widetilde{U}_{mvar}(\overline{\boldsymbol{\sigma}}) = (1-f)\sum_{s=1}^{K}\frac{\dot{\gamma}_0^{(s)}\tau_0^{(s)}}{n+1}\left(\frac{\sqrt{\overline{\boldsymbol{\sigma}}\cdot\widehat{\mathbf{S}}^{mvar,(s)}\cdot\overline{\boldsymbol{\sigma}}}}{\tau_0^{(s)}(1-f)}\right)^{n+1}, \tag{2.119}$$

where

$$\widehat{\mathbf{S}}^{mvar,(s)} = \widehat{\mathbf{S}}^{var,(s)} + \left(q_J^2-1\right)\mathbf{J}\cdot\widehat{\mathbf{S}}^{var,(s)}\cdot\mathbf{J}. \tag{2.120}$$

The label "mvar" refers to "modified variational" (MVAR), whereas the factor "q_J" remains to be identified so that the MVAR estimate recovers the exact result (2.118) in the limit of infinite number of slip systems $K \longrightarrow \infty$.

In view of this, we consider a purely hydrostatic loading $\overline{\boldsymbol{\sigma}}_{ij} = \overline{\sigma}_m\delta_{ij}$ and spherical voids (i.e., $w_1 = w_2 = 1$) embedded in a single crystal comprising slip systems with identical CRSS and reference slip rate, i.e. $(\tau_0)^{(s)} = \tau_0$, $(\dot{\gamma}_0)^{(s)} = \dot{\gamma}_0$, $\forall s = 1, K$. In the case of infinite equiangular slip systems and purely hydrostatic loadings, equation (2.119) becomes

$$\widetilde{U}_{mvar}(\overline{\boldsymbol{\sigma}}) \cong (1-f)^{-n}\left(\frac{3f}{20}q_J^2\right)^{\frac{n+1}{2}}\frac{\overline{\sigma}_m^{n+1}}{n+1}\lim_{K\to\infty}\left(\dot{\gamma}_0\,\tau_0^{-n}\,K\right). \tag{2.121}$$

Next, using equation (2.37), and setting equation (2.118) equal to (2.183), i.e., $\widetilde{U}_{mvar} = \widetilde{U}_{iso}$, we readily obtain

$$q_J = \sqrt{\frac{15}{f}}\left\{\frac{(1-f)\,(\beta_n)^{\frac{1}{n}}}{n(f^{-1/n}-1)}\right\}^{\frac{n}{n+1}}, \tag{2.122}$$

where β_n is given in (2.157).

While this correction establishes that the $\widetilde{U}_{mvar}$ in (2.119) recovers the isotropic limit (i.e., infinite number of slip systems and spherical voids), there is, to this day, no specific guarantee that this estimate will be sufficiently accurate for any void shape and orientation. Nonetheless, we will show in the results sections that the robust character of the original variational method together with the proposed correction in this section gives sufficiently good quantitative agreement when compared with full field finite element simulations for a large range of void shapes and orientations.

2.4.5 Summary of the modified variational model (MVAR)

To facilitate the reader with the main results of the present work, we summarize here the final equations of the proposed MVAR model. Therefore, the effective stress potential of a porous single crystal is given by (see equation (2.119))

$$\widetilde{U}_{mvar}\left(\overline{\boldsymbol{\sigma}}\right) = (1-f) \sum_{s=1}^{K} \frac{\dot{\gamma}_0^{(s)} \tau_0^{(s)}}{n+1} \left(\frac{\sqrt{\overline{\boldsymbol{\sigma}} \cdot \widehat{\mathbf{S}}^{mvar,(s)} \cdot \overline{\boldsymbol{\sigma}}}}{\tau_0^{(s)} (1-f)} \right)^{n+1}, \qquad (2.123)$$

where

$$\widehat{\mathbf{S}}^{mvar,(s)} = \widehat{\mathbf{S}}^{var,(s)} + \left(q_J^2 - 1\right) \mathbf{J} \cdot \widehat{\mathbf{S}}^{var,(s)} \cdot \mathbf{J}, \ q_J = \sqrt{\frac{15}{f}} \left\{ \frac{(1-f)\left(\beta_n\right)^{\frac{1}{n}}}{n(f^{-1/n}-1)} \right\}^{\frac{n}{n+1}}, \ \beta_n = \frac{4}{25} 6^{-\frac{n}{2}} \qquad (2.124)$$

Here,

$$\widehat{\mathbf{S}}^{var,(s)} = \frac{1}{2}\mathbf{E}^{(s)} + \frac{f}{K}\widehat{\mathbf{S}}^*, \quad \mathbf{E}^{(s)} = 2\boldsymbol{\mu}^{(s)} \otimes \boldsymbol{\mu}^{(s)}, \ \forall s = 1, K, \quad J_{ijkl} = \frac{1}{3}\delta_{ij}\delta_{kl}. \quad (2.125)$$

where $\boldsymbol{\mu}^{(s)}$ is the Schmid tensor defined in (2.26), $\widehat{\mathbf{S}}^*$ is evaluated by equations (2.106)-(2.107).

Furthermore, we can readily determine the corresponding macroscopic strain-rate $\overline{\boldsymbol{D}}$ through the relation

$$\overline{\boldsymbol{D}} = \frac{\partial \widetilde{U}_{mvar}}{\partial \overline{\boldsymbol{\sigma}}} = \sum_{s=1}^{K} \dot{\gamma}_0^{(s)} \left(\frac{\sqrt{\overline{\boldsymbol{\sigma}} \cdot \widehat{\mathbf{S}}^{mvar,(s)} \cdot \overline{\boldsymbol{\sigma}}}}{\tau_0^{(s)}(1-f)} \right)^{n} \frac{\widehat{\mathbf{S}}^{mvar,(s)} \cdot \overline{\boldsymbol{\sigma}}}{\sqrt{\overline{\boldsymbol{\sigma}} \cdot \widehat{\mathbf{S}}^{mvar,(s)} \cdot \overline{\boldsymbol{\sigma}}}} \qquad (2.126)$$

2.4.6 Rate-independent porous single crystals

In this section, we specialize the homogenization results developed in previous sections for the case of rate-independent porous single crystals. For this, we need to consider

the limit as $n \to \infty$ or, equivalently, $m \to 0$ for the nonlinear exponent of the single crystal matrix defined in relation (2.31).

Hence, making use of equation (7.2) for the MVAR estimate $\widetilde{U}_{mvar}$ for a viscoplastic porous single crystal, which is repeated here for convenience

$$\widetilde{U}_{mvar}(\overline{\boldsymbol{\sigma}}) = (1-f) \sum_{s=1}^{K} \frac{\dot{\gamma}_0^{(s)} \tau_0^{(s)}}{n+1} \left(\frac{\sqrt{\overline{\boldsymbol{\sigma}} \cdot \widehat{\mathbf{S}}^{mvar,(s)} \cdot \overline{\boldsymbol{\sigma}}}}{\tau_0^{(s)} (1-f)} \right)^{n+1}, \tag{2.127}$$

together with the limit $n \longrightarrow \infty$, we can define the corresponding equation describing the effective yield surface of the "modified variational" method in the rate-independent context in terms of the yield function $\widetilde{\Phi}_{mvar}$ via

$$\widetilde{\Phi}_{mvar}(\overline{\sigma}; s_\alpha) = \max_{s=1,K} \left\{ \frac{\sqrt{\overline{\boldsymbol{\sigma}} \cdot \widehat{\mathbf{S}}^{mvar,(s)} \cdot \overline{\boldsymbol{\sigma}}}}{1-f} - \tau_0^{(s)} \right\} = 0, \tag{2.128}$$

where, $s_\alpha = \left\{ f,\, w_1,\, w_2,\, \mathbf{n}^{(1)},\, \mathbf{n}^{(2)},\, \mathbf{n}^{(3)} = \mathbf{n}^{(1)} \times \mathbf{n}^{(2)} \right\}$ is the set of the microstructural variables defined in relation (2.18), while $\widehat{\mathbf{S}}^{(s)}$ is given by (7.3). In addition,

$$q_J = \sqrt{\frac{5}{2}} \frac{1-f}{\sqrt{f} \ln(1/f)}. \tag{2.129}$$

Next, the corresponding macroscopic strain-rate $\overline{\boldsymbol{D}}$ is given by differentiating the effective yield function $\widetilde{\Phi}_{mvar}$ in (2.128) with respect to $\overline{\boldsymbol{\sigma}}$, so that

$$\overline{\boldsymbol{D}} = \dot{\Lambda} \frac{\partial \widetilde{\Phi}_{mvar}}{\partial \overline{\boldsymbol{\sigma}}} = \frac{\dot{\Lambda}}{1-f} \frac{\widehat{\mathbf{S}}^{mvar,(s)} \cdot \overline{\boldsymbol{\sigma}}}{\sqrt{\overline{\boldsymbol{\sigma}} \cdot \widehat{\mathbf{S}}^{mvar,(s)} \cdot \overline{\boldsymbol{\sigma}}}}, \tag{2.130}$$

where $\dot{\Lambda}$ is a non-negative parameter known as the plastic multiplier computed by the consistency condition $\dot{\widetilde{\Phi}}_{mvar} = 0$.

2.4.7 Phase average fields

In this section, estimates for the phase average fields in the nonlinear composite will be provide in order to complete the study. It is known that (Idiart and Ponte Castañeda [2006]) in the variational method, the phase average fields in the nonlinear composite coincide with the phase average fields in the LCC.

In addition, in the limit of $\lambda^{(s)} \to \lambda$, one can easily show that the tensors $\boldsymbol{\mathcal{S}}$, $\widetilde{\boldsymbol{\mathcal{S}}}$ and $\widehat{\boldsymbol{\Pi}}$ defined in the following as

$$\boldsymbol{\mathcal{S}} = \lambda \lim_{\lambda^{(s)} \to \lambda} \mathbf{S} = \sum_{s=1}^{K} \frac{1}{2} \mathbf{E}^{(s)}, \tag{2.131}$$

$$\widetilde{\boldsymbol{S}} = \lambda \lim_{\lambda^{(s)} \to \lambda} \widetilde{\mathbf{S}} = \frac{1}{1-f} \sum_{s=1}^{K} \widehat{\mathbf{S}}^{mvar,(s)}, \tag{2.132}$$

$$\widehat{\boldsymbol{\Pi}}_{ijkl} = \lambda \lim_{\lambda^{(s)} \to \lambda} \boldsymbol{\Pi}_{ijkl} = \frac{1}{4\pi \det \boldsymbol{Z}} \int_{|\xi|=1} \frac{\left(\boldsymbol{S}_{iakb}^{-1}\xi_a\xi_b\right)^{-1} \xi_j\xi_l\big|_{[ij](kl)}}{\left|\boldsymbol{Z}^{-1} \cdot \xi\right|^3} dS. \tag{2.133}$$

are independent of λ.

Here the simple brackets indicate the symmetric part of the last two indices while the square brackets denote the skew-symmetric part of the first two indices.

Thus, using the relations developed in subsection 2.3.1, the following estimates are deduced for the phase average fields in the nonlinear porous single crystal

$$\overline{\boldsymbol{\sigma}}^{(1)} = \overline{\boldsymbol{\sigma}}_0^{(1)} = \frac{1}{1-f}\overline{\boldsymbol{\sigma}}_0 = \frac{1}{1-f}\overline{\boldsymbol{\sigma}}, \quad \overline{\boldsymbol{\sigma}}^{(2)} = \overline{\boldsymbol{\sigma}}_0^{(2)} = 0, \tag{2.134}$$

$$\overline{\boldsymbol{D}}^{(1)} = \mathbf{A}^{(1)}\,\overline{\boldsymbol{D}} = \frac{1}{1-f}\boldsymbol{S}\,\widetilde{\boldsymbol{S}}^{-1}\,\overline{\boldsymbol{D}}, \tag{2.135}$$

$$\overline{\boldsymbol{D}}^{(2)} = \mathbf{A}^{(2)}\,\overline{\boldsymbol{D}} = \frac{1}{f}\left(\mathbf{I} - \boldsymbol{S}\,\widetilde{\boldsymbol{S}}^{-1}\right)\overline{\boldsymbol{D}}, \tag{2.136}$$

$$\overline{\boldsymbol{\Omega}}^{(2)} = \overline{\boldsymbol{\Omega}} + (1-f)\,\widehat{\boldsymbol{\Pi}}\boldsymbol{S}^{-1}\overline{\boldsymbol{D}}, \tag{2.137}$$

with

$$\overline{\boldsymbol{D}} = \sum_{s=1}^{K} \dot{\gamma}_0^{(s)} \left(\frac{\sqrt{\overline{\boldsymbol{\sigma}} \cdot \widehat{\mathbf{S}}^{mvar,(s)} \cdot \overline{\boldsymbol{\sigma}}}}{\tau_0^{(s)}(1-f)} \right)^n \frac{\widehat{\mathbf{S}}^{mvar,(s)} \cdot \overline{\boldsymbol{\sigma}}}{\sqrt{\overline{\boldsymbol{\sigma}} \cdot \widehat{\mathbf{S}}^{mvar,(s)} \cdot \overline{\boldsymbol{\sigma}}}}. \tag{2.138}$$

Moreover, it is important to notice that in the work of (Idiart and Ponte Castañeda [2006]), the estimating the phase average spin in the nonlinear composite is not studied. However, based on the corresponding results for the average strain-rate $\overline{\boldsymbol{D}}^{(1)}$ or $\overline{\boldsymbol{D}}^{(2)}$, we can deduce that the same result could be applied to the average spin $\overline{\boldsymbol{\Omega}}^{(2)}$.

Finally, the second-order macroscopic spin tensor tensor $\overline{\boldsymbol{\Omega}}$ is applied externally to the problem.

2.5 Evolution of microstructure

The determination of the instantaneous effective behavior of nonlinear porous media with particulate microstructures has been carried out through a set of internal variables denoted as $s_\alpha = \left\{ f,\, w_1,\, w_2,\, \mathbf{n}^{(1)},\, \mathbf{n}^{(2)},\, \mathbf{n}^{(3)} \right\}$ (see fig. 2.1). For completeness, it is useful to recall here that these microstructural variables correspond to the volume fraction

of the voids or porosity f, the shape of the voids denoted with the two aspect ratios w_1 and w_2, and the orientation of the principal axes of the representative ellipsoidal void, i.e., the orientation vectors $\mathbf{n}^{(i)}$, $i = 1, 2, 3$.

On the other hand, in the present study, there esists two sources of anisotropy during the deformation process. The "natural" anisotropy of the matrix (crystal plasticity) which is coupled with the so called morphological anisotropy due to the non spherical void shapes. Indeed, when porous single crystals undergo large plastic deformations, the underlying microstructure (void volume, shape and orientation) evolves. The microstructure evolution, in turn, affects the response of the material itself since the yield condition and the plastic flow rule depend on the current state of the microstructure. Hence, one needs to prescribe relevant evolution laws for the microstructural state variables s_α. In the context of the present study, we assume that evolution of microstructure occurs only due to plastic deformation of the matrix. In addition, it is important to note that in homogenization models as for instance the MVAR model, the description of the effective behavior is described in average terms. Consequently, ellipsoidal voids, whose shape and orientation is described by the two aspect ratios w_1 and w_2 and the orientation vectors $\mathbf{n}^{(i)}$, $i = 1, 2, 3$, respectively, evolve on average to ellipsoidal voids with different shape and orientation. This, in turn, suggests that the average change in shape and orientation of the voids depends only upon the average strain-rate $\overline{\boldsymbol{D}}^{(2)}$ and the average spin $\overline{\boldsymbol{\Omega}}^{(2)}$ in the porous phase, discussed in the previous section (subsection 2.4.7). Then, the evolution laws for the microstructural variables are obtained simply by appropriate kinematic considerations.

At this stage of the work, we neglect elasticity. This is done for simplicity but elasticity effects could be added in future studies. This implies that $\overline{\boldsymbol{D}} = \overline{\boldsymbol{D}}^p$ since $\overline{\boldsymbol{D}}^e = 0$, where the superscript "p" and "e" refer to plastic and elastic parts.

2.5.1 Evolution of the average slip rate in the matrix

The changes in the microstructure are assumed to be due to the plastic deformation, i.e. elastic deformations are considered to have a negligible effect, but this could be considered in a future study if necessary.

If one defines $\dot{\bar{\gamma}}_{(1)}^{(s)}$ as the effective slip-rate of the slip system (s) in the matrix, its

evolution equation can be determined using the relation

$$\overline{\boldsymbol{D}}^{(1)} = \sum_{s=1}^{K} \dot{\overline{\gamma}}_{(1)}^{(s)} \boldsymbol{\mu}^{(s)}. \tag{2.139}$$

In addition, due to the LCC, we have

$$\overline{\boldsymbol{D}}^{(1)} = \mathbf{S}\,\overline{\boldsymbol{\sigma}}^{(1)} = \frac{1}{1-f}\left(\frac{1}{2\lambda^{(s)}}\mathbf{E}^{(s)}\right)\overline{\boldsymbol{\sigma}}, \tag{2.140}$$

where the $\lambda^{(s)}$ are determined in the variational optimization procedure through the equation (2.114).

Thus, the relation (2.140) becomes

$$\overline{\boldsymbol{D}}^{(1)} = \mathbf{S}\,\overline{\boldsymbol{\sigma}}^{(1)} = \frac{1}{1-f}\sum_{s=1}^{K}\dot{\gamma}_0^{(s)}\frac{\overline{\boldsymbol{\sigma}}\cdot\boldsymbol{\mu}^{(s)}}{\tau_0^{(s)}}\left(\frac{\sqrt{\overline{\boldsymbol{\sigma}}\cdot\widehat{\mathbf{S}}^{mvar,(s)}\cdot\overline{\boldsymbol{\sigma}}}}{\tau_0^{(s)}\left(1-f\right)}\right)^{n-1}\boldsymbol{\mu}^{(s)}, \tag{2.141}$$

and furthermore, the combination of relations (2.139) and (2.141) leads to

$$\overline{\boldsymbol{D}}^{(1)} = \frac{1}{1-f}\sum_{s=1}^{K}\dot{\gamma}_0^{(s)}\frac{\overline{\boldsymbol{\sigma}}\cdot\boldsymbol{\mu}^{(s)}}{\tau_0^{(s)}}\left(\frac{\sqrt{\overline{\boldsymbol{\sigma}}\cdot\widehat{\mathbf{S}}^{mvar,(s)}\cdot\overline{\boldsymbol{\sigma}}}}{\tau_0^{(s)}\left(1-f\right)}\right)^{n-1}\boldsymbol{\mu}^{(s)} = \sum_{s=1}^{K}\dot{\overline{\gamma}}_{(1)}^{(s)}\boldsymbol{\mu}^{(s)}. \tag{2.142}$$

Then, since the previous relation is true for any crystal anisotropy, the average shear strain $\dot{\overline{\gamma}}_{(1)}^{(s)}$ of any slip system (s) is given by

$$\dot{\overline{\gamma}}_{(1)}^{(s)} = \frac{1}{1-f}\dot{\gamma}_0^{(s)}\frac{\overline{\boldsymbol{\sigma}}\cdot\boldsymbol{\mu}^{(s)}}{\tau_0^{(s)}}\left(\frac{\sqrt{\overline{\boldsymbol{\sigma}}\cdot\widehat{\mathbf{S}}^{mvar,(s)}\cdot\overline{\boldsymbol{\sigma}}}}{\tau_0^{(s)}\left(1-f\right)}\right)^{n-1}. \tag{2.143}$$

Then the accumulated average slip in the matrix is given by

$$\overline{\gamma}_{(1)}^{(s)} = \int_t \dot{\overline{\gamma}}_{(1)}^{(s)} dt. \tag{2.144}$$

For strain hardening materials, $\tau_0^{(s)}$ is a function of the slip $\overline{\gamma}_{(1)}^{(s)}$, which, in general, is to be extracted from experimental uniaxial stress strain curves. As discussed by many authors (e.g. Asaro [1983], Wu et al. [1991], Huang [1991], Kysar [1997]), the strain hardening is characterized by the evolution of the strengths $\tau_0^{(s)}$ through the incremental relation

$$\tau_0^{(s)} = \sum_{\beta=1}^{K} h_{s\beta}\overline{\gamma}_{(1)}^{(\beta)}, \tag{2.145}$$

where $h_{s\beta}$ are the slip hardening moduli whereas the sum ranges over all the activated slip systems. Here h_{ss} and $h_{s\beta}$ ($s \neq \beta$) are called self and latent hardening moduli, respectively. It is important to precise at this stage that we have not considered the hardening response during the homogenization procedure, which has only been added at the end in an ad-hoc manner in relation (2.145). A full homogenization framework has for instance been proposed in Lahellec and Suquet [2013] but at this point it is not applied to this model in order to keep it simple.

2.5.2 Evolution of the porosity

Next by neglecting elastic contributions, the matrix material is plastically incompressible (crystal plasticity), and thus the evolution equation for the porosity f can be obtained from mass conservation and reads (Tvergaard and Needleman [1984])

$$\dot{f} = (1 - f)\overline{D}_{ii}, \ i = 1, 2, 3. \tag{2.146}$$

Furthermore, it is important to precise that void nucleation is not considered in the above relation but can be included by a convenient modification of (2.146) (see for instance Needleman and Rice [1978], Tvergaard [1990]).

2.5.3 Evolution of the aspect ratios

The evolution law for the aspect ratios is obtained by using standard kinematics and the definition $w_i = a_3/a_i$, $i = 1, 2$, such that (Ponte Castañeda and Zaidman [1994])

$$\dot{w}_i = \alpha_w \, w_i \left(\mathbf{n}^{(3)} \cdot \overline{\boldsymbol{D}}^{(2)} \mathbf{n}^{(3)} - \mathbf{n}^{(i)} \cdot \overline{\boldsymbol{D}}^{(2)} \mathbf{n}^{(i)} \right) = \alpha_w \, w_i \left(\mathbf{n}^{(3)} \otimes \mathbf{n}^{(3)} - \mathbf{n}^{(i)} \otimes \mathbf{n}^{(i)} \right) \cdot \overline{\boldsymbol{D}}^{(2)}, \tag{2.147}$$

where there is no summation on $i = 1, 2$, and $\overline{\boldsymbol{D}}^{(2)}$ is given by (2.134). The scalar factor α_w has been introduced in the last expression in a heuristic manner in order to enhance the accuracy of the evolution of the aspect ratios, since Danas and Aravas [2012] have showed that the original variational method and consequently the present MVAR tend to underestimate the evolution of the void shape at low stress triaxialities. The factor α_w is in general considered as a free parameter that can be calibrated from experiments.

2.5.4 Evolution of the orientation vectors

The evolution of the orientation vectors $\mathbf{n}^{(i)}, i = 1, 2, 3$ is determined by the spin of the Eulerian axes of the ellipsoidal voids, or microstructural spin ω, as

$$\dot{\mathbf{n}}^{(i)} = \omega \mathbf{n}^{(i)}, \ i = 1, 2, 3 \tag{2.148}$$

The microstructural spin ω is related to the average spin and the average strain-rate in the void, $\overline{\boldsymbol{\Omega}}^{(2)}$ and $\overline{\boldsymbol{D}}^{(2)}$ (given by 2.134), by the classical kinematic relation written in direct notation as (Hill [1978], Ogden [1984], Aravas and Ponte Castañeda [2004], Danas and Aravas [2012])

$$\omega = \overline{\boldsymbol{\Omega}}^{(2)} + \frac{1}{2} \sum_{\substack{i,j=1 \\ i \neq j \\ w_i \neq w_j}}^{3} \frac{w_i^2 + w_j^2}{w_i^2 - w_j^2} \left[\left(\mathbf{n}^{(i)} \otimes \mathbf{n}^{(j)} + \mathbf{n}^{(j)} \otimes \mathbf{n}^{(i)} \right) \cdot \overline{\boldsymbol{D}}^{(2)} \right] \mathbf{n}^{(i)} \otimes \mathbf{n}^{(j)}, \quad w_3 = 1. \tag{2.149}$$

The special case in which at least two aspect ratios are equal is discussed later in this section.

An equivalent equation to deal with both void aspect ratios and rotation has been proposed by Madou and Leblond [2013].

In addition, it is useful to discuss the evaluation of the Jaumann rate of the orientation vectors $\mathbf{n}^{(i)}$, denoted by $\overset{\triangledown}{\mathbf{n}}^{(i)}$, $(i = 1, 2, 3)$. The Jaumann rate is related to the standard time derivative of relation (2.148) by

$$\overset{\triangledown}{\mathbf{n}}^{(i)} = \dot{\mathbf{n}}^{(i)} - \overline{\boldsymbol{\Omega}} \, \mathbf{n}^{(i)} = \left(\omega - \overline{\boldsymbol{\Omega}} \right) \mathbf{n}^{(i)}, \quad i = 1, 2, 3, \tag{2.150}$$

with $\overline{\boldsymbol{\Omega}}$ being the macroscopic average spin applied externally in the problem. At this point, it is convenient to introduce the notion of the plastic spin (Dafalias [1985]), which is defined as the spin of the continuum relative to the microstructure, i.e.,

$$\boldsymbol{\Omega}^p = \overline{\boldsymbol{\Omega}} - \omega. \tag{2.151}$$

Consequently,

$$\overset{\triangledown}{\mathbf{n}}^{(i)} = -\boldsymbol{\Omega}^p \, \mathbf{n}^{(i)}, \quad i = 1, 2, 3. \tag{2.152}$$

Furthermore, we point out that special care needs to be taken for the computation of the spin of the Eulerian axes in the case of a spherical void, i.e., when $w_1 = w_2 = w_3 = 1$, as well as for a spheroidal void, i.e., when $w_1 = w_2 \neq w_3 = 1$ or

$w_1 \neq w_2 = w_3 = 1$ or $w_1 = w_3 \neq w_2 = 1$. More specifically, when two of the aspect ratios are equal, the component Ω_{12}^p becomes indeterminate. Since the spin $\overline{\Omega}_{12}^p$ is inconsequential in this case, it can be set equal to zero (Aravas [1992]), which implies that $\omega_{12} = \overline{\Omega}_{12}$. This notion can be applied whenever the shape of the void is spheroidal, in any given orientation. In the same way, when the voids are spherical, $\boldsymbol{\Omega}^p = 0$ and hence $\dot{\mathbf{n}}^{(i)} = \overline{\boldsymbol{\Omega}}\, \mathbf{n}^{(i)}$, $i = 1, 2, 3$.

2.6 Concluding remarks

A homogenization-based framework to estimate the effective behavior of viscoplastic porous single crystals subjected to general loading conditions is presented in this chapter. More precisely, the "variational" (Ponte Castañeda [1991a]) homogenization method has been used in order to derive models for porous crystals. These methods are based on the construction of suitable variational principles utilizing the concept of "linear comparison composite" (LCC). It is then possible to make use of available linear homogenization results into estimates for the nonlinear porous media. In addition, motivated by applications of practical interest, one has specialized on the case of porous crystals with particulate microstructures and a matrix phase which is described by a power-law stress potential.

In this regard then, we have firstly recalled the notion of particulate microstructures. In order to achieve this, we have defined the internal variables describing the volume fraction, shape and orientation of the voids. Hence, using the linear Willis estimates (Willis [1977]), one can determine the effective behavior of the LCC which is required to provide estimates for linear porous materials with particulate microstructures. However, it is worth noting that more general micro-geometries could be easily considered, including multiple families of aligned pores by exploiting for instance more general versions of the Willis (Ponte Castañeda and Willis [1995]) estimates for the LCC. Such studies are not performed in this study.

Furthermore, we have introduced the definitions associated with a commonly used power-law form of incompressible viscoplastic stress potential. Based on these definitions, we have been able to extract estimates of the effective viscoplastic stress potential for porous single crystals through the "variational" homogenization methods. Moreover, it is known (Ponte Castañeda [1991b], Michel and Suquet [1992]) that

in the case of isotropic matrix and hydrostatic loadings the variational estimates are overly stiff. In order to remedy this overly stiff response, we have used the fact that in the isotropic case (number of slip systems $K \longrightarrow \infty$), the hydrostatic limit of the effective behavior of composite spherical assemblages (CSA) is known exactly and in closed form (Hashin [1962], Gurson [1977], Leblond et al. [1994]). Hence, following (Danas et al. [2008a], Danas and Aravas [2012]), we have proposed "modified variational" estimates (MVAR) to make the estimates recovering the CSA result (2.118) in the limit of infinite number of slip systems, spherical voids and hydrostatic loadings, where the response becomes fully isotropic.

Finally, it should be precise that the porous single crystals are in general subjected to finite deformations. Consequently, the microstructure evolves-on average-to ellipsoidal voids in time with different shape and orientation. Thus, based on the work of (Ponte Castañeda and Zaidman [1994], Aravas and Ponte Castañeda [2004], Danas and Aravas [2012]), we have presented the relevant evolution laws for the internal microstructural variables used to describe the volume fraction, shape and orientation of the voids.

2.7 Appendix I. Relation between the single crystal and the isotropic matrix behaviors

As seen in subsection 2.2.1, in the special case of slip systems with identical critical resolved shear stress CRSS and reference slip rate $((\tau_0)^{(s)} = \tau_0, (\dot{\gamma}_0)^{(s)} = \dot{\gamma}_0, \forall s = 1, K)$, the viscoplastic stress potential of the single crystal is written as

$$U(\boldsymbol{\sigma}) = \frac{\dot{\gamma}_0 \tau_0^{-n}}{n+1} \sum_{s=1}^{K} \left| \tau^{(s)} \right|^{n+1}. \tag{2.153}$$

If we consider a triaxial loading state, with θ denoting the Lode angle, the stress tensor can be expressed as

$$\boldsymbol{\sigma} = \sigma_m \{1, 1, 1\} + \frac{2\sigma_{eq}}{3} \left\{ \cos\theta, -\cos\left(\theta + \frac{\pi}{3}\right), -\cos\left(\theta - \frac{\pi}{3}\right) \right\}. \tag{2.154}$$

Moreover, one can parameterized the slip normals and directions of all the slip systems using three Euler angles $\alpha_1^{(s)}$, $\alpha_2^{(s)}$ and $\alpha_3^{(s)}$, since $\mathbf{m}^{(s)} \perp \mathbf{s}^{(s)}$, such as

$$\mathbf{m}^{(s)} = \left(\sin \alpha_3^{(s)} \cos \alpha_1^{(s)}, \sin \alpha_3^{(s)} \sin \alpha_1^{(s)}, \cos \alpha_3^{(s)} \right)^T$$
$$\mathbf{s}^{(s)} = \cos \alpha_2^{(s)} \left(-\sin \alpha_1^{(s)}, \cos \alpha_1^{(s)}, 0 \right)^T + \sin \alpha_2^{(s)} \left(\cos \alpha_3^{(s)} \cos \alpha_1^{(s)}, \cos \alpha_3^{(s)} \sin \alpha_1^{(s)}, -\sin \alpha_3^{(s)} \right)^T$$

$$(2.155)$$

where $0 \leq \alpha_1^{(s)}, \alpha_3^{(s)} \leq 2\pi, \quad 0 \leq \alpha_2^{(s)} \leq \pi.$

Figure 2.3: (a) $\widehat{\beta}(n, \theta)$ represented as a function of the Lode angle θ for a creep exponent $n = 1$, (b) Representation of the numerical values and the approximate function of $\beta(n)$ for a range of creep exponents.

Thus, in the limiting case of isotropic matrix, i.e. $K \longrightarrow \infty$, the relations (2.26), (2.153), (2.154) and (2.155) lead to the following form of the potential

$$U(\boldsymbol{\sigma}) \cong \frac{\dot{\gamma}_0 \tau_0^{-n}}{n+1} \sigma_{eq}^{n+1} K \lim_{K \to \infty} \frac{1}{K} h \left(\alpha_1^{(s)}, \alpha_2^{(s)}, \alpha_3^{(s)}, \theta, n \right) \cong \frac{\dot{\gamma}_0 \tau_0^{-n}}{n+1} \sigma_{eq}^{n+1} K \widehat{\beta}(n, \theta).$$

$$(2.156)$$

The numerical computation of $\widehat{\beta}(n, \theta)$ for various values of the Lode angle and a large range of creep exponents exhibits a behavior that can be approximated as periodic on θ (see for instance fig 2.3a, in the case of $n = 1$). More precisely, one can write

$$U(\boldsymbol{\sigma}) \cong \frac{\dot{\gamma}_0 \tau_0^{-n}}{n+1} \sigma_{eq}^{n+1} K \widehat{\beta}(n, \theta), \qquad \widehat{\beta}(n, \theta) \cong \beta(n) g(\theta) \cong \frac{4}{25} 6^{-\frac{n}{2}} \left(\cos \left(\theta - \frac{\pi}{3} \right) \right)^{n+1}.$$

$$(2.157)$$

A representation of β_n is shown in fig 2.3b.

2.8 Appendix II. Computation of the microstructural tensors

This section deals with the computation of the microstructural tensor $\widehat{\mathbf{S}}_0^*$ (see equations 2.102 and 2.106) in the incompressibility limit. In order to achieve this goal, one needs to determine the associated Eshelby tensor $\mathbf{Q}$ or equivalently $\mathbf{P}$ (see 2.103), recalled here for completeness

$$\mathbf{P}_{ijkl} = \frac{1}{4\pi \, \det \mathbf{Z}} \int_{|\xi|=1} \frac{\left((\mathbf{S}^{-1})_{iakb} \, \xi_a \xi_b\right)^{-1} \xi_j \xi_l|_{(ij)(kl)}}{\left|\mathbf{Z}^{-1} \cdot \xi\right|^3} dS, \quad \mathbf{Q} = \mathbf{S}^{-1} - \mathbf{S}^{-1} \mathbf{P} \mathbf{S}^{-1}. \tag{2.158}$$

However, in the present single crystal case, the compliance tensor $\mathbf{S}_0$ is anisotropic and is given in equation 2.99. Thus, it becomes very hard to get either analytical expressions in the general case, or to carry out numerical computations even by making use of the commercial package Mathematica.

Once the incompressibility limit is considered, the corresponding integral (2.158) can be determined numerically. For this, one needs to evaluate surface integrals of the form

$$I = \int_{|\zeta|=1} A(\zeta) \, dS(\zeta) = \int_{\phi=0}^{\pi} \int_{\theta=0}^{2\pi} A(\zeta(\phi,\theta)) \sin(\theta) \, d\theta \, d\phi, \tag{2.159}$$

where $\zeta = \{\sin\phi\cos\theta, \sin\phi\sin\theta, \cos\phi\}$.

This integration scheme has been observed to become inaccurate when the aspect ratios become large or small, such as $w_1 = 5$ and $w_2 = 0.2$ (Aravas and Ponte Castañeda [2004]). For this reason, it is useful to write the vector ζ in cylindrical coordinates, such that

$$\zeta_1 = \sqrt{1-z}\cos\theta, \ \zeta_2 = \sqrt{1-z}\sin\theta, \ \zeta_3 = z \tag{2.160}$$

Then, the aforementioned integral I can be rewritten as

$$I = \int_{z=-1}^{1} \int_{\theta=0}^{2\pi} A(\zeta(\theta,z)) \, d\theta \, dz. \tag{2.161}$$

By using the transformation $\theta(r) = (r+1)\pi$ in the previous equation, we get the following expression

$$I = \pi \int_{z=-1}^{1} \int_{r=-1}^{1} A(\zeta(\theta(r),z)) \, dr \, dz. \tag{2.162}$$

This integral can be evaluated numerically by using Gauss integration of the form

$$I \cong \pi \sum_{i=1}^{NG} \sum_{j=1}^{NG} W_i W_j A\left(\zeta\left(r_i, z_i\right)\right), \tag{2.163}$$

where r_i and z_i are the integration stations, W_i and W_j the corresponding weights, and NG the number of Gauss integration stations.

2.9 Appendix III. Microstructural tensor in the limiting case of $K \to \infty$ (isotropic matrix)

In the case of slip systems with identical CRSS τ_0 and reference slip-rate $\dot{\gamma}_0$, the compliance tensor $\mathbf{S}$ of the linear comparison composite is given by equation (2.99) by setting $\lambda^{(s)} = \lambda$ and $\rho^{(s)} = \rho$,

$$\mathbf{S} = \frac{1}{2\lambda} \sum_{s=1}^{K} \mathbf{E}^{(s)} + \frac{1}{2\rho} \sum_{s=1}^{K} \mathbf{F}^{(s)} + \frac{1}{3\kappa} \mathbf{J}, \text{ with } \mathbf{E}^{(s)} = 2\boldsymbol{\mu}^{(s)} \otimes \boldsymbol{\mu}^{(s)}, \mathbf{F}^{(s)} = \mathbf{K} - \mathbf{E}^{(s)}, \forall s = 1, K. \tag{2.164}$$

On the other hand, the microstructural tensor can easily be computed in the case of an isotropic compliance matrix (Von Mises matrix, $\mathbf{S}_{Mises} = \frac{1}{2\mu_0} \mathbf{K} + \frac{1}{3\kappa_0} \mathbf{J}$), an expressed as

$$\mathbf{S}^*_{Mises} = \frac{1}{3\mu_0} \mathbf{K} + \frac{1}{4\mu_0} \mathbf{J}, \tag{2.165}$$

for isotropic microstructures and incompressible matrix material (i.e. $\kappa_0 \to \infty$).

Moreover, the numerical computation of the hydrostatic part of $\frac{\mathbf{S}^*}{K}$ in the infinite number of slip systems case (i.e. Tresca matrix) for spherical voids leads to closer result (up to 2%) than the hydrostatic part of the microstructural tensor associated to the compliance tensor of a Von Mises matrix. Hence, one can, as a first approximation, use the tensor $\mathbf{S}_{Mises}$ instead of $\mathbf{S}$ in the limit isotropic case $K \to \infty$. Suitable values for μ_0 and κ_0 must consequently be used. In order to achieve this goal, the deviatoric and hydrostatic projections of both tensors lead to

$$\mu_0 = \frac{5}{\frac{K}{\lambda} + \frac{K}{\rho}}, \; \kappa_0 = \kappa \tag{2.166}$$

Thus, using the identity (2.166) into (2.165), one can readily show that in the limit $\rho \to \infty$, $\kappa \to \infty$ and $K \to \infty$, the microstructural tensor $\mathbf{S}^*$ defined in equation

(2.102) becomes

$$\lim_{K\to\infty}\lim_{\rho\to\infty}\lim_{\kappa\to\infty}\frac{\mathbf{S}^*}{K}\cong\frac{1}{5\lambda}\left(\frac{1}{3}\mathbf{K}+\frac{1}{4}\mathbf{J}\right),\qquad(2.167)$$

or equivalently

$$\lim_{K\to\infty}\lim_{\rho\to\infty}\lim_{\kappa\to\infty}\frac{\hat{\mathbf{S}}^*}{K}\cong\frac{1}{5}\left(\frac{1}{3}\mathbf{K}+\frac{1}{4}\mathbf{J}\right),\qquad(2.168)$$

for spherical voids.

2.10 Appendix IV. MVAR fully analytical model for cylindrical microstructures

In the case of cylindrical microstructures, one can provide analytical expressions for the microstructural tensor $\widehat{\mathbf{S}}^*$, which reads

$$\widehat{\mathbf{S}}^* = \frac{1}{2w\sqrt{2}}\sqrt{\sum_{j\neq l}\left(1-\cos 4\left(\theta^{(j)}-\theta^{(l)}\right)\right)}\mathbf{G},\qquad(2.169)$$

where the components of tensor $\mathbf{G}$ are given by

$$\begin{aligned}
\mathbf{G}_{1111} &= w^2\cos^2\psi+\sin^2\psi, \quad \mathbf{G}_{1122}=0, \quad \mathbf{G}_{1112}=\frac{1}{4}\left(w^2-1\right)\sin 2\psi,\\
\mathbf{G}_{2222} &= \cos^2\psi+w^2\sin^2\psi, \quad \mathbf{G}_{2212}=\mathbf{G}_{1112}, \quad \mathbf{G}_{1212}=\frac{1}{4}\left(1+w^2\right).
\end{aligned}\qquad(2.170)$$

It should be mentioned here that $\mathbf{G}$ possesses both major and minor symmetry, and has a similar form to that obtained for an isotropic matrix comprising elliptical voids (see Danas [2008]).

In the following sections, we will provide a MVAR fully analytical model for porous single crystals comprising cylindrical voids with elliptical cross-section at arbitrary orientations and subjected to general plane-strain loadings (i.e. 2D porous single crystals).

2.10.1 Relation between the single crystal and the isotropic matrix behaviors

In the following, we consider K equiangular slip systems by orientation angles $\theta^{(s)}$ equally partitioned in the interval $(-\pi/2,\pi/2)$, with K being the number of slip systems and $s=1,K$ (see for instance Table 1).

Next, we consider the special, albeit very common, case of identical CRSS and reference slip-rate such that

$$\tau_0^{(s)} = \tau_0, \ \dot{\gamma}_0^{(s)} = \dot{\gamma}_0, \quad \forall s = 1, K. \tag{2.171}$$

This analysis will be shown to be of critical importance in the following sections.

As a consequence of the plane-strain conditions, the resolved shear of each slip system is then written as

$$
\begin{aligned}
\tau^{(s)} = \boldsymbol{\sigma} \cdot \boldsymbol{\mu}^{(s)} &= \left(\frac{\sigma_{11} - \sigma_{22}}{2} \right) \sin 2\theta^{(s)} + \sigma_{12} \cos 2\theta^{(s)} \\
&= \frac{\sigma_{eq}}{\sqrt{3}} \sin \left(2\theta^{(s)} + \delta \right), \quad \forall s = 1, K,
\end{aligned} \tag{2.172}
$$

with $\delta = \arctan \left(2\sigma_{12}/(\sigma_{11} - \sigma_{22}) \right)$. By introducing this relation in equation (2.31), the viscoplastic stress potential U becomes

$$U(\boldsymbol{\sigma}) = \frac{\dot{\gamma}_0 \tau_0}{n+1} \left(\frac{\sigma_{eq}}{\tau_0 \sqrt{3}} \right)^{n+1} \sum_{s=1}^{K} \left| \sin \left(2\theta^{(s)} + \delta \right) \right|^{n+1}. \tag{2.173}$$

Moreover, when we tend to the limiting case of isotropic matrix, i.e. $K \longrightarrow \infty$, or when we consider "equiangular slip systems" for $K \geq 3$,

$$\sum_{s=1}^{K} \left| \sin \left(2\theta^{(s)} + \delta \right) \right|^{n+1} = K.\frac{1}{K} \left| \sin \left(2\theta^{(s)} + \delta \right) \right|^{n+1} \cong K.\frac{2}{\pi} \int_0^{\pi/2} (\sin \theta)^{n+1} \, d\theta. \tag{2.174}$$

One then recognize a "Wallis" integral (see Wallis [1656]),

$$\int_0^{\pi/2} (\sin \theta)^{n+1} \, d\theta = \frac{\sqrt{\pi}}{(n+1)} \frac{\Gamma \left(\frac{n+2}{2} \right)}{\Gamma \left(\frac{n+1}{2} \right)}, \tag{2.175}$$

Finally, one can recover the constitutive behavior of an isotropic matrix phase, characterized by its viscoplastic stress potential

$$U(\boldsymbol{\sigma}) = \frac{\dot{\epsilon}_0 \sigma_0}{n+1} \left(\frac{\sigma_{eq}}{\sigma_0} \right)^{n+1}, \tag{2.176}$$

with $\dot{\epsilon}_0$ denoting the reference strain-rate, and σ_0 the isotropic flow stress by setting

$$\dot{\gamma}_0 \tau_0^{-n} \left(\frac{1}{\sqrt{3}} \right)^{n+1} \beta_n K = \dot{\epsilon}_0 \sigma_0^{-n}, \tag{2.177}$$

2.10.2 Microstructural tensor in the limiting case infinite number of slip systems

In the case of slip systems with identical CRSS τ_0 and reference slip-rate $\dot{\gamma}_0$, the compliance tensor $\mathbf{S}$ of the linear comparison composite is given by equation (2.99) by setting $\lambda^{(s)} = \lambda$ and $\rho^{(s)} = \rho$.

Then using the fact that $\mathbf{F}^{(s)} = \mathbf{K} - \mathbf{E}^{(s)}$ for all $s = 1, K$ leads to

$$\frac{\mathbf{S}}{K} = \frac{1}{2\lambda}\left(\frac{1}{K}\sum_{s=1}^{K}\mathbf{E}^{(s)}\right) + \frac{1}{2\rho}\left(\mathbf{K} - \frac{1}{K}\sum_{s=1}^{K}\mathbf{E}^{(s)}\right) + \frac{1}{3\kappa\,K}\mathbf{J}. \tag{2.178}$$

Next, in the limit $K \to \infty$, we have the following identity

$$\lim_{K\to\infty}\frac{1}{K}\sum_{s=1}^{K}\mathbf{E}^{(s)} = \frac{1}{2\pi}\int_{0}^{2\pi}\mathbf{E}(\theta)d\theta = \frac{1}{2}\mathbf{K}, \tag{2.179}$$

where θ denotes any arbitrary slip orientation (see Fig. 2.2). Using the identity (2.179) into (2.178), one can readily show that in the limit $\rho \to \infty$, $\kappa \to \infty$ and $K \to \infty$, the microstructural tensor $\mathbf{S}_0^*$ defined in equation (2.102) becomes

$$\lim_{K\to\infty}\lim_{\rho\to\infty}\lim_{\kappa\to\infty}\frac{\mathbf{S}^*}{K} = \frac{1}{2}\left(\frac{1}{2w}\mathbf{G}\right), \tag{2.180}$$

for general 2D elliptical cross-section voids (see Danas [2008]).

2.10.3 Correction of the hydrostatic point

In this subsection, we introduce a correction to the $\widetilde{U}_{var}$ estimate (2.116) in the limit of purely hydrostatic loadings. It is well known from Ponte Castañeda [1991b] and Michel and Suquet [1992]) that in the case of isotropic matrix and hydrostatic loadings the variational estimates are overly stiff. This is also the case in the present work, i.e. the estimate (2.116) for $\widetilde{U}_{var}$ is also very stiff when compared to numerical unit-cell calculations.

The way to remedy this overly stiff response is to use the fact that in the isotropic case, the hydrostatic limit of the effective behavior of composite cylinder assemblages (CCA) is known exactly and in closed form (Hashin [1962], Gurson [1977], Leblond et al. [1994]) and can be expressed as

$$\frac{\overline{\sigma}_m}{\sigma_0} = n\left(f^{-1/n} - 1\right) \cdot \frac{1}{3^{\frac{n+1}{2n}}} \cdot \left(\frac{2\overline{D}_m}{\dot{\epsilon}_0}\right)^{1/n}. \tag{2.181}$$

In the present case of anisotropic crystal plasticity no simple analytic solution is available similar to the one in (2.181). Nevertheless, one can insist that the estimate (2.116) should recover the result (2.181) in the limit of infinite equiangular slip systems, circular voids and hydrostatic loadings, where the response becomes fully isotropic.

To achieve this goal and motivated by similar work on isotropic matrix systems (Danas and Aravas [2012] but see also Danas et al. [2008a]), we propose the following modification in (2.116)

$$\widetilde{U}_{mvar}\left(\overline{\boldsymbol{\sigma}}\right) = (1-f)\sum_{s=1}^{K}\frac{\dot{\gamma}_0^{(s)}\tau_0^{(s)}}{n+1}\left(\frac{\sqrt{\overline{\boldsymbol{\sigma}}\cdot\widehat{\mathbf{S}}^{mvar,(s)}\cdot\overline{\boldsymbol{\sigma}}}}{\tau_0^{(s)}(1-f)}\right)^{n+1}, \quad \widehat{\mathbf{S}}^{mvar,(s)} = \widehat{\mathbf{S}}^{var,(s)}+\left(q_J^2-1\right)\mathbf{J}\cdot\widehat{\mathbf{S}}^{var,(s)}\cdot\mathbf{J}.$$

$$(2.182)$$

The label "mvar" refers to "modified variational" (MVAR), whereas the factor "q_J" remains to be defined so that we obtain the CCA result (2.181) in the limit $K \longrightarrow \infty$.

In this connection, we consider a purely hydrostatic loading $\overline{\boldsymbol{\sigma}}_{ij} = \overline{\sigma}_m\delta_{ij}$ and circular voids (i.e., $w = 1$) embedded in a single crystal comprising slip systems with identical CRSS and reference slip rate, i.e. $\tau_0^{(s)} = \tau_0$, $\dot{\gamma}_0^{(s)} = \dot{\gamma}_0$, $\forall s = 1, K$. In the case of infinite and/or equiangular slip systems, we can write (see relations (2.190) and (2.180) where $w = 1$)

$$\widehat{\mathbf{S}}^{var,(s)} = \frac{1}{2}\mathbf{E}^{(s)} + \frac{f}{4}\mathbf{I}, \ \forall s = 1, K \implies \widetilde{U}_{mvar}\left(\overline{\boldsymbol{\sigma}}\right) = (1-f)^{-n}K\frac{\dot{\gamma}_0\tau_0^{-n}}{n+1}\overline{\sigma}_m^{n+1}\left(\frac{f}{2}q_J^2\right)^{\frac{n+1}{2}}.$$

$$(2.183)$$

Thus, by using relations (2.8), (2.37), (2.119) and (2.183), one obtains the correction for q_J to be

$$q_J = \sqrt{\frac{2}{f}}\left\{\frac{(1-f)\left(\beta_n\right)^{\frac{1}{n}}}{n(f^{-1/n}-1)}\right\}^{\frac{n}{n+1}},$$

$$(2.184)$$

where β_n is given by expression (2.157).

2.10.4 Summary of the modified variational model (MVAR)

Thus the main result of the present paper can be summarized as follows

$$\widetilde{U}_{mvar}\left(\overline{\boldsymbol{\sigma}}\right) = (1-f)\sum_{s=1}^{K}\frac{\dot{\gamma}_0^{(s)}\tau_0^{(s)}}{n+1}\left(\frac{\sqrt{\overline{\boldsymbol{\sigma}}\cdot\widehat{\mathbf{S}}^{mvar,(s)}\cdot\overline{\boldsymbol{\sigma}}}}{\tau_0^{(s)}(1-f)}\right)^{n+1},$$

$$(2.185)$$

where

$$\widehat{\mathbf{S}}^{mvar,(s)} = \widehat{\mathbf{S}}^{var,(s)} + \left(q_J^2-1\right)\mathbf{J}\cdot\widehat{\mathbf{S}}^{var,(s)}\cdot\mathbf{J},$$

$$(2.186)$$

and

$$\widehat{\mathbf{S}}^{var,(s)} = \frac{1}{2}\mathbf{E}^{(s)} + \frac{f}{2\,K\,w\sqrt{2}}\sqrt{\sum_{j\neq l}\left(1 - \cos 4\left(\theta^{(j)} - \theta^{(l)}\right)\right)}\mathbf{G}, \ \forall s = 1, K. \qquad (2.187)$$

The components of tensor $\mathbf{G}$ are given by equation (2.170) and are repeated here for completeness

$$\begin{aligned}
\mathbf{G}_{1111} &= w^2 \cos^2 \psi + \sin^2 \psi, \quad \mathbf{G}_{1122} = 0, \quad \mathbf{G}_{1112} = \frac{1}{4}\left(w^2 - 1\right)\sin 2\psi, \\
\mathbf{G}_{2222} &= \cos^2 \psi + w^2 \sin^2 \psi, \quad \mathbf{G}_{2212} = \mathbf{G}_{1112}, \quad \mathbf{G}_{1212} = \frac{1}{4}\left(1 + w^2\right).
\end{aligned} \qquad (2.188)$$

In addition, q_J and β_n are

$$q_J = \sqrt{\frac{2}{f}}\left\{\frac{(1-f)\,(\beta_n)^{\frac{1}{n}}}{n(f^{-1/n} - 1)}\right\}^{\frac{n}{n+1}}, \qquad \beta_n = \frac{2}{(n+1)\sqrt{\pi}}\frac{\Gamma\left(\frac{n+2}{2}\right)}{\Gamma\left(\frac{n+1}{2}\right)}, \qquad (2.189)$$

with Γ being the $\Gamma-$function.

Two special cases of interest can be further spelled out here. First, the special case of circular voids leads to $\mathbf{G} = \mathbf{I} = \mathbf{K} + \mathbf{J}$ through the relation (2.170). This implies that the purely hydrostatic part of $\widehat{\mathbf{S}}^{var,(s)}$ in equation (7.4) depends strongly on both the number of slip systems K as well as on their orientation angles $\theta^{(s)}$. This effect is discussed in detail later in the results sections.

Second, if we consider a single crystal with "equiangular slip systems", as shown in table 1, one gets

Table 2.1: Set of angles $\theta^{(s)}$ in several cases of equiangular slip systems

$K = 3$	$K = 4$	$K = 5$
$\theta^{(s)} = \{0, \pm\pi/3\}$	$\theta^{(s)} = \{0, \pm\pi/4, \pi/2\}$	$\theta^{(s)} = \{0, \pm\pi/5, \pm 2\pi/5\}$

$$\sqrt{\sum_{j\neq l}\left(1 - \cos 4\left(\theta^{(j)} - \theta^{(l)}\right)\right)} = \frac{K}{\sqrt{2}}, \implies \widehat{\mathbf{S}}^{var,(s)} = \frac{1}{2}\mathbf{E}^{(s)} + \frac{f}{4w}\mathbf{G}. \qquad (2.190)$$

Chapter 3

Other models for porous materials

The aim of this chapter is to summarize the main results of several approaches for the estimation of the effective behavior of porous materials, in order to get an historical overview of the problem and a brief review of the previous studies. Then, it is useful to precise that the pioneering works in ductile fracture were carried out by (Mc Clintock [1968], Rice and Tracey [1969]), who studied the problem of estimating the behavior of a porous material with an ideally-plastic matrix phase and dilute concentration of voids. Based on a conveniently chosen stream function, they proposed a set of trial velocity fields that they used to minimize a suitably constructed variational dissipation principle. Following the idea of trial velocity fields, Gurson [1977] proposed a two-velocity field model for non-dilute porous media. Precisely, the author made use of the analytical solution for a spherical (or cylindrical) hollow shell subjected to purely hydrostatic pressure to propose an approximate yield criterion for isotropic porous media.

In the first section, we will focuss on the context of two-phase material systems comprising an isotropic rate-(in)dependent matrix phase (metal usually described by von Mises yield criterion or creep potential) and a voided phase (pores of spherical, spheroidal or arbitrary ellipsoidal shapes). In this regard then, one will present models based either on limit analysis (as for instance Tvergaard and Needleman [1984], Gologanu and Leblond [1993], Leblond et al. [1994], Madou and Leblond [2012a], Monchiet et al. [2014]) based on (Gurson [1977]) work, or a variational homogenization theory using the concept of a linear comparison composite (see for instance Ponte Castañeda [1991a], Danas and Ponte Castañeda [2009a], Danas and Aravas [2012], Agoras and Ponte Castañeda [2013]).

Next, we present results obtained for rate-(in)dependent anisotropic matrix systems. Generally, such models are based based on a phenomenological Hill-type matrix (as for instance Benzerga and Besson [2001], Monchiet et al. [2008a], Keralavarma and Benzerga [2010]). Indeed, the case of porous single crystals have only been studied through discrete dislocations dynamic by (Huang et al. [2007], Hussein et al. [2008], Segurado and Llorca [2010], Huang et al. [2012]) and molecular dynamics at smaller scales (Traiviratana et al. [2008], Zhao et al. [2009], Tang et al. [2010a,b]), or using finite element simulations (Yerra et al. [2010], Ha and Kim [2010]). Such anisotropic matrix systems have known slip directions and contain usually a small volume fraction of impurities. When these material systems are subjected to external loads impurities fail or decohere leading to the creation of pores, which in turn evolve in size, shape and orientation (Srivastava and Needleman [2012]). This complex evolution of microstructure together with the evolution of the rate-dependent matrix anisotropy is critical in the prediction of the eventual fracture of the specimen under monotonic and cyclic loading conditions.

Nevertheless, there have been only a handful of models for porous single crystals which deal with special void geometries, loading conditions and slip system orientations. Such contributions involve the study of cylindrical voids with circular cross-section in a rigid-ideally plastic face-centered cubic (FCC) single crystals using slip line theory (Kysar et al. [2005], Gan et al. [2006], Gan and Kysar [2007]), the study two-dimensional "out of plane" cylindrical voids with circular cross-section subjected to anti-plane loadings (Idiart and Ponte Castañeda [2007]) and that of spherical voids (Han et al. [2013], Paux et al. [2015]). While each one of these studies has its own significant contribution to the understanding of the effective response of porous single crystals none of them is general enough in the sense of arbitrary void shapes and orientations, fully crystal anisotropy and general loading conditions.

3.1   A brief review of porous isotropic materials

A brief review of models for porous isotropic materials is made in this section. In order to achieve this goal, we will present "Gurson type models", which result from limit analysis as well as "variational type estimates".

3.1.1 Gurson type models

The Gurson (Gurson [1977]) model was developed to estimate the overall behavior of porous solids with an ideally-plastic matrix phase and cylindrical (2D) or spherical (3D) microstructures. It makes use of the exact solution for a shell (spherical or cylindrical cavity) under hydrostatic loadings, suitably modified, to obtain estimates for the effective behavior of ideally-plastic solids with isotropic or transversely isotropic distributions of porosity.

In the case of cylindrical cavities, Gurson's yield criterion is written as

$$\Phi_{Gur}^{2D}\left(\overline{\boldsymbol{\sigma}}\right) = \frac{\overline{\sigma}_{eq}^2}{\sigma_0^2} + 2\,f\,\cosh\left(\frac{\sqrt{3}}{2}\frac{\overline{\sigma}_{kk}}{\sigma_0}\right) - 1 - f^2 = 0, \quad k = 1, 2, \tag{3.1}$$

while for spherical pores

$$\Phi_{Gur}^{3D}\left(\overline{\boldsymbol{\sigma}}\right) = \frac{\overline{\sigma}_{eq}^2}{\sigma_0^2} + 2\,f\,\cosh\left(\frac{1}{2}\frac{\overline{\sigma}_{kk}}{\sigma_0}\right) - 1 - f^2 = 0, \quad k = 1, 3, \tag{3.2}$$

where σ_0 is the flow stress of the matrix material.

It is interesting to remark that for purely hydrostatic loadings, i.e., $\overline{\sigma}_{eq} = 0$, both criteria recover the exact solution for a cylindrical or a spherical shell. Moreover, for purely deviatoric loadings, i.e., $\overline{\sigma}_m = 0$, the Gurson criterion recovers the Voigt bound (uniform strain-rate in the entire shell).

Furthermore, this classical model has been extended by (Tvergaard and Needleman [1984], Tvergaard [1990]) to incorporate coalescence, expressed as

$$\Phi_{GTN}\left(\overline{\boldsymbol{\sigma}}\right) = \frac{\overline{\sigma}_{eq}^2}{\sigma_0^2} + 2\,q_1\,f_\star\,\cosh\left(\frac{q_2}{2}\frac{\overline{\sigma}_{kk}}{\sigma_0}\right) - 1 - q_1^2 f_\star^2 = 0, \quad k = 1, 3. \tag{3.3}$$

In this model, so-called "GTN" model, q_1 and q_2 are constant parameters, when $f_\star$ is a function of the porosity used to represent coalescence. Moreover, Leblond et al. [1994] have proposed extended models in order to take into account more general viscoplastic isotropic porous materials.

A recurrent critic about the Gurson or the GTN model is that it contains no information about other microstructural variables such as the shape and orientation of the voids which have critical importance, as we will see in the following chapters. Indeed, the microstructural anisotropy can cause significant geometrical softening or hardening, as opposed to the softening or hardening that the evolution of porosity may induce in the porous material. However, the Gurson model can only predict the

evolution of the porosity and consequently deliver inaccurate estimates when the shape and the orientation of the voids is expected to change significantly, such as in the case of low triaxiality loading. More precisely, the hardening rate predicted by the Gurson model can be expressed as

$$H_{GUR} = -\left(1 - f\right) \frac{\partial \Phi_{GTN}}{\partial \overline{\sigma}_{kk}} \frac{\partial \Phi_{GTN}}{\partial f} \tag{3.4}$$

Hence, when the loading is such that the porosity increases, the porous medium exhibits an overall softening behavior, i.e a negative hardening rate $H_{GUR} < 0$. In contrast, when the loading causes a decrease in the porosity, the material hardens ($H_{GUR} > 0$). In the special case of pure stress or strain-rate deviatoric loadings, however, there is no change in the porosity and the hardening rate is null ($H_{GUR} = 0$). Consequently, the Gurson criterion contains information only for the volume fraction of the voids f, which implies that these models are valid only for isotropic (spherical or cylindrical) microstructures. Thus, Gurson's model is expected to be sufficiently good for high triaxial loadings, where the initially cylindrical or spherical voids preserve their shape during the deformation process. Nevertheless, for low triaxial loadings the shape and orientation of the voids evolve significantly resulting in a highly anisotropic behavior for the porous material. In this last case, the Gurson model is expected to be inaccurate.

For these reasons, several studies have include the microstructural anisotropy in the limit analysis framework. For instance, Gologanu and Leblond [1993] provided analytical expressions for the effective yield function of porous solids with ideally-plastic matrix phase by considering a spheroidal hollow shell (the spheroidal void is confocal with the external boundary of the shell) subjected to axisymmetric loadings, such that the spheroidal symmetry is preserved during the deformation process.

Flandi and Leblond [2005a] later extended these models to the more general case of viscoplastic porous materials. They consider a spheroidal shell containing a confocal spheroidal void. In their analysis they made use of spheroidal coordinates, where they proposed trial velocity fields in order to approximate the effective stress potential of the porous material. Their trial velocity fields were based on an exact solution that can be achieved under certain axisymmetric loading conditions. More specifically, these axisymmetric loading conditions reduce to purely hydrostatic loading conditions in the limiting case of a spherical void. In addition, by setting $w_1 = w_2 = w$, the

spheroidal symmetry is preserved only if the non-zero components of the stress tensor are $\overline{\sigma}_{11} = \overline{\sigma}_{33}$ and $\overline{\sigma}_{33}$. The expressions for the effective stress potential are not be repeated here in detail. However, for completeness, we include the effective yield criterion for a porous solid with ideally-plastic matrix phase, expressed as

$$\Phi_{FL}(\boldsymbol{\sigma}) = \frac{C}{\sigma_0^2}(\overline{\sigma}_{33} - \overline{\sigma}_{11} + \eta\overline{\sigma}_h) + 2q(g+1)(g+f)\cosh\left(\kappa\frac{\overline{\sigma}_h}{\sigma_0}\right) - (g+1)^2 - q^2(g+f)^2 = 0, \tag{3.5}$$

with

$$\overline{\sigma}_h = 2\alpha_2\overline{\sigma}_{11} + (1-\alpha_2)\overline{\sigma}_{33}, \tag{3.6}$$

where $C = C(f, w)$, $\eta = \eta(f, w)$, $\kappa = \kappa(f, w)$, $\alpha_2 = \alpha_2(w)$ and $g = g(w)$. The above criterion reduces to the Gurson [1977] model in the case of purely hydrostatic loading and the "variational" method (Ponte Castañeda [1991a]) for isochoric loadings. Furthermore, in expression (3.5), q plays the same role than the q_1 parameter introduced by Tvergaard and Needleman [1984].

In addition, Monchiet et al. [2014] also derive a new expression of the macroscopic yield function for a rigid ideal-plastic von Mises matrix containing spheroidal cavities, by considering Eshelby-like velocity fields (Eshelby [1957]). Such fields are built by taking advantage of the solution of the equivalent inclusion problem in which the eigenstrains rate are unknown for the plasticity problem. The corresponding criterion takes the form

$$\Phi_{MO}(\boldsymbol{\sigma}) = \frac{\overline{\sigma}_Y^2}{\sigma_0^2} + 2(1+g)(f+g)\cosh\left(\frac{\overline{\sigma}_X}{\sigma_0}\right) - (1+g)^2 - (f+g)^2 = 0, \tag{3.7}$$

where

$$\overline{\sigma}_X^2 = \frac{3}{2}\boldsymbol{\sigma}\cdot\mathbf{S}(\mathbf{e}_2)\cdot\mathbf{P}^{-1}\cdot\mathbf{S}^T(\mathbf{e}_2)\cdot\boldsymbol{\sigma}, \quad \overline{\sigma}_Y^2 = \widetilde{\sigma}_{eq}^2 - (1+g)(f+g)\overline{\sigma}_X^2 \tag{3.8}$$

and

$$\widetilde{\sigma}_{eq}^2 = \overline{\sigma}_{eq}^2 + \frac{3f}{2}\boldsymbol{\sigma}\cdot[\mathbf{S}(\mathbf{e}_1) - f\mathbf{S}(\mathbf{e}_2)]\cdot[\mathbf{L}(\mathbf{e}_1) - f\mathbf{L}(\mathbf{e}_2)]^{-1}\boldsymbol{\sigma}. \tag{3.9}$$

The expressions of the tensors $\mathbf{S}$, $\mathbf{P}$ and $\mathbf{L}$ are detailed in their article and will not be repeated here.

Finally, Madou and Leblond [2012a] have recently proposed a limit-analysis based model for general (non spheroidal) ellipsoidal cavities, through approximate homogenization of some representative elementary porous cell. The associated yield criterion

takes the following form

$$\Phi_{MA}\left(\overline{\boldsymbol{\sigma}}\right) = \frac{\mathcal{Q}\left(\overline{\boldsymbol{\sigma}}\right)}{\sigma_0^2} + 2\left(1+g\right)\left(f+g\right)\cosh\left(\frac{\mathcal{L}\left(\overline{\boldsymbol{\sigma}}\right)}{\sigma_0}\right) - \left(1+g\right)^2 - \left(f+g\right)^2 = 0. \quad (3.10)$$

Thus, through the complex form of $\mathcal{Q}$ and $\mathcal{L}$, a large number of parameters is involved, in which some are totally induced from micromechanical analysis.

3.1.2 Variational type models

In addition to the Gurson-like limit analysis kinematic approach, general constitutive models for porous ductile solid subjected to general three-dimensional loading conditions have also been developed based on the early works of Ponte Castañeda [1991a], Kailasam and Ponte Castañeda [1998] for viscoplastic composites, which can describe the change of void shape and orientation. Indeed, in pioneering contributions, Ponte Castañeda [1991a], Ponte Castañeda and Zaidman [1994, 1996] first introduced a nonlinear homogenization variational structure for composites comprising different nonlinear phases. More specifically, defining linear comparison composites as proper linearization of the nonlinear ones, this new structure allows for the estimation of the effective energy densities of nonlinear composites through a suitable optimization process.

One of the main advantages of this framework is the description of the microstructure evolution (i.e. porosity, void shape and orientation) following for instance the study of Kailasam and Ponte Castañeda [1998], which proposed a general constitutive theory for nonlinear composite materials with microstructure evolution as a consequence of finite-strain boundary conditions. However, it has been shown by Ponte Castañeda [1991b], Michel and Suquet [1992] that this porous Von Mises estimates, so-called variational ("VAR") models, are overly stiff at high stress triaxiality loadings.

In order to remedy to this problem, Danas and Ponte Castañeda [2009a] proposed an improvement of the earlier VAR method for high triaxiality loading conditions, while still being able to handle completely general loading conditions and ellipsoidal microstructures. The corresponding estimates, so-called second-order ("SOM") estimated. Based on the works of Ponte Castañeda [2002a,b], the second method makes use of the tangent moduli, evaluated at the phase averages (or first moments) of the strain field, and yields estimates that are exact to second-order in the contrast, but that can violate the bounds in some special cases. The SOM estimate for the effective

stress potential of the nonlinear porous isotropic material can be expressed as

$$\widetilde{U}_{SOM}\left(\overline{\boldsymbol{\sigma}}\right) = (1-f)\left[\frac{\dot{\epsilon}_0\sigma_0}{1+n}\left(\frac{\widehat{\sigma}_{eq}}{\sigma_0}\right)^{n+1} - \dot{\epsilon}_0\left(\frac{\check{\sigma}_{eq}}{\sigma_0}\right)^n\left(\widehat{\sigma}_{||} - \frac{\overline{\sigma}_{eq}}{1-f}\right)\right], \qquad (3.11)$$

where σ_0, $\dot{\epsilon}_0$ denote the flow stress and the reference strain-rate, respectively. In addition, $\widehat{\sigma}_{eq}$ and $\widehat{\sigma}_{||}$ depend on the matrix behavior while $\check{\boldsymbol{\sigma}}$ is the reference tensor specified in detail in Danas and Ponte Castañeda [2009a].

Nevertheless, the SOM model, although accurate, is computationally expensive. Thus, another contribution, the "MVAR" model proposed by Danas and Aravas [2012], is currently used since give fairly good estimates when compared with the SOM model while being relatively simpler. This model is based on a modification of the initial variational estimate. Indeed, in the original variational method, the effective yield function is given by the explicit expression

$$\widetilde{\Phi}_{VAR}\left(\overline{\boldsymbol{\sigma}}\right) = \sqrt{\frac{\overline{\boldsymbol{\sigma}}\cdot\widehat{\mathbf{S}}\cdot\overline{\boldsymbol{\sigma}}}{1-f}} - \sigma_0 = 0, \qquad (3.12)$$

where the fourth-order tensor $\widehat{\mathbf{S}}$ is written in terms of the microstructural tensor $\mathbf{Q}$, as defined by

$$\widehat{\mathbf{S}} = \widehat{\mathbf{S}}^{var} = \frac{3}{2}\mathbf{K} + \frac{3f}{1-f}\lim_{\kappa\to\infty}\mu\mathbf{Q}^{-1}. \qquad (3.13)$$

The tensor $\widehat{\mathbf{S}}$ is independent of μ. In addition, $\lim_{\kappa\to\infty}\mu\mathbf{Q}^{-1}$ and consequently $\widehat{\mathbf{S}}$ are functions of the microstructural variables s_α. Thus, when the voids become non-spherical, i.e., when the aspect ratios take values other than unity, $\widehat{\mathbf{S}}$ becomes anisotropic. The explicit expressions for the evaluation of the microstructural tensor $\lim_{\kappa\to\infty}\mu\mathbf{Q}^{-1}$ are detailed in the Appendix of Aravas and Ponte Castañeda [2004].

The idea behind the "MVAR" model is to modify only the hydrostatic part of $\widehat{\mathbf{S}}$, such that

$$\widehat{\mathbf{S}}^{mvar} = \widehat{\mathbf{S}}^{var} + \left(q_j^2 - 1\right)\mathbf{J}\cdot\widehat{\mathbf{S}}^{var}\cdot\mathbf{J}, \quad q_j = \frac{1-f}{\sqrt{f}\,\ln f}. \qquad (3.14)$$

The scalar factor q_j brings the yield function into alignment with the spherical shell (or equivalently the "composite sphere assemblage") and the cylindrical shell (or equivalently the "composite cylinder assemblage") solutions when subjected to purely hydrostatic loadings, while preserving standard requirements, such as convexity and smoothness of the yield surface for the entire range of microstructural configurations. In addition, it reproduces the Gurson model (Gurson [1977]) in the special case of spherical

voids and purely hydrostatic loading, while satisfying exactly the variational bound for all range of stress triaxialities and microstructures. Moreover, the correction factor q_j brings into alignment the "MVAR" with "SOM" model for any choice of the microstructural variables s_α in the case of purely hydrostatic loadings.

On the other hand, a recent model (Cao et al. [2015]) has been constructed by combining different ingredients from the Gurson-like and variational-derived models to form a Gurson-like variational model, namely GVAR. This model accounts for both void shape change and void rotation in three dimension.

Furthermore, it should be mentioned that a novel strategy for generating bounds has been developed in (Ponte Castañeda [2012]) utilizing iterated homogenization. Hence Agoras and Ponte Castañeda [2013] have for instance proposed some "iterated variational estimates" ("ITVAR") that were found to be quite accurate for general ellipsoidal microstructures and a large range of stress triaxialities. Nonetheless, the implementation of such approach seems at this point relatively difficult and numerical costly.

3.2 A brief review of porous anisotropic materials

In this section, the role of the plastic anisotropy on ductile damage growth is discussed through a little review of porous anisotropic models. More precisely, the case of phenomenological Hill-type matrix as well as the case of single crystals matrix will be studied in the following.

3.2.1 Hill matrix

To begin with, in the context of phenomenological Hill-type matrix, Benzerga and Besson [2001] proposed an extension of the Gurson model for spherical and cylindrical voids. More specifically, these authors derive an upper bound of the yield surface of a hollow sphere, or a hollow cylinder, made of a perfectly plastic matrix obeying the Hill criterion. The associated criterion takes the following form

$$\Phi_{BB}^{3D}\left(\overline{\boldsymbol{\sigma}}\right) = \frac{3\overline{\boldsymbol{\sigma}}^d \cdot \mathbf{H} \cdot \overline{\boldsymbol{\sigma}}^d}{\sigma_0^2} + 2\,f\,\cosh\left(\frac{1}{h}\frac{\overline{\sigma}_{kk}}{\sigma_0}\right) - 1 - f^2 = 0, \quad k = 1, 3, \qquad (3.15)$$

where

$$h = \left[\frac{8}{5}\frac{h_1 + h_2 + h_3}{h_1 h_2 + h_2 h_3 + h_3 h_1} + \frac{4}{5}\left(\frac{1}{h_4} + \frac{1}{h_5} + \frac{1}{h_6}\right)\right]^{1/2}. \qquad (3.16)$$

The relation (3.15) represents the approximate analytic criterion for a porous orthotropic Hill type material containing spherical voids. This equation may be reduced to the isotropic case by setting $\mathbf{H} = \mathbf{I}$. Consequently, the scalar factor h given by equation (3.16) takes the value 2. Thus we obtain exactly the equation derived by Gurson [1977] for a sphere made of an isotropic material.

Furthermore, in order to capture the microstructure anisotropy (void shape and orientation) which has, as already observed in the case of isotropic matrix, a strong influence on ductile damage growth, some studies has extended the previous model for non spherical voids. For instance, Monchiet et al. [2008a], Keralavarma et al. [2011] investigated the combined effects of void shape and matrix anisotropy on the macroscopic response of ductile porous solids. The Keralavarma et al. [2011] model, made in the context of spheroidal voids, is expressed as

$$\Phi_{KE}\left(\overline{\boldsymbol{\sigma}}\right) = C\frac{3\overline{\boldsymbol{\sigma}} \cdot \mathbf{H} \cdot \overline{\boldsymbol{\sigma}}}{\sigma_0^2} + 2\left(1 + g\right)\left(f + g\right)\cosh\left(\kappa\frac{\overline{\boldsymbol{\sigma}} \cdot \boldsymbol{X}}{\sigma_0}\right) - \left(1 + g\right)^2 - \left(f + g\right)^2 = 0,$$
(3.17)

where $C = C\left(f, w\right)$, $\kappa = \kappa\left(f, w\right)$ and $g = g\left(w\right)$. In addition, evolution laws were also derived for the microstructure and the model extends previous analyses of uncoupled effects of void shape and material anisotropy on the effective plastic behavior of solids containing voids.

3.2.2 Other porous single crystal models

Although recent experimental observations (Srivastava et al. [2012]) at high enough temperatures on tensile specimens indicated that the growth of initially present processing induced voids in a nickel based single crystal superalloy as well as in standard polycrystals played a significant role in limiting creep life, very little has been achieved in the context of rate-dependent single crystals comprising voids of arbitrary ellipsoidal shape subjected to finite deformation loading states.

Indeed, porous single crystals have mostly been studied through discrete dislocations dynamic by (Huang et al. [2007], Hussein et al. [2008], Segurado and Llorca [2010], Huang et al. [2012]) and molecular dynamics at smaller scales (Traiviratana et al. [2008], Zhao et al. [2009], Tang et al. [2010a,b]), or using finite element simulations (Yerra et al. [2010], Ha and Kim [2010], Srivastava and Needleman [2015]).

However, there have been some models which deal with special void geometries,

particular loading conditions and slip system orientations. Theses studies involve for instance the study of cylindrical voids with circular cross-section in a rigid-ideally plastic face-centered cubic (FCC) single crystals using slip line theory (Kysar et al. [2005], Gan et al. [2006], Gan and Kysar [2007]), the study two-dimensional "out of plane" cylindrical voids with circular cross-section subjected to anti-plane loadings (Idiart and Ponte Castañeda [2007]).

On the other hand, more recently, Han et al. [2013] have proposed a yield function for rate-independent single crystals containing spherical voids. This model, based on a variational approach and phenomenologically extended by modifying the dependence on the mean stress, can be expressed as

$$\max_{s=1,K} (\tau_s^* - \tau_0) = 0, \tag{3.18}$$

with

$$\left(\frac{\tau_s}{\tau_s^*}\right)^2 + \alpha\frac{2}{45}f\left(\frac{\overline{\sigma}_{eq}}{\tau_s^*}\right)^2 + 2\,q_1\,f\,\cosh\left(q_2\sqrt{\frac{3}{20}}\frac{\overline{\sigma}_m}{\tau_s^*}\right) - 1 - (q_1 f)^2 = 0. \tag{3.19}$$

In the relations (3.18) and (3.19), K denotes the number of slip systems, τ_s the resolved shear stress of the sth slip system while τ_0 represents the critical resolved shear stress (CRSS) of the slip system. For the sake of simplicity, the authors have assumed that each slip system the same CRSS. In addition, the parameters q_1 and q_2 play a similar role as in the work by Tvergaard and Needleman [1984] whereas α is a new parameter weighting the relative contribution of the resolved shear stress on each slip system and the usual isotropic equivalent von Mises stress measure.

Moreover, we can observed that in the Han et al. [2013] model, which has been built for isotropic microstructures (spherical voids) and assessed for FCC crystals, the corresponding response under purely hydrostatic stressing is independent of the orientation of the systems. However, as we will see in the present study in following chapters, the purely hydrostatic response is extremely sensitive to the number of the slip systems K as well as on the slip orientations in the context of highly anisotropic porous single crystals.

Next, it should be mentioned that Paux et al. [2015] proposed an approximate yield function for spherical voids embedded in cubic single crystals matrix. Indeed, the authors deduced a Gurson-type yield criterion by making use of a regularized form of the Schmid law and solving approximately the hydrostatic case with a limit-analysis

calculation. It takes the form

$$\left(\frac{\left(\sum_{s=1}^{K} |\tau_s|^{n_h}\right)^{1/n_h}}{\tau_0}\right)^2 + 2\,q\,f\,\cosh\left(\kappa'\frac{\overline{\sigma}_m}{\tau_0}\right) - 1 - (q\,f)^2 = 0, \qquad (3.20)$$

where n_h is the regularized parameter taken large enough to ensure coincidence between the regularized and the Schmid criteria, $\kappa' \cong 0.506$ an anisotropic parameter coming from the limit-analysis process and q an heuristic coefficient which plays a role of adjustment of the porosity. It is interesting to notice that in the absence of porosity, this criterion is arbitrarily close to the Schmid yield surface by considering $n_h \longrightarrow \infty$. The authors proposed $n_h = 100$ to ensure a correct description in practise.

Furthermore, the corresponding effective response under purely hydrostatic stressing is independent of the number and the orientation of the systems which has a critical importance, as explained before. In addition, hexagonal single crystals and void shape effects need to be take into account in future contributions.

Thus, while each one of these studies are significant contribution to the study of the effective response of porous single crystals, none of them is general enough in the sense of general void shapes and orientations, arbitrary crystal anisotropy, general loading conditions and microstructure evolution.

3.3 Concluding remarks

In this chapter, we have made an attempt to summarize some of the many methods proposed over the last twenty years for viscoplastic porous materials, and in particular viscoplastic porous single crystals. These models will be compared with the "MVAR" model proposed in the previous chapter.

In a first step, we discussed briefly the case of two-phase material systems comprising an isotropic rate-(in)dependent matrix phase (metal usually described by von Mises yield criterion or creep potential) and a voided phase (pores of spherical, spheroidal or arbitrary ellipsoidal shapes). Thus, we recalled the well-known Gurson model (Gurson [1977]), which is based on the exact solution for a shell (spherical or cylindrical cavity) under hydrostatic loadings, suitably perturbed, to obtain estimates for the effective behavior of ideally-plastic solids with isotropic or transversely isotropic distributions of porosity. Following this model, several models (limit analysis models) were pre-

sented, extending the initial contribution to viscoplasticity and void shape effects. On the other hand, we present effective estimates based on the variational homogenization theory using the concept of a linear comparison composite (see for instance Ponte Castañeda [1991a], Danas and Ponte Castañeda [2009a], Danas and Aravas [2012], Agoras and Ponte Castañeda [2013]), which are able to deal well with void shape and orientation, fully loading conditions and microstructure evolutions.

Next, we presented some results for rate-(in)dependent anisotropic matrix systems. In this regard then, we discussed either models based on phenomenological Hill-type matrix (as for instance Benzerga and Besson [2001], Monchiet et al. [2008a], Keralavarma and Benzerga [2010], or porous single crystals models. For the last class of anisotropy, which has been observed numerically and experimentally (Srivastava et al. [2012], Srivastava and Needleman [2012]) as critical in the modeling of anisotropic ductile damage growth, nevertheless, there exist very few models in the literature. Indeed, most contributions are restricted to special void geometries, loading conditions and slip system orientations. For instance, Kysar et al. [2005], Gan et al. [2006], Gan and Kysar [2007] have focussed on the study of cylindrical voids with circular cross-section in a rigid-ideally plastic face-centered cubic (FCC) single crystals using slip line theory, while Idiart and Ponte Castañeda [2007] has studied two-dimensional "out of plane" cylindrical voids with circular cross-section subjected to anti-plane loadings. In addition, more recently, Han et al. [2013], Paux et al. [2015] proposed models for single crystals containing spherical voids without possible evolution of their shape.

Then, we have emphasizing that none of these methods, while being very important steps, are complete enough to account for general crystal anisotropy, general ellipsoidal microstructure, loading conditions as well as large deformations.

Finally, in order to address the "MVAR" model through numerical accurate simulations, one should discussed the numerical evaluation of the effective behavior of porous single crystals. Such discussion will be carried out in the next chapter.

Chapter 4

Numerical homogenization

Numerical techniques (e.g. finite element method) are able, in principle, to solve for the local field in a porous material, provided that the exact location and distribution of the pores is known. Nevertheless, in most cases of interest, the only available information is the void volume fraction (or porosity) and, possibly, the two-point probability distribution function of the voids (i.e., isotropic, orthotropic etc). Moreover, for sufficient accuracy the element size that should be used in a finite element program must be much smaller than the size of the voids, which in turn is smaller than the size of the periodic unit-cell, especially when multiple pores are considered. This makes the computation very intensive in time. Due to all these reasons, it is very difficult to use the numerical results in a multi-scale analysis, especially when the unit-cell is rather complex.

Nonetheless, one could use the numerical periodic homogenization technique as rigorous test-bed to assess the simpler analytical models as the one proposed in the previous section. More precisely, we can analyze the problem of a periodic porous material considering a unit-cell that contains a given distribution of voids. On the other hand, it is well known that a random porous material (e.g., the one in the analytical model presented in this work) and the periodic material exhibit similar effective behavior either in the case where the distribution of voids is complex enough (adequate for large porosity) or in the limiting case where the porosity is small enough. Furthermore, in these cases, the periodic unit-cell estimates, and consequently the effective properties of the periodic composite, are independent of the prescribed periodic boundary conditions (Gilormini and Michel [1998]). In this regard then, the comparison between the proposed model and the FE periodic unit-cell calculations are meaningful provided

that complex periodic geometries are considered or porosity is small.

The following FE calculations have been carried out with the commercial code Abaqus (Abaqus [2009]) by use of the crystal plasticity user-material subroutine of (Huang [1991], Kysar [1997]) for 3D unit-cell computations. Furthermore, in the context of 2D unit-cell computations, a specific user-material subroutine has been written for specific 2D crystal plasticity based on the notes of (Huang [1991], Kysar [1997]).

4.1   2D unit-cell geometries and periodic boundary conditions

As already seen before, FE periodic unit-cell calculations need to be carried out in order to validate the model. Then, different 2D unit-cell geometries used in our computations, for cylindrical microstructures subjected to periodic boundary conditions, would be presented in this section. The present FE calculations are carried out using a small strain formulation since the scope of the study is the estimation of the effective response of the porous crystal with a given microstructural realization. Moreover, it is important to notice that the entire unit-cell is considered here because there exist no planes of symmetry due to the coupling between the crystal anisotropy and the microstructure anisotropy except in few special cases such as circular voids and particular slip orientations.

4.1.1   2D unit-cell geometries

In the case of small porosities ($f = 1\%$ in the present study), geometries with one void in the middle of the unit-cell can be used to estimate the effective behavior of the porous material. In order to achieve this goal, a unit-cell made up of a long cylindrical void with an initially circular (or even elliptical) cross-section in the plane $1 - 2$ (see fig. 4.1a and fig. 4.1b) is considered. Moreover, plane-strain elements are used to simulate the x_3 direction.

On the other hand, for large porosities ($f = 5\%$ in the present study), one needs more complex distribution of voids, i.e. multipore geometries to achieve isotropic distributions. In this regard, we make use of monodisperse distributions (e.g. Fig. 4.1c) that are constructed by means of a random sequential adsorption algorithm (see Rin-

toul and Torquato [1997], Torquato [2002]) which generates the coordinates of the pore centers. For monodisperse distributions, the radius of each void is

$$R_m = L \left(\frac{f}{\pi N} \right)^{1/2}, \tag{4.1}$$

with N being the number of pores in the unit-cell and f the porosity.

In addition, the sequential addition of voids is constrained so that the distance between a given void and the rest of the voids as well as the boundaries of the unit-cell takes a minimum value that guaranties adequate spatial discretization. In order to achive this we write down the following rules Segurado and Llorca [2002], Fritzen et al. [2012], Jimenez and Pellegrino [2012], Lopez-Pamies et al. [2013], López Jiménez [2014])

• The center-to-center distance between a new pore i in the sequential algorithm and any previously generated pore $j = 1, ..., i - 1$ has to exceed the minimum value fixed here as $s_1 = 2.04 R_m$. If the surface of particle i cuts any of the unit-cell surfaces, this condition has to be checked with the pores near the opposite surface because the microstructure of the composite is periodic. Mathematically, these conditions can be expressed as

$$\| \mathbf{X}^i - \mathbf{X}^j - \mathbf{h} \| \geq s_1, \tag{4.2}$$

where $\mathbf{X}^i \left(\mathbf{X}^j \right)$ denotes the location of the center of particle i (j) and $\mathbf{h}$ is a vector with entries $0, L,$ or $-L$ where L is the dimension of the unit-cell.

• The void surface must be far enough from the unit-cell faces to prevent the occurrence of distorted finite element during meshing. This is expressed by the conditions

$$\left| X_k^i - R_m \right| \geq s_2 \text{ and } \left| X_k^i + R_m - L \right| \geq s_2 \quad (k = 1, 2), \tag{4.3}$$

where L is the length of the unit-cell s_2 has been fixed as $s_2 = 0.05 R_m$.

Furthermore, periodic boundary conditions have to be applied to these geometries since the validation of the model requires periodic FE unit-cell calculations.

4.1.2 2D periodic boundary conditions

The periodic boundary conditions are expressed in this case as (Michel et al. [1999], Miehe et al. [1999])

$$\mathbf{v}(\mathbf{x}) = \overline{\boldsymbol{D}} \cdot \mathbf{x} + \mathbf{v}^*(\mathbf{x}), \ \mathbf{v}^* \text{ periodic}, \tag{4.4}$$
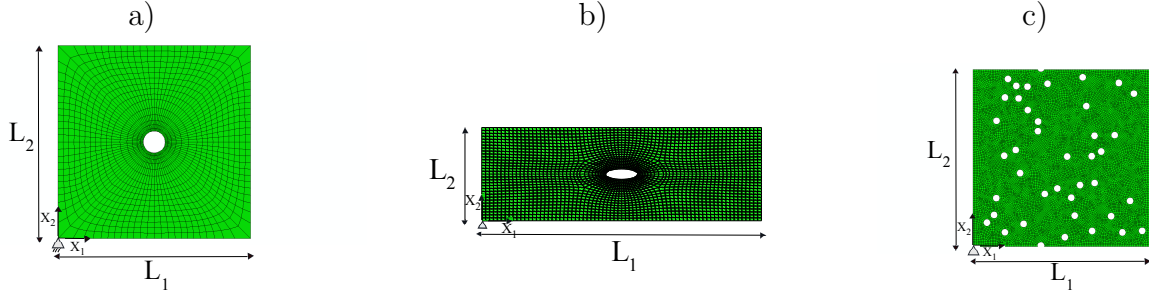
Figure 4.1: Undeformed unit-cell "square" geometry in the case of (a) a single circular void (b) a distribution of several circular voids (c) a single elliptical void.

where the second-order tensor $\overline{\boldsymbol{D}}$ denotes the symmetric part of the average velocity gradient, $\mathbf{x}$ denotes the spatial coordinates and $\mathbf{v}^*$ is a periodic field.

Next, one needs to fix one node to cancel the rigid body motion in the FE calculations. For convenience, we choose this node to be at the origin such that $v_i(0,0) = 0$ $(i = 1, 2)$.

Subsequently, one can subtract the nodal velocities of opposite boundary sides (where $\mathbf{v}^*$ is equal) so that we get the following nodal constraints for the corner nodes, i.e.,

$$
\begin{aligned}
v_i(L_1, 0) - v_i(0, 0) &= \overline{D}_{i1} L_1 = v_i(L_1, 0) \\
v_i(0, L_2) - v_i(0, 0) &= \overline{D}_{i2} L_2 = v_i(0, L_2), \quad \forall i = 1, 2
\end{aligned}
\tag{4.5}
$$

The above simple relations show that the velocity components of the nodes $(L_1, 0)$ and $(0, L_2)$ are one-to-one connected to the symmetric part of the average velocity gradient $\overline{\boldsymbol{D}}$. Then, one can write the constraint equations for the rest of the nodes making use of the result (4.5), i.e.,

$$
\begin{aligned}
v_i(L_1, L_2) - v_i(0, L_2) &= \overline{D}_{i1} L_1 = v_i(L_1, 0) \\
v_i(L_1, x_2) - v_i(0, x_2) &= \overline{D}_{i1} L_1 = v_i(L_1, 0) \\
v_i(x_1, L_2) - v_i(x_1, 0) &= \overline{D}_{i2} L_2 = v_i(0, L_2), \quad \forall i = 1, 2
\end{aligned}
\tag{4.6}
$$

The above algebraic analysis reveals that all periodic linear constraints between all nodes can be written in terms of the velocities of two corner nodes, i.e., $v_i(L_1, 0)$ and $v_i(0, L_2)$, which, in turn, are given in terms of $\overline{\boldsymbol{D}}$ by equation (4.5). This, further, implies that the only nodes that boundary conditions need to be applied are $(L_1, 0)$ and $(0, L_2)$ (together with the axes origin $(0, 0)$ which is fixed).

In order, to validate the model proposed in this study, it is convenient to apply $\overline{\boldsymbol{D}}$ in such a way that the average stress triaxiality in the unit-cell remains constant.

4.1.3   Loading through stress triaxiality control

In this subsection, we will discuss the methodology for the application of a constant average stress triaxiality in the unit-cell. This methodology has been originally proposed by (Barsoum and Faleskog [2007b]) and further discussed in (Mbiakop et al. [2015]).

Specifically, the applied load is such that the principal axes of the void do not rotate around the 3^{rd}axis, and consequently the only non-zero components of the macroscopic stress tensor are

$$\overline{\boldsymbol{\sigma}} = \overline{\sigma}_{11}\,\mathbf{e}_1 \otimes \mathbf{e}_1 + \overline{\sigma}_{22}\,\mathbf{e}_2 \otimes \mathbf{e}_2, \tag{4.7}$$

As a consequence of above-defined load and the periodic boundary conditions, the average deformation in the unit-cell is entirely described by the displacements of the two corner nodes, e.g., $u_1(L_1, 0) = U_1(t)$ and $u_2(0, L_2) = U_2(t)$, denoted compactly as

$$\mathbf{U} = \{U_1(t), U_2(t)\}, \quad \dot{\mathbf{U}} = \{\dot{U}_1(t), \dot{U}_2(t)\} \equiv \{v_1(t), v_2(t)\}. \tag{4.8}$$

Recalling that the average strain-rate and stress tensors involve only two non-zero components due to the applied triaxial loading, they can be expressed in vectorial form (i.e., using the Voigt notation) as

$$\overline{\boldsymbol{D}} = \left\{ \frac{\dot{U}_1}{L_1 + U_1}, \frac{\dot{U}_2}{L_2 + U_2} \right\}, \qquad \overline{\boldsymbol{\sigma}} = \{\overline{\sigma}_{11}, \overline{\sigma}_{22}\}. \tag{4.9}$$

To proceed further, we rewrite the strain-rate tensor as

$$\overline{\boldsymbol{D}} = \boldsymbol{\mathcal{Q}}^{-1} \cdot \dot{\mathbf{U}}, \qquad \boldsymbol{\mathcal{Q}} = \mathrm{diag}\left(L_1 + U_1, L_2 + U_2\right). \tag{4.10}$$

We, next, define an external fictitious node[1], whose generalized force, $\mathbf{P}_G$, and generalized displacement, $\mathbf{p}_G$, vectors, respectively, take the form $\mathbf{P}_G = \left\{ P_1^G(t), 0 \right\}$, $\mathbf{p}_G = \left\{ p_1^G(t), p_2^G(t) \right\}$.

---

[1]The fictitious node introduced in the present study has no specific physical interpretation, but serves only as a mathematical tool to apply the required boundary conditions at the unit-cell.

The stress state in the unit-cell is then controlled via a time-dependent kinematic constraint (Michel et al. [1999]) obtained by equilibrating the rate of work in the unit-cell with the rate of work done by the fictitious node on the unit-cell at time t, such that

$$\dot{W} = S \, \overline{\boldsymbol{\sigma}} \cdot \overline{\boldsymbol{D}} = \mathbf{P}_G \cdot \dot{\mathbf{p}}_G. \tag{4.11}$$

Next, in order to control the loading path in the stress space, we couple the average stress $\overline{\boldsymbol{\sigma}}$ in the unit-cell with the generalized force vector associated with the fictitious node $\mathbf{P}_G$ via the constraint equation

$$S \, \overline{\boldsymbol{\sigma}} = \mathbf{C} \cdot \mathbf{P}_G, \qquad \mathbf{C} = \left(\frac{\mathbf{c}_1}{|\mathbf{c}_1|} \, ; \, \frac{\mathbf{c}_2}{|\mathbf{c}_2|} \right)^T, \qquad \mathbf{C}^{-1} = \mathbf{C}^T, \tag{4.12}$$

where $\mathbf{C}$ is a non-dimensional proper orthogonal matrix since $\mathbf{c}_i$ (i=1,2) are two dimensional vectors that form an orthogonal basis set. The vectors $\mathbf{c}_i$ (i=1,2) depend on the three components of the average stress $\overline{\boldsymbol{\sigma}}$, such that

$$\mathbf{c}_1 = \{\overline{\sigma}_{11}, \overline{\sigma}_{22}\}, \quad \mathbf{c}_2 = \{-\overline{\sigma}_{22}, \overline{\sigma}_{11}\}. \tag{4.13}$$

On the other hand, the principal components of the stress field can be expressed as a function of X_Σ, via

$$\frac{1}{\overline{\sigma}_{eq}} \{\overline{\sigma}_{11}, \overline{\sigma}_{22}\} = \frac{1}{\sqrt{3}} \{-1, 1\} + X_\Sigma \{1, 1\}, \tag{4.14}$$

where $\overline{\sigma}_{eq}$ denotes the equivalent Von Mises part of $\overline{\boldsymbol{\sigma}}$, and we set $\overline{\sigma}_{22} - \overline{\sigma}_{11} > 0$ since the gauge surface is symmetric with respect to the origin.

The above expressions for the vectors $\mathbf{c}_i$ (i=1,2) together with the relation (4.14) further imply that the matrix $\mathbf{C}$ in equation (4.27) is only a function of the stress triaxiality X_Σ but not of the equivalent stress $\overline{\sigma}_{eq}$. By substitution of equations (4.24) and (4.27) in (4.26), one gets

$$\dot{\mathbf{U}} = \boldsymbol{\mathcal{Q}} \cdot \mathbf{C} \cdot \dot{\mathbf{p}}_G. \tag{4.15}$$

The above expression provides the kinematic constraints between the degrees of freedom corresponding to the sides of the unit-cell (i.e., $\mathbf{U}$) and the degrees of freedom of the fictitious node (i.e., $\mathbf{p}_G$). These nonlinear constraints are applied in the finite element software ABAQUS by use of the multi-point constraint user subroutine (MPC).

4.2 3D unit-cell geometries and periodic boundary conditions

In order to validate the model for general ellipsoidal microstructure, 3D FE periodic unit-cell calculations need to be carried out. Hence, several 3D unit-cell geometries used in our computations, subjected to periodic boundary conditions, would be presented in this section.

4.2.1 3D unit-cell geometries

In the case of ellipsoidal voids, geometries with one void in the middle of the unit-cell can be used to estimate the effective behavior of the porous material, since small porosities ($f = 1\%$) would be considered in the present study (see fig 4.3).

On the other hand, for spherical voids, one should considered more complex distribution of voids in order to address possible distribution effects. Indeed, let us consider for instance an infinite number of slip systems matrix (Tresca matrix) various porosities $f = 0.01\%$, 0.1%, 1%, 2%, hydrostatic loading conditions applied on different geometries. First of all, an axisymmetric spherical shell consisting of quadrilateral 4-node elements CAX4 (see 4.2c), secondly an axisymmetric cylindrical unit-cell "one pore geometry" with elements CAX4 (see 4.2d) and finally multipore geometries to achieve isotropic distributions (fig 4.2a,b)). In this context, i.e. rate-independent Tresca matrix, the results obtained are compared in fig 4.4 with the theoretical hydrostatic limit of the effective behavior of composite spherical assemblages CSA (Hashin [1962], Gurson [1977], Leblond et al. [1994]), expressed as $\overline{\sigma}_m = -2\,\sigma_0\,\ln(f)/3$. As it is shown, the axisymmetric spherical shell geometry leads to the exact average hydrostatic behavior in all the cases, as expected. Moreover, the axisymmetric cylindrical unit-cell tends to significantly underestimate the overall response, from $\sim 3\%$ at lower porosities ($f = 0.01\%$) to $\sim 10\%$ at moderate ones ($f = 2\%$). These differences were also observed in Cazacu et al. [2014b] where the same geometry was used to carry out the calculations. Furthermore, the multipore geometries seems to deal well with the average hydrostatic behavior, since more sophisticated distribution of voids is chosen and thus tend to achieve isotropic distributions.

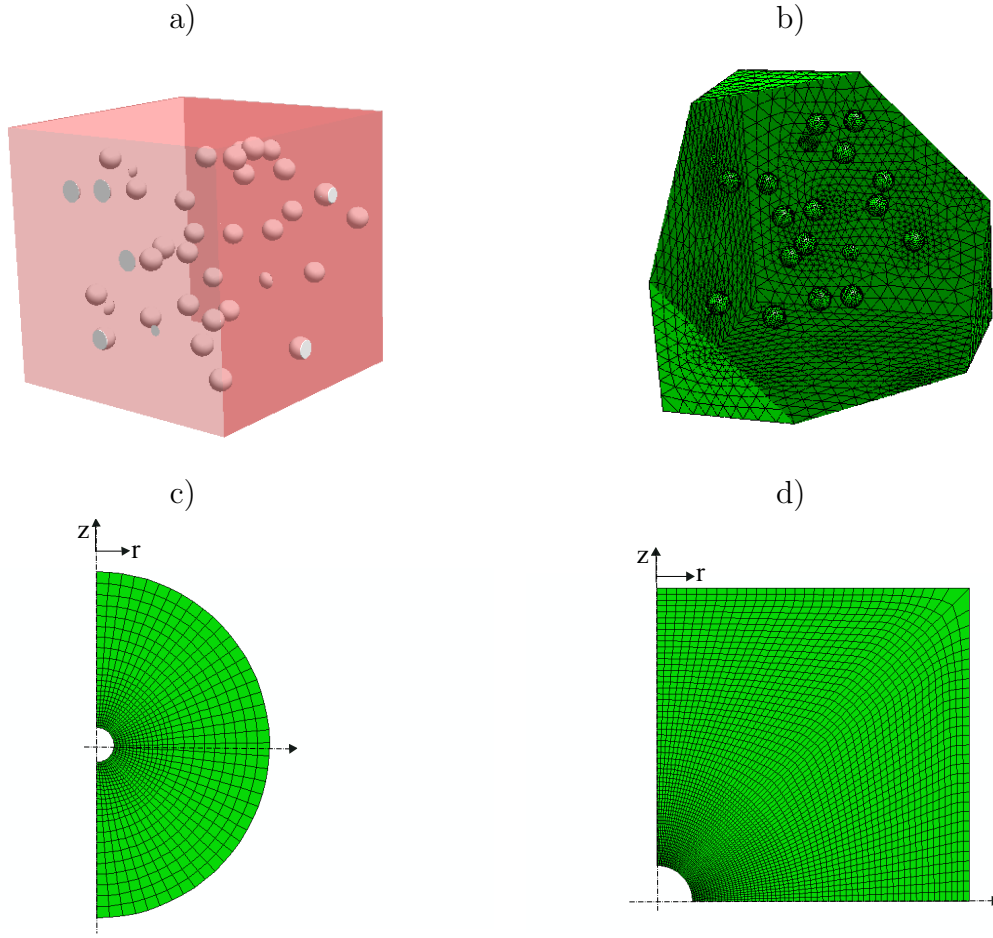Consequently, in the case of spherical voids, we should make use of monodisperse

Figure 4.2: Undeformed unit-cell geometry in the case of (a), (b) a distribution of several spherical voids (the cut is made on the plane [1 1 1]) (c) an axisymmetric spherical shell (d) an axisymmetric cylindrical unit-cell "one pore geometry" (only 1/2 of the unit-cell).

distributions (e.g. fig 4.2a) that are constructed by means of a random sequential adsorption algorithm (see Rintoul and Torquato [1997], Torquato [2002]) which generates the coordinates of the pore centers. For monodisperse distributions, the radius of each void is

$$R_m = L \left(\frac{3 f}{4 \pi N} \right)^{1/3}, \tag{4.16}$$

with N being the number of pores in the unit-cell and f the porosity.

In addition, the sequential addition of voids is constrained so that the distance between a given void and the rest of the voids as well as the boundaries of the unit-cell takes a minimum value that guaranties adequate spatial discretization. In order to achieve this goal, we use the following rules detailed in (Segurado and Llorca [2002], Fritzen et al. [2012], Jimenez and Pellegrino [2012], Lopez-Pamies et al. [2013],
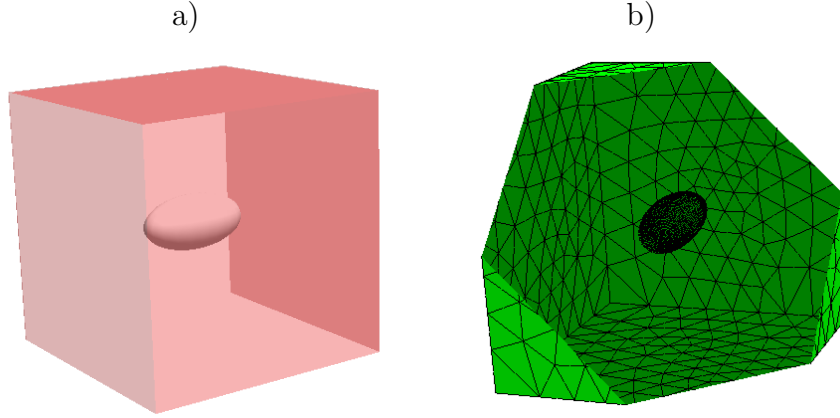
a)   b)

Figure 4.3: Undeformed unit-cell geometry with a single ellipsoidal void (the cut is made on the plane $[1\,1\,1]$).
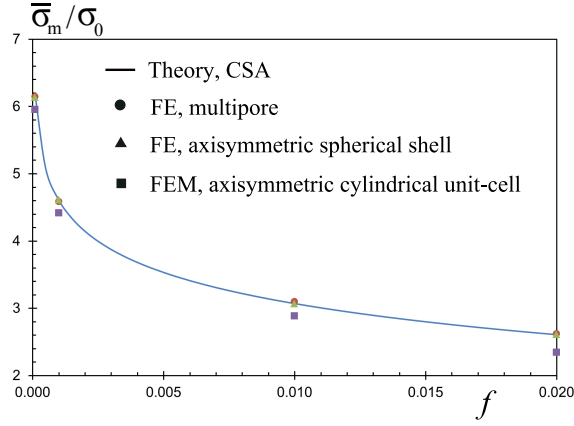

Figure 4.4: Representation of the average hydrostatic stress as a function of the porosity in a porous Tresca matrix, for several mesh geometries.

López Jiménez [2014])

  • The center-to-center distance between a new pore i in the sequential algorithm and any previously generated pore $j = 1, ..., i - 1$ has to exceed the minimum value fixed here as $s_1 = 2.04R_m$. If the surface of particle i cuts any of the unit-cell surfaces, this condition has to be checked with the pores near the opposite surface because the microstructure of the composite is periodic. Mathematically, these conditions can be expressed as

$$\parallel \mathbf{X}^i - \mathbf{X}^j - \mathbf{h} \parallel \geq s_1, \tag{4.17}$$

where $\mathbf{X}^i\left(\mathbf{X}^j\right)$ denotes the location of the center of particle $i\,(j)$ and $\mathbf{h}$ is a vector with entries $0, L,$ or $-L$ where L is the dimension of the unit-cell.

• The void surface must be far enough from the unit-cell faces to prevent the occurrence of distorted finite element during meshing. This is expressed by the conditions

$$\left|X_k^i - R_m\right| \geq s_2 \text{ and } \left|X_k^i + R_m - L\right| \geq s_2 \quad (k = 1, 3), \tag{4.18}$$

where L is the length of the unit-cell s_2 has been fixed as $s_2 = 0.05 R_m$.

Furthermore, periodic boundary conditions have to be applied to these geometries since the validation of the model requires periodic FE unit-cell calculations.

4.2.2   3D periodic boundary conditions

The periodic boundary conditions are expressed in this case as (Michel et al. [1999], Miehe et al. [1999])

$$\mathbf{v}(\mathbf{x}) = \overline{\boldsymbol{D}} \cdot \mathbf{x} + \mathbf{v}^*(\mathbf{x}), \ \mathbf{v}^* \text{ periodic}, \tag{4.19}$$

where the second-order tensor $\overline{\boldsymbol{D}}$ denotes the symmetric part of the average velocity gradient, $\mathbf{x}$ denotes the spatial coordinates and $\mathbf{v}^*$ is a periodic field.

Next, one needs to fix one node to cancel the rigid body motion in the FE calculations. For convenience, we choose this node to be at the origin such that $v_i(0,0,0) = 0$ $(i = 1, 3)$.

Subsequently, one can subtract the nodal velocities of opposite boundary sides (where $\mathbf{v}^*$ is equal) so that we get the following nodal constraints for the corner nodes, i.e.,

$$\begin{aligned}
v_i(L_1, 0, 0) - v_i(0, 0, 0) &= \overline{D}_{i1} L_1 = v_i(L_1, 0, 0) \\
v_i(0, L_2, 0) - v_i(0, 0, 0) &= \overline{D}_{i2} L_2 = v_i(0, L_2, 0) \\
v_i(0, 0, L_3) - v_i(0, 0, 0) &= \overline{D}_{i3} L_3 = v_i(0, 0, L_3), \quad \forall i = 1, 3
\end{aligned} \tag{4.20}$$

The above simple relations show that the velocity components of the nodes $(L_1, 0, 0)$, $(0, L_2, 0)$ and $(0, 0, L_3)$ are one-to-one connected to the symmetric part of the average velocity gradient $\overline{\boldsymbol{D}}$. Then, one can write the constraint equations for the rest of the nodes making use of the result (4.20), i.e.,

$$\begin{aligned}
v_i(L_1, x_2, x_3) - v_i(0, x_2, x_3) &= \overline{D}_{i1} L_1 = v_i(L_1, 0, 0) \\
v_i(x_1, L_2, x_3) - v_i(x_1, 0, x_3) &= \overline{D}_{i2} L_2 = v_i(0, L_2, 0) \\
v_i(x_1, x_2, L_3) - v_i(x_1, x_2, 0) &= \overline{D}_{i3} L_3 = v_i(0, 0, L_3), \quad \forall i = 1, 3.
\end{aligned} \tag{4.21}$$

The above algebraic analysis reveals that all periodic linear constraints between all nodes can be written in terms of the velocities of three corner nodes, i.e., $v_i(L_1, 0, 0)$, $v_i(0, L_2, 0)$ and $v_i(0, 0, L_3)$, which, in turn, are given in terms of $\overline{\boldsymbol{D}}$ by equation (4.20). This, further, implies that the only nodes that boundary conditions need to be applied are $(L_1, 0, 0)$, $(0, L_2, 0)$ and $(0, 0, L_3)$ (together with the axes origin $(0, 0, 0)$ which is fixed).

In order, to validate the model proposed in this study, it is convenient to apply $\overline{\boldsymbol{D}}$ in such a way that the average stress triaxiality in the unit-cell remains constant.

4.2.3   Loading through stress triaxiality control

In this subsection, we will discuss the methodology for the application of a constant average stress triaxiality in the unit-cell. This methodology has been originally proposed by (Barsoum and Faleskog [2007b]) and further discussed in (Mbiakop et al. [2015]).

As a consequence of above-defined load and the periodic boundary conditions, the average deformation in the unit-cell is entirely described by the displacements of the three corner nodes, e.g., $u_1(L_1, 0, 0) = U_1(t)$, $u_2(0, L_2, 0) = U_2(t)$ and $u_3(0, 0, L_2) = U_3(t)$, denoted compactly as

$$\mathbf{U} = \{U_1(t), U_2(t), U_3(t)\}, \quad \dot{\mathbf{U}} = \{\dot{U}_1(t), \dot{U}_2(t), \dot{U}_3(t)\} \equiv \{v_1(t), v_2(t), v_3(t)\}. \quad (4.22)$$

Recalling that the average strain-rate and stress tensors involve only two non-zero components due to the applied triaxial loading, they can be expressed in vectorial form (i.e., using the Voigt notation) as

$$\overline{\boldsymbol{D}} = \left\{ \frac{\dot{U}_1}{L_1 + U_1}, \frac{\dot{U}_2}{L_2 + U_2}, \frac{\dot{U}_3}{L_3 + U_3} \right\}, \qquad \overline{\boldsymbol{\sigma}} = \{\overline{\sigma}_1, \overline{\sigma}_2, \overline{\sigma}_3\}. \quad (4.23)$$

To proceed further, we rewrite the average strain-rate tensor as

$$\overline{\boldsymbol{D}} = \boldsymbol{\mathcal{Q}}^{-1} \cdot \dot{\mathbf{U}}, \qquad \boldsymbol{\mathcal{Q}} = \text{diag}\left(L_1 + U_1, L_2 + U_2, L_3 + U_3\right), \quad (4.24)$$

where $\boldsymbol{\mathcal{Q}}$ is diagonal matrix of dimension three.

We, next, define an external fictitious node[2], whose generalized force, $\mathbf{P}_G$, and

---

[2]The fictitious node introduced in the present study has no specific physical interpretation, but serves only as a mathematical tool to apply the required boundary conditions at the unit-cell.

generalized displacement, $\mathbf{p}_G$, vectors, respectively, take the form

$$\mathbf{P}_G = \left\{ P_1^G(t), 0, 0 \right\}, \qquad \mathbf{p}_G = \left\{ p_1^G(t), p_2^G(t), p_3^G(t) \right\}. \tag{4.25}$$

The stress state in the unit-cell is then controlled via a time-dependent kinematic constraint Michel et al. [1999] obtained by equilibrating the rate of work in the unit-cell with the rate of work done by the fictitious node on the unit-cell at time t, such that

$$\dot{W} = V\boldsymbol{\sigma} \cdot \boldsymbol{D} = \mathbf{P}_G \cdot \dot{\mathbf{p}}_G. \tag{4.26}$$

Next, in order to control the loading path in the stress space, we couple the average stress $\boldsymbol{\sigma}$ in the unit-cell with the generalized force vector associated with the fictitious node $\mathbf{P}_G$ via the constraint equation

$$V\boldsymbol{\sigma} = \mathbf{C} \cdot \mathbf{P}_G, \qquad \mathbf{C} = \left(\frac{\mathbf{c}_1}{|\mathbf{c}_1|} \; ; \; \frac{\mathbf{c}_2}{|\mathbf{c}_2|} \; ; \; \frac{\mathbf{c}_3}{|\mathbf{c}_3|} \right)^T, \qquad \mathbf{C}^{-1} = \mathbf{C}^T, \tag{4.27}$$

where $\mathbf{C}$ is a non-dimensional proper orthogonal matrix since $\mathbf{c}_i$ (i=1,2,3) are three dimensional vectors that form an orthogonal basis set. The vectors $\mathbf{c}_i$ (i=1,2,3) depend on the three components of the average stress $\boldsymbol{\sigma}$, such that

$$\mathbf{c}_1 = \left\{ \overline{\sigma}_1, \overline{\sigma}_2, \overline{\sigma}_3 \right\}, \quad \mathbf{c}_2 = \left\{ \overline{\sigma}_1\overline{\sigma}_3, \overline{\sigma}_2\overline{\sigma}_3, -(\overline{\sigma}_1^2 + \overline{\sigma}_2^2) \right\}, \quad \mathbf{c}_3 = \left\{ -\overline{\sigma}_2, \overline{\sigma}_1, 0 \right\}. \tag{4.28}$$

On the other hand, the principal components of the stress field can be expressed as a function of the average stress triaxiality X_Σ and the average Lode angle $\overline{\theta}$, via

$$\frac{3}{2\overline{\sigma}_{eq}} \{\overline{\sigma}_1, \overline{\sigma}_2, \overline{\sigma}_3\} = \left\{ \cos\overline{\theta}, -\cos\left(\overline{\theta} + \frac{\pi}{3}\right), -\cos\left(\overline{\theta} - \frac{\pi}{3}\right) \right\} + \frac{3}{2} X_\Sigma \{1, 1, 1\}. \tag{4.29}$$

where $\overline{\sigma}_{eq}$ denotes the equivalent Von Mises part of $\overline{\boldsymbol{\sigma}}$.

The above expressions for the vectors $\mathbf{c}_i$ (i=1,2,3) further imply that the matrix $\mathbf{C}$ in equation (4.27) is only a function of the average stress triaxiality X_Σ and the average Lode angle $\overline{\theta}$ but not of the equivalent stress $\overline{\sigma}_{eq}$. By substitution of equations (4.24) and (4.27) in (4.26), one gets

$$\dot{\mathbf{U}} = \boldsymbol{\mathcal{Q}} \cdot \mathbf{C} \cdot \dot{\mathbf{p}}_G. \tag{4.30}$$

The above expression provides the kinematic constraints between the degrees of freedom corresponding to the sides of the unit-cell (i.e., $\mathbf{U}$) and the degrees of freedom of the fictitious node (i.e., $\mathbf{p}_G$). These nonlinear constraints are applied in the finite element software ABAQUS Abaqus [2009] by use of the multi-point constraint user subroutine (MPC).

4.3   Concluding remarks

The numerical evaluation of the effective behavior of porous single crystals has been discussed in this chapter. In order to achieve this goal, we have first recalled that a random porous material like the one presented in this study and a periodic material exhibits similar effective behavior when the distribution of voids is complex enough (appropriate for large porosity) or when the porosity is small enough. Thus, it is possible to make use of numerical periodic homogenization technique, and precisely to analyze the problem of a periodic porous material considering a unit-cell that contains a given distribution of voids. Hence, the comparison between the proposed model and the FE periodic unit-cell calculations seems relevant in this context. Furthermore, the unit-cells are subjected to finite deformations, leading to an evolution of the underlying microstructure.

Finally, the results obtained by the finite element method for the evolution of the microstructural variables (i.e., porosity, shape and orientation of the voids) as well as of the effective behavior of the porous medium will be used to assessed the corresponding results obtained by the "MVAR" model.

Chapter 5

Instantaneous behavior: cylindrical voids

In the previous chapters, several theoretical and numerical homogenized models have been described to estimate the effective behavior and the evolution of the underlying microstructure in viscoplastic porous single crystals subjected to large deformations. In the present and subsequent chapters, these models will be used to study the behavior of porous media with specific microstructures.

In this chapter, the instantaneous response of porous materials consisting of aligned cylindrical voids in the 3-direction distributed randomly in a viscoplastic single crystal matrix phase subjected to plane-strain loading conditions (see Fig.2.2) is studied.

In addition, it is important to precise that in the present context, the equivalent and in-plane hydrostatic macroscopic stresses are defined by

$$\overline{\sigma}_{eq} = \frac{\sqrt{3}}{2} \left[(\overline{\sigma}_{11} - \overline{\sigma}_{22})^2 + 4\,\overline{\sigma}_{12}^2 \right]^{1/2}, \ \overline{\sigma}_m = \frac{\overline{\sigma}_{11} + \overline{\sigma}_{22}}{2}, \ X_\Sigma = \frac{\overline{\sigma}_m}{\overline{\sigma}_{eq}}, \qquad (5.1)$$

where X_Σ is the stress triaxiality defined in the context of two-dimensional plane-strain problems.

5.1 General expressions

Before proceeding to the discussion of the results, it is useful to present first analytical expressions for the evaluation of the effective viscoplastic stress potential delivered by the "MVAR" method. As already discussed, the effective stress potential of the porous

single crystal is given by (2.186), which is recalled here for completeness to

$$\widetilde{U}_{mvar}\left(\overline{\boldsymbol{\sigma}}\right) = (1-f)\sum_{s=1}^{K}\frac{\dot{\gamma}_0^{(s)}\tau_0^{(s)}}{n+1}\left(\frac{\sqrt{\overline{\boldsymbol{\sigma}}\cdot\widehat{\mathbf{S}}^{(s)}\cdot\overline{\boldsymbol{\sigma}}}}{\tau_0^{(s)}\left(1-f\right)}\right)^{n+1}, \tag{5.2}$$

where

$$\widehat{\mathbf{S}}^{(s)} \equiv \widehat{\mathbf{S}}^{mvar,(s)} = \widehat{\mathbf{S}}^{var,(s)} + \left(q_J^2-1\right)\mathbf{J}\cdot\widehat{\mathbf{S}}^{var,(s)}\cdot\mathbf{J}, \tag{5.3}$$

and

$$\widehat{\mathbf{S}}^{var,(s)} = \frac{1}{2}\mathbf{E}^{(s)} + \frac{f}{2\,K\,w\sqrt{2}}\sqrt{\sum_{j\neq l}\left(1-\cos 4\left(\theta^{(j)}-\theta^{(l)}\right)\right)}\mathbf{G}, \quad \forall s=1,K. \tag{5.4}$$

The components of tensor $\mathbf{G}$ are given by equation (2.170) and are repeated here

$$\begin{aligned}\mathbf{G}_{1111} &= w^2\cos^2\psi + \sin^2\psi, \quad \mathbf{G}_{1122} = 0, \quad \mathbf{G}_{1112} = \frac{1}{4}\left(w^2-1\right)\sin 2\psi, \\ \mathbf{G}_{2222} &= \cos^2\psi + w^2\sin^2\psi, \quad \mathbf{G}_{2212} = \mathbf{G}_{1112}, \quad \mathbf{G}_{1212} = \frac{1}{4}\left(1+w^2\right).\end{aligned} \tag{5.5}$$

In addition, q_J and β_n are

$$q_J = \sqrt{\frac{2}{f}}\left\{\frac{(1-f)\left(\beta_n\right)^{\frac{1}{n}}}{n(f^{-1/n}-1)}\right\}^{\frac{n}{n+1}}, \qquad \beta_n = \frac{2}{(n+1)\sqrt{\pi}}\frac{\Gamma\left(\frac{n+2}{2}\right)}{\Gamma\left(\frac{n+1}{2}\right)}, \tag{5.6}$$

with Γ being the $\Gamma-$function.

5.2 Results: Assessment of MVAR model via FE simulations

This section presents results for the effective behavior of rate-dependent porous single crystals as predicted by the modified variational model (MVAR) proposed in this work. The predictions of the MVAR are compared with corresponding results obtained by the FE simulations described in chapter 4. Before proceeding with the discussion of the results, it is useful to introduce first the various material and loading parameters used in the following figures. The present study investigates a range of creep exponents $n = (1, 2, 5, 10)$, porosities $f = (1\%, 5\%)$, void shapes and orientations (e.g., circular and elliptical) as well as a number of slip systems $K = (1, 2, 3, 4, 5, 10)$ with various orientations.

Moreover, motivated by common practice in crystal plasticity studies, we consider the case where all the slip systems of the matrix have the same critical resolved shear stress (CRSS) and reference slip-rate, i.e

$$\tau_0^{(s)} = \tau_0, \qquad \dot{\gamma}_0^{(s)} = \dot{\gamma}_0. \tag{5.7}$$

5.2.1 Computation of the gauge surface in the numerical homogenization

The evaluation of the gauge surfaces resulting from the numerical computations is non trivial and is described in the following. The general idea follows from the earlier study of Flandi and Leblond [2005b] but is rather different since it has to be appropriately modified to apply for the general commercial code Abaqus used in the present study.

By making use of the homogeneity of degree $n+1$ in $\overline{\Sigma}$ of the function $\widetilde{U}$, one can write

$$\widetilde{U}(\overline{\Sigma}) = \left(\overline{\Sigma}_{eq}\right)^{n+1} \widetilde{U}_N(\boldsymbol{N}, X_\Sigma) = \frac{\dot{\gamma}_0 \tau_0^{-n}}{n+1}, \tag{5.8}$$

while $\boldsymbol{N} = \overline{\Sigma}^d / \overline{\Sigma}_{eq}$ describes the loading direction in the deviatoric space, with $\overline{\Sigma}^d$ and $\overline{\Sigma}_{eq}$ denoting the deviatoric and equivalent Von Mises part of the average stress $\overline{\Sigma}$, respectively, corresponding to the equi-potential surface.

Next, given any average stress, $\overline{\boldsymbol{\sigma}}$, one can write

$$\widetilde{U}(\overline{\boldsymbol{\sigma}}) = (1 - f) \min_{\boldsymbol{\sigma} \in S(\overline{\boldsymbol{\sigma}})} \langle U(\boldsymbol{\sigma}) \rangle^{(1)} = \left(\overline{\sigma}_{eq}\right)^{n+1} \widetilde{U}_N(\boldsymbol{N}, X_\Sigma). \tag{5.9}$$

Due to the homogeneity of $\widetilde{U}$, it is noted that $\widetilde{U}_N(\boldsymbol{N}, X_\Sigma)$ is the same function in (5.8) and (5.9), and hence combination of these two equations gives

$$\overline{\Sigma}_{eq} = \left[(n+1)\dot{\gamma}_0^{-1} \tau_0^n \widetilde{U}(\overline{\boldsymbol{\sigma}})\right]^{\frac{-1}{n+1}} \overline{\sigma}_{eq}. \tag{5.10}$$

In the FE code, $\overline{D}_{11}$ and the average X_Σ in the unit-cell are applied and remain constant throughout the process, as discussed in chapter 4 (subsection 4.1.3), whereby $\overline{D}_{22}$ and $\overline{\sigma}_{eq}$ are calculated. In addition, postprocessing of the numerical results provides $\widetilde{U}(\overline{\boldsymbol{\sigma}})$ (via definition (2.16)). Finally, $\overline{\Sigma}_{eq}$ is readily obtained from equation (5.10), while $\overline{\Sigma}_m = X_\Sigma \overline{\Sigma}_{eq}$ given the known stress triaxiality X_Σ.

At this point it is perhaps necessary to clarify that the present work focuses on two-dimensions (i.e., plane-strain loadings) and the porous crystal exhibits two types

of anisotropy. The first is that of the crystal matrix and the corresponding slip systems and the second is that of the void shape which is elliptical in general. Therefore, the effective response of the porous crystal is a function of all the three in-plane stress components $\overline{\sigma}_{11}$, $\overline{\sigma}_{22}$ and $\overline{\sigma}_{12}$ (or equivalently $\overline{\Sigma}_{11}$, $\overline{\Sigma}_{22}$ and $\overline{\Sigma}_{12}$). Following traditional notation in the context of porous materials, the following results are broken down into two major groups. The first group shows the effective response of the porous crystals in the space $\overline{\Sigma}_m - \overline{\Sigma}_{eq}$, which is equivalent to setting $\overline{\Sigma}_{12} = 0$ and working in the space $\overline{\sigma}_{11} - \overline{\sigma}_{22}$. This stress space is very important since it involves directly the hydrostatic component $\overline{\Sigma}_m$. The second group shows results in the deviatoric plane as this is defined by the in-plane shear stresses $(\overline{\Sigma}_{11} - \overline{\Sigma}_{22})/2$-$\overline{\Sigma}_{12}$, and for given constant hydrostatic stress $\overline{\Sigma}_m$. This way, our results are complete in the sense that they cover the entire stress space but using traditional and well-understood stress measures, as discussed above.

5.2.2   Purely hydrostatic loadings for circular voids

In this section, we present results for the effective behavior of porous single crystals submitted to purely hydrostatic loadings for a range of creep exponents $n = (1, 2, 5, 10)$ and porosities $f = (1\%, 5\%)$.

First, we consider the case of K "equiangular" slip systems (i.e., systems forming equal angles with each other in the interval $[-\pi/2, \pi/2]$). Fig. 5.1 shows MVAR and FE comparisons for the average hydrostatic stress $\overline{\Sigma}_m$ as a function of the number of slip systems K. The MVAR is found to be in very good agreement with the FE results for the entire range of creep exponents (i.e., nonlinearities) n and porosities f considered here. Rather interestingly, for large values of $n = 5, 10$ a slightly non-monotonic response is observed in the FE calculations for $K = 4$ slip systems, as observed in Fig. 5.1c,d, and in this specific case the MVAR model tends to underestimate slightly the value of the hydrostatic point for $K = 4$. Moreover, as K increases we attain the isotropic limit where the Composite Cylinder Assemblage (CCA) result has been used to correct the original VAR model.

Interestingly, it is found that for highly anisotropic equianglular crystals, $K = 1$ and $K = 2$ (with 90° angle between the systems) the obtained hydrostatic point is infinite, i.e., the porous single crystal is incompressible, and thus it is not shown in
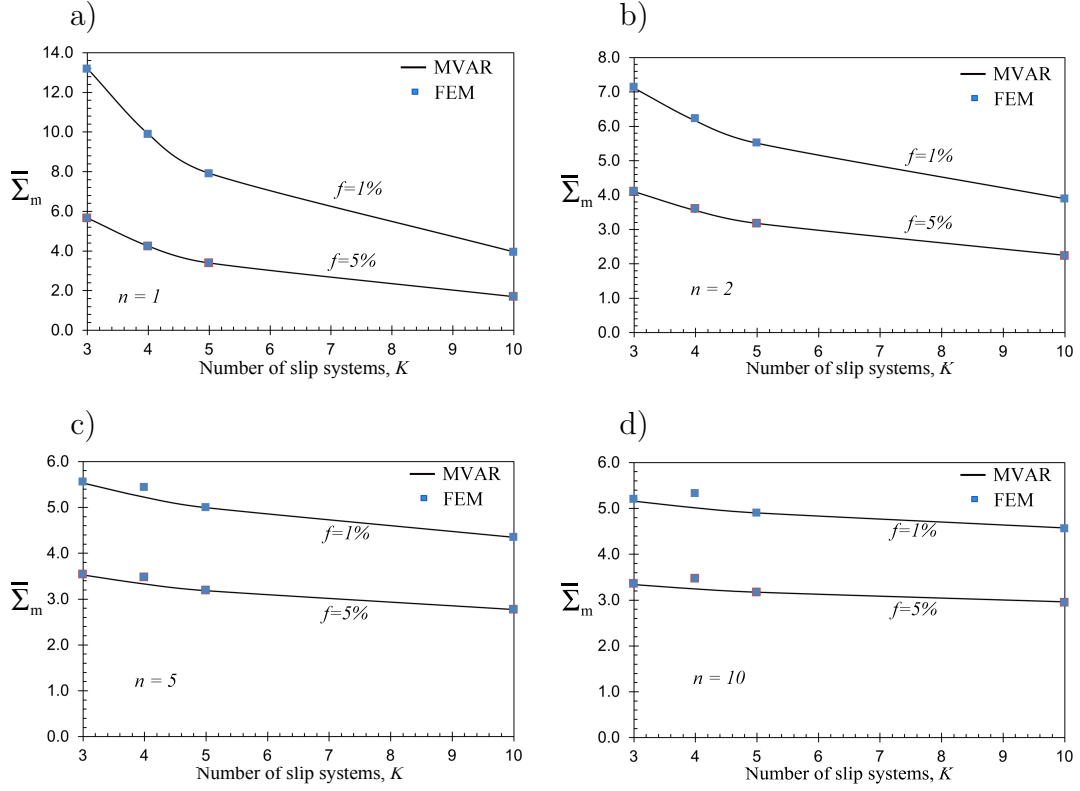
Figure 5.1: Comparison between the average hydrostatic stress obtained by the model (MVAR) and the one resulting from FE results for a range of porosity $f = (1\%, 5\%)$, in the cases of $K = (3, 4, 5, 10)$ "equiangular slip systems" for (a) $n = 1$, (b) $n = 2$, (c) $n = 5$, (d) $n = 10$.

Fig. 5.1. In order to further analyze this very critical effect, we consider next crystals with $K = 2$ slip systems that form arbitrary angles $\theta^{(1,2)}$. The porosity is set equal to $f = 1\%$ (the conclusions drawn in this case are independent of the porosity considered) and the creep exponents are $n = (1, 2, 5, 10)$. A parametric study of the relative angle $\Delta\theta = \theta^{(1)} - \theta^{(2)} = (20^o, 30^o, 40^o, 45^o, 50^o, 60^o, 70^o)$ between the two slip systems is carried out next. It is mentioned however, that in the case of highly anisotropic crystals (i.e., $0^o < \Delta\theta < 20^o$ and $70^o < \Delta\theta < 90^o$) the numerical simulations exhibit convergence issues and thus no FE results are shown in this range (see also (Willot et al. [2008]). In this regard, Fig. 5.2 presents MVAR and FE normalized average hydrostatic stresses, $\overline{\Sigma}_m(\Delta\theta = 45^o)/\overline{\Sigma}_m$ as function of the difference between slip orientations $\Delta\theta$, for several creep exponents. The major observation in the context of this figure is that for $\Delta\theta = 0^o$ (i.e., $K = 1$ slip system) and $\Delta\theta = 90^o$ (i.e., equiangular

slip systems) the normalized stresses $\overline{\Sigma}_m(\Delta\theta = 45^o)/\overline{\Sigma}_m = 0$ or equivalently $\overline{\Sigma}_m \to \infty$. This implies that even if pores are present in this case the effective porous crystal response is entirely *incompressible* for all creep exponents considered here. This result suggests that for such low symmetry crystals certain directions appear as "rigid" to plastic deformation thus constraining slip under highly symmetric loads such as purely hydrostatic tension or compression.

In turn, the maximum value of $\overline{\Sigma}_m(\Delta\theta = 45^o)/\overline{\Sigma}_m$ (i.e., the minimum value for $\overline{\Sigma}_m$) is found for $\Delta\theta = 45^o$. More specifically, as observed in Fig. 5.2a ($n = 1$) and Fig. 5.2b ($n = 2$), there is very good agreement between the MVAR and the FE for all slip orientations considered, as expected for small nonlinearities. The agreement becomes less good for higher creep exponents $n = 5, 10$ but still remains relatively good.
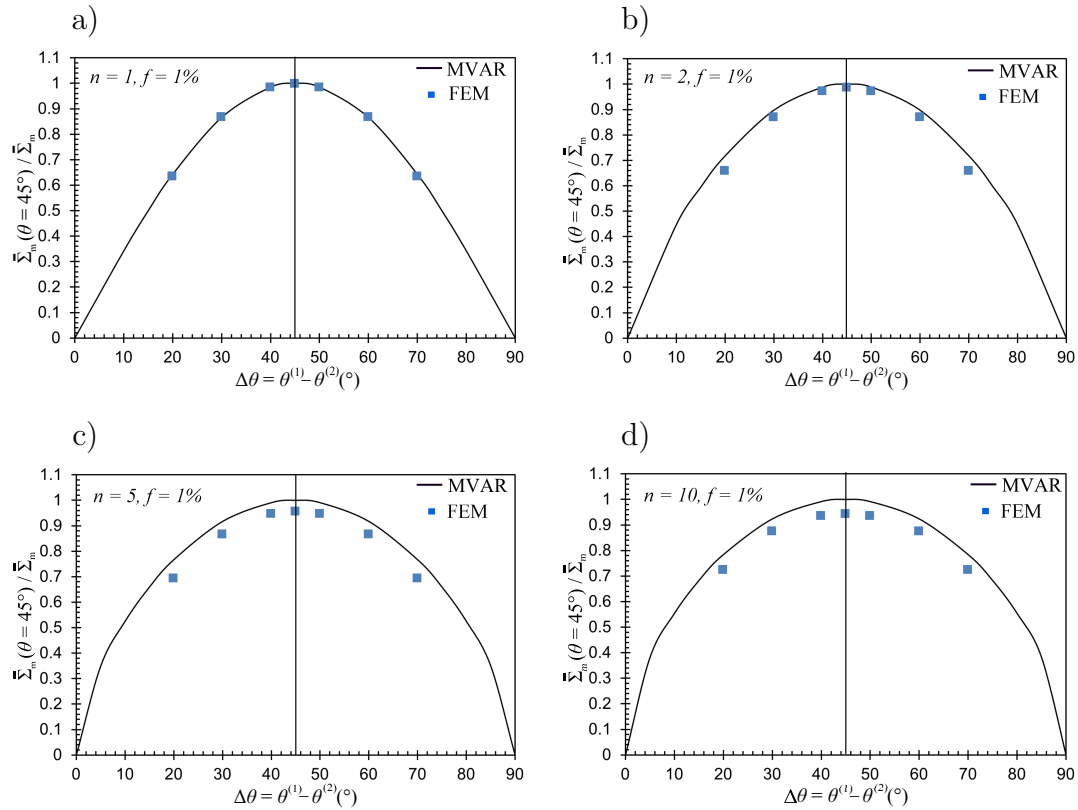

Figure 5.2: Comparison between the average normalized hydrostatic stress obtained by the model (MVAR) and the one resulting from FE results for a single porous crystal $K = 2$ slip systems, a porosity $f = 1\%$ and a range of slip orientations $\Delta\theta = (20^o, 30^o, 40^o, 45^o, 50^o, 60^o, 70^o)$ in the cases (a) $n = 1$, (b) $n = 2$, (c) $n = 5$, (b) $n = 10$.

5.2.3 Gauge surfaces for circular voids

Figure 5.3 shows cross-sections of the effective gauge surfaces in the $\overline{\Sigma}_m - \overline{\Sigma}_{eq}$ plane in the case of a single crystal comprising $K = 3$ slip systems with slip orientations (a) $\theta^{(s)} = (-60^o, 0^o, 60^o)$ (equiangular slip systems) and (b) $\theta^{(s)} = (-54.7^o, 0^o, 54.7^o)$ which correspond to a face cubic-centered (FCC) single crystal in the $2-$dimensional context Rice [1987]. Various creep exponents $n = (1, 2, 5, 10)$ are considered while the porosity is set to $f = 1\%$. In the context of this figure, we observe a very good agreement between the MVAR predictions and the FE results for the entire range of creep exponents n. A rather interesting observation is that as the nonlinearity n increases the porous crystal becomes more compliant at large values of $\overline{\Sigma}_m$ (i.e., high triaxialities) but more stiff at small $\overline{\Sigma}_m$ (i.e. low stress triaxialities). As a consequence this leads to the inter-crossing of the curves corresponding to different n as observed in Fig. 5.3.
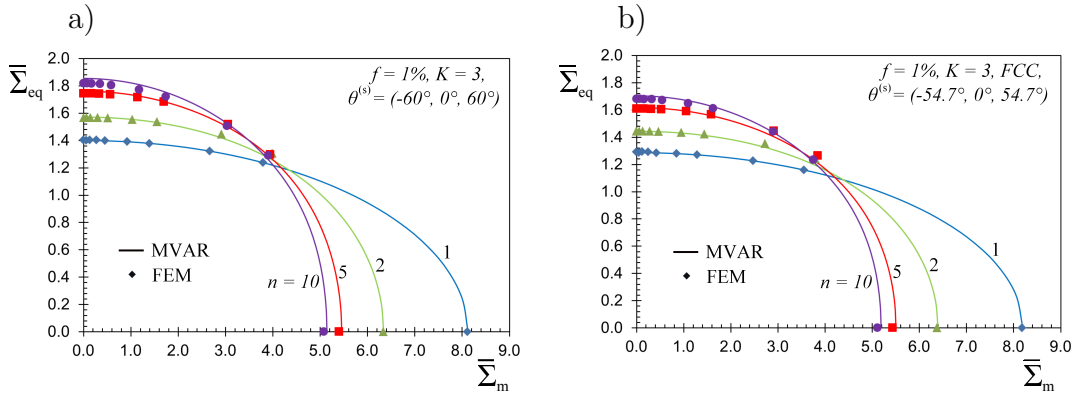

Figure 5.3: Gauge surfaces in the $\overline{\Sigma}_m - \overline{\Sigma}_{eq}$ plane for a porous single crystal with circular voids of $K = 3$ slip systems, a porosity $f = 1\%$ and a range of creep exponent $n = (1, 2, 5, 10)$. Comparison between the model (MVAR) and the FE results in the cases of (a) slip orientations $\theta^{(s)} = (-60^o, 0^o, 60^o)$ (equiangular), (b) slip orientations $\theta^{(s)} = (-54.7^o, 0^o, 54.7^o)$ (FCC).

In Fig. 5.4, we present cross-sections of the effective gauge surfaces in the $\overline{\Sigma}_m - \overline{\Sigma}_{eq}$ plane in the case of $K = 2$ slip systems crystal for a porosity $f = 1\%$ and the same range of creep exponents. Specifically we consider slip orientations (a) $\theta^{(s)} = (-22.5^o, 22.5^o)$ and (b) $\theta^{(s)} = (-15^o, 15^o)$. The main observation in the context of this figure is that for several slip orientations as well as for several number of slip systems (see previous cases with $K = 3$), there is a very good agreement between the MVAR

predictions and the FE results for $f = 1\%$, at the full range of creep exponents and the entire range of the stress triaxialities considered here.
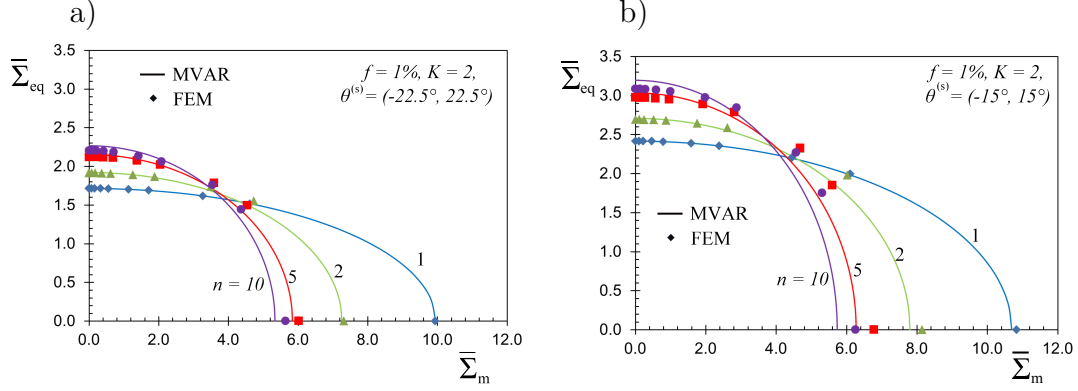
a)   b)

Figure 5.4: Gauge surfaces in the $\overline{\Sigma}_m - \overline{\Sigma}_{eq}$ plane for a porous single crystal with circular voids of $K = 2$ slip systems, a porosity $f = 1\%$ and a range of creep exponent $n = (1, 2, 5, 10)$. Comparison between the model (MVAR) and the FE results in the cases of (a) slip orientations $\theta^{(s)} = (-22.5^o, 22.5^o)$, (b) slip orientations $\theta^{(s)} = (-15^o, 15^o)$.

In order to assess the accuracy of the MVAR model at higher porosities $f = 5\%$ we carry out FE simulations using the more complex periodic "multipore" unit-cell presented in chapter 4. As detailed further in the next section, at $f = 5\%$ the void interactions become much more critical and thus a square unit-cell with one single void in the middle can lead to inconsistent comparisons when compared with the corresponding MVAR estimates for isotropic pore distributions (i.e., aspect ratio $w = 1$). In this regard, Fig. 5.5 shows cross-sections of the effective gauge surfaces in the $\overline{\Sigma}_m - \overline{\Sigma}_{eq}$ plane in the case of a higher porosity $f = 5\%$ and single crystals comprising (a) $K = 3$ slip systems with slip orientations $\theta^{(s)} = (-54.7^o, 0^o, 54.7^o)$ (FCC) and (b) $K = 2$ slip systems with slip orientations $\theta^{(s)} = (-15^o, 15^o)$, respectively. Again, the agreement between the MVAR predictions and the FE results is very good for small nonlinearities $n = 1, 2$, whereas it tends to overestimate the effective response at higher ones (i.e., $n = 5, 10$). In any case, the maximum error is found to be in the order of $\sim 6\%$. It is also noted that the MVAR model deals extremely well with increasing anisotropy, i.e., as we go from $K = 3$ to $K = 2$ slip systems.

As we will see next, these differences between the MVAR and FE results with increasing nonlinearity (i.e., creep exponent) can be attributed to the increasing void interaction at high n.
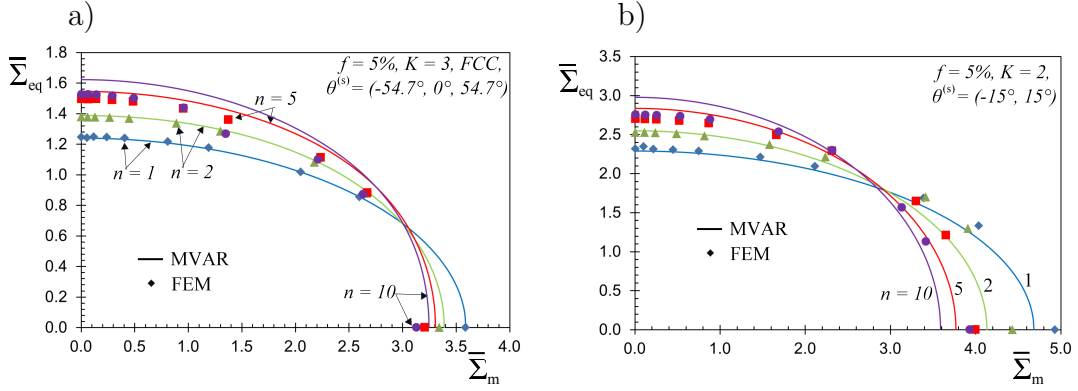
a)

b)

Figure 5.5: Gauge surfaces in the $\overline{\Sigma}_m - \overline{\Sigma}_{eq}$ plane for a porous single crystal with circular voids of a porosity $f = 5\%$ and a range of creep exponent $n = (1, 2, 5, 10)$. Comparison between the model (MVAR) and the FE results in the cases of (a) $K = 3$ slip systems and slip orientations $\theta^{(s)} = (-54.7^o, 0^o, 54.7^o)$ (FCC), (b) $K = 2$ slip systems and slip orientations $\theta^{(s)} = (-15^o, 15^o)$.

5.2.4   Full field contours for periodic unit-cells

Following the last remark of the previous section, we show, next, contours of the the total slip, defined as the sum of the absolute value of the slip on each individual slip system γ_{tot} normalized by the reference slip-rate $\dot{\gamma}_0$ (see Niordson and Kysar [2014] for more details) for several periodic unit cells, porosities and creep exponents.

First, we consider the simplest periodic geometry which consists of a single pore in the middle of a square unit-cell such that the porosity $f = 1\%$. Figure 5.6 shows countours of $\gamma_{tot}/\dot{\gamma}_0$ for $n = 10$, $K = 3$ equiangular slip systems and three applied stress triaxialities (a) $X_\Sigma = 0$, (b) $X_\Sigma = 3$ and (c) $X_\Sigma \to \infty$ (i.e., pure hydrostatic tension). A dramatic change of the deformation mechanism is observed as one goes from low X_Σ (see Fig. 5.6a) to high ones (see Fig. 5.6c). While for $X_\Sigma = 0$ the deformation map exhibits a 90° symmetry, as we increase hydrostatic tension the fields become highly localized around the pore geometry exhibiting 12-fold symmetry as already observed by Niordson and Kysar [2014] in this last case. At a value of $X_\Sigma = 3$ in Fig. 5.6b, the slip fields show a combination of both of the above observed symmetries.

In the following, we analyze the results obtained for a unit-cell comprising a large number of uniformly distributed voids, as described in chapter 4. More specifically, in Fig. 5.7, we consider purely hydrostatic loads (i.e., $X_\Sigma \to \infty$) with three different creep exponents $n = 1, 5, 10$ and two porosities $f = 1, 5\%$. First, we compare the effect
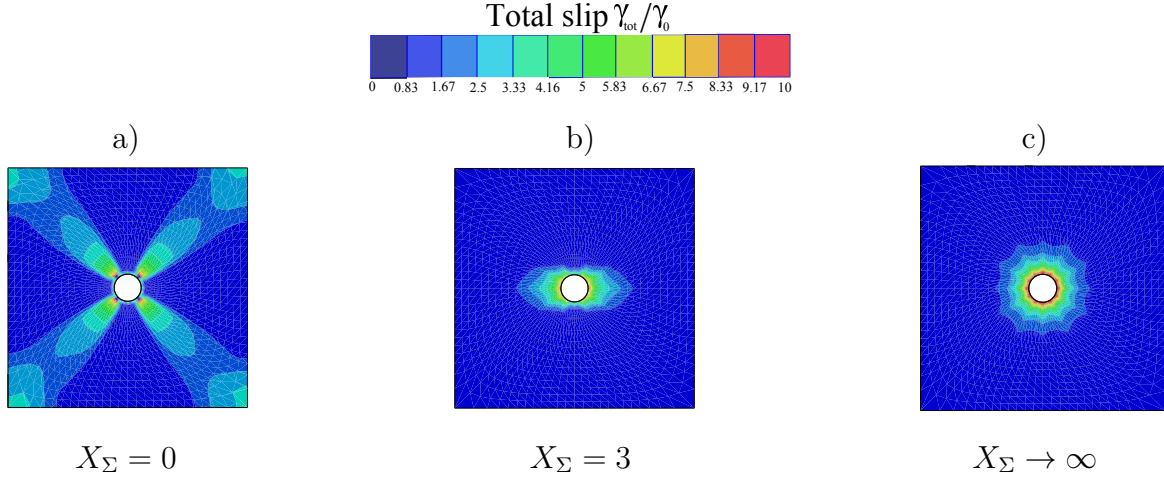
Figure 5.6: Contour of the total slip for a $K = 3$ equiangular slip systems with a "one pore" geometry and a porosity of $f = 1\%$. Case of (a) $X_\Sigma = 0$ (b) $X_\Sigma = 3$ and (c) $X_\Sigma = \infty$.

of the porosity and subsequently the effect of the nonlinearity n upon the obtained fields. Comparison of Figs. 5.7a-c with the corresponding Figs. 5.7d-e shows that when $f = 1\%$ the total slip $\gamma_{tot}/\dot{\gamma}_0$ is rather concentrated around each individual pore even for larger exponents n. In contrast when $f = 5\%$, the pore interactions become more significant as expected. Moreover, in the case of $f = 5\%$, we observe a gradual deformation localization with increasing nonlinearity n as one goes from Fig. 5.7d towards Fig. 5.7e. The pore interaction and deformation localization becomes so pronounced that material around a significant number of pores is not at all loaded. This effect is much less pronounced when $f = 1\%$ and $n = 10$ in Figs. 5.7c. These last observations imply that for low porosities $f = 1\%$ the use of the simpler unit-cell shown in Fig. 5.6 is accurate enough, while for larger porosities (even for 5%) the pore interactions become non-negligible and unit-cells with large number of pores should be used. Finally, this strong deformation localization observed in Fig. 5.6e explains why the MVAR model is in less good agreement with the FE with increasing creep exponent n and increasing porosity f.

5.2.5 Macroscopic strain-rates for circular voids

In this section, for the sake of conciseness, we present only representative results for the macroscopic strain-rates. Those constitute a direct measure of the normal (i.e., slope) to the previously shown gauge surfaces and hence have important implications
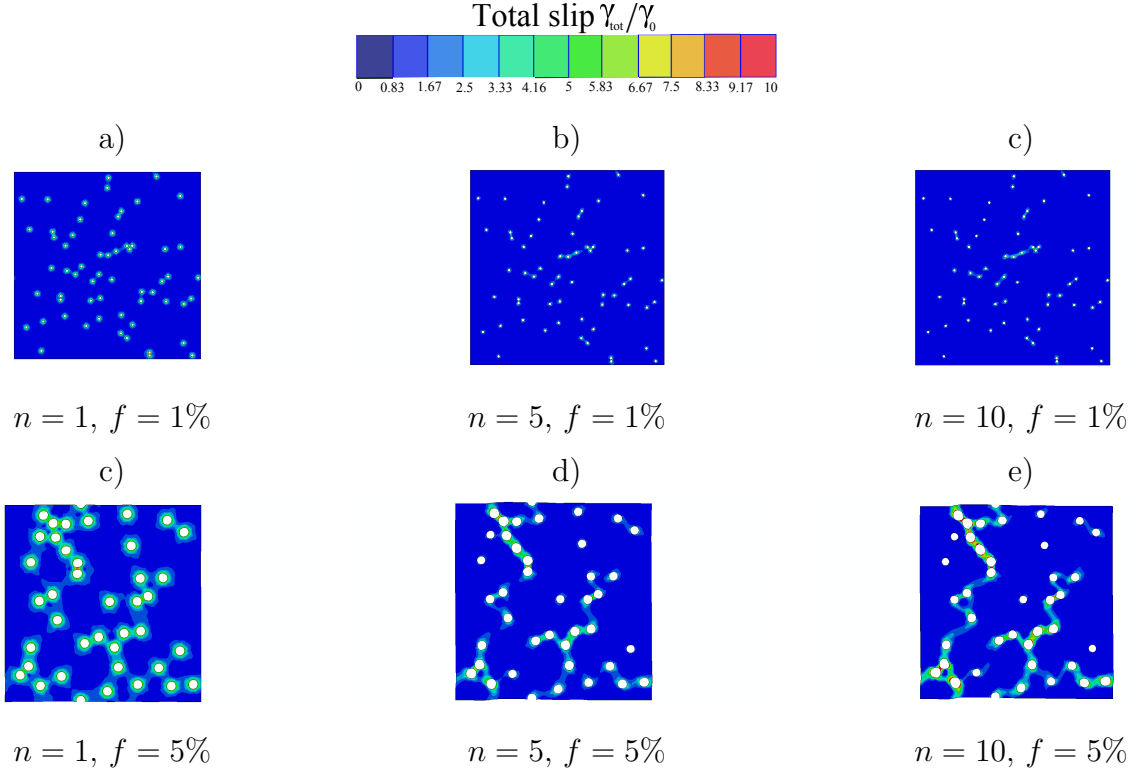
Total slip γ_{tot}/γ_0

0 0.83 1.67 2.5 3.33 4.16 5 5.83 6.67 7.5 8.33 9.17 10

a)

$n = 1, f = 1\%$

b)

$n = 5, f = 1\%$

c)

$n = 10, f = 1\%$

c)

$n = 1, f = 5\%$

d)

$n = 5, f = 5\%$

e)

$n = 10, f = 5\%$

Figure 5.7: Contour of the total slip for a FCC single crystal with two "multipore" geometries of 60 pores ($f = 1\%$) and 40 pores ($f = 5\%$), in macroscopic hydrostatic loading state ($X_\Sigma = \infty$). Case of (a) $f = 1\%$, $n = 1$ (b) $f = 1\%$, $n = 5$ (c) $f = 1\%$, $n = 10$ (d) $f = 5\%$, $n = 1$ (e) $f = 5\%$, $n = 5$ (f) $f = 5\%$, $n = 10$.

on the developed plastic anisotropy as well as void growth (see Danas et al. [2008a]). More specifically, Fig. 5.8 shows the average strain-rates in the $\overline{D}_m - \overline{D}_{eq}$ plane in the case of a single crystal comprising (a) $K = 3$ slip systems with slip orientations $\theta^{(s)} = (-54.7^o, 0^o, 54.7^o)$ (FCC) and (b) $K = 2$ slip systems with slip orientations $\theta^{(s)} = (-22.5^o, 22.5^o)$. Results are obtained for several creep exponents $n = (1, 2, 5, 10)$ and a porosity $f = 1\%$. As observed in the context of this figure, the MVAR predictions are in good agreement with the FE results for the entire range of parameters used. Conversely with the corresponding gauge surfaces, the hydrostatic strain-rate $\overline{D}_m$ increases with increasing n at high triaxialities and vice verse for low triaxialities. This has direct implications on the corresponding void growth at large triaxialities and as already expected Danas and Ponte Castañeda [2009b] the voids will grow much faster at higher creep exponents n and higher triaxialities.
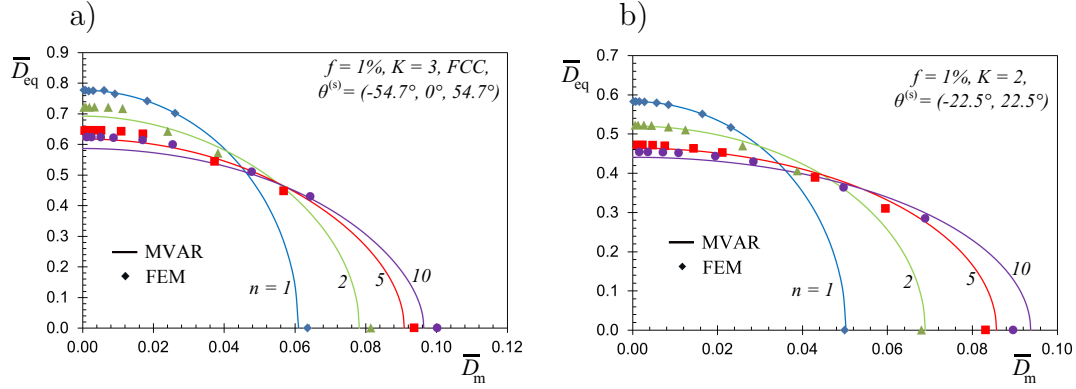
Figure 5.8: Macroscopic strain-rates in the $\overline{D}_m - \overline{D}_{eq}$ plane for a porous single crystal with circular voids of a porosity $f = 1\%$ and a range of creep exponent $n = (1, 2, 5, 10)$. Comparison between the model (MVAR) and the FE results in the cases of (a) $K = 3$ slip systems and slip orientations $\theta^{(s)} = (-54.7^o, 0^o, 54.7^o)$ (FCC) and (b) $K = 2$ slip systems and slip orientations $\theta^{(s)} = (-22.5^o, 22.5^o)$, .

5.2.6 Gauge surfaces for elliptical voids

In this subsection, we show results for porous single crystals comprising elliptical voids, i.e., with aspect ratio $w \neq 1$ and angles $\psi \neq 0$. The first microstructure considered is defined by porosity $f = 1\%$, void aspect ratio $w = 1/3$ and void orientation $\psi = 0$. Figure 5.9 presents various cross-sections of the effective gauge surfaces in the $\overline{\Sigma}_m - \overline{\Sigma}_{eq}$ plane in the case of $K = 3$ slip systems with slip orientations $\theta^{(s)} = (-60^o, 0^o, 60^o)$ (equiangular slip systems) and creep exponents $n = (1, 10)$. In the context of this figure, the MVAR predictions are in relatively good agreement with the FE results for both $n = (1, 10)$. In particular, for $n = 1$, the MVAR is in excellent agreement with the FE results except at purely hydrostatic loadings where an error in the order of 7% is observed. Nonetheless, in that case numerical convergence issues appeared and the FE results should be interpreted with caution. In turn, when $n = 10$, the MVAR exhibits very good qualitative agreement with the FE results where the corresponding gauge surface exhibits a rather significant "asymmetry" with respect to the $\overline{\Sigma}_{eq}$ axis but tends to underestimate this effect especially at small stress triaxialities (i.e., for $\overline{\Sigma}_m \sim 0$). This asymmetry, which is present in the case of elliptical voids, is a direct consequence of the coupling between $\overline{\Sigma}_m$ and $\overline{\Sigma}_{eq}$) resulting from the complex form of the tensor $\mathbf{G}$ (see equation 5.5). Such effects observed in shearing of ellipsoidal voids have also been addressed either in numerical micromechanical calculations (see

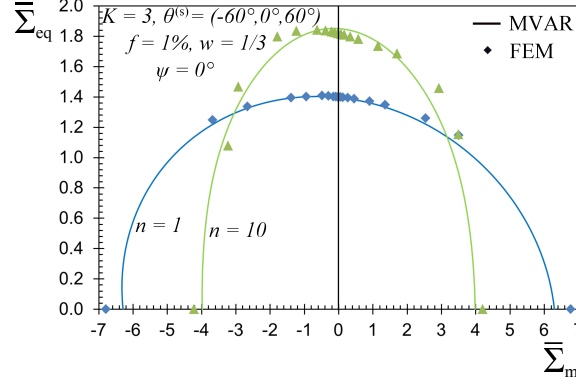for instance Tvergaard and Nielsen [2010]), or in multiaxial experiments (see Combaz et al. [2011]).

Figure 5.9: Gauge surfaces in the $\overline{\Sigma}_m - \overline{\Sigma}_{eq}$ plane for a single porous crystal with elliptical voids ($w = 1/3$, $\psi = 0^o$) of $K = 3$ slip systems, $f = 1\%$, slip orientations $\theta^{(s)} = (-60^o, 0^o, 60^o)$ (equiangular) and a range of creep exponent $n = (1, 10)$. Comparison between the MVAR model and the FE results.

To summarize, the MVAR model has been assessed in great detail and it was found to be in good agreement with the corresponding FE results. Therefore, for simplicity and conciseness, only MVAR estimates will be shown in the following section.

5.3 Results: MVAR predictions

Hereafter, we attempt to reveal the complex coupling between the crystal anisotropy as characterized by the number of slip systems and their orientation, and the (morphological) void anisotropy resulting from the elliptical void shape and orientation.

5.3.1 Effect of the void shape and orientation

More specifically, Fig. 5.10 shows MVAR gauge surfaces in the $\overline{\Sigma}_m - \overline{\Sigma}_{eq}$ plane for a porous single crystal comprising $K = 3$ slip systems with slip orientations $\theta^{(s)} = (-60^o, 0^o, 60^o)$ (i.e., equiangular slip systems) and a creep exponent $n = 5$. The effect of porosity is investigated by choosing $f = (1\%, 5\%, 10\%)$ for different void shapes (a) $w = 1$, $\psi = 0^o$ and (b) $w = 0.2$, $\psi = 0^o$. In Fig. 5.10, the gauge surfaces exhibit a gradual decrease with increasing porosity for both circular ($w = 1$) and elliptic ($w = 0.2$) voids, as already expected. Nonetheless, while for the case of a circular

void ($w = 1$), in Fig. 5.10a, the curves are symmetric with respect to the $\overline{\Sigma}_{eq}$ axis, the curves for the elliptical void ($w = 0.2$), in Fig. 5.10b, become asymmetric as already discussed in the context of Fig. 5.9. As a consequence of this asymmetry, the MVAR estimates are found to be stiffer in the negative pressure regime ($\overline{\Sigma}_m < 0$). The observed asymmetry becomes more pronounced with increasing porosity.
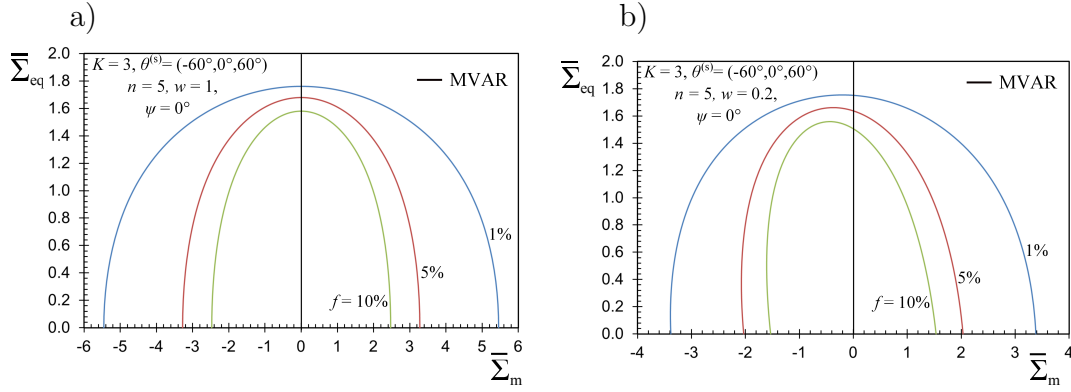

Figure 5.10: Gauge surfaces in the $\overline{\Sigma}_m - \overline{\Sigma}_{eq}$ plane for a single porous crystal with elliptical voids, $K = 3$ slip systems with slip orientations $\theta^{(s)} = (-60^o, 0^o, 60^o)$ and a creep exponent $n = 5$. The effect of porosity is investigated by choosing $f = (1\%, 5\%, 10\%)$ for different void shapes (a) $w = 1$, $\psi = 0^o$ and (b) $w = 0.2$, $\psi = 0^o$.
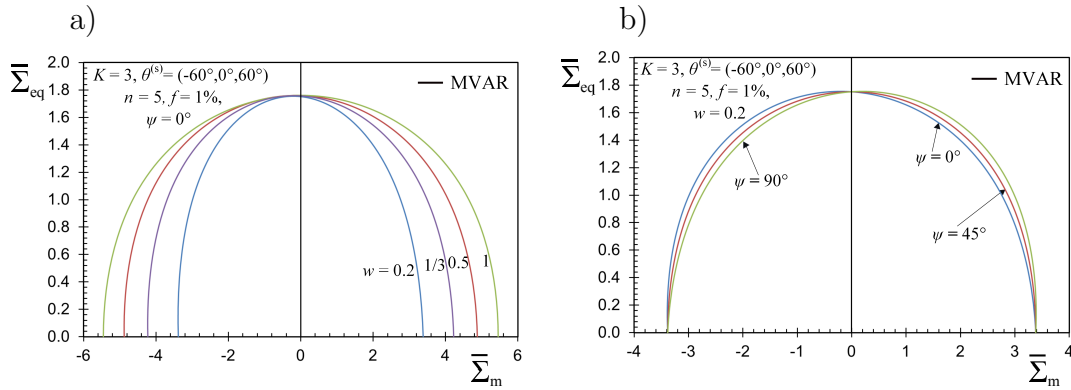

Figure 5.11: Gauge surfaces in the $\overline{\Sigma}_m - \overline{\Sigma}_{eq}$ plane for a single porous crystal with elliptical voids, $K = 3$ slip systems, slip orientations $\theta^{(s)} = (-60^o, 0^o, 60^o)$ and a creep exponent $n = 5$. The porosity of set to $f = 1\%$. The effect of (a) the void aspect ratio is investigated by choosing $w = (0.2, 0.5, 1)$ for an angle $\psi = 0$ and (b) of the void orientation by choosing $\psi = (0^o, 45^o, 90^o)$ for a given aspect ratio $w = 0.2$.

Figure 5.11 shows gauge surfaces in the $\overline{\Sigma}_m - \overline{\Sigma}_{eq}$ plane for a single porous crystal

comprising $K = 3$ slip systems with slip orientations $\theta^{(s)} = (-60^o, 0^o, 60^o)$ and a creep exponent $n = 5$. The porosity of set to $f = 1\%$. The effect of (a) the void aspect ratio is investigated by choosing $w = (0.2, 0.5, 1)$ for an angle $\psi = 0$ and (b) of the void orientation by choosing $\psi = (0^o, 45^o, 90^o)$ for a given aspect ratio $w = 0.2$. In Fig. 5.11a, we observe that with decreasing w, the gauge surface becomes gradually asymmetric while diminishing in size. This last effect implies that for the same porosity $f = 1\%$, an elliptical void $w < 1$ leads to softer response than a circular one.

In Fig. 5.11b, we study the effect of the void orientation angle $\psi = (0^o, 45^o, 90^o)$. Note that the case $\psi = 90^o$ is equivalent to setting $w \rightarrow 1/w$ and $\psi = 0^o$. In particular, the $\psi = 90^o$ curve is simply a reflection of that for $\psi = 0^o$ about the $\overline{\Sigma}_{eq}$ axis, as naturally expected from purely geometrical arguments. In turn, the $\psi = 45^o$ curve exhibits full symmetry with respect to the $\overline{\Sigma}_{eq}$ axis contrary to the other two cases $\psi = 0^o, 90^o$. Finally, as already expected from earlier studies Danas and Ponte Castañeda [2009b], the hydrostatic point for all these cases is independent of the angle ψ. This is intuitively expected since the hydrostatic loading has no preferential direction and can be easily attributed to the form of the $\mathbf{G}$ tensor defined in equation (5.5), since the sum of its diagonal components $\mathbf{G}_{1111} + 2\mathbf{G}_{1122} + \mathbf{G}_{2222} = w^2 + 1$, is independent of the angle ψ.

5.3.2   Effect of the crystal anisotropy

In this subsection, we discuss in more detail the effect of matrix crystal anisotropy upon the effective response of the porous composite. As already discussed in the context of Fig. 5.2, where circular voids are embedded in a two slip systems single crystal, the average hydrostatic response is strongly influenced by the slip orientations. Specifically, both the MVAR model and the FE results predict that the effective behavior of a porous single crystal with $K = 1$ slip system (i.e., highly anisotropic case) or $K = 2$ slip systems with 90° relative angle lead to a completely incompressible response.

In order to analyze this further, Fig. 5.12 shows gauge surfaces in the $\overline{\Sigma}_m - \overline{\Sigma}_{eq}$ plane of porous single crystals with circular voids ($w = 1$), porosity $f = 5\%$ and a creep exponent $n = 10$. In order to reveal the effect of the number of slip systems as well as of their orientations upon the effective response of the porous crystal, we consider the case of $K = (1, 2, 3, 4, 5)$ with (a) equiangular slip system orientations

and (b) with arbitrary non-equiangular slip system orientations. The specific choices of the different orientations can be found in Table 2 for both cases considered here.

Table 5.1: Set of angles $\theta^{(s)}$ for equiangular and non equiangular slip systems

type	$K = 1$	$K = 2$	$K = 3$	$K = 4$	$K = 5$
equiangular	$\theta^{(s)} = \pi/8$	$\theta^{(s)} = \{\pm\pi/4\}$	$\theta^{(s)} = \{0, \pm\pi/3\}$	$\theta^{(s)} = \{0, \pm\pi/4, \pi/2\}$	$\theta^{(s)} = \{0, \pm\pi/5, \pm 2\pi/5\}$
non equiangular	$\theta^{(s)} = \pi/8$	$\theta^{(s)} = \{\pm\pi/8\}$	$\theta^{(s)} = \{\pi/8, \pi/10, \pi/12\}$	$\theta^{(s)} = \{\pi/8, \pi/9, \pi/10, \pi/11\}$	$\theta^{(s)} = \{\pi/8, 2\pi/15, 4\pi/31, 4\pi/33, 2\pi/17\}$

Equiangular slip systems. More specifically, in Fig. 5.12a, we observe a strong dependence of the effective response upon K. While for $K = 1$ and $K = 2$ the porous crystal exhibits a fully incompressible response (in agreement with the observations made in Fig. 5.2, the porous crystal becomes gradually softer with increasing K. On the other hand, one could observe that the response for $K = 3, 4, 5$ is very similar quantitatively, especially near the hydrostatic point (i.e., $\overline{\Sigma}_{eq} = 0$).

Non equiangular slip systems. By contrast, in Fig. 5.12b, we observe an even stronger dependence of the effective response upon the crystal anisotropy. In this case, the porous crystal is still incompressible for $K = 1$ but not for the rest of the cases $K \geq 2$. In addition, in Fig. 5.12b, the dependence of the effective response for $K \geq 2$ at moderate and high triaxialities is completely reversed (for instance, the material with $K = 2$ is softer than those for $K = 3$ or $K = 4$) when compared to that in Fig. 5.12a.
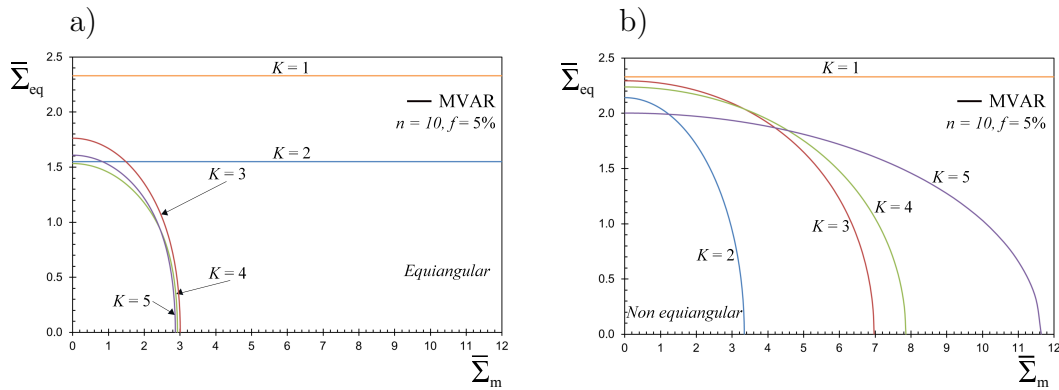

Figure 5.12: Gauge surfaces in the $\overline{\Sigma}_m - \overline{\Sigma}_{eq}$ plane for a single porous crystal with circular voids, porosity $f = 5\%$, creep exponent $n = 10$, for several number of slip systems $K = (1, 2, 3, 4, 5)$. Part (a) corresponds to equiangular and (b) to non-equiangular slip system orientations. Their precise definition is detailed in Table 2.

At this point, it is perhaps relevant to make contact with the corresponding three-dimensional models proposed by Han et al. [2013] and Paux et al. [2015]. In these models—which have been assessed for an FCC crystal (near equiangular case in our notation)—even though the deviatoric response includes the effect of the crystal anisotropy (i.e., number of slip systems and orientations), the corresponding response under purely hydrostatic stressing is independent of the orientation of the systems in Han et al. [2013] and independent of the number and orientation of slip systems in Paux et al. [2015]. The present study, albeit in two-dimensions, shows that in the context of highly anisotropic porous single crystals, the purely hydrostatic response is extremely sensitive to the number of the slip systems K as well as on the slip orientations, as clearly shown in Fig. 5.12. Of course, the present model needs to be extended in the three-dimensional case in order to have a more complete picture of the coupling between crystal anisotropy and (morphological) void anisotropy. Such work is underway and therein comparisons will be given with available models in the literature.

5.3.3 Fully anisotropic effective response on the deviatoric plane

In this section, we investigate the effective response of the porous single crystal in the deviatoric plane $\overline{\Sigma}_{12}$ — $\left(\overline{\Sigma}_{11} - \overline{\Sigma}_{22}\right)/2$ for given hydrostatic stress $\overline{\Sigma}_m$. This allows to probe the complete response of the porous crystal and reveal in a more clear way the combined coupling between the anisotropy of crystal and that induced by the void shape and orientation. For the sake of conciseness, in the following, we consider only crystals comprising $K = 3$ slip systems with slip orientations $\theta^{(s)} = (-54.7^o, 0^o, 54.7^o)$ (FCC) and $K = 2$ slip systems with slip orientations $\theta^{(s)} = (-22.5^o, 22.5^o)$, respectively, porosity $f = 5\%$ and creep exponent $n = 10$.

First, for illustration purposes and in order to give the reader a more complete viewpoint of the porous crystal effective response, we show in Fig. 5.13 two representative three-dimensional gauge surfaces defined by the axes $\overline{\Sigma}_{12}$ — $\left(\overline{\Sigma}_{11} - \overline{\Sigma}_{22}\right)/2 - \overline{\Sigma}_m$ for (a) $K = 3$ and (b) $K = 2$. The void aspect ratio and orientation are set to $w = 0.2$ and $\psi = 0$, respectively. Further discussion of these (and even more) surfaces is done in the following by considering projections in the deviatoric planes.
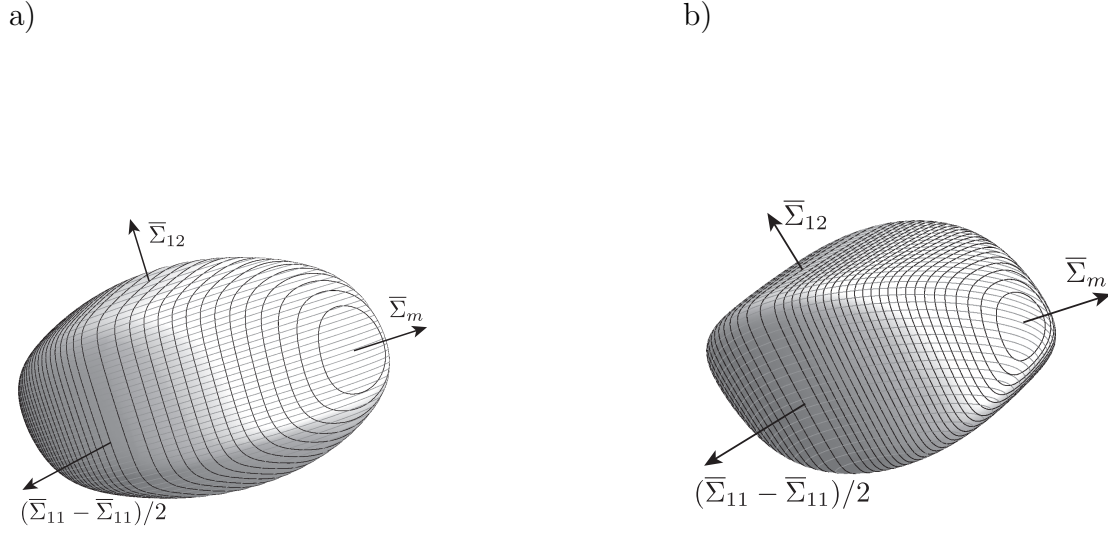
a)   b)

Figure 5.13: Three-dimensional gauge surfaces defined by the axes $\overline{\Sigma}_{12} - \left(\overline{\Sigma}_{11} - \overline{\Sigma}_{22}\right)/2 - \overline{\Sigma}_m$ for (a) $K = 3$ ($\theta^{(s)} = (-54.7^o, 0^o, 54.7^o)$) and (b) $K = 2$ ($\theta^{(s)} = (-22.5^o, 22.5^o)$). The void aspect ratio and orientation are set to $w = 0.2$ and $\psi = 0$, porosity is $f = 5\%$ and creep exponent $n = 10$.

In this connection, Fig. 5.14 shows MVAR gauge surfaces in the deviatoric plane $\overline{\Sigma}_{12}$ — $\left(\overline{\Sigma}_{11} - \overline{\Sigma}_{22}\right)/2$ for a single porous crystal with $K = 3$ slip systems, slip orientations $\theta^{(s)} = (-54.7^o, 0^o, 54.7^o)$, void shapes $w = (0.2, 1)$ and void orientations $\psi = (0^o, 22.5^o, 67.5^o)$. The various cross-sections correspond to different hydrostatic stresses $\overline{\Sigma}_m = 0$, $\overline{\Sigma}_m = \pm 0.5\overline{\Sigma}_m^H$, $\overline{\Sigma}_m = \pm 0.9\overline{\Sigma}_m^H$, where $\overline{\Sigma}_m^H$ denotes the hydrostatic point delivered by the model MVAR for hydrostatic loading for each of the given cases in Fig. 5.14a-d, respectively.

More specifically, in Fig. 5.14a, which corresponds to a circular void, we observe a gradual shrinking of the curves with increasing $\overline{\Sigma}_m$ as expected. At small values of $\overline{\Sigma}_m = 0$, the curve exhibits an almost discrete character which tends to become more rounded (convexify) with increasing $\overline{\Sigma}_m$. Note at this point that since the porous crystal is considered to be rate-dependent (i.e., finite value of the creep exponent n), the corresponding effective response is strictly convex and the curves exhibit large but finite curvature areas (i.e., smooth-corners) leading to an almost hexagonal symmetry of the curves. When the void is circular ($w = 1$), the porous crystal preserves the original symmetries of the crystal matrix for all values of $\overline{\Sigma}_m$ considered. In particular,

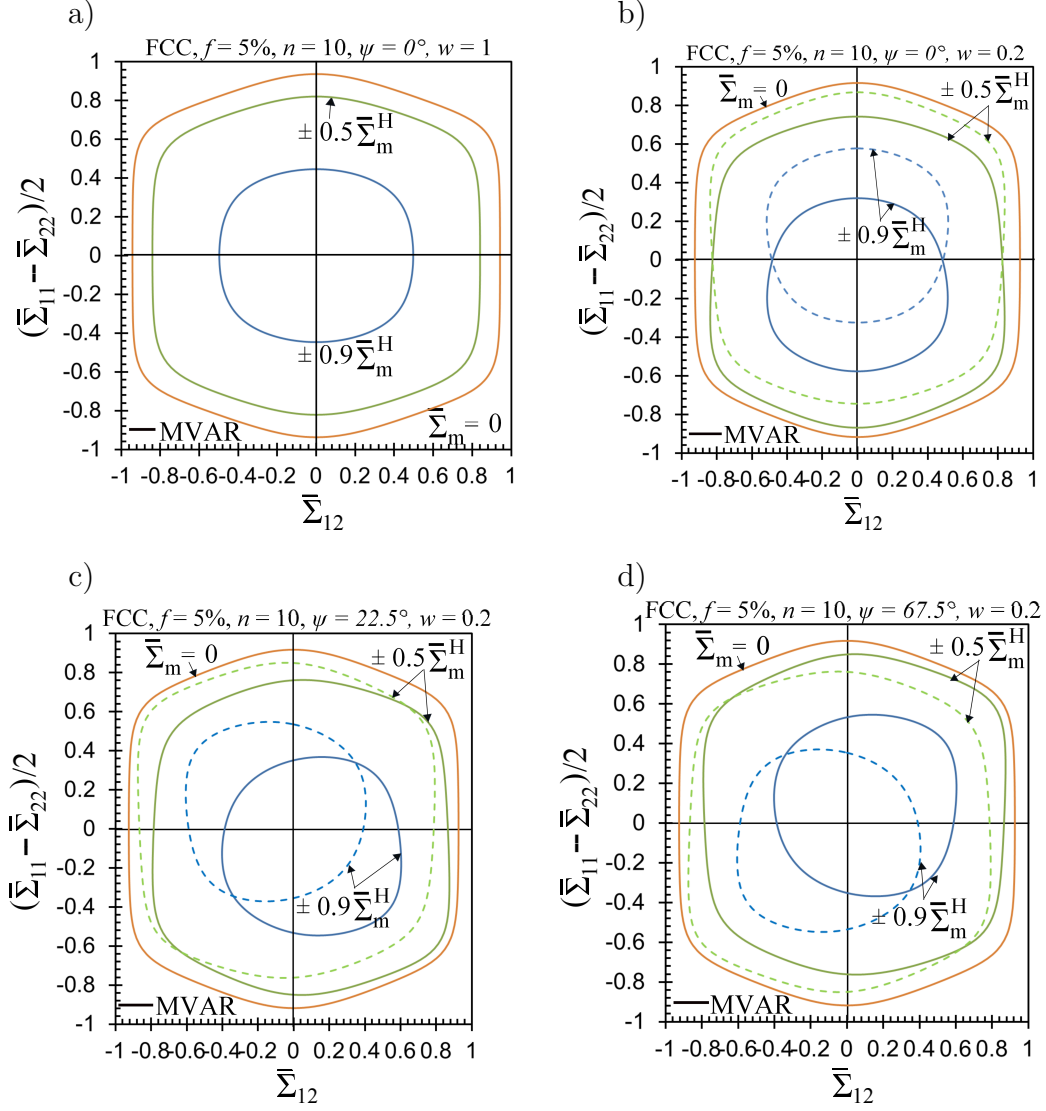in this case the curve is fully symmetric with respect to the two axes $\overline{\Sigma}_{12}$ and $(\overline{\Sigma}_{11} - \overline{\Sigma}_{22})/2$.

Figure 5.14: Gauge surfaces in the deviatoric plane $\overline{\Sigma}_{12} - - \left(\overline{\Sigma}_{11} - \overline{\Sigma}_{22}\right)/2$ for a single porous crystal with elliptical voids, $K = 3$ slip systems, slip orientations $\theta^{(s)} = (-54.7^o, 0^o, 54.7^o)$ (FCC), a porosity $f = 5\%$, a creep exponent $n = 10$, at different level of pressure. The dashed line curves correspond to the negative pressure regime while the continuous one correspond to the positive pressure regime. Case of (a) $\psi = 0^o$, $w = 1$, (b) $\psi = 0^o$, $w = 0.2$, (c) $\psi = 22.5^o$, $w = 0.2$, (d) $\psi = 67.5^o$, $w = 0.2$.

By contrast, as shown in Fig. 5.14b (see Fig. 5.13a for the three-dimensional surface), if one considers an elliptical void with aspect ratio $w = 0.2$ (but still $\psi = 0^o$), the corresponding MVAR curves exhibit an asymmetry with respect to the $\overline{\Sigma}_{12}$-axis, but
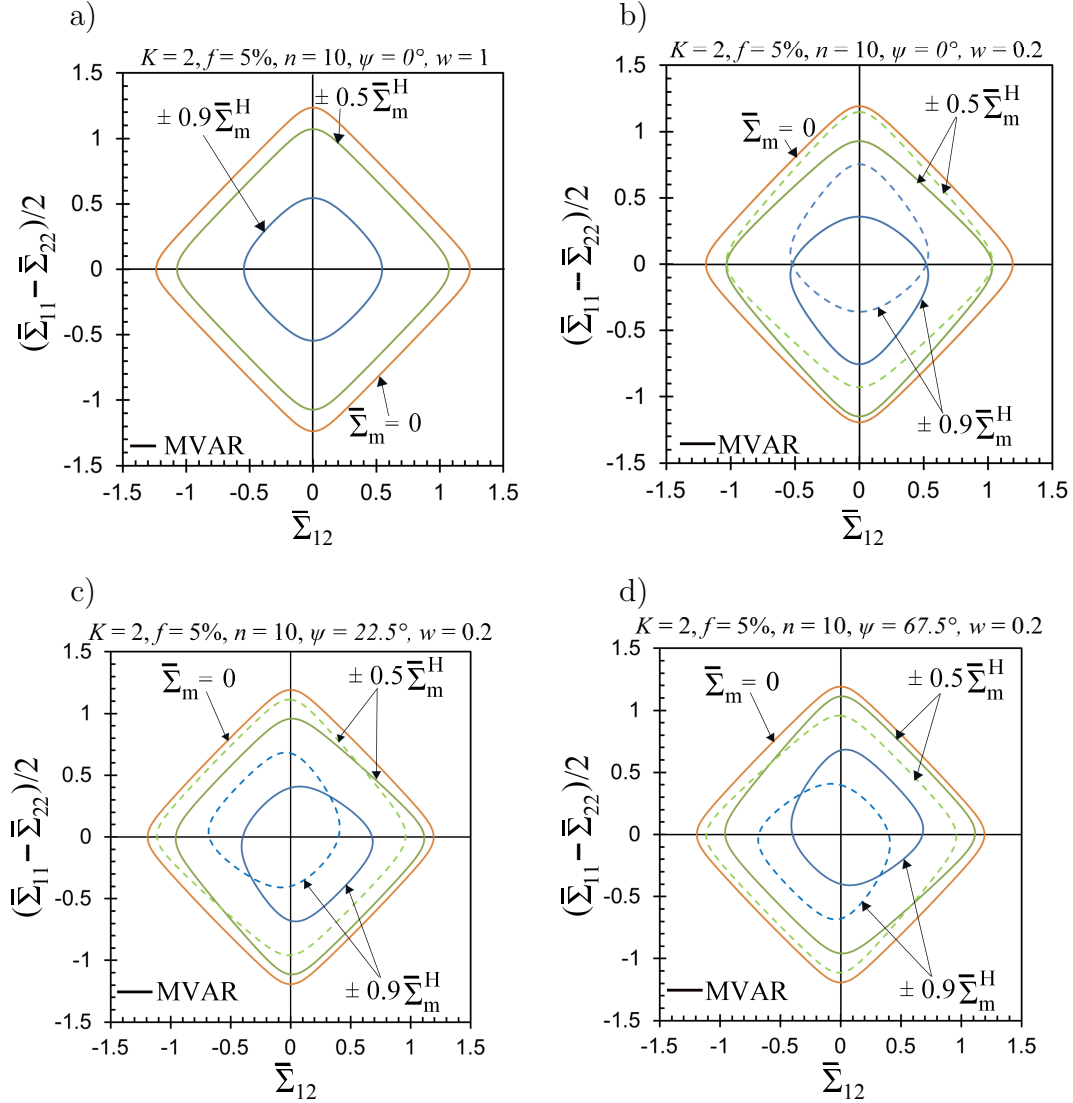
Figure 5.15: Gauge surfaces in the deviatoric plane $\overline{\Sigma}_{12}-- \left(\overline{\Sigma}_{11} - \overline{\Sigma}_{22}\right)/2$ for a single porous crystal with elliptical voids, $K = 2$ slip systems, slip orientations $\theta^{(s)} = (-22.5^o, 22.5^o)$, a porosity $f = 5\%$, a creep exponent $n = 10$, at different level of pressure. The dashed line curves correspond to the negative pressure regime while the continuous one correspond to the positive pressure regime. Case of (a) $\psi = 0^o$, $w = 1$, (b) $\psi = 0^o$, $w = 0.2$, (c) $\psi = 22.5^o$, $w = 0.2$, (d) $\psi = 67.5^o$, $w = 0.2$.

still preserve the symmetry with respect to the $(\overline{\Sigma}_{11} - \overline{\Sigma}_{22})/2$ axis for $\overline{\Sigma}_m > 0$. Rather interestingly, the almost hexagonal symmetry still prevails for $\overline{\Sigma}_m = 0$. This response is a direct consequence of the geometric coupling of the crystal slip orientations and the void shape at finite hydrostatic stresses. Note further that point symmetry of the curves with respect to the global origin $\left(\overline{\Sigma}_{12}, \pm(\overline{\Sigma}_{11} - \overline{\Sigma}_{22})/2\right) = (0,0)$ and $\overline{\Sigma}_m = 0$

is still preserved. This is easily observed by noting the point symmetries between the continuous lines corresponding to $\overline{\Sigma}_m > 0$ and the dashed ones for $\overline{\Sigma}_m < 0$.

Subsequently, in Fig. 5.14c,d, an elliptical void ($w = 0.2$) with angles $\psi = 22.5^o, 67.5^o$ are shown, respectively. In these two cases, the gauge surfaces exhibit full asymmetry with respect to both axes for finite hydrostatic stresses $\overline{\Sigma}_m \neq 0$, but preserve the hexagonal symmetry for $\overline{\Sigma}_m = 0$. The observed asymmetry is much more pronounced at higher values of $\overline{\Sigma}_m$. Note that the curves for $\psi = 67.5$ in Fig. 5.14d can be reproduced from the $\psi = 22.5^o$ ones in Fig. 5.14c by counter-clockwise rotation of 90° about the deviatoric origin $\left(\overline{\Sigma}_{12}, \pm(\overline{\Sigma}_{11} - \overline{\Sigma}_{22})/2\right) = (0,0)$. Again, it is stressed that point symmetry of the curves with respect to the global origin $\left(\overline{\Sigma}_{12}, \pm(\overline{\Sigma}_{11} - \overline{\Sigma}_{22})/2\right) = (0,0)$ and $\overline{\Sigma}_m = 0$ is still preserved if one compares the continuous ($\overline{\Sigma}_m > 0$) with the dashed lines ($\overline{\Sigma}_m < 0$).

Figure 5.15 shows MVAR gauge surfaces in the deviatoric plane $\overline{\Sigma}_{12} - \left(\overline{\Sigma}_{11} - \overline{\Sigma}_{22}\right)/2$ for a porous crystal with $K = 2$ slip systems, slip orientations $\theta^{(s)} = (-22.5^o, 22.5^o)$, void shapes $w = (0.2, 1)$ and void orientations $\psi = (0^o, 22.5^o, 67.5^o)$. The various cross-sections correspond to different hydrostatic stresses $\overline{\Sigma}_m = 0$, $\overline{\Sigma}_m = \pm 0.5\overline{\Sigma}_m^H$ and $\overline{\Sigma}_m = \pm 0.9\overline{\Sigma}_m^H$, where $\overline{\Sigma}_m^H$ denotes the hydrostatic point delivered by the model MVAR for hydrostatic loading for each of the given cases in Fig. 5.15a-d, respectively.

As observed in Fig. 5.15a, which deals with circular voids, a gradual shrinking of the curves appears while increasing $\overline{\Sigma}_m$, as expected. Moreover, as also seen in the previous case, the curve exhibits an almost discrete character at small values of $\overline{\Sigma}_m = 0$ with tetragonal symmetry. These symmetries are preserved with the addition of hydrostatic stress even though some additional rounding is observed at high $\overline{\Sigma}_m = \pm 0.9\overline{\Sigma}_m^H$.

However, as shown in Fig. 5.15b (see Fig. 5.13b for the three-dimensional surface), for an elliptical void with aspect ratio $w = 0.2$ (but still $\psi = 0^o$), the corresponding MVAR curves exhibit an asymmetry with respect to the $\overline{\Sigma}_{12}$ axis, but still preserve the symmetry with respect to the $(\overline{\Sigma}_{11} - \overline{\Sigma}_{22})/2$ axis for $\overline{\Sigma}_m > 0$. In addition, the almost tetragonal symmetry still prevails for $\overline{\Sigma}_m = 0$. As already discussed, this response is a direct consequence of the geometric coupling of the crystal slip orientations and the void shape at finite hydrostatic stresses. Note further that point symmetry of the curves with respect to the global origin $\left(\overline{\Sigma}_{12}, \pm(\overline{\Sigma}_{11} - \overline{\Sigma}_{22})/2\right) = (0,0)$ and $\overline{\Sigma}_m = 0$ is still preserved. Finally, in Fig. 5.15c,d, an elliptical void ($w = 0.2$) with angles $\psi = 22.5^o, 67.5^o$ are shown, respectively. In these two cases, the gauge surfaces exhibit

full asymmetry with respect to both axes for finite hydrostatic stresses $\overline{\Sigma}_m \neq 0$, but preserve the tetragonal symmetry for $\overline{\Sigma}_m = 0$. As in the case of $K = 3$ slip systems, the curves for $\psi = 67.5$ in Fig. 5.15d can be reproduced from the $\psi = 22.5^o$ ones in Fig. 5.15c by counter-clockwise rotation of 90° about the deviatoric origin $\left(\overline{\Sigma}_{12}, \pm(\overline{\Sigma}_{11} - \overline{\Sigma}_{22})/2\right) = (0, 0)$. Again, it is stressed that point symmetry of the curves with respect to the global origin $\left(\overline{\Sigma}_{12}, \pm(\overline{\Sigma}_{11} - \overline{\Sigma}_{22})/2\right) = (0, 0)$ and $\overline{\Sigma}_m = 0$ is still preserved if one compares the continuous ($\overline{\Sigma}_m > 0$) with the dashed lines ($\overline{\Sigma}_m < 0$).

5.4 Concluding remarks

In this chapter, a fully analytical constitutive model has been developed for porous rate-dependent single crystals comprising cylindrical voids with elliptical cross-section, subjected to plane-strain loading conditions, accounting for full crystal anisotropy. In order to achieve this goal, the variational nonlinear homogenization method of Ponte Castañeda [1991a] has been used and modified Danas and Aravas [2012] to derive estimates but not bounds. The modified variational (MVAR) model presented in this study has been validated by comparison with full field FE calculations of single- and multi-void periodic unit-cells. The MVAR model has been found to be in good agreement with the FE results for a very wide range of parameters describing the number and orientation of the slip systems (i.e., crystal anisotropy), the creep exponent (i.e., nonlinearity) of the matrix crystal, the porosity and the void shapes and orientations. The MVAR model has shown strong predictive capabilities while exhibiting critical qualitative features.

Specifically, the MVAR model has been able to predict the strong dependence of the effective response, and especially of the average hydrostatic stress upon the number and orientation of the slip systems as well as the shape and orientation of the voids. The major finding of this work, is that for highly anisotropic crystals (e.g., one or even two active slip systems) the porous crystal can exhibit fully incompressible response, even in the presence of voids. This of course affects the entire effective response of the porous crystal for the entire range of stress states. That is the first time such a result is presented in the literature and reveals the significance of plastic anisotropy of the underlying phases upon the macroscopic response of the material. Furthermore, it has been shown that the void shape and orientation affect strongly the response of the

porous crystal. In particular, the effective response becomes much softer as one goes from a circular void to an elliptical one (which is suggestive of a crack-type geometry). In the general case of elliptical voids oriented at an arbitrary angle (with respect to the laboratory axes) and arbitrary number of slip systems, we have shown that the effective response exhibits no symmetries when plotted in the purely deviatoric plane (and at finite hydrostatic stresses) thus indicating the non-trivial coupling between the anisotropy of the underlying crystal and the (morphological) anisotropy induced by the shape and orientation of the voids.

In addition, the present model, which includes at present no calibration parameters, has been assessed to a large extent with robust periodic unit-cell calculations and for a wide range of parameters (different number and orientation of slip systems, void shapes and orientations, creep exponents and porosity values). This gives confidence on the accuracy of the corresponding three-dimensional model, which will be presented in the next chapter.

Chapter 6

Instantaneous behavior: spherical and ellipsoidal voids

This chapter deals with the instantaneous effective behavior of porous single crystals consisting of ellipsoidal voids distributed randomly in the specimen.

6.1 General expressions

In this section, we present first analytical expressions for the evaluation of the effective viscoplastic stress potential delivered by the MVAR method, before proceeding to the discussion of the results. As already discussed, the effective stress potential of the porous single crystal is given in chapter 2, and recalled here for completeness to

$$\widetilde{U}_{mvar}\left(\overline{\boldsymbol{\sigma}}\right) = (1-f)\sum_{s=1}^{K}\frac{\dot{\gamma}_0^{(s)}\tau_0^{(s)}}{n+1}\left(\frac{\sqrt{\overline{\boldsymbol{\sigma}}\cdot\widehat{\mathbf{S}}^{(s)}\cdot\overline{\boldsymbol{\sigma}}}}{\tau_0^{(s)}\left(1-f\right)}\right)^{n+1}, \tag{6.1}$$

where

$$\widehat{\mathbf{S}}^{(s)} = \widehat{\mathbf{S}}^{var,(s)} + \left(q_J^2 - 1\right)\mathbf{J}\cdot\widehat{\mathbf{S}}^{var,(s)}\cdot\mathbf{J}, \tag{6.2}$$

and

$$\widehat{\mathbf{S}}^{var,(s)} = \frac{1}{2}\mathbf{E}^{(s)} + \frac{f}{K}\widehat{\mathbf{S}}_0^*, \quad \mathbf{E}^{(s)} = 2\boldsymbol{\mu}^{(s)}\otimes\boldsymbol{\mu}^{(s)}, \ \forall s = 1, K, \quad J_{ijkl} = \frac{1}{3}\delta_{ij}\delta_{kl}. \tag{6.3}$$

In addition,

$$\widehat{\mathbf{S}}_0^* = \lambda\lim_{\lambda^{(s)}\to\lambda}\lim_{\rho^{(s)}\to\infty}\lim_{\kappa\to\infty}\mathbf{Q}^{-1} - \sum_{s=1}^{K}\frac{1}{2}\mathbf{E}^{(s)},$$

$$q_J = \sqrt{\frac{15}{f}}\left\{\frac{(1-f)\left(\beta_n\right)^{\frac{1}{n}}}{n(f^{-1/n}-1)}\right\}^{\frac{n}{n+1}}, \qquad \beta_n = \frac{4}{25}\,6^{-\frac{n}{2}}. \tag{6.4}$$

In the following, we present a numerical homogenization analysis which will serve to assess the accuracy of the proposed homogenization model.

6.2 Results: Assessment of MVAR model via FE simulations

This section presents results for the effective behavior of rate-dependent porous single crystals as predicted by the modified variational model (MVAR) proposed in this work. Before proceeding with the discussion of the results, it is useful to introduce first the various material and loading parameters used in the following figures. The present study investigates a range of creep exponents $n = (1, 2, 5, 10)$, porosities $f = (1\%, 5\%)$, void shapes and orientations (e.g., spherical and ellipsoidal) as well as Face-Centered Cubic (FCC), Body-Centered Cubic (BCC) and Hexagonal Closed Packed (HCP) single crystals. These choices of single crystals correspond to the large majority of metals.

In addition, motivated by common practice in crystal plasticity studies, we consider the case where all the slip systems of the matrix have the same critical resolved shear stress (CRSS) and reference slip-rate. The crystallographic orientation will be defined independently in the following sections.

In turn, we will focus on two different types of loading conditions. In the first one, the principal directions of the macroscopic stress tensor $\overline{\boldsymbol{\sigma}}$, or equivalently $\overline{\boldsymbol{\Sigma}}$ are aligned with the fixed Cartesian laboratory frame of reference defined by the three unit vectors $\mathbf{e}^{(i)}$, $i = 1, 2, 3$. In this case, one could rewrite the principal stresses in terms of the average equivalent von Mises stress, $\overline{\Sigma}_{eq}$, the average (macroscopic) Lode angle, $\overline{\theta}$, and the average stress triaxiality X_Σ. This reads, in diagonal matrix notation

$$\overline{\boldsymbol{\Sigma}} = \overline{\Sigma}_m \{1, 1, 1\} + \frac{2}{3} \overline{\Sigma}_{eq} \left\{ \cos \overline{\theta}, -\cos \left(\overline{\theta} + \frac{\pi}{3} \right), -\cos \left(\overline{\theta} - \frac{\pi}{3} \right) \right\}. \qquad (6.5)$$

The second set of loading conditions involves the two average shear components $\overline{\Sigma}_{13}$ and $\overline{\Sigma}_{23}$ with superimposed hydrostatic stressing $\overline{\Sigma}_m$, such that (in tensorial notation)

$$\overline{\boldsymbol{\Sigma}} = \overline{\Sigma}_m \sum_{i=1}^{3} \mathbf{e}^{(i)} \otimes \mathbf{e}^{(i)} + \overline{\Sigma}_{13} \left(\mathbf{e}^{(1)} \otimes \mathbf{e}^{(3)} + \mathbf{e}^{(3)} \otimes \mathbf{e}^{(1)} \right) + \overline{\Sigma}_{23} \left(\mathbf{e}^{(2)} \otimes \mathbf{e}^{(3)} + \mathbf{e}^{(3)} \otimes \mathbf{e}^{(2)} \right).$$
$$(6.6)$$

Since the response of the porous single crystal is anisotropic these are simply two out of several possible sets of loading conditions. Nevertheless, as we will show in the following, they are sufficient to reveal the most important features of the porous single crystal response.

Furthermore, it is important to clarify that the porous crystal exhibits two types of anisotropy. The first is that of the crystal matrix as a result of the corresponding slip systems and the second is that of the void shape and orientation, which is ellipsoidal in general. Therefore, the effective response of the porous crystal is a function of all the six stress components. Of course showing cross-sections with all possible combination of stress components is to cumbersome and of a little value to the understanding of the porous single crystal response. Thus, following traditional notation in the context of porous materials, as well as similar studies of Han et al. [2013], Paux et al. [2015], the following results are broken down into three major groups following the above mentioned loading conditions. The first group shows the effective response of the porous crystals in the space $\overline{\Sigma}_m - \overline{\Sigma}_{eq}$. This stress space is very important since it involves directly the dependence upon the hydrostatic component $\overline{\Sigma}_m$. The second group shows results in deviatoric planes such as for instance the one defined by the out-of-plane shear stresses $\overline{\Sigma}_{13}$-$\overline{\Sigma}_{23}$, for $\overline{\Sigma}_{12} = 0$ and for given constant hydrostatic stress $\overline{\Sigma}_m$. This cross-section reveals the non trivial coupling of crystal anisotropy and void shape (morphological) anisotropy. The last group displays results in the Π-plane (or octahedral plane), defined by polar coordinates $(r, \phi) = (\overline{\Sigma}_{eq}, \overline{\theta})$ at different levels of superimposed pressure $\overline{\Sigma}_m$. These choices lead to more complete results in the sense that they cover a significant range of the stress space but at the same time using traditional and well-understood stress measures.

6.2.1 Computation of the gauge surface in the numerical homogenization

The evaluation of the gauge surfaces resulting from the numerical computations can be expressed using the same framework defined in chapter 5. For sake of completeness, we recall here the main features of such approach.

By making use of the homogeneity of degree $n + 1$ in $\overline{\Sigma}$ of the function $\widetilde{U}$, one can

write

$$\widetilde{U}(\overline{\mathbf{\Sigma}}) = \left(\overline{\Sigma}_{eq}\right)^{n+1} \widetilde{U}_N(\mathbf{N}, X_\Sigma) = \frac{\dot{\gamma}_0 \tau_0^{-n}}{n+1}, \tag{6.7}$$

while $\mathbf{N} = \overline{\mathbf{\Sigma}}^d / \overline{\Sigma}_{eq}$ describes the loading direction in the deviatoric space, with $\overline{\mathbf{\Sigma}}^d$ and $\overline{\Sigma}_{eq}$ denoting the deviatoric and equivalent Von Mises part of the average stress $\overline{\mathbf{\Sigma}}$, respectively, corresponding to the equi-potential surface.

Next, given any average stress, $\overline{\boldsymbol{\sigma}}$, one can write

$$\widetilde{U}(\overline{\boldsymbol{\sigma}}) = (1 - f) \min_{\boldsymbol{\sigma} \in S(\overline{\boldsymbol{\sigma}})} \langle U(\boldsymbol{\sigma}) \rangle^{(1)} = \left(\overline{\sigma}_{eq}\right)^{n+1} \widetilde{U}_N(\mathbf{N}, X_\Sigma). \tag{6.8}$$

Due to the homogeneity of $\widetilde{U}$, it is noted that $\widetilde{U}_N(\mathbf{N}, X_\Sigma)$ is the same function in (6.7) and (6.8), and hence combination of these two equations gives

$$\overline{\Sigma}_{eq} = \left[(n+1) \dot{\gamma}_0^{-1} \tau_0^n \widetilde{U}(\overline{\boldsymbol{\sigma}}) \right]^{\frac{-1}{n+1}} \overline{\sigma}_{eq}. \tag{6.9}$$

In the FE code, $\overline{D}_{11}$ and the average X_Σ in the unit-cell are applied and remain constant throughout the process, as discussed in chapter 4, whereby $\overline{D}_{22}$, $\overline{D}_{33}$ and $\overline{\sigma}_{eq}$ are calculated. In addition, postprocessing of the numerical results provides $\widetilde{U}(\overline{\boldsymbol{\sigma}})$. Finally, $\overline{\Sigma}_{eq}$ is readily obtained from equation (6.9), while $\overline{\Sigma}_m = X_\Sigma \overline{\Sigma}_{eq}$ given the prescribed average stress triaxiality X_Σ in the unit-cell.

6.2.2 Porous crystals with spherical voids

Face-Centered Cubic single crystal

In this section Face-Centered Cubic (FCC) single crystals are considered. In the FCC crystalline structure, plastic slip occurs on a group of 12 slip systems following $\{111\} \langle 110 \rangle$ (see Table 6.1).

In this loading configuration, Fig. 6.1 shows cross-sections of the effective gauge surfaces in the $\overline{\Sigma}_m - \overline{\Sigma}_{eq}$ plane, for a creep exponent $n = 10$, a porosity $f = 1\%$ and several Lode angles $\overline{\theta} = 0^o, 10^o, 30^o$. As we can observe, the MVAR gauge surfaces are symmetric with respect to the $\overline{\Sigma}_{eq}$ axis for all the Lode angles considered. On the other hand, the FE computations predict symmetric gauge surfaces for $\overline{\theta} = 0^o, 30^o$ (see Fig. 6.1a,c) whereas a rather small "asymmetry" with respect to the $\overline{\Sigma}_{eq}$ axis is observed for $\overline{\theta} = 10^o$ (see Fig. 6.1b). Following the observations of this figure for spherical voids, which indicate only a minor asymmetry of the gauge surface and only

slip system s	1	2	3	4	5	6
slip plane **m**		(111)			(1$\bar{1}$1)	
slip direction **s**	[$\bar{1}$01]	[0$\bar{1}$1]	[$\bar{1}$10]	[$\bar{1}$01]	[011]	[110]
slip system s	7	8	9	10	11	12
slip plane **m**		($\bar{1}$11)			(11$\bar{1}$)	
slip direction **s**	[0$\bar{1}$1]	[110]	[101]	[$\bar{1}$10]	[101]	[011]

Table 6.1: Slip systems in FCC crystalline structure.

in some cases, we will choose in most of the results presented in the sequel a Lode angle $\overline{\theta} = 0^o$. Therefore, for this case of spherical voids only one quarter of the surface is shown.

Figure 6.1: Gauge surfaces in the $\overline{\Sigma}_m - \overline{\Sigma}_{eq}$ plane in the case of a porous FCC single crystal comprising spherical voids, for a creep exponent $n = 10$ and a porosity $f = 1\%$. Comparison between the model (MVAR) and the FE results for Lode angles $\overline{\theta} = 0^o, 10^o, 30^o$.

Specifically, Figure 6.2 shows cross-sections of the effective gauge surfaces in the $\overline{\Sigma}_m - \overline{\Sigma}_{eq}$ plane. Various creep exponents $n = (1, 2, 5, 10)$ are considered while the porosity is set to $f = 1\%$ (Fig. 6.2a) and $f = 5\%$ (Fig. 6.2b). In the context of this figure, we observe a very good agreement between the MVAR predictions and the FE results for the entire range of creep exponents n. More precisely, the agreement between the MVAR predictions and the FE results is very good for small nonlinearities $n = 1, 2$, whereas it slightly tends to underestimate the effective response at higher ones (i.e., $n = 5, 10$) and for very large triaxialities. In any case, the maximum error is found to be in the order of $\sim 5\%$. For $f = 1\%$, in Fig. 6.2a, and relatively high triaxialities, the $n = 1$ curve crosses the rest of the curves leading to a stiffer

response at large stress triaxialities X_Σ. This feature is validated qualitatively by the FE computations, but quantitatively may involve errors from both the FE calculations as well as inaccuracies of the MVAR model in this regime.
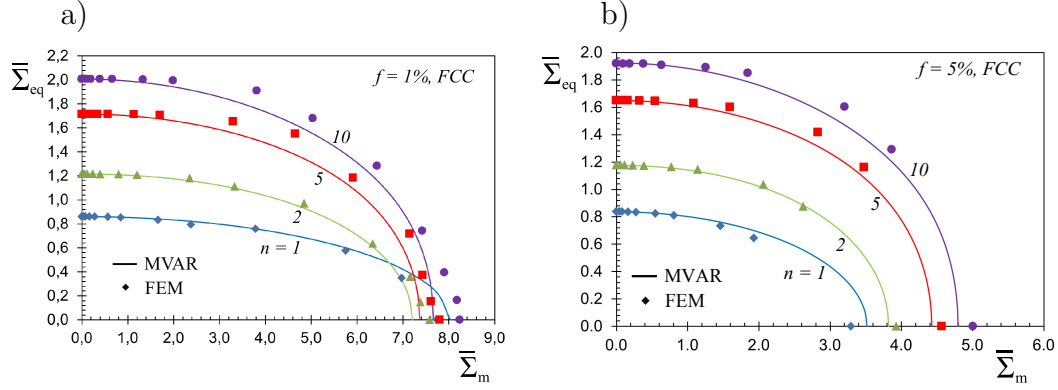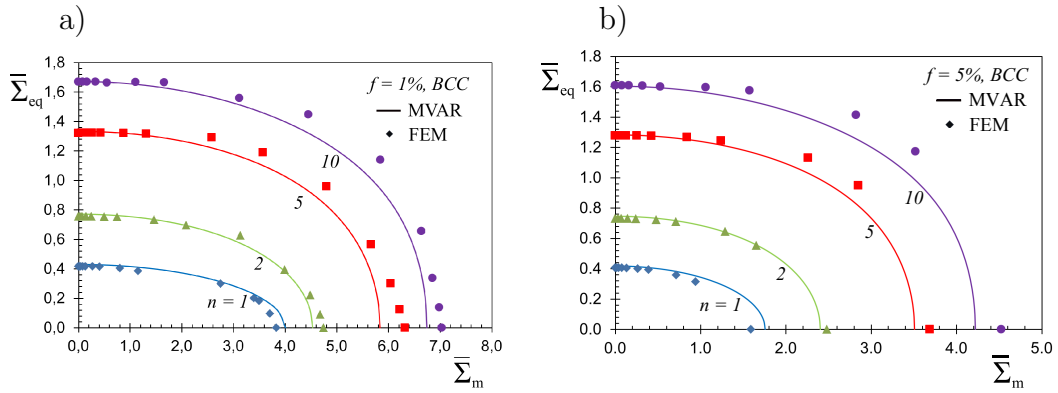

Figure 6.2: Gauge surfaces in the $\overline{\Sigma}_m - \overline{\Sigma}_{eq}$ plane in the case of a porous FCC single crystal comprising spherical voids, for a Lode angle $\overline{\theta} = 0$ and a range of creep exponent $n = (1, 2, 5, 10)$. Comparison between the model (MVAR) and the FE results for a porosity (a) $f = 1\%$, (b) $f = 5\%$.

Body-Centered Cubic single crystal

In the BCC crystalline structure, plastic slip occurs on a group of 48 slip systems following $\{123\}\langle 111\rangle$, $\{112\}\langle 111\rangle$ and $\{110\}\langle 111\rangle$ (see for instance Table 6.2).

slip system s	1	2	3	4	5	6
slip plane **m**	(110)		(1$\bar{1}$1)		(101)	
slip direction **s**	[1$\bar{1}$1]	[1$\bar{1}\bar{1}$]	[111]	[11$\bar{1}$]	[11$\bar{1}$]	[$\bar{1}$11]
slip system s	7	8	9	10	11	12
slip plane **m**	(10$\bar{1}$)		(011)		(01$\bar{1}$)	
slip direction **s**	[111]	[1$\bar{1}$1]	[11$\bar{1}$]	[1$\bar{1}$1]	[111]	[$\bar{1}$11]

Table 6.2: Slip systems $\{110\}\langle 111\rangle$ in BCC crystalline structure.

In Fig. 6.3, we present cross-sections of the effective gauge surfaces in the $\overline{\Sigma}_m - \overline{\Sigma}_{eq}$ plane for the same range of creep exponents and the same porosities, as before. The main observation in the context of this figure is that as in the previous case (FCC single crystal), there is a very good agreement between the MVAR predictions and

the FE results for $f = 1\%$, at the full range of creep exponents and the entire range of the stress triaxialities considered here. Again, the agreement between the MVAR predictions and the FE results is excellent for small nonlinearities $n = 1, 2$, whereas it tends to underestimate the effective response at higher ones (i.e., $n = 5, 10$) and for very large triaxialities. As before, the maximum error is found to be in the order of $\sim 5\%$. As discussed in chapter 5 for two-dimensional microstructures, these differences between the MVAR and FE results with increasing nonlinearity (i.e., creep exponent) are attributed to the increasing void interaction at high nonlinearities n.

Figure 6.3: Gauge surfaces in the $\overline{\Sigma}_m - \overline{\Sigma}_{eq}$ plane in the case of a porous BCC single crystal comprising spherical voids, for a Lode angle $\overline{\theta} = 0$ and for a range of creep exponent $n = (1, 2, 5, 10)$. Comparison between the model (MVAR) and the FE results for a porosity (a) $f = 1\%$, (b) $f = 5\%$.

Hexagonal Closed Packed single crystal

In the context of HCP porous crystals, we consider three distinct cases as described in Table 3. Those three cases are chosen such that the crystal goes from an extremely anisotropic response (case C_1 in Table 6.3) to those that involve a larger number of active slip systems, i.e., cases C_2 and C_3 in Table 6.3.

Let us consider first the case C_1 in Table 6.3 where plastic slip occurs only in the so called basal planes, such as for instance pure Titanium. The crystalline structure is consequently $\{0001\} \langle 1\overline{2}10 \rangle$. In this case, rather surprisingly, the computation of the microstructural tensor leads to $\widehat{\mathbf{S}}^* = \mathbf{0}$ (see equation 6.4), and thus, the MVAR

estimate becomes

$$\widetilde{U}_{mvar}\left(\overline{\boldsymbol{\sigma}}\right) = (1-f)^{-n} \sum_{s=1}^{K} \frac{\dot{\gamma}_0^{(s)} \tau_0^{(s)}}{n+1} \left(\frac{\left|\overline{\boldsymbol{\sigma}} \cdot \boldsymbol{\mu}^{(s)}\right|}{\tau_0^{(s)}}\right)^{n+1}. \tag{6.10}$$

Cases	slip plane $\mathbf{m}$	slip direction $\mathbf{s}$	number of slip systems
C_1	Basal $\{0001\}$	Type $\langle a \rangle$ $\langle 1\bar{2}10 \rangle$	3
C_2	Pyramidal Π_2 $\{11\bar{2}2\}$	Type $\langle c+a \rangle$ $\langle 11\bar{2}3 \rangle$	6
C_3	Basal $\{0001\}$ & Prismatic $\{10\bar{1}0\}$ & Pyramidal Π_2 $\{11\bar{2}2\}$	Type $\langle a \rangle$ $\langle 1\bar{2}10 \rangle$ & Type $\langle a \rangle$ $\langle 1\bar{2}10 \rangle$ & Type $\langle c+a \rangle$ $\langle 11\bar{2}3 \rangle$	$3+3+6=12$

Table 6.3: Slip systems in some hexagonal crystalline structures.

This implies that the MVAR estimate leads to a fully incompressible response in this case C_1, irrespective of the value of porosity, void shape or orientation used, as shown in Fig. 6.4a. The deviatoric part on the other hand is affected by the voids. It is important to mention at this point that even though the crystal matrix has only a few active systems, the porous composite can, in general, accommodate all possible loads since the vacuous phase is fully isotropic and compressible. Thus, the fact that an HCP porous crystal with only three active systems still remains incompressible is a highly non-trivial result. The explanation of such a response can be attributed to virtual "rigid" directions in the composite thus leading to pressure-independent response. To investigate this further, we consider the cases of HCP singles crystal with pyramidal Π_2 (C_2 in Table 6.3) and combination of basal, prismatic and pyramidal Π_2 active slip systems (C_3 in Table 6.3), as shown in Table 6.3. In these cases where more slip systems are activated, the MVAR predictions lead gradually to more compressible responses. In other words, in Fig. 6.4a, one observes that the HCP crystal C_3, with 12 slip systems is more compressible than the HCP crystal C_2, with 6 slip systems. These predictions are fully confirmed via corresponding FE calculations, as shown in Fig. 6.4a.

In turn, in Fig. 6.4b,c, we show the effect of the creep exponent $n = 1, 2, 5, 10$ for an HCP crystal with $K = 6, 12$ slip systems that are described by cases C_2, C_3 in Table 6.3, respectively. The agreement between the MVAR predictions and the FE

results is relatively good for all exponents n shown here. More interestingly, perhaps, there exists a crossing of the gauge curves as one goes from low to high triaxialities. For instance, the while at low X_Σ the $n = 1$ curve is more compliant than that of $n = 10$, the inverse occurs at higher triaxialities. This feature is completely validated qualitatively and quantitatively by the FE computations. Direct comparison between the cases of HCP with $K = 6, 12$ (Fig. 6.4b,c) and those for FCC (Fig. 6.2a) and BCC (Fig. 6.3a) reveal the nontrivial coupling between the creep exponent n, the presence of the pores and the slip system orientation.

Figure 6.4: Gauge surfaces in the $\overline{\Sigma}_m - \overline{\Sigma}_{eq}$ plane in the cases of (a) three porous HCP single crystal (with $K = 3$, $K = 6$ and $K = 12$ slip systems) comprising spherical voids, for a Lode angle $\overline{\theta} = 0$, a porosity $f = 1\%$ and a creep exponent $n = 10$, (b) for different exponents $n = 1, 2, 5, 10$ and $K = 6$ slip systems and (c) for different exponents $n = 1, 2, 5, 10$ and $K = 12$ slip systems.

To summarize, the previous cases of several HCP crystalline structures show that the MVAR model deals extremely well with the strong sensitivity of the porous single crystals behavior on the crystal anisotropy (i.e., number and orientation of slip systems), as already discussed in the context of two-dimensional microstructures. This implies that by default the present model is able to distinguish with high accuracy between different crystals (and effective loadings). Even though this choice of slip systems is somewhat theoretical in nature, the fact that for HCP with 3 slip systems the response is incompressible as well as that 6 slip systems lead to less pressure-dependence than 12 slip systems has strong implications on void growth. Moreover, it is important to mention here that in real HCP crystals the different sets of slip systems (i.e., basal, pyramidal, etc) could exhibit different critical resolved shear stresses, $\tau_0^{(s)}$. This case is not studied here since the goal is to present more general qualitative

features of the model. However, such effects could be readily considered in the present framework, since the MVAR model is general.

6.2.3 Porous crystals with ellipsoidal voids

In this section, we show results for porous single crystals comprising ellipsoidal voids, i.e., with aspect ratios $w_1 \neq 1$ and $w_2 \neq 1$. The microstructure considered here is defined by porosity $f = 1\%$, void aspect ratios $w_1 = w_2 = 3$ and void orientations $\mathbf{n}^{(1)} = \mathbf{e}^{(1)}$, $\mathbf{n}^{(2)} = \mathbf{e}^{(2)}$, $\mathbf{n}^{(3)} = \mathbf{e}^{(3)}$. Figure 6.5 presents various cross-sections of the effective gauge surfaces in the $\overline{\Sigma}_m - \overline{\Sigma}_{eq}$ plane in the case of creep exponents $n = (1, 10)$, for FCC and BCC single crystals, respectively. In the context of this figure, the MVAR predictions are in relatively good agreement with the FE results for both $n = (1, 10)$. In particular, for $n = 1$, the MVAR is in excellent agreement with the FE results except at purely hydrostatic loadings where an error in the order of 8% is observed. Nonetheless, in that case numerical convergence issues appeared and the FE results should be interpreted with caution. In turn, when $n = 10$, the MVAR exhibits very good qualitative agreement with the FE results where the corresponding gauge surface exhibits a rather significant "asymmetry" with respect to the $\overline{\Sigma}_{eq}$ axis but tends to underestimate this effect especially at small stress triaxialities (i.e., for $\overline{\Sigma}_m \sim 0$). This asymmetry, which is present in the case of ellipsoidal voids, is a direct consequence of the coupling between $\overline{\Sigma}_m$ and $\overline{\Sigma}_{eq}$ resulting from the complex form of the tensor $\widehat{\mathbf{S}}_0^*$ defined in equation 6.4. Such effects observed in shearing of ellipsoidal voids have also been addressed either in numerical micromechanical calculations (see for instance Tvergaard and Nielsen [2010]), or in multiaxial experiments (see Combaz et al. [2011]).

To summarize, the MVAR model has been assessed in great detail and it was found to be in good agreement with the corresponding FE results. Therefore, for simplicity and conciseness, MVAR estimates will be shown in a future section while later the MVAR model will be compared with existing models in the literature in the rate-independent limit.

6.2.4 Full field contours for periodic unit-cells

In order to have a better understanding on the differences between gauge surfaces for several crystal anisotropies (FCC, BCC, HCP), we present, next, contours of the
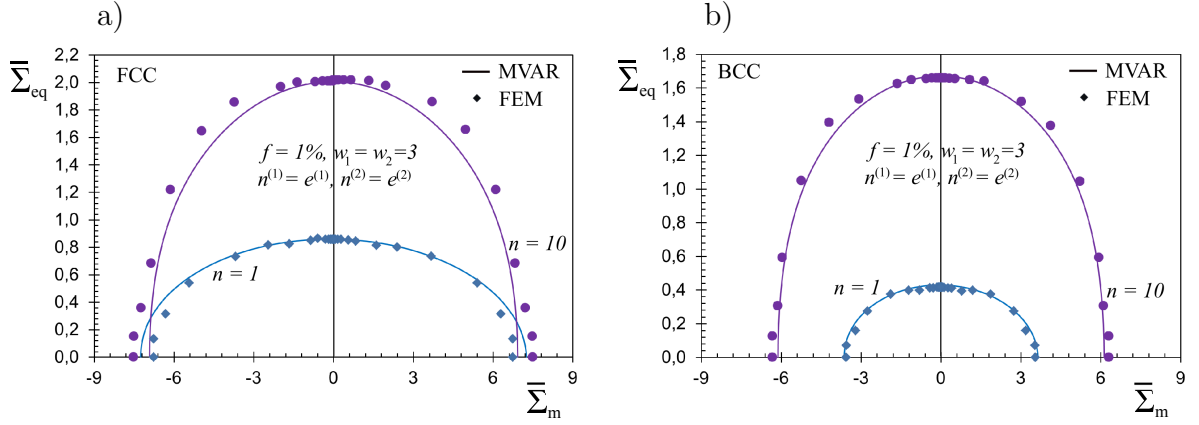
Figure 6.5: Gauge surfaces in the $\overline{\Sigma}_m - \overline{\Sigma}_{eq}$ plane for a porous single crystal comprising ellipsoidal voids of $f = 1\%$, void aspect ratios $w_1 = w_2 = 3$, void orientations $\mathbf{n}_{(1)} = \mathbf{e}_{(1)}$, $\mathbf{n}_{(2)} = \mathbf{e}_{(2)}$, $\mathbf{n}_{(3)} = \mathbf{e}_{(3)}$ and a range of creep exponent $n = (1, 10)$. Comparison between the model (MVAR) and the FE results in the cases of (a) FCC, (b) BCC.

maximum principal logarithmic strain, for spherical voids, a creep exponent $n = 5$, a porosity $f = 1\%$ and a triaxiality $X_\Sigma = 3$. As displayed in Fig. A.16, the strain amplitude is in most of the unit-cell regions lower in the case C_1 (see Table 6.3) with $K = 3$ HCP slip systems than in the FCC single crystal which is itself lower than in the BCC single crystal. These observations can explain at one hand the incompressible macroscopic response of the HCP porous single crystal, but on the other hand the fully compressible response of the BCC and FCC single crystals.

Moreover, we observe that pore interaction and deformation localization can becomes rather significant leading to several completely unloaded regions around a significant number of pores. This effect of strong field fluctuations is much less pronounced for higher number of slip systems $K = 48$ (BCC) as shown in Fig. A.16a. The observed deformation localization also explains why the MVAR model tends to underestimate effective response when compared with the FE results at increasing creep exponent n and increasing porosity f. Such effects have already been observed in porous materials with isotropic matrix and high nonlinearity (see for instance Idiart et al. [2006]). In view of this, more advanced models incorporating better description of these field fluctuations (see for instance Danas and Ponte Castañeda [2009a]) could possibly yield a better agreement with a cost of more complexity in the obtained model. In turn, one could calibrate the present MVAR model similar to the work of Cao et al. [2015]
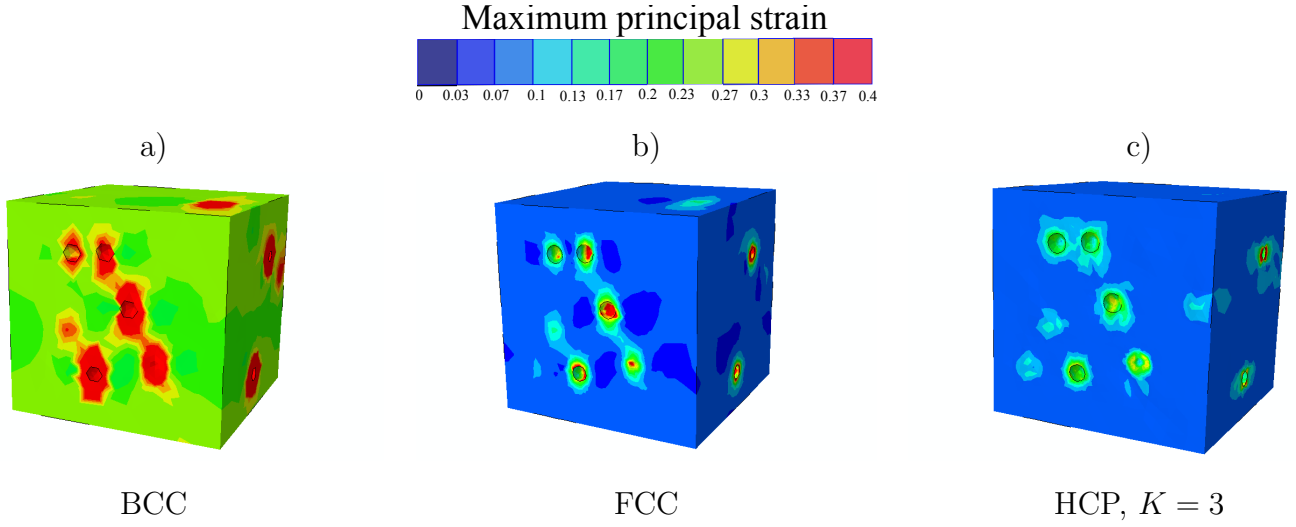
Figure 6.6: Contour of the maximum principal logarithmic strain for a porous single crystal with a "multipore" geometry, a creep exponent $n = 5$, a porosity $f = 1\%$ a triaxiality $X_\Sigma = 3$ and a Lode angle $\overline{\theta} = 0$. Case of (a) BCC (b) FCC and (c) HCP, $K = 3$.

retaining the simplicity. Such an attempt is done in Section 6.4.1, where it is shown that such calibration can increase the accuracy of the MVAR model at very high nonlinearities such as the rate-independent limit.

6.3 Results - II: Coupling between crystal anisotropy, void shape and orientation

In the previous sections, the MVAR model has been assessed in great detail and it was found to be in good agreement with the corresponding FE results. Hereafter, we will focus on MVAR estimates only and explore the effect of a large number of parameters including different loading states, nonlinearities and void orientations. The goal is to reveal the complex coupling between the crystal anisotropy (FCC, BCC, HCP), and the (morphological) void anisotropy resulting from the ellipsoidal void shape and orientation, using the MVAR model without insisting on quantitative aspects.

6.3.1 Effect of the crystal anisotropy

Fig. 6.7 shows gauge surfaces in the $\overline{\Sigma}_m - \overline{\Sigma}_{eq}$ plane of FCC and BCC porous single crystals with spherical voids ($w_1 = w_2 = 1$), a range of porosities $f = (1\%, 5\%, 10\%)$,

various creep exponents $n = 10$ and $n \to \infty$ (rate independent case). We observe a significant dependence of the average deviatoric response on the crystal anisotropy (FCC, BCC) either in the rate dependent ($n = 10$) or in the rate independent ($n \to \infty$) context. Rather interestingly, the hydrostatic point for BCC and FCC coincides in the case of rate-independent context ($n \longrightarrow \infty$) but such a feature is not preserved in the rate dependent regime (finite n values). This important result is of special interest to limit analysis approaches which are derived in the rate-independent limit and are extended to the rate-dependent limit in a heuristic manner.

Figure 6.7: Gauge surfaces in the $\overline{\Sigma}_m - \overline{\Sigma}_{eq}$ plane for porous FCC and BCC single crystals with spherical voids, a Lode angle $\overline{\theta} = 0$, various creep exponents $n = 10$ (continuous lines) and $n \to \infty$ (dashed lines). Cases of (a) $f = 1\%$, (b) $f = 5\%$.

The effect of matrix crystal anisotropy upon the effective response of the porous composite is discussed next. As already observed in the context of Fig. 6.4, where spherical voids are embedded in several HCP crystal structures, the average hydrostatic response is strongly influenced by the number and orientation of the slip systems. Specifically, both the MVAR model and the FE results predict that the effective behavior of a HCP porous single crystal with $K = 3$ three basal slip systems (i.e., highly anisotropic case C_1 in Table 6.3) leads to a completely incompressible response while it exhibits a compressible one for HCP porous crystals with $K = 6$ pyramidal Π_2 slip systems (case C_2 in Table 6.3) as well as with a combination of 3 basal, 3 prismatic and 6 pyramidal Π_2 slip systems (case C_3 in Table 6.3).

On the other hand, let us considers now, as shown in Fig. 6.8, gauge surfaces in a deviatoric $\overline{\Sigma}_{13} - \overline{\Sigma}_{23}$ plane of HCP (with $K = 3$ slip systems), FCC and BCC porous single crystals with spherical voids ($w_1 = w_2 = 1$), a porosity $f = 5\%$ and a
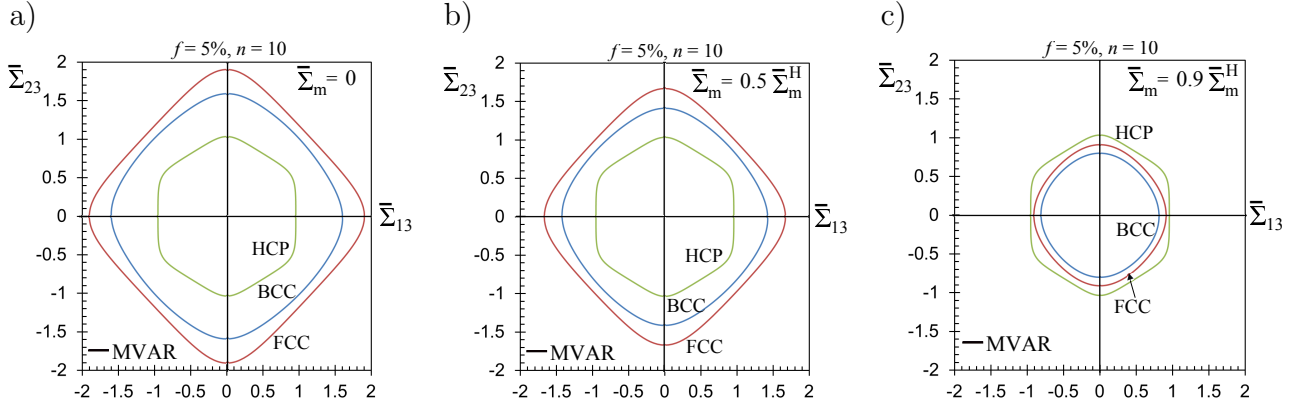
Figure 6.8: Gauge surfaces in the $\overline{\Sigma}_{13} - \overline{\Sigma}_{23}$ plane HCP (with $K = 3$ slip systems), FCC and BCC porous single crystals with spherical voids ($w_1 = w_2 = 1$), a Lode angle $\overline{\theta} = 0$, a porosity $f = 1\%$ and a creep exponent $n = 10$. Cases of (a) $\overline{\Sigma}_m = 0$, (b) $\overline{\Sigma}_m = \pm 0.5\overline{\Sigma}_m^H$, (c) $\overline{\Sigma}_m = \pm 0.9\overline{\Sigma}_m^H$, where $\overline{\Sigma}_m^H$ denotes the hydrostatic point.

creep exponent $n = 10$. The various cross-sections Fig. 6.8a, Fig. 6.8b and Fig. 6.8c correspond to different hydrostatic stresses $\overline{\Sigma}_m = 0$, $\overline{\Sigma}_m = \pm 0.5\overline{\Sigma}_m^H$ and $\overline{\Sigma}_m = \pm 0.9\overline{\Sigma}_m^H$, respectively, where $\overline{\Sigma}_m^H$ denotes the hydrostatic point delivered by the model MVAR for hydrostatic loading. We precise that we have set $\overline{\Sigma}_{12} = 0$. One of the main observation in this figure is the strong dependence of the average deviatoric response on the crystal anisotropy, in the context of cubic systems FCC and BCC. However, even more interestingly, in the porous HCP incompressible (with $K = 3$ slip systems) single crystals, the behavior does not evolve from Fig. 6.8a to Fig. 6.8c. Hence, while at lower hydrostatic stresses ($\left|\overline{\Sigma}_m\right| \leq 0.5\overline{\Sigma}_m^H$) the HCP porous crystal is more compliant than the FCC and BCC ones, as the pressure increases the FCC and BCC become gradually softer than the HCP.

At this point, it is perhaps helpful to summarize that in the context of highly anisotropic porous single crystals, the purely hydrostatic response is extremely sensitive to the number of the slip systems K as well as on the slip orientations, as clearly shown in Fig. 6.4, Fig. 6.7 and Fig. 6.8 but also confirmed with the FE results in the previous section. These observations have strong implications on void growth and final failure of such single porous crystals. Similar conclusions have also been made recently by Yerra et al. [2010] and Srivastava and Needleman [2015], where the combined effect of crystal orientation and loading directions can lead to the activation of a small or large number of slip systems and subsequently to moderate or significant void growth.

Such effects are physically included in the MVAR model as shown in this study.

Moreover, it is maybe relevant to make a first contact with the corresponding three-dimensional models proposed by Han et al. [2013] and Paux et al. [2015]. In these rate independent models, built for spherical voids,—which have been assessed for an FCC crystal—even though the deviatoric response includes the effect of the crystal anisotropy (i.e., number of slip systems and orientations), the corresponding response under purely hydrostatic stressing is independent of the number and orientation of the slip systems. Nonetheless, the present study shows that in the context of highly anisotropic porous single crystals, the purely hydrostatic response is extremely sensitive to the number of the slip systems K as well as on the slip orientations, as clearly shown in Fig. 6.4, Fig. 6.7 and Fig. 6.8 but also confirmed with the FE results in the previous section. Furthermore, detailed comparison with these models in the rate independent context are discussed in section 6.4.

6.3.2 Effect of the void shape and orientation

In this section, we discuss in more detail the effect of microstructure anisotropy upon the effective response of the porous composite. More precisely, Fig. 6.9 shows MVAR gauge surfaces in the $\overline{\Sigma}_m - \overline{\Sigma}_{eq}$ plane for a porous FCC single crystal and a creep exponent $n = 10$. The effect of porosity is investigated by choosing $f = (1\%, 5\%, 10\%)$ for different microstructures (a) $w_1 = w_2 = 1$ and (b) $w_1 = 5$, $w_2 = 0.2$, $\mathbf{n}^{(1)} = \mathbf{e}^{(1)}$, $\mathbf{n}^{(2)} = \mathbf{e}^{(2)}$. In Fig. 6.9, the gauge surfaces exhibit a gradual decrease with increasing porosity for both ellipsoidal ($w_1 = w_2 = 1$) and ellipsoidal ($w_1 = w_2^{-1} = 5$) voids, as already expected. Nevertheless, while for the case of spherical voids ($w_1 = w_2 = 1$), in Fig. 6.9a, the curves are symmetric with respect to the $\overline{\Sigma}_{eq}$ axis, the curves for the ellipsoidal voids ($w_1 = w_2^{-1} = 5$), in Fig. 6.9b, become asymmetric as already discussed in the context of Fig. 6.5. As a consequence of this asymmetry, the MVAR estimates are found to be stiffer in the negative pressure regime ($\overline{\Sigma}_m < 0$). The observed asymmetry becomes more pronounced with increasing porosity.

Figure 6.10 shows gauge surfaces in the $\overline{\Sigma}_m - \overline{\Sigma}_{eq}$ plane for a FCC porous single crystal and a creep exponent $n = 10$. The porosity of set to $f = 5\%$ and the void orientation is O_{11} (see Table 6.4). The effect of the void aspect ratios is investigated by choosing spherical voids ($w_1 = w_2 = 1$), prolate voids ($w_1 = w_2 = 5$), oblate voids
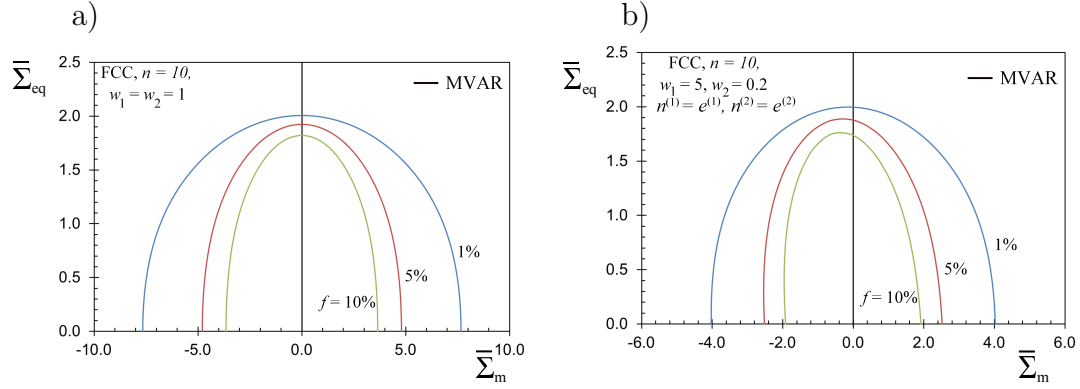
a)

b)

Figure 6.9: Gauge surfaces in the $\overline{\Sigma}_m - \overline{\Sigma}_{eq}$ plane for a FCC porous single crystal with ellipsoidal voids , a creep exponent $n = 10$ and a Lode angle $\overline{\theta} = 0$. The effect of porosity is investigated by choosing $f = (1\%, 5\%, 10\%)$ for different void shapes (a) $w_1 = w_2 = 1$ and (b) $w_1 = 5$, $w_2 = 0.2$, $\mathbf{n}^{(1)} = \mathbf{e}^{(1)}$, $\mathbf{n}^{(2)} = \mathbf{e}^{(2)}$.

$(w_1 = w_2 = 0.2)$ and arbitrary ellipsoidal voids $(w_1 = w_2^{-1} = 5$. The main observation here is that non-spherical void shapes have an important influence on the effective response of the porous single crystal. Indeed, the slopes of the gauge surfaces depend for instance strongly on the void shape. More specifically, a porous single crystal with ellipsoidal voids $(w_1 = w_2^{-1} = 5)$ is softer than that with oblate voids $(w_1 = w_2 = 0.2)$ in the full range of stress triaxialities whereas they exhibit closed maximum average Von Mises stress. Moreover, for the same value of porosity, non-spherical void shapes lead to a significantly more compliant response at high values of the mean stress, especially in the case of oblate and arbitrary ellipsoidal voids. $\overline{\Sigma}_m$ almost double from the considered ellipsoidal microstructures $(w_1 = w_2^{-1} = (0.2, 1, 5))$ to the spherical one $(w_1 = w_2 = 1)$. Moreover, it is evident from this figure that arbitrary ellipsoidal shapes $(w_1 = w_2^{-1} = 5)$ lead to very different responses when compared with spheroidal shapes $(w_1 = w_2 = 5$ or $w_1 = w_2 = 0.2)$.

Void Orientation	$\mathbf{n}^{(1)}$	$\mathbf{n}^{(2)}$	$\mathbf{n}^{(3)} = \mathbf{n}^{(1)} \times \mathbf{n}^{(2)}$
O_{11}	$[1, 0, 0]$	$[0, 1, 0]$	$[0, 0, 1]$
O_{12}	$[1, 0, \overline{1}]$	$[0, 1, 0]$	$[1, 0, 1]$
O_{13}	$[0, \overline{1}, 0]$	$[1, 0, 0]$	$[0, 0, 1]$

Table 6.4: Coordinates of the orientations O_{11}, O_{12}, O_{13} (section 6.3.2) in the reference laboratory frame axes $\mathbf{e}^{(i)}$, $i = 1, 2, 3$.
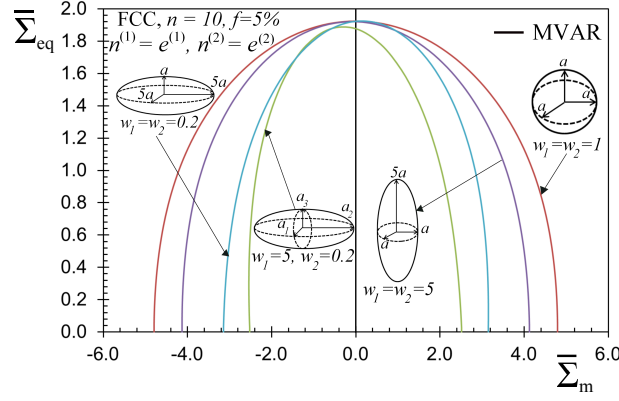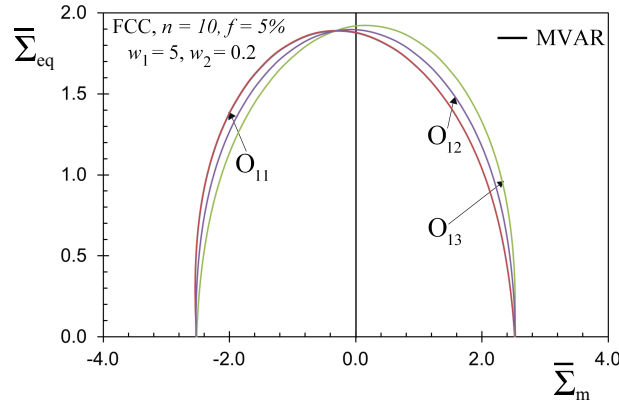
Figure 6.10: Gauge surfaces in the $\overline{\Sigma}_m - \overline{\Sigma}_{eq}$ plane for a FCC porous single crystal with ellipsoidal voids, a Lode angle $\overline{\theta} = 0$ and a creep exponent $n = 10$. The porosity of set to $f = 5\%$ and the void orientation is O_{11} of table 6.4. The effect of the void aspect ratios is investigated by choosing spherical voids $w_1 = w_2 = 1$, prolate voids $w_1 = w_2 = 5$, oblate voids $w_1 = w_2 = 0.2$ and ellipsoidal voids $w_1 = w_2^{-1} = 5$.

Figure 6.11: Gauge surfaces in the $\overline{\Sigma}_m - \overline{\Sigma}_{eq}$ plane for a FCC porous single crystal with ellipsoidal voids, a Lode angle $\overline{\theta} = 0$ and a creep exponent $n = 10$. The porosity of set to $f = 5\%$. The effect of the void orientation by choosing O_{11}, O_{12}, O_{13} of Table 6.4 for given aspect ratios $w_1 = w_2^{-1} = 5$.

Figure 6.11 shows gauge surfaces in the $\overline{\Sigma}_m - \overline{\Sigma}_{eq}$ plane for a FCC porous single crystal and a creep exponent $n = 10$. The porosity of set to $f = 5\%$. The effect of the void orientation is addressed by choosing O_{11}, O_{12}, O_{13} (see table 4) for given aspect ratios $w_1 = w_2^{-1} = w = 5$. Note that, as already expected from earlier studies (Danas and Ponte Castañeda [2009b]), the hydrostatic point for all these cases is independent of the void orientation. This is intuitively expected since the hydrostatic loading has no preferential direction (i.e., is isotropic). However, the entire behavior,

and in particular the asymmetry with respect to the $\overline{\Sigma}_{eq}$ axis is strongly influenced by the void orientation.

6.3.3   Coupling between crystal anisotropy and void shape and orientation

In this section, we investigate the effective response of the porous single crystal in the deviatoric plane $\overline{\Sigma}_{13} - \overline{\Sigma}_{23}$ for given hydrostatic stress $\overline{\Sigma}_m$. This allows to probe a more detailed response of the porous crystal and reveal in a more clear way the combined coupling between the anisotropy of the crystal and that induced by the void shape and orientation. For the sake of conciseness, in the following, we consider only porous FCC single crystal with porosity $f = 5\%$, void shape $w_1 = w_2^{-1} = 5$ and creep exponent $n = 10$. The several void orientations considered are summarized in Table 6.5. In addition, for simplicity, we have set $\overline{\Sigma}_{12} = 0$.

Orientation	$\mathbf{n}^{(1)}$	$\mathbf{n}^{(2)}$	$\mathbf{n}^{(3)} = \mathbf{n}^{(1)} \times \mathbf{n}^{(2)}$
O_{21}	$[1, 0, 0]$	$[0, 1, 0]$	$[0, 0, 1]$
O_{22}	$[1, 0, 1]$	$[0, 1, 0]$	$[1, 0, \bar{1}]$

Table 6.5: Coordinates of the orientations O_{21}, O_{22} (subsection 6.3.3) in the reference laboratory frame axes $\mathbf{e}^{(i)}$, $i = 1, 2, 3$.

In this connection, Fig. 6.12 shows MVAR cross-sections corresponding to different fixed overall hydrostatic stresses $\overline{\Sigma}_m = 0$, $\overline{\Sigma}_m = \pm 0.5 \overline{\Sigma}_m^H$, $\overline{\Sigma}_m = \pm 0.9 \overline{\Sigma}_m^H$, where $\overline{\Sigma}_m^H$ denotes the hydrostatic point of the MVAR model for each of the given cases in Fig. 6.12a,b, respectively.

More specifically, in Fig. 6.12a, which corresponds to void orientation O_{21} (voids aligned with the principal loading directions), we observe a gradual shrinking of the curves with increasing $\overline{\Sigma}_m$ as expected. At small values of $\overline{\Sigma}_m = 0$, the curve exhibits an almost discrete character which tends to become more rounded (convexify) with increasing $\overline{\Sigma}_m$. Note at this point that since the FCC porous crystal is considered to be rate-dependent (i.e., finite value of the creep exponent n), the corresponding effective response is strictly convex and the curves exhibit large but finite curvature areas (i.e., smooth vertices) leading to an almost tetragonal symmetry of the curves. When the voids are aligned with the principal loading directions (orientation O_{21}), the porous

crystal preserves the original deviatoric symmetries of the crystal matrix for all values of $\overline{\Sigma}_m$ considered. In particular, in this case the curve is fully symmetric with respect to the two axes $\overline{\Sigma}_{13}$ and $\overline{\Sigma}_{23}$.

By contrast, as shown in Fig. 6.12b, if one considers a non aligned ellipsoidal void oriented as in the case O_{22} in table 5, the corresponding MVAR curves exhibit an asymmetry with respect to the $\overline{\Sigma}_{13}$-axis, but still preserve the symmetry with respect to the $\overline{\Sigma}_{23}$ axis for $\overline{\Sigma}_m > 0$. Rather interestingly, the almost tetragonal symmetry still prevails for $\overline{\Sigma}_m = 0$. This response is a direct consequence of the geometric coupling of the crystal slip orientations and the void shape at finite hydrostatic stresses. Note further that point symmetry of the curves with respect to the global origin $(\overline{\Sigma}_{13}, \pm\overline{\Sigma}_{23}) = (0,0)$ and $\overline{\Sigma}_m = 0$ is still preserved. This is easily observed by noting the point symmetries between the continuous lines corresponding to $\overline{\Sigma}_m > 0$ and the dashed ones for $\overline{\Sigma}_m < 0$.

Figure 6.12: Gauge surfaces in the deviatoric plane $\overline{\Sigma}_{13} - \overline{\Sigma}_{23}$ for a FCC porous single crystal with porosity $f = 5\%$, a Lode angle $\overline{\theta} = 0$, void shape $w_1 = 1/w_2 = 5$ and creep exponent $n = 10$, at different level of pressure. The dashed line curves correspond to the negative pressure regime while the continuous one correspond to the positive pressure regime. Case of void orientation (a) O_{21}, (b) O_{22} of table 5.

Moreover, Fig. 6.13 displays gauge surfaces for the FCC and BCC porous single crystals in the Π-plane (or octahedral plane) corresponding to different fixed overall hydrostatic stresses $\overline{\Sigma}_m = 0$, $\overline{\Sigma}_m = \pm0.5\overline{\Sigma}_m^H$, $\overline{\Sigma}_m = \pm0.9\overline{\Sigma}_m^H$, where $\overline{\Sigma}_m^H$ denotes the

hydrostatic point of the MVAR model for each of the given cases in Fig. 6.12a,b,c,d, respectively. In these cases, a gradual shrinking of the curves appears while increasing $\overline{\Sigma}_m$, as expected. At small values of $\overline{\Sigma}_m = 0$, the curve exhibits a quasi discrete character which tends to become more rounded with increasing $\overline{\Sigma}_m$. In addition, the gauge surfaces exhibit full asymmetry for finite hydrostatic stresses $\overline{\Sigma}_m = 0$, but preserve the hexagonal symmetry for $\overline{\Sigma}_m \neq 0$. The observed asymmetry is much more pronounced at higher values of $\overline{\Sigma}_m$, which is consistent with similar studies in isotropic systems (see for instance Danas et al. [2008b]). Furthermore, it should be stressed that point symmetry of the curves with respect to the global origin and $\overline{\Sigma}_m = 0$ is still preserved if one compares the continuous ($\overline{\Sigma}_m \geq 0$) with the dashed lines ($\overline{\Sigma}_m \leq 0$).

6.4 Results: Calibration of the MVAR in rate-independent context and comparison with other models

In this section, we investigate the MVAR predictions in the special, albeit very important case, of the rate-independent porous single crystals by considering the limit of the rate sensitivity exponent $n \longrightarrow \infty$. Comparison with existing models in the literature (Han et al. [2013], Paux et al. [2015]) and FE calculations in the context of spherical voids is carried out. Supplementary results for ellipsoidal voids are also shown where the MVAR is compared with FEM. As stated earlier the MVAR gradually underestimates the gauge surface at large nonlinearities. This effect is mainly attributed to the inherent quadratic character of the MVAR model due to the LCC methodology used here, whereas studies in the context of isotropic porous materials have shown that a "cosh" (i.e., exponential) (see for instance the recent study of Cao et al. [2015]) dependence on pressure is more appropriate. However, even if the MVAR model is qualitatively and in most of the cases quantitatively quite accurate (up to $\sim 5\%$, as seen previously in other cases), the numerical results obtained with FEM in the rate-independent case exhibit a non elliptical shape of the yield surface (see for instance Han et al. [2013]). In order to get better quantitative agreement with the numerical results and still in the context of LCC methods, one needs either to use a more sophisticated approach such as the second-order method (see Ponte Castañeda [2002a,b], Danas et al. [2008a], Danas and Ponte Castañeda [2009a]), the fully numer-
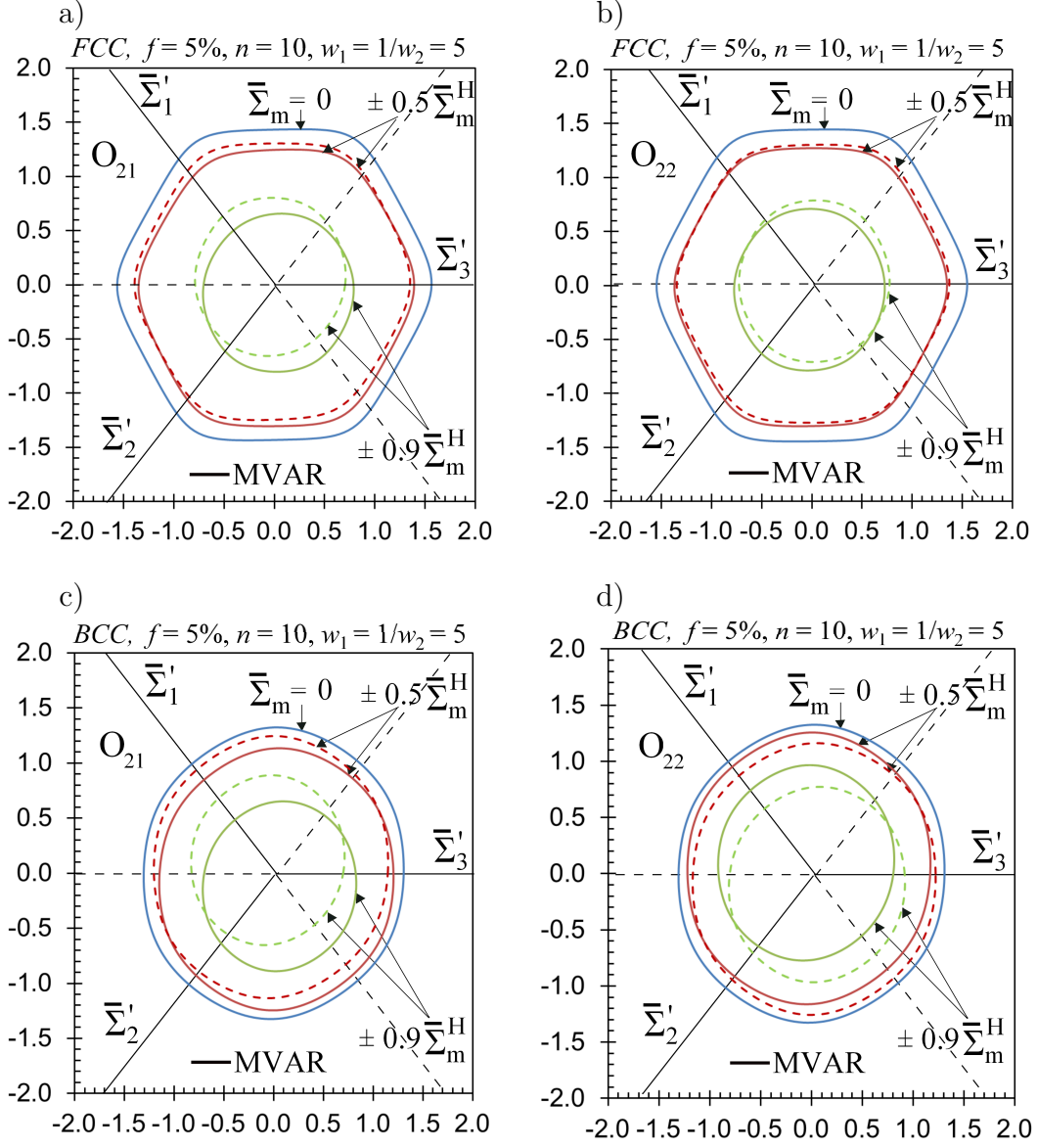
Figure 6.13: Gauge surfaces in the Π-plane (or octahedral plane) for FCC (a,b) and BCC (c,d) porous single crystal with porosity $f = 5\%$, a Lode angle $\overline{\theta} = 0$, void shape $w_1 = 1/w_2 = 5$ and creep exponent $n = 10$, at different level of pressure. The dashed line curves correspond to the negative pressure regime while the continuous one correspond to the positive pressure regime. Case of void orientation (a),(c) O_{21}, (b),(d) O_{22} of Table 6.5.

ical variational method (Idiart and Ponte Castañeda [2007]) and iterated variational methods (Agoras and Ponte Castañeda [2013]), or to calibrate the present model which is numerically much easier to be implemented. As will be shown in this section, the best calibration lies somewhere in between the quadratic and "cosh" terms.

6.4.1   Calibration of the MVAR

The MVAR predicts, as expected due to the LCC used in the optimization procedure, a quadratic response for the yield surface. In this regard and motivated by the works of Han et al. [2013], Paux et al. [2015] and Cao et al. [2015], we propose the following simple modification to the original quadratic estimate, which becomes

$$
\max_{s=1,K} \left\{ \left(\frac{\tau^{(s)}}{\tau_0^{(s)}} \right)^2 + \frac{f\,\alpha_2}{K\left(\tau_0^{(s)}\right)^2} \overline{\boldsymbol{\sigma}} \cdot \left(\widehat{\mathbf{S}}^* - \mathbf{J} \cdot \widehat{\mathbf{S}}^* \mathbf{J} \right) \cdot \overline{\boldsymbol{\sigma}} + \frac{5\,\alpha_1\,(1-f)^2}{2\,K\,(\ln f)^2 \left(\tau_0^{(s)}\right)^2} \overline{\boldsymbol{\sigma}} \cdot \mathbf{J} \cdot \widehat{\mathbf{S}}^* \mathbf{J} \cdot \overline{\boldsymbol{\sigma}} + \right.
$$

$$
\left. f\,(1-\alpha_1) \left[\cosh\left(\sqrt{\frac{5}{2\,K}} \frac{\cosh^{-1}\left(\frac{1-f+f^2}{f}\right)}{\ln f} \frac{\sqrt{\overline{\boldsymbol{\sigma}} \cdot \mathbf{J} \cdot \widehat{\mathbf{S}}^* \mathbf{J} \cdot \overline{\boldsymbol{\sigma}}}}{\tau_0^{(s)}} \right) - 1 \right] - (1-f)^2 \right\} = 0,
$$

(6.11)

where α_2 is a function of the porosity f weighting the relative contribution of the resolved shear stress on each slip system, whereas α_1 is a parameter introduced to interpolate the shape of the yield surface between an elliptical shape ($\alpha_1 = 1$, quadratic) and an exponential "cosh" shape ($\alpha_1 = 0$). Moreover, following the result of Ponte Castañeda [2002b] for dilute isotropic porous materials, $\alpha_2 \sim f^{-1/3}$ so that

$$
\frac{\widetilde{\tau}_0^{(s)}}{\tau_0^{(s)}} - 1 \sim 1.5\,(f/2)^{2/3}\,,
$$

(6.12)

in the dilute limit. The calibration procedure of the above defined coefficients α_1 and α_2 leads to the following values

$$
\alpha_1 = 0.65, \qquad \alpha_2 \cong 6\,f^{-1/3}
$$

(6.13)

It is perhaps interesting to note that the calibration procedure has led to a larger contribution of the original quadratic terms due to the LCC methodology (65%) than the "cosh" terms (35%). Moreover, the form of the yield criterion (6.11) is very similar to the well-known Gurson [1977] model, even though the analysis used here is rather different than the standard limit analysis proposed by the later author. Even so this last model can be thought as a generalization of the Gurson model in the context of porous single crystals and general ellipsoidal void shapes and orientations.

Finally, it should be mentioned that similar modifications as the one in (6.11) can also be done in the context of the rate-dependent porous single crystals. In those cases, α_1 becomes readily a function of the rate sensitivity exponent n since at $n = 1$

no correction is needed and thus $\alpha = 1$ in that case. Nonetheless, due to the fact that the original quadratic MVAR model exhibits good accuracy (max error of $\sim 5\%$) for exponents up to $n = 10$ such an attempt was not carried out for the rate-independent case in the present work.

In the next section, the MVAR will be compared with others models in the literature, more precisely those of Han et al. [2013] and Paux et al. [2015], developed for spherical voids in the rate independent context.

6.4.2 Comparison with other models

In this section, the above-described calibrated MVAR model is compared with the models of Han et al. [2013] and Paux et al. [2015], developed for spherical voids in the rate-independent context. In order to assess these models, numerical FE results with complex distribution of voids is used. It is important to precise that for FCC porous single crystals our FE results are quite similar to those obtained by Han et al. [2013] for an FCC crystal with a single-void cubic unit-cell (difference less than 1%) for relatively low porosity $f \leq 5\%$.

Figures 6.14, 6.15 and 6.16 show cross-sections of the effective yield surfaces in the $\overline{\Sigma}_m - \overline{\Sigma}_{eq}$ plane for all the different models. Various porosities $f = (1\%, 5\%)$ are considered for both FCC (Fig. 6.14 and Fig. 6.15) and BCC crystal structure (Fig. 6.16). In the context of these figures, we observe a very good agreement between the MVAR predictions and the FE results for the entire range of stress triaxialities. Similarly, Han et al. [2013] and Paux et al. [2015] models are also in very good agreement. In Fig. 6.15, the principal directions of the stress tensor are oriented along (a) [111] and (b) [210] contrary to most of the figures in the present study that are oriented along the [100] direction. For a more detailed description of this notation the reader is referred to the work of Han et al. [2013]. More specifically, for the loading [100] and [111], the MVAR model is in slightly better agreement than the models of Han et al. [2013] and Paux et al. [2015], whereas MVAR tends to slightly underestimate the effective response for the loading [210].

Next, we consider HCP porous single crystals comprising spherical voids with $K = 3, 6, 12$ slip systems. In the case where plastic slip occurs only in the so called basal planes, the slip systems are described by the crystallographic orienta-
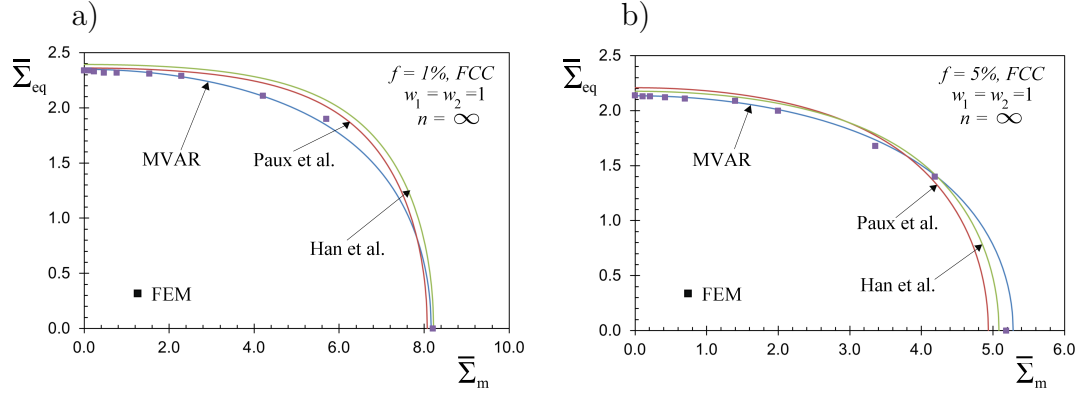
Figure 6.14: Yield surfaces in the $\overline{\Sigma}_m - \overline{\Sigma}_{eq}$ plane for a porous rate independent FCC single crystal comprising spherical voids. Comparison between MVAR model, Han et al. [2013] model, Paux et al. [2015] model and the FE results for a Lode angle $\overline{\theta} = 0$ and a porosity (a) $f = 1\%$, (b) $f = 5\%$.
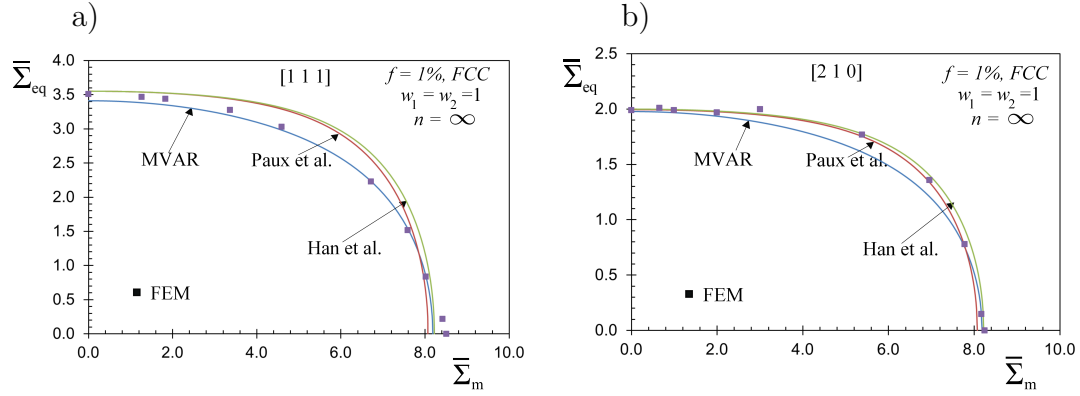

Figure 6.15: Yield surfaces in the $\overline{\Sigma}_m - \overline{\Sigma}_{eq}$ plane for a porous rate independent FCC single crystal comprising spherical voids and porosity $f = 1\%$. Comparison between MVAR model, Han et al. [2013] model, Paux et al. [2015] model and the FE results for Lode angle $\overline{\theta} = 0$ where the stress principal directions are oriented along (a) [111] and (b) [210]. The FE results are those in Han et al. [2013].

tions $\{0001\} \langle 1\overline{2}10 \rangle$ ($K = 3$ slip systems, see table 3). Then, the computation of the microstructural tensor leads to $\widehat{\mathbf{S}}^* = 0$, and the MVAR estimate (6.11) becomes incompressible, i.e.

$$\max_{s=1,K} \left\{ \left| \tau^{(s)} \right| - \tau_0^{(s)} (1 - f) \right\} = 0. \tag{6.14}$$

As already seen (see Fig. 6.4), this prediction is confirmed numerically by FE calculations. In turn, if one considers a crystalline structure with more slip systems such
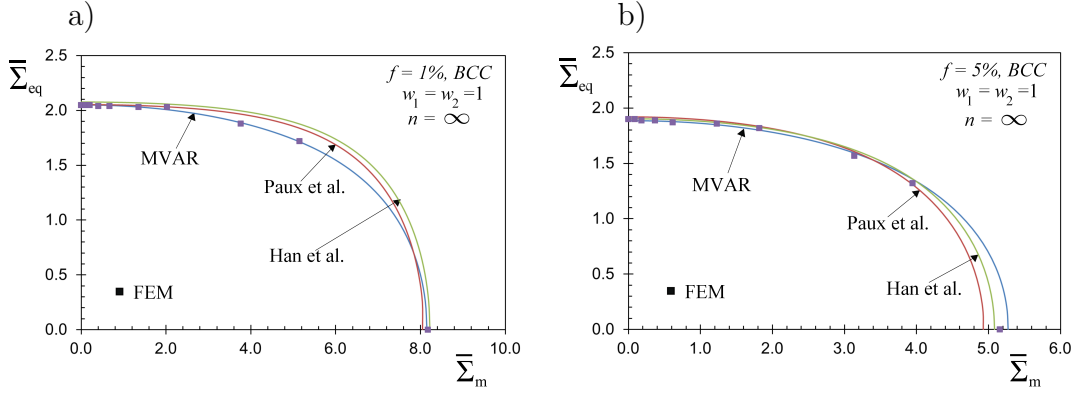
Figure 6.16: Yield surfaces in the $\overline{\Sigma}_m - \overline{\Sigma}_{eq}$ plane for a porous rate independent BCC single crystal comprising spherical voids. Comparison between MVAR model, Han et al. [2013] model, Paux et al. [2015] model and the FE results for a Lode angle $\overline{\theta} = 0$ and a porosity (a) $f = 1\%$, (b) $f = 5\%$.

as the case C_2 with $K = 6$ or case C_3 with $K = 12$ slip systems (see Table 6.3), the porous single crystal becomes compressible. In this context, as shown in Fig. 6.17, an excellent agreement between the MVAR predictions and the FE results for the entire range of stress triaxialities is obtained for both porosities $f = 1, 5\%$ used. This result shows clearly that the response at a highly anisotropic porous single crystal is strongly dependent on *both* the number and the orientation of the slip systems, especially at large hydrostatic stressing. It further suggests that for such low symmetry crystals certain directions appear as "rigid" to plastic deformation thus constrain slip under highly symmetric loads such as purely hydrostatic tension or compression. As a consequence very weak (or even no) void growth is expected in such a case.

At this point it should be mentioned that the models of Han et al. [2013] and Paux et al. [2015] have only been calibrated for FCC crystals and therefore at their present form exhibit no such qualitative feature. Indeed, as shown in Fig. 6.18, an excellent agreement between the MVAR predictions and the FE results for the entire range of stress triaxialities is obtained while such models (Han et al. [2013], Paux et al. [2015]) seems to predict compessibility in the context of strong anisotropy, i.e. low number of slip systems (see for instance Fig. 6.18a,d).

Furthermore, Fig. 6.19 displays MVAR, Han et al. [2013] model, Paux et al. [2015] model predictions of gauge surfaces in the Π-plane (or octahedral plane) for a FCC rate independent porous single crystals with spherical voids corresponding to different fixed
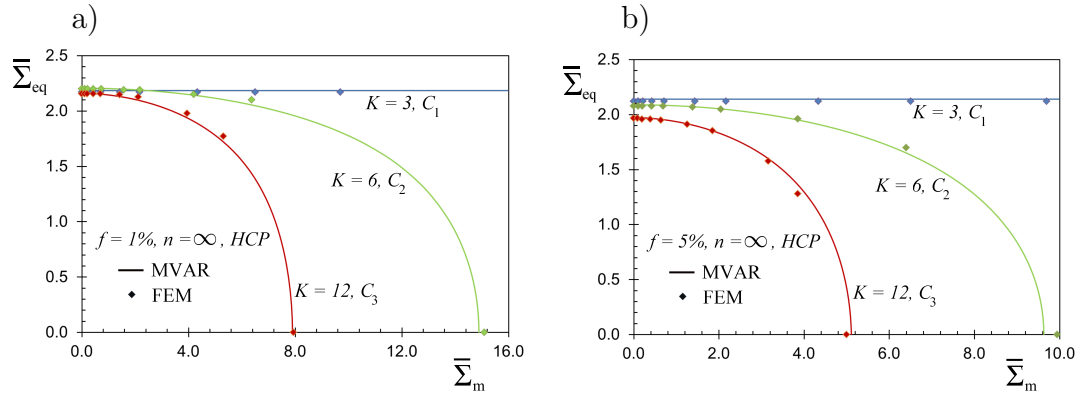
Figure 6.17: Yield surfaces in the $\overline{\Sigma}_m - \overline{\Sigma}_{eq}$ plane for a porous rate independent HCP single crystal comprising spherical voids with $K = 3, 6, 12$ slip systems. Comparison between MVAR model and the FE results for a Lode angle $\overline{\theta} = 0$ and a porosity (a) $f = 1\%$, (b) $f = 5\%$.
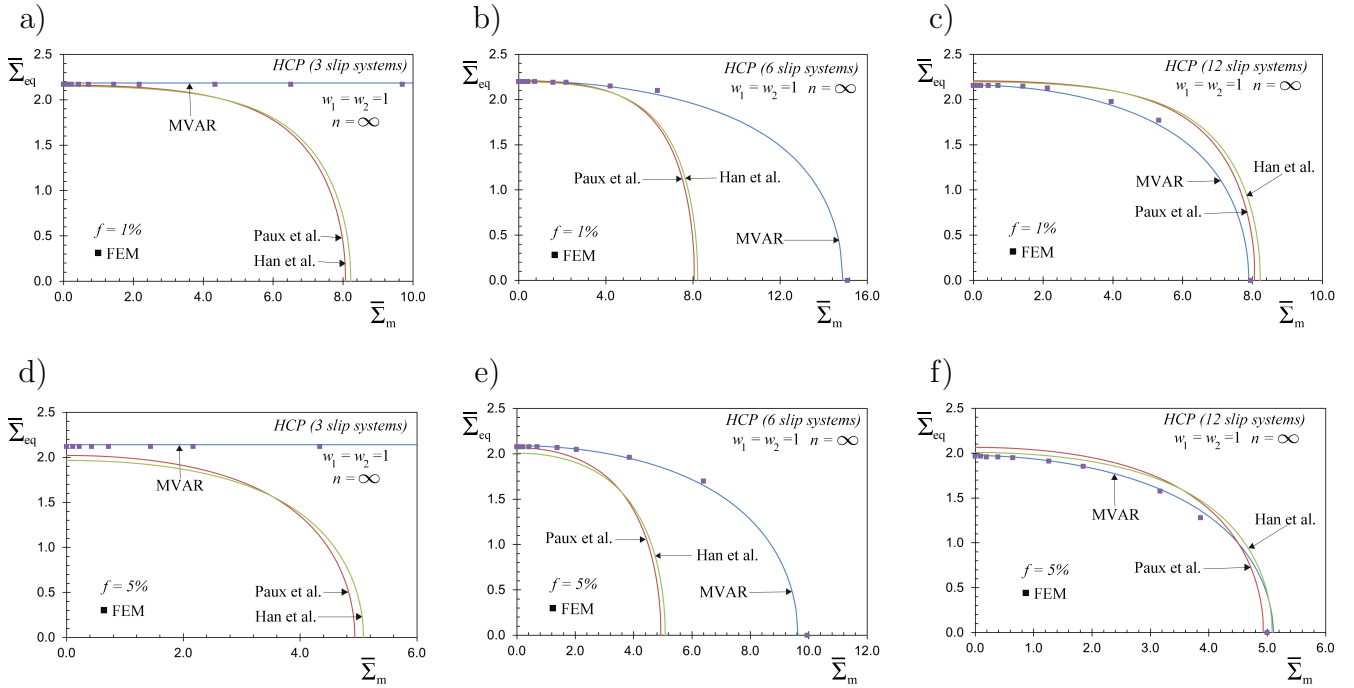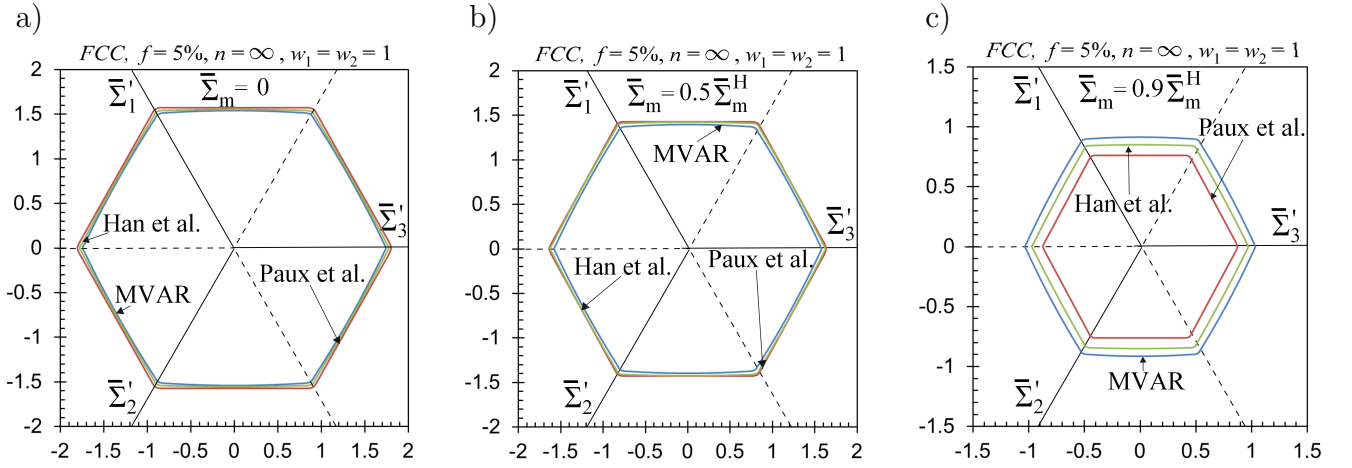

Figure 6.18: Gauge surfaces in the $\overline{\Sigma}_m - \overline{\Sigma}_{eq}$ plane for a porous rate independent HCP single crystal comprising spherical voids. Comparison between MVAR model, Han et al. [2013] model, Paux et al. [2015] model and the FE results for a Lode angle $\overline{\theta} = 0$ in the context of (a) $K = 3$, $f = 1\%$, (b) $K = 6$, $f = 1\%$, (c) $K = 12$, $f = 1\%$, (d) $K = 3$, $f = 5\%$, (e) $K = 6$, $f = 5\%$, (f) $K = 12$, $f = 5\%$,.

overall hydrostatic stresses $\overline{\Sigma}_m = 0$, $\overline{\Sigma}_m = 0.5\overline{\Sigma}_m^H$, $\overline{\Sigma}_m = 0.9\overline{\Sigma}_m^H$, where $\overline{\Sigma}_m^H$ denotes the hydrostatic point of the MVAR model. In these cases, it is important to observe that in the rate independent context, the gauge surfaces exhibit corners in all the considered models, even with the presence of voids and at high pressure (see Fig. 6.19b,c) in the single crystal. Such feature, which is not the case for general viscoplastic case (see for instance Fig. 6.13), seems to appear as a limitation of the modeling approaches used.

Figure 6.19: MVAR, Han et al. [2013] model, Paux et al. [2015] model predictions of gauge surfaces in the Π-plane (or octahedral plane) for a FCC rate independent porous single crystals with spherical voids ($w_1 = w_2 = 1$), a Lode angle $\overline{\theta} = 0$ and a porosity $f = 5\%$. Cases of (a) $\overline{\Sigma}_m = 0$, (b) $\overline{\Sigma}_m = 0.5\overline{\Sigma}_m^H$, (c) $\overline{\Sigma}_m = 0.9\overline{\Sigma}_m^H$, where $\overline{\Sigma}_m^H$ denotes the hydrostatic point.

Finally, in Fig.6.20, we show FE results and MVAR predictions for rate-independent porous single crystals comprising ellipsoidal voids, i.e., with aspect ratios $w_1 \neq 1$ and $w_2 \neq 1$. The microstructures considered are defined by porosity $f = 1\%$, void orientations $\mathbf{n}^{(1)} = \mathbf{e}^{(1)}$, $\mathbf{n}^{(2)} = \mathbf{e}^{(2)}$, $\mathbf{n}^{(3)} = \mathbf{e}^{(3)}$ and a range of void aspect ratios $w_1 = w_2 = (1, 2, 3, 4)$ (prolate voids). Figure 6.20a and Fig. 6.20b present various effective yield surfaces in the $\overline{\Sigma}_m - \overline{\Sigma}_{eq}$ plane for FCC and BCC single crystals, respectively. In the context of these figures, the MVAR predictions are in very good agreement with the FE results for several crystal anisotropy types (BCC and FCC) and microstructure anisotropy. The yield surfaces exhibit as expected a rather significant "asymmetry" with respect to the $\overline{\Sigma}_{eq}$ axis. This asymmetry, which is strongly sensitive upon the microstructure, is a direct consequence of the coupling between $\overline{\Sigma}_m$
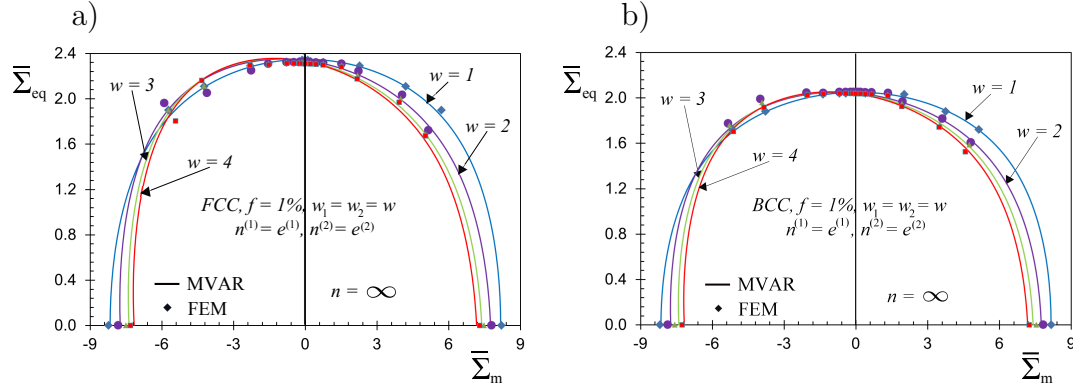
Figure 6.20: Yield surfaces in the $\overline{\Sigma}_m - \overline{\Sigma}_{eq}$ plane for a porous rate independent single crystal comprising ellipsoidal voids of $f = 1\%$, a Lode angle $\overline{\theta} = 0$, void orientations $\mathbf{n}_{(1)} = \mathbf{e}_{(1)}$, $\mathbf{n}_{(2)} = \mathbf{e}_{(2)}$, $\mathbf{n}_{(3)} = \mathbf{e}_{(3)}$, and a range of void aspect ratios $w_1 = w_2 = (1, 2, 3, 4)$. Comparison between the model (MVAR) and the FE results in the cases of (a) FCC, (b) BCC.

and $\overline{\Sigma}_{eq}$ resulting from the complex form of the tensor $\hat{\mathbf{S}}_0^*$ defined in equation (6.4). Furthermore, it is interesting to notice that in the positive pressure regime ($\overline{\Sigma}_m \geq 0$) the effective response is more softer when the void is more prolate, i.e. when $w_1 = w_2$ increases. In this case, the MVAR model is less accurate in qualitative terms even if qualitatively it exhibits the correct trends.

6.5   Concluding remarks

In this chapter, an analytical constitutive model has been presented for porous rate-dependent single crystals comprising ellipsoidal voids, subjected to general loading conditions, accounting for full crystal anisotropy. The modified variational (MVAR) model presented in this study has been validated by comparison with full field FE calculations of single- and multi-void periodic unit-cells. It has been found to be in good agreement with the FE results for a very wide range of parameters describing the number and orientation of the slip systems (i.e., crystal anisotropy), the creep exponent (i.e., nonlinearity) of the matrix crystal, the porosity and the void shapes and orientations. The MVAR model has shown strong predictive capabilities while exhibiting critical qualitative features.

More specifically, the MVAR model has been able to predict the strong dependence of the effective response, and especially of the average hydrostatic stress upon

the number and orientation of the slip systems as well as the shape and orientation of the voids. One of the major finding of this work, is that for highly anisotropic crystals (e.g., three basal active slip systems in certain HCP crystal structure) the porous crystal can exhibit fully incompressible response, even in the presence of voids. This of course affects the entire effective response of the porous crystal for the entire range of stress states. That is the first time such a result is presented in the literature and reveals the significance of plastic anisotropy of the underlying phases upon the macroscopic response of the material. Furthermore, it has been shown that the void shape and orientation affect strongly the response of the porous crystal. In particular, the effective response becomes much softer as one goes from a spherical void to an ellipsoidal one (which is suggestive of a crack-type geometry). In the general case of ellipsoidal voids arbitrary oriented (with respect to the laboratory axes) and arbitrary crystal structure, we have shown that the effective response exhibits no symmetries when plotted in a purely deviatoric plane (and at finite hydrostatic stresses) thus indicating the non-trivial coupling between the anisotropy of the underlying crystal and the (morphological) anisotropy induced by the shape and orientation of the voids. In addition, it has been found that the creep exponent has a very strong influence on the effective response of the porous single crystal. Since a large number of technological applications (e.g., single crystals in aerospace industry as well as polycrystalline alloys in nuclear reactors) involve high-temperature and rate-dependent conditions, the MVAR model exhibits promising features that could be important in dealing with such problems.

Furthermore, the present model has been assessed to a large extent with robust periodic unit-cell calculations and for a wide range of parameters (different crystal structures i.e. FCC, BCC, HCP, void shapes and orientations, creep exponents and porosity values), exhibiting good agrement without any calibration parameters. In addition, a simple way of calibrating the MVAR with just two adjustable parameters is depicted in the rate-independent context so that an excellent agreement with respect to the numerical results is obtained. This calibration procedure can, in the future (if needed), be extended to the rate-dependent case in a straightforward manner. But such an attempt has not been pursued here since the difference between the MVAR estimates and the FE results was found to no more than $\sim 5\%$ in the worst case studied (i.e., creep exponent $n = 10$). On the other hand. it should be mentioned that

the results shown in the present study, albeit very extensive, do not cover the entire space of loadings and slip orientations as this would make the study extremely long. Hence, the present model should be considered with caution if used in a range of loads or slip system configurations that are very different from those assessed in the present study.

In view of this, it should be mentioned that several important features present mainly at finite strains, such as lattice rotations, evolution of porosity (e.g., void growth), void shape and orientation are not included in the present analysis (*c.f.* Danas and Ponte Castañeda [2009b], Danas and Aravas [2012]). These additional features would inevitably lead to well known phenomena in porous materials such as material softening, void shape effects, deformation localization (*c.f.* Danas and Ponte Castañeda [2012] and Danas and Aravas [2012]) and ultimately void coalescence (see for instance (Benzerga [2002], Pardoen and Hutchinson [2000], Yerra et al. [2010], Morin et al. [2015])). In this regard then, the microstructure evolution will be included in the next chapter. We are confident that the present model can be readily extended to deal with the aforementioned issues in a straightforward manner while still being able to account for crystal anisotropy, anisotropic microstructures and general loading conditions.

Chapter 7

Particular case of infinte number of slip systems: A porous Tresca model

The large majority of available theories in ductile damage growth have been carried out in the context of two-phase material systems comprising an isotropic rate-(in)dependent von Mises matrix phase and a voided phase (pores of spherical, spheroidal or arbitrary ellipsoidal shapes). In general, these studies use either limit analysis (see for instance Tvergaard and Needleman [1984], Gologanu and Leblond [1993], Leblond et al. [1994], Monchiet et al. [2007]) based on (Gurson [1977]) pioneering work, or a variational homogenization theory using the idea of a linear comparison composite (see for instance Ponte Castañeda [1991a], deBotton and Ponte Castañeda [1995], Danas and Ponte Castañeda [2009a]).

Nevertheless, as discussed in Drucker [1949], for most isotropic metals the yield surface is between the Von Mises and the Tresca one's. In addition, the yield Tresca criterion is supported by more physical basis since it is the limiting case on infinte number of slip systems of the Schmid law describing slip at single crystal level. Hence, an important question is the understanding of the overall mechanical response of porous solids with Tresca matrix, i.e. exhibiting a J_2 and a third invariant dependence, and a morphological anisotropy induced by the shape and orientation of the voids.

Nonetheless, there have been only very few models for porous plastic Tresca materials in the literature. These studies involve the study of rate-independent metals containing spherical voids under axisymmetric (Cazacu et al. [2014b]) or general loading conditions (Revil-Baudard and Cazacu [2014]). While each one of these studies

has its own significant contribution to the understanding of the effective response of porous plastic Tresca materials none of them is general enough in the sense of arbitrary void shapes and orientations and general loading conditions.

Then, the scope of the present chapter is to develop a three-dimensional model that is able to deal with Tresca matrix, arbitrary ellipsoidal void shapes and general loading conditions. The model would be derived from the porous single crystal model by considering the limiting case on infinte number of slip systems.

7.1   General expressions

Before proceeding to the discussion of the results, it is useful to present first analytical expressions for the evaluation of the effective stress potential delivered by the "MVAR" method.

Figure 7.1: Representative volume element (b) constituted of representative ellipsoidal voids (c) embedded in a Tresca plastic matrix (a).

In order to achieve this goal, let us first discuss about the constitutive behavior of the constituents. The matrix phase is an isotropic plastic material obeying to the Tresca yield criterion. Thus, the onset of plastic deformation occurs when the maximum shear stress over all planes reaches a certain critical value, as described with the following relation

$$\max_{i,j} |\sigma_i - \sigma_j| = \sigma_0, \tag{7.1}$$

where $\sigma_i, \forall i = 1, 2, 3$ and σ_0 denote respectively the Cauchy principal stresses and the uniaxial yield in tension.

It is useful to recall at this point that the Tresca yield criterion is a particular case of the Schmid yield criterion, when all the slip systems have the same critical resolved

shear stress CRSS, and their number tends to infinite. This remark will be of major importance in the further developments.

Furthermore, we will make use of the general, nonlinear homogenization methods developed by Ponte Castañeda [1991a, 2002a], which are based on the construction of a linear comparison composite (LCC) with the same microstructure as the nonlinear composite. Using this suitably designed variational principle, it is shown in chapter 2 that a modified variational estimate of the effective viscoplastic stress potential of a general crystalline porous material can be defined such that

$$
\widetilde{U}_{mvar}\left(\overline{\boldsymbol{\sigma}}\right) = (1-f)\sum_{s=1}^{K} \frac{\dot{\gamma}_0^{(s)}\tau_0^{(s)}}{n+1}\left(\frac{\sqrt{\overline{\boldsymbol{\sigma}}\cdot\widehat{\mathbf{S}}^{(s)}\cdot\overline{\boldsymbol{\sigma}}}}{\tau_0^{(s)}(1-f)}\right)^{n+1}, \tag{7.2}
$$

with

$$
\widehat{\mathbf{S}}^{(s)} \equiv \widehat{\mathbf{S}}^{mvar,(s)} = \widehat{\mathbf{S}}^{var,(s)} + \left(q_J^2 - 1\right)\mathbf{J}\cdot\widehat{\mathbf{S}}^{var,(s)}\cdot\mathbf{J}, \tag{7.3}
$$

$$
\widehat{\mathbf{S}}^{var,(s)} = \boldsymbol{\mu}^{(s)}\otimes\boldsymbol{\mu}^{(s)} + \frac{f}{K}\widehat{\mathbf{S}}^{*}, \ \forall s = 1, K, \tag{7.4}
$$

where $n \geq 1$, K, $\dot{\gamma}_0^{(s)}$, $\tau_0^{(s)}$ and $\boldsymbol{\mu}^{(s)}$ denote the creep exponent, the number of slip systems, the reference slip-rate, the reference flow stress (also denoted critical resolved shear stress CRSS) and the second-order Schmid tensor of the sth slip system, respectively. In addition, $\widehat{\mathbf{S}}^{*}$ is a microstructural tensor related to the Eshelby tensor $\mathbf{P}$ (Eshelby [1957]) through the relations

$$
\widehat{\mathbf{S}}^{*} = \lambda\lim_{\rho^{(s)},\kappa\to\infty}\mathbf{Q}^{-1} - \sum_{s=1}^{K}\boldsymbol{\mu}^{(s)}\otimes\boldsymbol{\mu}^{(s)}, \qquad \text{with} \quad \mathbf{Q} = \mathbf{S}^{-1} - \mathbf{S}^{-1}\mathbf{P}\mathbf{S}^{-1}. \tag{7.5}
$$

In addition, as recalled in the previous subsection, the Tresca yield criterion can be seen as a single crystal criterion consisting of infinte number of slip systems with equal CRSS $\tau_0^{(s)} = \tau_0$. Hence, in the limit cases $K \longrightarrow \infty$ (Tresca matrix) and $n \longrightarrow \infty$ (rate-independent plasticity), the relation (7.2) reduces to

$$
\max_{s=1,K}\left\{\left(\frac{\overline{\tau}^{(s)}}{\tau_0}\right)^2 + \frac{f}{\tau_0^2}\overline{\boldsymbol{\sigma}}\cdot\left(\widehat{\mathbf{S}}^{*}_{lim} - \mathbf{J}\cdot\widehat{\mathbf{S}}^{*}_{lim}\mathbf{J}\right)\cdot\overline{\boldsymbol{\sigma}} + \frac{f\,q_J^2}{\tau_0^2}\overline{\boldsymbol{\sigma}}\cdot\mathbf{J}\cdot\widehat{\mathbf{S}}^{*}_{lim}\mathbf{J}\cdot\overline{\boldsymbol{\sigma}} - (1-f)^2\right\} = 0,
$$
$$\tag{7.6}$$

where the fourth order tensor $\widehat{\mathbf{S}}^{*}_{lim}$ is defined as

$$
\widehat{\mathbf{S}}^{*}_{lim} = \lim_{K\to\infty}\lim_{\rho\to\infty}\lim_{\kappa\to\infty}\frac{\widehat{\mathbf{S}}^{*}}{K} \cong \frac{1}{5}\widehat{\mathbf{S}}^{*}_{Mises} = \frac{1}{5}\widehat{\mathbf{S}}^{*}, \tag{7.7}
$$

where $\widehat{\mathbf{S}}^*_{Mises} \equiv \widehat{\mathbf{S}}^*$ denotes the microstructural tensor associated to the compliance tensor of a Von Mises matrix, as shown in appendix 2.9 of chapter 2.

Moreover, by introducing in equation (7.6) the following relations

$$\max_{s=1,K} \left| \overline{\tau}^{(s)} \right| = \frac{\max_{i,j} \left| \overline{\sigma}_i - \overline{\sigma}_j \right|}{2}, \quad \tau_0 = \frac{\sigma_0}{2}, \quad \sigma_0 \equiv \textit{uniaxial yield in tension} \qquad (7.8)$$

together with the following expression of q_J that leads to recover the closed form of the hydrostatic limit of the effective behavior of composite spherical assemblages CSA (Hashin [1962], Gurson [1977], Leblond et al. [1994]), i.e.

$$q_J = \sqrt{\frac{15}{4f}} \, \frac{1-f}{\ln(1/f)}, \qquad (7.9)$$

one gets a homogenization based yield criterion for a plastic Tresca material with ellipsoidal voids, so-called "MVAR" model,

$$\frac{\left(\max_{i,j} \left| \overline{\sigma}_i - \overline{\sigma}_j \right|\right)^2}{\sigma_0^2} + \frac{4\,f}{5\,\sigma_0^2} \overline{\boldsymbol{\sigma}} \cdot \left(\widehat{\mathbf{S}}^* - \mathbf{J} \cdot \widehat{\mathbf{S}}^* \mathbf{J} \right) \cdot \overline{\boldsymbol{\sigma}} + \frac{3\,(1-f)^2}{(\sigma_0\,\ln f)^2} \overline{\boldsymbol{\sigma}} \cdot \mathbf{J} \cdot \widehat{\mathbf{S}}^* \mathbf{J} \cdot \overline{\boldsymbol{\sigma}} = (1-f)^2 \qquad (7.10)$$

with $\overline{\sigma}_i, \forall i = 1, 2, 3$, σ_0 and $\widehat{\mathbf{S}}^*$ denoting respectively the average principal stresses, the uniaxial yield in tension and the microstructural tensor associated to an isotropic Von Mises matrix.

In the particular case of spherical voids,

$$\widehat{\mathbf{S}}^* = \frac{1}{3}\mathbf{K} + \frac{1}{4}\mathbf{J}, \qquad (7.11)$$

and consequently the "MVAR" model is reduced to

$$\frac{\left(\max_{i,j} \left| \overline{\sigma}_i - \overline{\sigma}_j \right|\right)^2}{\sigma_0^2} + \frac{8\,f}{45\,\sigma_0^2} \overline{\sigma}_{eq}^2 + \frac{9\,(1-f)^2}{(2\,\sigma_0\,\ln f)^2} \overline{\sigma}_m^2 = (1-f)^2 \qquad (7.12)$$

However, in the general context of ellipsoidal voids, a numerical computation is necessary, which can be performed following similar framework than several authors (Aravas and Ponte Castañeda [2004], Danas [2008]).

7.2 Results: Assessment of the MVAR via FE simulations

This section presents results for the instantaneous effective behavior of the rate-independent porous Tresca material comprising voids with spherical and non-spherical

shape, as predicted by the modified variational model (MVAR) proposed in this work. Next, the predictions of the yield surface obtained using the MVAR are compared with the FE simulations described in chapter 4. The effect of the void shape on the resulting yield surface will ba particularly analyzed. Moreover, in the case of axisymmetric loadings, results will also be compared with predictions proposed by Cazacu et al. [2014b] model.

7.2.1 Isotropic microstructures

The Fig. 7.2 displays yield surfaces for spherical voids (i.e., $w_1 = w_2 = 1$) as predicted by the FE simulations, the modified variational model (MVAR), the Cazacu et al. [2014b] model, for four different porosities $f = (0.1, 1, 2\,4)\,\%$ and both axisymmetric (Lode angle $\theta = 0^o, 60^o$) and non axisymmetric loadings conditions ($\theta = 30^o$). The agreement between the MVAR and the FE calculations is satisfactory for a large range of porosities and for full loading conditions (stress triaxiality, Lode angle). The largest difference between the MVAR and the FE is found for larger porosities ($f = 4\%$). In the axisymmetric configuration, when the Cazacu et al. [2014b] model is also tested, we remark that the predictions coincide at deviatoric loadings, i.e. $\overline{\sigma}_m = 0$. In addition, the MVAR gives a significantly softer prediction when $\overline{\sigma}_m$ increases. In the purely hydrostatic limit, i.e. $\overline{\sigma}_{eq} = 0$, the MVAR model attains the analytical spherical shell solution and coincides with the Cazacu et al. [2014b] model.

At this point, it is worth noting for axisymmetric loadings, the Cazacu et al. [2014b] yield surface is not symmetric with respect to the $\overline{\sigma}_m = 0$ vertical axis. This implies that the plastic Tresca strain-rate corresponding to the normal of the yield surface for a purely deviatoric part exhibits an hydrostatic part, as already discussed in Danas et al. [2008a], Cazacu et al. [2014b]. This is attributed to the fact that the isotropic Cazacu et al. [2014b] yield surface exhibits a very specific coupling between first and the third invariant, i.e., mean stress and Lode angle. Such dependence, also confirmed by the FE simulations, is not addressed in the more accurate MVAR model, where the "porous additional term" has a quadratic stress character and hence depend only on the first two invariants, the mean stress $\overline{\sigma}_m$ and the Von Mises stress $\overline{\sigma}_{eq}$. Nonetheless, the dependence of the yield surface upon the third invariant of the stress is rather negligible, especially for small porosities and, as will be discussed later in this section,
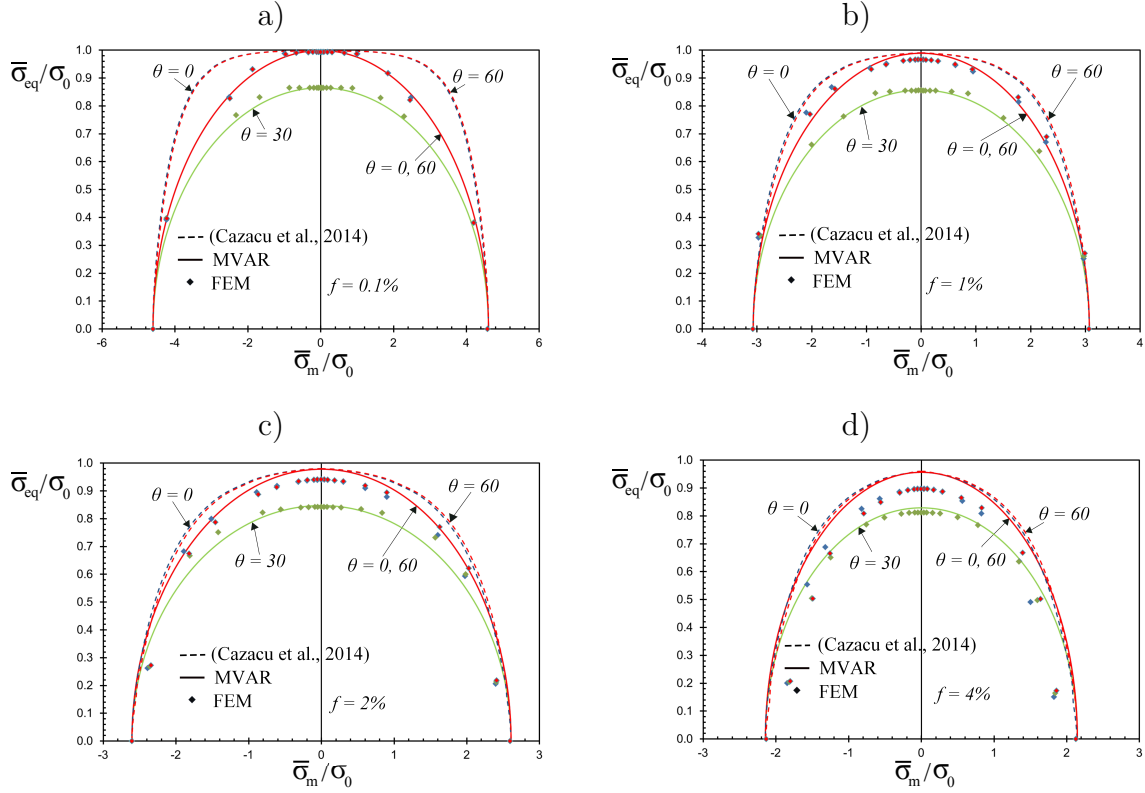
Figure 7.2: Yield surfaces in the $\overline{\sigma}_m - \overline{\sigma}_{eq}$ plane for isotropic microstructures, i.e. spherical voids $w_1 = w_2 = 1$. Comparison between the FE simulations and the modified variational MVAR for three Lode angles $\theta = 0^o, 30^o, 60^o$ and various porosities (a) $f = 0.1\%$, (b) $f = 1\%$, (c) $f = 2\%$, (d) $f = 4\%$.

it is of minor importance when compared to the corresponding void shape effects at a given level of porosity.

In addition, the fig. 7.3 shows yield surfaces for spherical voids ($w_1 = w_2 = 1$) as predicted by the FE simulations, the MVAR-Tresca porous model and the MVAR-Von Mises porous model (Danas and Aravas [2012]) for the porosity $f = 1, \%$ and both axisymmetric ($\theta = 0^o$) and non axisymmetric loadings conditions ($\theta = 30^o$).

Let us first consider the axisymmetric configuration, $\theta = 0^o$. The MVAR-Von Mises yield surface is as expected closer to the MVAR-Tresca yield surface as the Von Mises model is not dependent on the third invariant. Moreover, in the intermediate stress triaxiality region, when $1 < |X_\Sigma| < 3$, a significant difference between FE simulations and MVAR-Von Mises porous model is observed while there is a good agrement between the MVAR-Tresca porous model and the FE in the full range of

stress triaxiality. Indeed, the porous Von Mises material has a non quadratic effective behavior for relative small porosities, which thus cannot be well captured by the MVAR method.
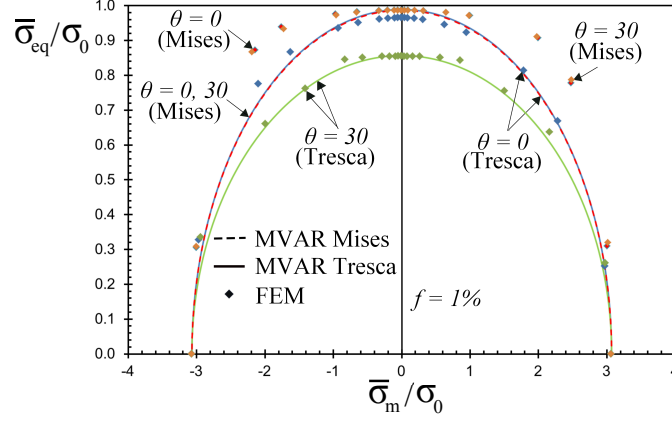

Figure 7.3: Yield surfaces in the $\overline{\sigma}_m - \overline{\sigma}_{eq}$ plane for isotropic microstructures, i.e. spherical voids $w_1 = w_2 = 1$, a porosity $f = 1\%$, Lode angle $\theta = 0^o$, 30°. Comparison between the FE simulations, the MVAR-Tresca porous model and the MVAR-Von Mises porous model.

In order to have a better understanding on the differences between porous Tresca and porous Von Mises yield surfaces, we present, next, contours of the equivalent Von Mises stress, for spherical voids, a porosity $f = 1\%$, a triaxiality $X_\Sigma = 3$ and a Lode angle $\theta = 0^o$. Then, as observed in fig. 7.4, the stress amplitude is in most of the unit-cell regions lower in the case of a Tresca matrix than in the Von Mises one. Thus, as previously discussed, the porous Tresca material is expected to be softer than a porous Von Mises material for the same microstructure considered.

7.2.2 Anisotropic microstructures

The fig. 7.5 shows FE simulations and MVAR yield surfaces for spherical voids ($w_1 = w_2 = 1$), prolate voids ($w_1 = w_2 = 3$), oblate voids ($w_1 = w_2 = 1/3$) and arbitrary ellipsoidal voids ($w_1 = 3$, $w_2 = 1/3$). The porosity is set equal to $f = 1\%$, whereas the loading is axisymmetric along the x1-axis ($\theta = 0^o$). A good agrement between the numerical FE predictions and the MVAR is seen for the full range of stress triaxialities, except in the case of average purely deviatoric, where a relative difference in the order of $2 - 6\%$ is noticed. Furthermore, the main observation in this figure is that non-spherical void shapes have a dramatic influence on the yield surface of the porous
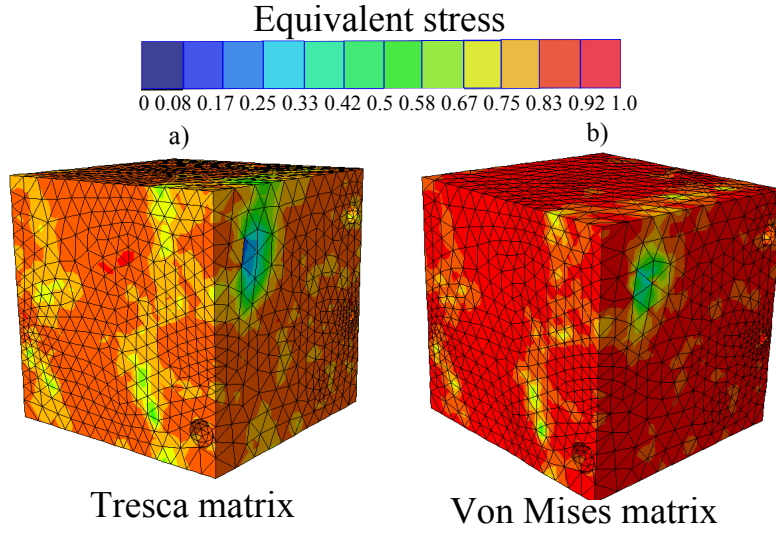
Figure 7.4: Contours of the equivalent Von Mises stress in the case of spherical voids, a porosity $f = 1\%$, a triaxiality $X_\Sigma = 3$ and a Lode angle $\theta = 0^o$ for (a) a Tresca matrix and (b) a Von Mises matrix.

material as predicted the MVAR and confirmed through FE simulations. First, the slopes of the yield surfaces depend strongly on the void shape. For instance, a porous material with ellipsoidal voids ($w_1 = 3$, $w_2 = 1/3$) is softer than that with oblate voids ($w_1 = w_2 = 1/3$) in the full range of stress triaxialities whereas they exhibit the same maximum average Von Mises stress. Moreover, for the same value of porosity, non-spherical void shapes lead to a significantly more compliant response at high values of the mean stress, especially in the case of oblate and arbitrary ellipsoidal voids. Moreover, it is evident from this figure that arbitrary ellipsoidal shapes ($w_1 = 3$, $w_2 = 1/3$) lead to very different responses when compared with spheroidal shapes ($w_1 = w_2 = 3$ or $w_1 = w_2 = 1/3$).

Finally, one should mentioned at this point that a series of additional triaxial loading conditions and several void shapes have also been considered and the MVAR has been found to be in good agreement (similar to the one observed in the previous results) with the corresponding FE calculations. However, no such results are shown here for brevity.
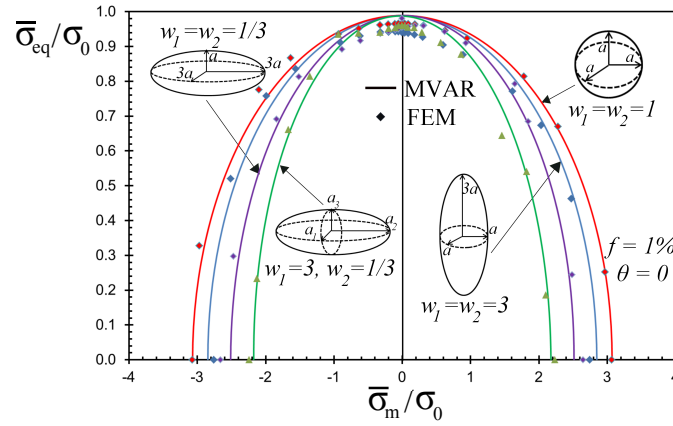
Figure 7.5: Yield surfaces in the $\overline{\sigma}_m - \overline{\sigma}_{eq}$ plane for isotropic (spherical voids $w_1 = w_2 = 1$) and anisotropic microstructures: prolate voids $w_1 = w_2 = 3$, oblate voids $w_1 = w_2 = 1/3$ and ellipsoidal voids $w_1 = 3$, $w_2 = 1/3$. Comparison between the FE simulations and the modified variational MVAR for $f = 1\%$ and Lode angle $\theta = 0^o$.

7.3 MVAR predictions

Hereafter, we attempt to reveal the complex coupling between the Tresca yield criterion features and the (morphological) void anisotropy resulting from the ellipsoidal void shape and orientation.

In this section, we discuss in more detail the effect of microstructure anisotropy upon the effective response of the porous composite. The figure 7.6 displays several MVAR yield surfaces for a porous plastic Tresca material. The effect of porosity is investigated by setting $f = (1\%, 5\%, 10\%)$ for different microstructures (a) $w_1 = w_2 = 1$ and (b) $w_1 = 3$, $w_2 = 1/3$, $\mathbf{n}^{(1)} = \mathbf{e}^{(1)}$, $\mathbf{n}^{(2)} = \mathbf{e}^{(2)}$. In these figures, the yield surfaces exhibit as expected a gradual decrease when increasing porosity for both ellipsoidal ($w_1 = w_2 = 1$) and ellipsoidal ($w_1 = w_2^{-1} = 3$) voids. However, while for the case of spherical voids ($w_1 = w_2 = 1$), in fig. 7.6a, the curves are symmetric with respect to the $\overline{\Sigma}_{eq}$ axis, the curves for the ellipsoidal voids ($w_1 = w_2^{-1} = 3$), in Fig. 7.6b, become asymmetric as already discussed in the context of Fig. 7.5. As a consequence of this asymmetry, the MVAR estimates are found to be slightly stiffer in the negative pressure regime ($\overline{\Sigma}_m < 0$).

The figure 7.7 shows yield surfaces in the $\overline{\Sigma}_m - \overline{\Sigma}_{eq}$ plane for a porous plastic Tresca material. The porosity of set to $f = 10\%$. The effects of the void aspect ratios and orientation are investigated by choosing $w_1 = w_2^{-1} = (1/3, 1, 3)$ for an orientation
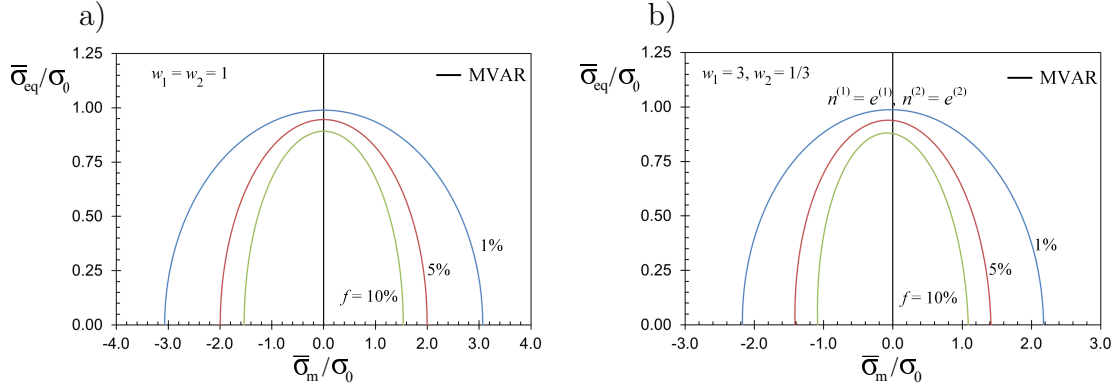
Figure 7.6: Yield surfaces for a porous plastic Tresca material. The effect of porosity is investigated by choosing $f = (1\%, 5\%, 10\%)$ for different void shapes (a) $w_1 = w_2 = 1$ and (b) $w_1 = 3$, $w_2 = 1/3$, $\mathbf{n}^{(1)} = \mathbf{e}^{(1)}$, $\mathbf{n}^{(2)} = \mathbf{e}^{(2)}$.

$\mathbf{n}^{(1)} = \mathbf{e}^{(1)}$, $\mathbf{n}^{(2)} = \mathbf{e}^{(2)}$. For the two considered anisotropic microstructures , i.e. $w_1 = w_2^{-1} = w = 3$ and $w_1 = w_2^{-1} = w = 1/3$, the porous solids exhibit the same hydrostatic behavior. This can be explained by the fact that the second microstructure is derived from the first one through a $\pi/2$ simple rotation around the x_3 axis (see fig. 7.7). Thus, since the hydrostatic loading possesses an isotropic character i.e. doesn't exhibit any preferential direction, the overall hydrostatic response is expected to be the same in both cases. This feature was also discussed in earlier studies (Danas and Ponte Castañeda [2009b]). In addition, the MVAR estimates are found to be stiffer in the negative pressure regime ($\overline{\Sigma}_m < 0$) for $w_1 = w_2^{-1} = w = 3$ while the average behavior is softer in the negative pressure regime ($\overline{\Sigma}_m < 0$) for $w_1 = w_2^{-1} = w = 0.2$. Moreover, there is a strong sensitivity of the hydrostatic average behavior on the void aspect ratios, since $\overline{\Sigma}_m$ gets an increase of 50% from the considered ellipsoidal microstructures ($w_1 = w_2^{-1} = (1/3, 3)$) to the spherical one ($w_1 = w_2 = 1$).

7.4 Calibration of the model

The MVAR yield surface is quadratic as a function of the stress, due to the LCC used in the optimization procedure. The MVAR model predicts, as expected due to the LCC used in the optimization procedure, a quadratic response for the yield surface. However, even if qualitatively and in a several cases quantitatively quite accurate the MVAR deals well with simulations, the numerical results obtained through FEM
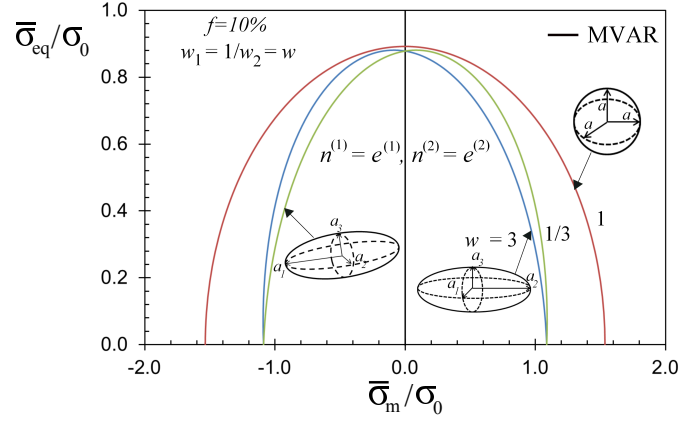
Figure 7.7: Yield surfaces for a porous plastic Tresca material with ellipsoidal voids. The porosity of set to $f = 10\%$. The effect of (a) the void aspect ratios is investigated by choosing $w_1 = w_2^{-1} = (1/3, 1, 3)$ for an orientation $\mathbf{n}^{(1)} = \mathbf{e}^{(1)}$, $\mathbf{n}^{(2)} = \mathbf{e}^{(2)}$.

exhibit in general a non elliptical shape of the yield surface (see for instance fig 7.2 and fig 7.5). This defect can be corrected using (i) a more sophisticated approach such as the second-order method (see Ponte Castañeda [2002a,b], Danas et al. [2008a], Danas and Ponte Castañeda [2009a]) , or (ii) by a direct analytical calibration of the present model.

In the present study, we choose the direct analytical calibration of the model, since the goal is to obtained analytical tractable estimates. Moreover, this technique is also of interest as it illustrates an effective method to calibrate the model in order to match accurately experimental results.

The calibrated MVAR, is characterized by the following expression of the yield surface

$$
\frac{\left(\max_{i,j} |\overline{\sigma}_i - \overline{\sigma}_j|\right)^2}{\sigma_0^2} + \frac{4 f \alpha_2}{5 \sigma_0^2} \overline{\boldsymbol{\sigma}} \cdot \left(\widehat{\mathbf{S}}^* - \mathbf{J} \cdot \widehat{\mathbf{S}}^* \mathbf{J}\right) \cdot \overline{\boldsymbol{\sigma}} + \frac{3 \alpha_1 (1 - f)^2}{(\sigma_0 \ln f)^2} \overline{\boldsymbol{\sigma}} \cdot \mathbf{J} \cdot \widehat{\mathbf{S}}^* \mathbf{J} \cdot \overline{\boldsymbol{\sigma}}
$$

$$
+ f (1 - \alpha_1) \left[\cosh \left(\frac{\sqrt{3} \cosh^{-1}\left(\frac{1 - f + f^2}{f}\right)}{\sigma_0 \ln f} \sqrt{\overline{\boldsymbol{\sigma}} \cdot \mathbf{J} \cdot \widehat{\mathbf{S}}^* \mathbf{J} \cdot \overline{\boldsymbol{\sigma}}} \right) - 1 \right] = (1 - f)^2 ,
$$

$$
\tag{7.13}
$$

where α_2 is a parameter weighting the relative contribution of the Tresca stress and a non hydrostatic stress measure, whereas α_1 is a parameter introduced to interpolate the shape of the yield surface between an elliptical shape ($\alpha_1 = 1$, MVAR) and an exponential shape ($\alpha_1 = 0$).

In addition, the parameters α_1 and α_2 depend on the porosity. For the porosity $f = 1\%$, the identification leads to $\alpha_1 = 0.8$ and $\alpha_2 = 12 + 11\cos 6\theta$. Furthermore, fig. 7.8 shows FE simulations and MVAR yield surfaces for spherical voids ($w_1 = w_2 = 1$), prolate voids ($w_1 = w_2 = 3$), oblate voids ($w_1 = w_2 = 1/3$) for a porosity $f = 1\%$, and both axisymmetric (Lode angle $\theta = 0^o, 60^o$) and non axisymmetric loading ($\theta = 30^o$). The main observation in this context of this figures is that there is a very good agreement between the MVAR and the FE calculations for the full range of loading conditions (stress triaxiality, Lode angle), validating this simple calibration procedure.
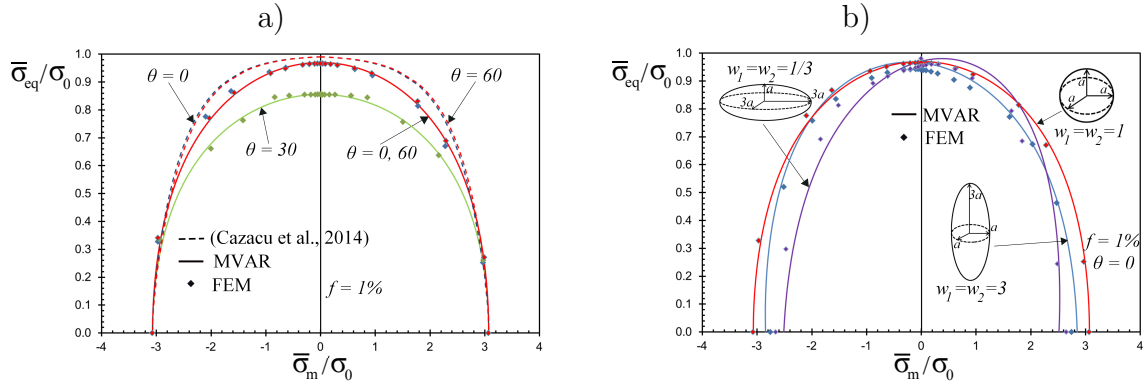

Figure 7.8: Yield surfaces in the $\overline{\sigma}_m - \overline{\sigma}_{eq}$ plane for isotropic and anisotropic microstructures. Comparison between the FE simulations and the calibrated modified variational CMVAR for porosity $f = 1\%$, (a) three Lode angles $\theta = 0^o, 30^o, 60^o$, spherical voids and (b) spherical voids $w_1 = w_2 = 1$, prolate voids $w_1 = w_2 = 3$, oblate voids $w_1 = w_2 = 1/3$.

Moreover, fig. 7.9 shows yield surfaces for spherical voids (i.e., $w_1 = w_2 = 1$) as predicted by the FE simulations, the MVAR-Tresca porous model and the corresponding MVAR-Von Mises porous model for the porosity $f = 1, \%$ and both axisymmetric ($\theta = 0^o$) and non axisymmetric loadings conditions ($\theta = 30^o$). There is a good agrement between the MVAR porous models and the FE in the full range of stress triaxiality, emphasizing the present calibration approach.

7.5   Concluding remarks

An analytical yield function in closed form for porous plastic Tresca materials has been proposed in this chapter. It is theoretically motivated using an original approach that
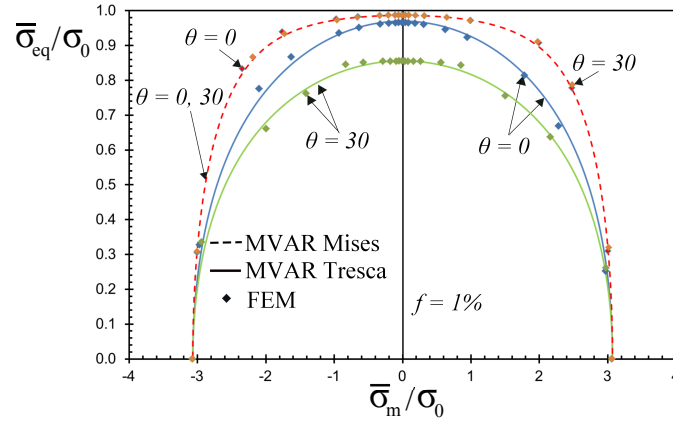
Figure 7.9: Yield surfaces in the $\overline{\sigma}_m - \overline{\sigma}_{eq}$ plane for isotropic microstructures, i.e. spherical voids $w_1 = w_2 = 1$, a porosity $f = 1\%$, Lode angle $\theta = 0^o$, 30°. Comparison between the FE simulations, the MVAR-Tresca porous model and the MVAR-Von Mises porous model.

consists to consider the limiting case of infinte number of slip systems in a variational micromechanical based novel porous single crystal model. The modified variational (MVAR) model presented in this study has been validated by comparison with full field FE calculations of single- and multi-void periodic unit-cells. The MVAR model has been found to be in good agreement with the FE results for a very wide range of parameters describing the porosity, the void shapes and orientations. The MVAR model has shown strong predictive capabilities while exhibiting critical qualitative features.

More precisely, the MVAR model has been able to predict the strong dependence of the effective response, and especially of the average hydrostatic stress upon the shape and orientation of the voids. In addition, to better match a non quadratic dependence on the stress (observed through FEM computations), this yield function was phenomenologically extended following a procedure similar to the one introduced in chapter 6. The extension introduces two adjustable parameters (α_1 and α_2), calibrated with unit-cell computations.

Finally, it is important to mentioned that several important issues, such as rate-dependent effects, strain-hardening and microstructure evolution that were neglected for simplicity in this paper will be considered in further studies. Moreover, it would be interesting to study the effects of cyclic loading conditions upon microstructure evolution using similar ideas.

Chapter 8

Evolution of microstructure: spherical and ellipsoidal voids

This chapter is concerned with some preliminary predictions of the effective response and evolution of microstructure of random porous single crystals subjected to general loading conditions. More precisely, the evolutions laws of the microstructural variables depicted in chapter 2 are applied to several crystalline structures for a large range of material parameters. At present due to lack of time, the study of the microstructure evolution is not exhaustive and more work is needed at this level.

8.1   Material parameters and initial conditions

The matrix phases considered (FCC and BCC single crystals) are taken to be initially unloaded with no hardening, i.e. $\tau_0^{(s)} = \tau_0$, $\forall s = 1, K$, while the voids are initially spherical with $w_1 = w_2 = 1$. The initial porosity is taken to be $f_0 = 1\%$ and the elasticity effects are neglected. It should be noted that the macroscopic response of the porous material at large deformations is strongly affected by the hardening, the viscoplastic creep exponent, the initial porosity f_0 and the initial aspect ratios w_1 and w_2, but we will not carry out an exhaustive parametric study with respect to those parameters here. Moreover, in the following, the microstructural variables will be plotted as functions of the equivalent strain $\overline{\varepsilon}_e$ defined as

$$\overline{\varepsilon}_e = \int_t \sqrt{\frac{2}{3}\overline{\boldsymbol{D}}' \cdot \overline{\boldsymbol{D}}'} \, dt, \tag{8.1}$$

where $\overline{\boldsymbol{D}}'$ refers to the deviatoric part of the average strain-rate $\overline{\boldsymbol{D}}$.

8.2 Low stress triaxialities

Fig. 8.1 shows MVAR plots of (a) the equivalent stress $\overline{\sigma}_e$, (b) the porosity f, and the aspect ratios (c) w_1 and (d) w_2, as a function of the equivalent strain $\overline{\varepsilon}_e$, for a BCC single crystal, a creep exponent $n = 10$, four Lode angles $\theta = 0^o$, 20°, 30°, 60° and a low value of the stress triaxiality ($X_\Sigma = 0.1$). The main observation in Fig. 8.1a is that there is a slight effect of the Lode angle on the overall mechanical response of the porous single crystal.

In addition, let us analyze plots for the evolution of f, w_1 and w_2 in Fig. 8.1b-d, respectively, as a function of the equivalent strain $\overline{\varepsilon}_e$. In graph. 8.1b, one observes an overall reduction in the porosity f as a function of $\overline{\varepsilon}_e$, except in the case of the Lode angle $\theta = 60^o$. Furthermore, as shown in part (c), w_1 can become significantly low for all values of θ. Moreover, as shown in part (d), w_2 decreases very fast for all values of θ except for $\theta = 60^o$, as expected. This suggests that a void collapse mechanism (i.e., flattened cracks) is developed with increasing strain, which is also the mechanism in the context of low stress triaxiality for porous materials with isotropic matrix (see Danas and Aravas [2012]). This observation is not surprising since a BCC single crystal possesses a high number of slip systems ($K = 48$) and thus, its response is intuitively expected to be "closer" to an isotropic one.

Next, in order to investigate the influence of the crystal anisotropy on the evolution of the microstructure, the Fig. 8.2 presents MVAR plots of (a) the equivalent stress $\overline{\sigma}_e$, (b) the porosity f, and the aspect ratios (c) w_1 and (d) w_2, as a function of the equivalent strain $\overline{\varepsilon}_e$, for a FCC single crystal, a creep exponent $n = 10$, four Lode angles $\theta = 0^o$, 20°, 30°, 60° and a low value of the stress triaxiality ($X_\Sigma = 0.1$).

Then, in Fig. 8.2b, one can observe that in the context of FCC crystal (contrary to the previous case of BCC crystal) an overall increasing of the porosity as a function of $\overline{\varepsilon}_e$ for all the Lode angles is observed.

Moreover, as in the context of porous BCC single crystal, the aspect ratios w_1 and w_2 become significantly low for all values of θ, except in the special case $\theta = 60^o$ for w_2. Consequently, in low stress triaxiality, a void collapse mechanism (i.e., flattened cracks) is developed with increasing strain for both BCC or FCC porous single crystals.

On the other hand, Fig. 8.3 presents MVAR plots of (a) the equivalent stress $\overline{\sigma}_e$ and (b) the porosity f as a function of the equivalent strain $\overline{\varepsilon}_e$, for a HCP single crystal
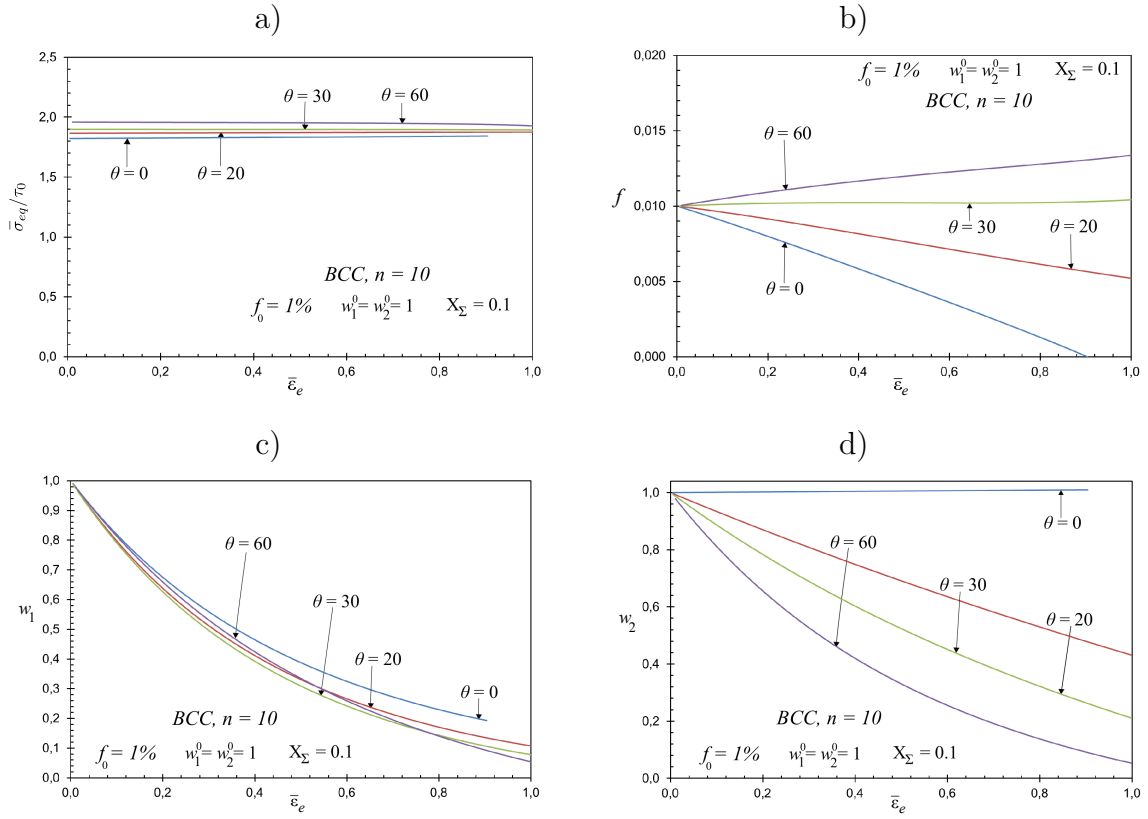
Figure 8.1: Plots of the MVAR estimates in the context of a porous BCC single crystal, for (a) the equivalent stress $\overline{\sigma}_e$, (b) the porosity f, and the aspect ratios (c) w_1 and (d) w_2 as a function of the equivalent strain $\overline{\varepsilon}_e$, for a low value of the stress triaxiality ($X_\Sigma = 0.1$) and four values of the Lode angle. The creep exponent is $n = 10$ and the voids are initially spherical, with a porosity $f_0 = 1\%$.

with $K = 3$ and $K = 12$ slip systems, a creep exponent $n = 10$, a Lode angle $\theta = 60^o$ and a low value of the stress triaxiality ($X_\Sigma = 0.1$). As we can seen in Fig. 8.3b, the porosity slightly increases for the HCP porous crystal with $K = 12$ (basal, prismatic and pyramidal Π_2) active slip systems while it doesn't evolve for the HCP crystal with $K = 3$ basal active slip systems, since such single crystal exhibits an incompressible overall response.

Furthermore, in order to address the influence of the nonlinearity (viscoplastic creep exponent) on the evolution of the microstructure, Fig. 8.4 presents MVAR plots of (a) the equivalent stress $\overline{\sigma}_e$, (b) the porosity f, and the aspect ratios (c) w_1 and (d) w_2, as a function of the equivalent strain $\overline{\varepsilon}_e$, for a FCC single crystal, a Lode angle $\theta = 60^o$, a low value of the stress triaxiality ($X_\Sigma = 0.1$) and two creep exponents
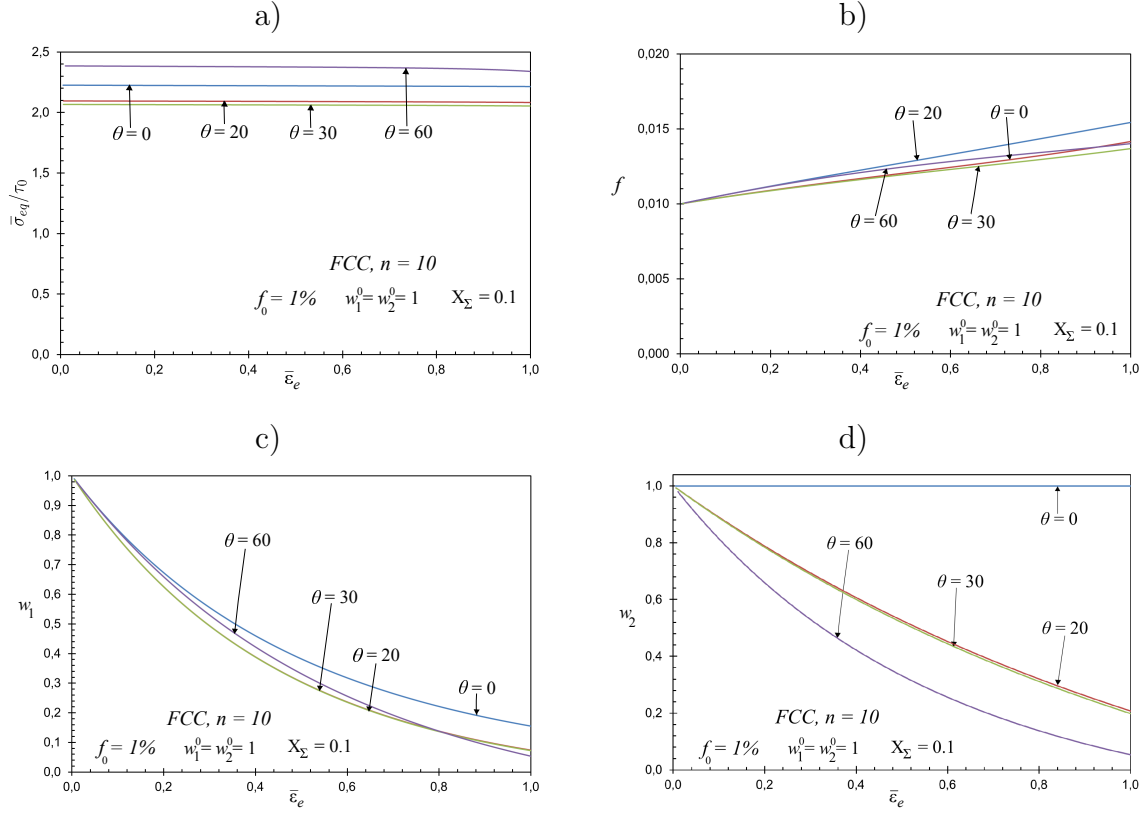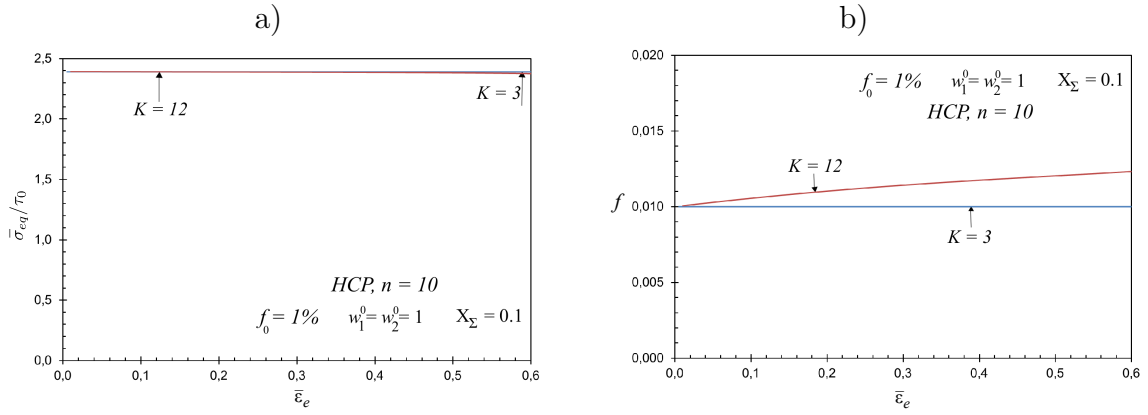
Figure 8.2: Plots of the MVAR estimates in the context of a porous FCC single crystal, for (a) the equivalent stress $\overline{\sigma}_e$, (b) the porosity f, and the aspect ratios (c) w_1 and (d) w_2 as a function of the equivalent strain $\overline{\varepsilon}_e$, for a low value of the stress triaxiality ($X_\Sigma = 0.1$) and four values of the Lode angle. The creep exponent is $n = 10$ and the voids are initially spherical, with a porosity $f_0 = 1\%$.

a)   b)

Figure 8.3: Plots of the MVAR estimates in the context of a porous HCP single crystal with $K = 3$ and $K = 12$ slip systems, for (a) the equivalent stress $\overline{\sigma}_e$ and (b) the porosity f as a function of the equivalent strain $\overline{\varepsilon}_e$, for a low value of the stress triaxiality ($X_\Sigma = 1$) and a Lode angle $\theta = 60^o$. The creep exponent is $n = 10$ and the voids are initially spherical, with a porosity $f_0 = 1\%$.

$n = 10, \infty$. The evolution of the void shape is not affected by the creep exponent, whereas porosity evolution exhibits much more significant differences. More precisely, the void volume fraction increases slightly in a case ($n = 10$) while decreasing slightly in the other case ($n = \infty$).

However, the microstructural mechanisms are not expected to change with the nonlinearity.

8.3   High stress triaxialities

Fig. 8.5 shows MVAR plots of (a) the equivalent stress $\overline{\sigma}_e$, (b) the porosity f, and the aspect ratios (c) w_1 and (d) w_2, as a function of the equivalent strain $\overline{\varepsilon}_e$, for a BCC single crystal, a creep exponent $n = 10$, four Lode angles $\theta = 0^o, 20^o, 30^o, 60^o$ and a high value of the stress triaxiality ($X_\Sigma = 1$). The main result in Fig. 8.5a is that the effect of the Lode parameter on the overall mechanical response of the porous single crystal is less important, since all the $\overline{\sigma}_e - \overline{\varepsilon}_e$ curves almost coincide for the largest range of the applied strain.

The fact that the stress strain curve seems independent of the Lode angle at $X_\Sigma = 1$ can be explained by referring to Fig. 8.5b, where the increase of porosity is significant for all values of the Lode angle ($\theta = 0^o, 20^o, 30^o, 60^o$). In addition, by observation of
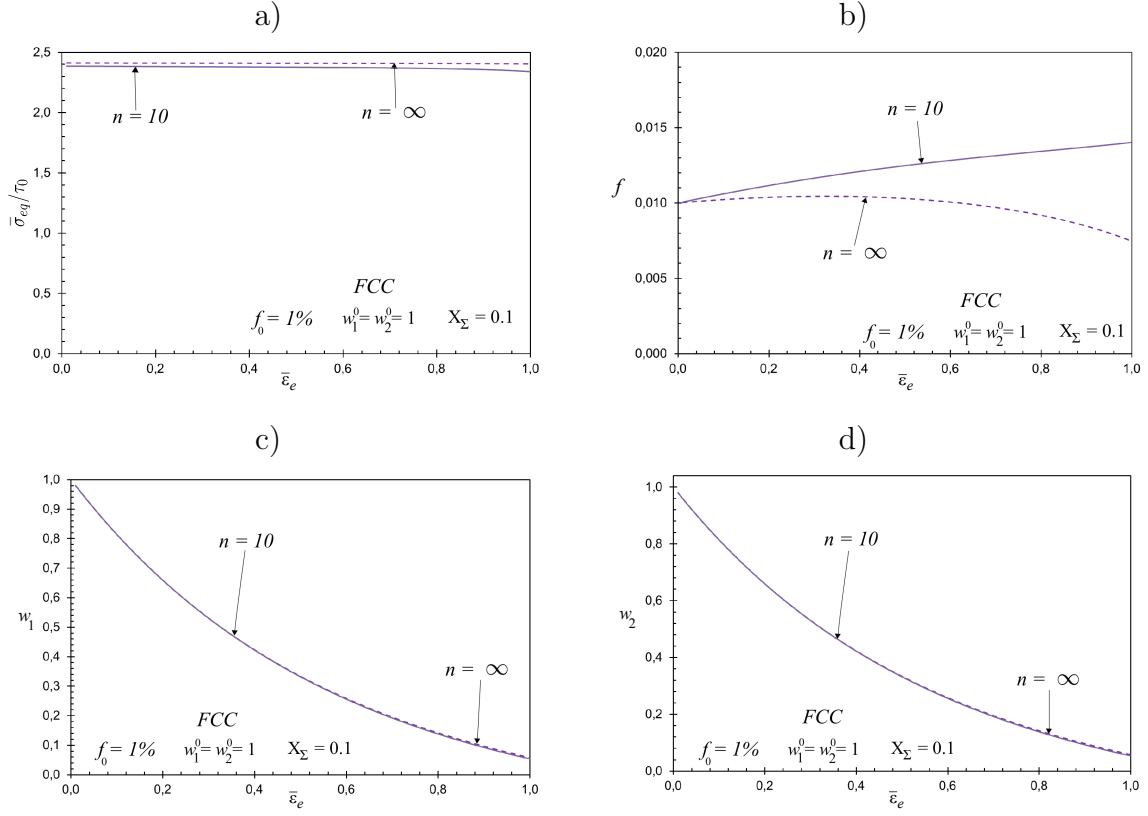
Figure 8.4: Plots of the MVAR estimates in the context of a porous FCC single crystal, for (a) the equivalent stress $\overline{\sigma}_e$, (b) the porosity f, and the aspect ratios (c) w_1 and (d) w_2 as a function of the equivalent strain $\overline{\varepsilon}_e$, for a low value of the stress triaxiality ($X_\Sigma = 0.1$), a Lode angle $\theta = 60^o$ and two creep exponents $n = 10, \infty$. The voids are initially spherical, with a porosity $f_0 = 1\%$.

parts (c) and (d) of Fig. 8.5, we note that the void shape still evolves as a function of $\overline{\varepsilon}_e$. Thus, the main softening mechanism in this high triaxiality context ($X_\Sigma = 1$) is clearly the evolution of porosity which is found to lead to significant softening of the effective response of the porous single crystal. Nonetheless, the void shape evolution for the various Lode angles leads to weak differences on the evolution of $\overline{\sigma}_e$ and f. Then, this void growth mechanism leads to the well-known "high-triaxiality coalescence" of the voids (see for instance Thomason [1985], Pardoen and Hutchinson [2000], Gologanu et al. [2001], Benzerga [2002], Morin et al. [2015]). The present model doesn't include coalescence effects which would increase the evolution of porosity in much more pronounced way after a certain critical strain. In addition, it is clear that the dominance of the evolution of porosity will prevail at larger stress triaxialities

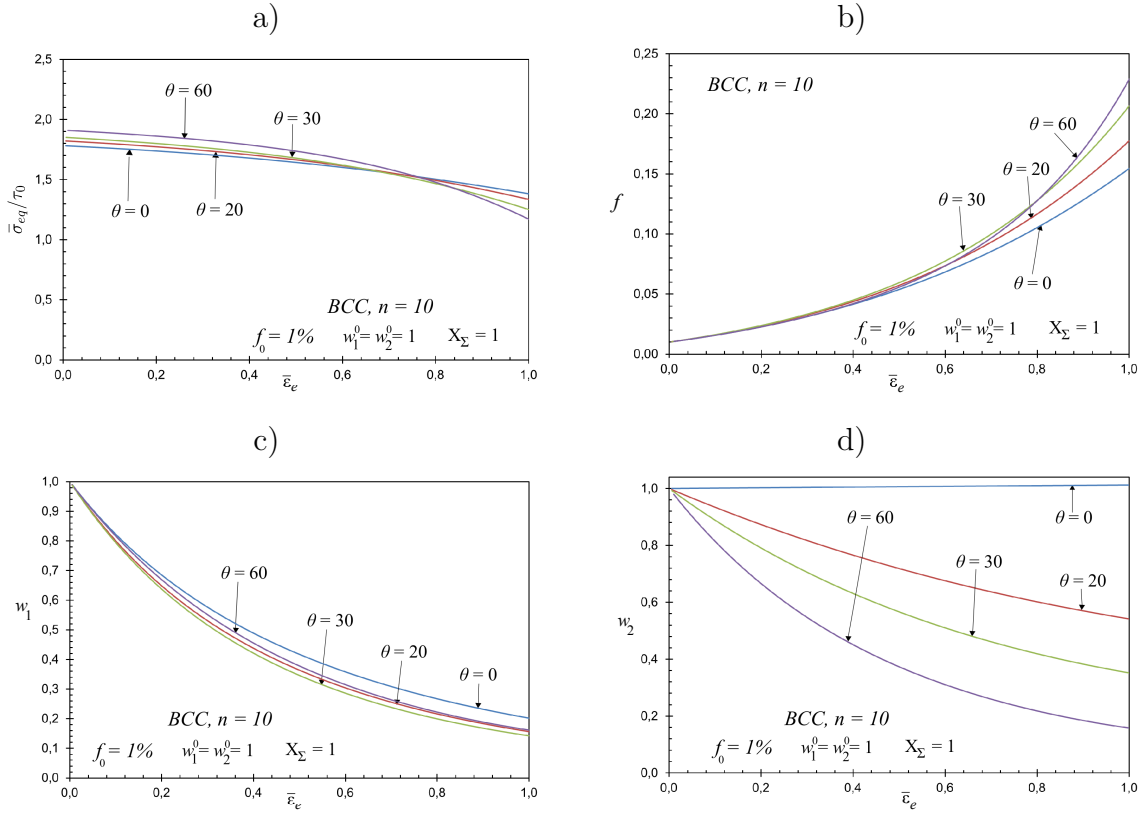$X_\Sigma > 1$ not shown in this preliminary study.

Figure 8.5: Plots of the MVAR estimates in the context of a porous BCC single crystal, for (a) the equivalent stress $\overline{\sigma}_e$, (b) the porosity f, and the aspect ratios (c) w_1 and (d) w_2 as a function of the equivalent strain $\overline{\varepsilon}_e$, for a high value of the stress triaxiality ($X_\Sigma = 1$) and four values of the Lode angle. The creep exponent is $n = 10$ and the voids are initially spherical, with a porosity $f_0 = 1\%$.

Moreover, in order to study the influence of the crystal anisotropy on the evolution of the microstructure at high stress triaxiality, Fig. 8.6 presents MVAR plots of (a) the equivalent stress $\overline{\sigma}_e$, (b) the porosity f, and the aspect ratios (c) w_1 and (d) w_2, as a function of the equivalent strain $\overline{\varepsilon}_e$, for a FCC single crystal, a creep exponent $n = 10$, four Lode angles $\theta = 0^o$, 20°, 30°, 60° and a high value of the stress triaxiality ($X_\Sigma = 1$).

As already observed for porous BCC single crystal, the stress strain curve seems independent of the Lode parameter at $X_\Sigma = 1$ (Fig. 8.6a), due to the significant increase of porosity for all values of the Lode angle (see Fig. 8.5b). Consequently, the principal softening mechanism in the high triaxiality regime is the evolution of

porosity which is found to lead to significant softening of the effective response of the porous single crystal.
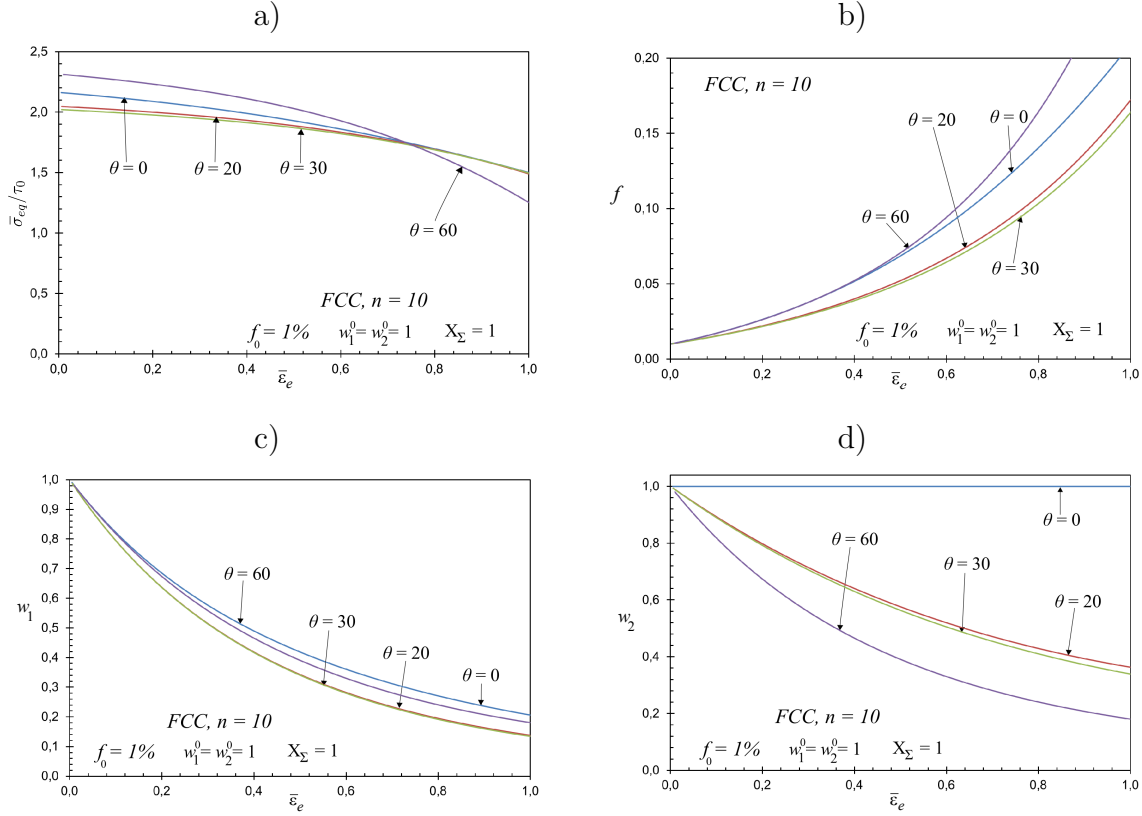

Figure 8.6: Plots of the MVAR estimates in the context of a porous FCC single crystal, for (a) the equivalent stress $\overline{\sigma}_e$, (b) the porosity f, and the aspect ratios (c) w_1 and (d) w_2 as a function of the equivalent strain $\overline{\varepsilon}_e$, for a high value of the stress triaxiality ($X_\Sigma = 1$) and four values of the Lode angle. The creep exponent is $n = 10$ and the voids are initially spherical, with a porosity $f_0 = 1\%$.

In addition, Fig. 8.7 presents MVAR plots of (a) the equivalent stress $\overline{\sigma}_e$ and (b) the porosity f as a function of the equivalent strain $\overline{\varepsilon}_e$, for a HCP single crystal with $K = 3$ and $K = 12$ slip systems, a creep exponent $n = 10$, a Lode angle $\theta = 60^o$ and a high value of the stress triaxiality ($X_\Sigma = 1$). The main observation in the context of this graph (see Fig. 8.7b) is that the porosity doesn't evolve for the HCP crystal with $K = 3$ basal active slip systems since such single crystal exhibits an incompressible overall response whereas it significantly increases for the HCP porous crystal with $K = 12$ (basal, prismatic and pyramidal Π_2) active slip systems. The evolution of the porosity for $K = 12$ slip systems leads to the softening observed in Fig. 8.7a.
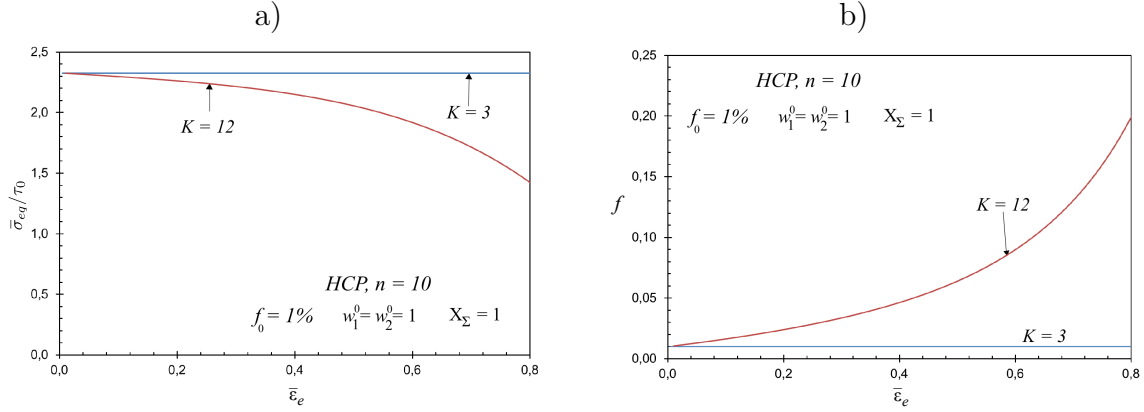
Figure 8.7: Plots of the MVAR estimates in the context of a porous HCP single crystal with $K = 3$ and $K = 12$ slip systems, for (a) the equivalent stress $\overline{\sigma}_e$ and (b) the porosity f as a function of the equivalent strain $\overline{\varepsilon}_e$, for a high value of the stress triaxiality $(X_\Sigma = 1)$ and a Lode angle $\theta = 60^o$. The creep exponent is $n = 10$ and the voids are initially spherical, with a porosity $f_0 = 1\%$.

Finally, the influence of the nonlinearity (creep exponent) on the evolution of the microstructure is investigated. Then, Fig. 8.8 presents MVAR plots of (a) the equivalent stress $\overline{\sigma}_e$, (b) the porosity f, and the aspect ratios (c) w_1 and (d) w_2, as a function of the equivalent strain $\overline{\varepsilon}_e$, for a FCC single crystal, a Lode angle $\theta = 60^o$, a high value of the stress triaxiality $(X_\Sigma = 1)$ and two creep exponents $n = 10, \infty$. The evolution of the void aspect ratios w_1 and w_2 seems unaffected by the creep exponent. However, the increase in porosity is twice more important for $n = 10$ (from $f_0 = 1\%$ to $f = 20\%$) than for $n = \infty$ (from $f_0 = 1\%$ to $f = 10\%$) at the same level of final equivalent strain $\overline{\varepsilon}_e = 100\%$. As a consequence, the matrix softening is less pronounced for $n = \infty$ than for $n = 10$.

8.4   Concluding remarks

In this chapter, the evolution laws for the microstructural variables presented in 2 are used in order to provide some preliminary predictions for a large range of material parameters in the context of porous single crystals subjected to general loading conditions. More precisely, an investigation of the several microstructural mechanisms has been carried out at both high and low triaxiality regime for several crystal structure (BCC, HCP and FCC) and different creep exponents. Then, a void collapse
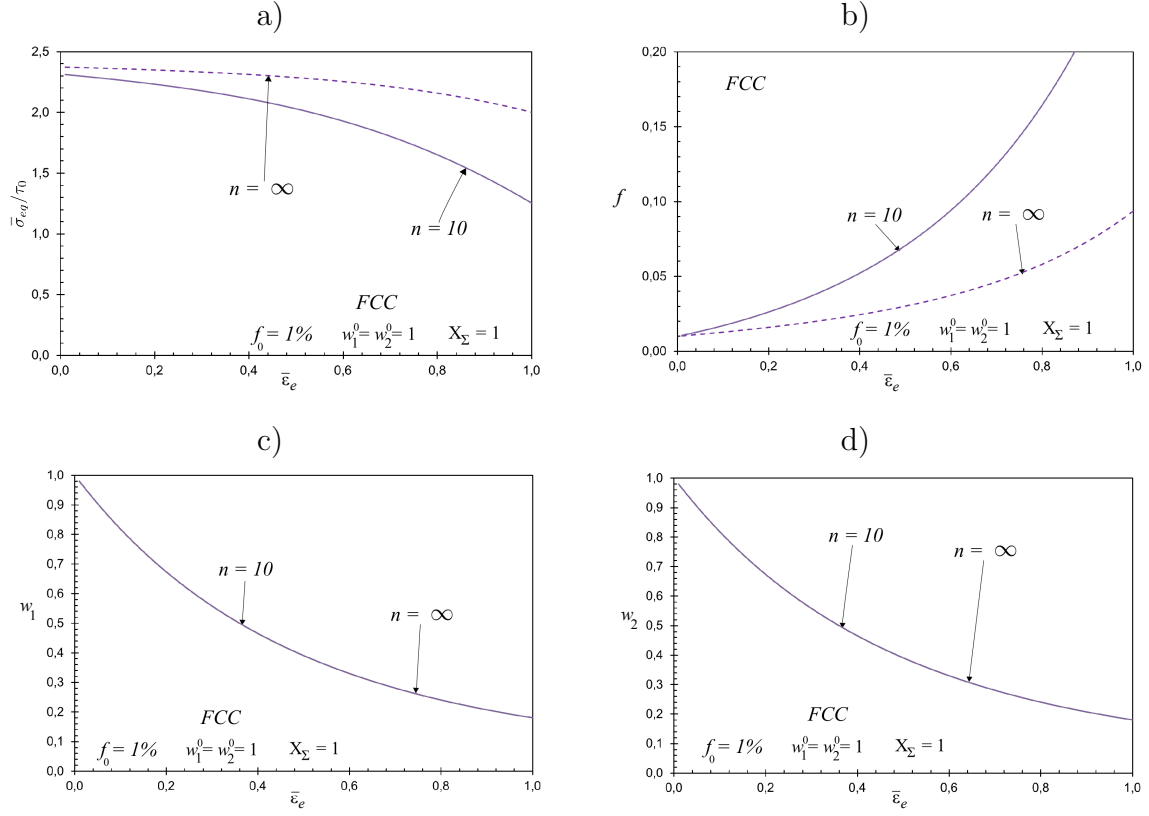
Figure 8.8: Plots of the MVAR estimates in the context of a porous FCC single crystal, for (a) the equivalent stress $\overline{\sigma}_e$, (b) the porosity f, and the aspect ratios (c) w_1 and (d) w_2 as a function of the equivalent strain $\overline{\varepsilon}_e$, for a high value of the stress triaxiality ($X_\Sigma = 1$), a Lode angle $\theta = 60^o$ and two creep exponents $n = 10, \infty$. The voids are initially spherical, with a porosity $f_0 = 1\%$

mechanism (i.e., flattened cracks) developed with increasing strain was found as the dominant mechanism at low stress triaxiality while the evolution of porosity was the main softening mechanism in the high triaxiality context, leads to "high-triaxiality coalescence" of the voids. Furthermore, we have observed that the creep exponent has an important influence on the porosity evolution, whereas the void shape evolution is less affected by the nonlinearity.

Chapter 9

Closure

In this thesis, an analytical homogenization-based constitutive model has been developed for porous rate-(in)dependent single crystals subjected to finite strains. This model, so-called "MVAR", is based on the variational nonlinear homogenization method of Ponte Castañeda [1991a], modified by Danas and Aravas [2012] to derive estimates but not bounds that are accurate at large triaxialities. The MVAR takes into account the nonlinear anisotropic response of the single crystal, i.e. arbitrary number of slip systems and orientations, microstructural information, such as the volume fraction, shape, orientation and distribution of the voids, as well as the evolution of these microstructural and macroscopic variables along a given loading path. This model attempts to bridge the gap at the modeling of porous solids in the micron (grain) scale.

In this regard then, we have first recalled in Chapter 2 the notion of particulate microstructures, introduced by Willis [1977] as a generalization of the Eshelby [1957] dilute microstructures in the nondilute regime. Thus, one can provide the effective behavior of the linear comparison composite (LCC) using the linear Willis estimates (Willis [1977]) and subsequently, determine estimates for linear porous materials with particulate microstructures. Moreover, by making use of the definitions associated with a commonly used power-law form of incompressible viscoplastic stress potential, it was then possible to derive estimates of the effective viscoplastic stress potential for porous single crystals through the variational homogenization methods. In addition, in order to remedy the stiff response of variational estimates in the case of hydrostatic loadings (Ponte Castañeda [1991a], Michel and Suquet [1992]), we have used the fact that in the isotropic case (number of slip systems $K \longrightarrow \infty$), the hydrostatic limit of the effective behavior of composite spherical assemblages (CSA) is known exactly and

in closed form (Hashin [1962], Gurson [1977], Leblond et al. [1994]). Hence, following (Danas and Aravas [2012]), we have proposed a modified variational estimate (MVAR) so that it recovers the CSA result (2.114) in the limit of infinite slip systems, spherical voids and hydrostatic loadings, where the response becomes fully isotropic. Furthermore, since the porous single crystals are in general subjected to finite deformations, its microstructure evolves-on average-to ellipsoidal voids in time with different shape and orientation. Consequently, based on the work of (Ponte Castañeda and Zaidman [1994], Aravas and Ponte Castañeda [2004], Danas and Aravas [2012]), we have presented the relevant evolution laws for the internal microstructural variables used to describe the volume fraction, shape and orientation of the voids.

Next, in Chapter 3, we have carried out a brief reiew of existing models for viscoplastic porous materials that have been developed since the last twenty years. In particular, a brief summary of recent rate-independent porous single crystals models has been made. Then, the case of two-phase material systems comprising an isotropic rate-(in)dependent matrix phase (metal usually described by von Mises yield criterion or creep potential) and a voided phase (pores of spherical, spheroidal or arbitrary ellipsoidal shapes) is briefly discussed. More specifically, we have recalled the well-known Gurson model (Gurson [1977]) that is based on the exact solution for a shell (spherical or cylindrical cavity) under hydrostatic loadings, suitably perturbed, to obtain estimates for the effective behavior of ideally-plastic solids with isotropic or transversely isotropic distributions of porosity. Following this idea, several other "limit analysis models" were presented, extending the initial contribution to viscoplasticity and void shape effects. Moreover, some effective estimates based on the variational homogenization theory using the concept of a linear comparison composite (such as Ponte Castañeda [1991a], Danas and Ponte Castañeda [2009a], Danas and Aravas [2012], Agoras and Ponte Castañeda [2013]), which are able to deal well with void shape and orientation, general loading conditions and microstructure evolution were also presented. On the other hand, we have presented some results for rate-(in)dependent anisotropic matrix systems. More precisely, we have discussed either models based on phenomenological Hill-type matrix (see for instance Benzerga and Besson [2001], Monchiet et al. [2008a], Keralavarma and Benzerga [2010]), or porous single crystals models. This last case of porous single crystals has been studied both numerically and experimentally (Srivastava et al. [2012], Srivastava and Needleman [2012, 2015]) to ad-

dress the modeling of anisotropic ductile damage growth. Nonetheless, there exist very few models in the literature. Indeed, the large majority of the studies are restricted to special void geometries, loading conditions and slip system orientations. Kysar et al. [2005], Gan et al. [2006], Gan and Kysar [2007] have for instance used slip line theory to study cylindrical voids with circular cross-section in a rigid-ideally plastic face-centered cubic (FCC) single crystals, whereas Idiart and Ponte Castañeda [2007] have studied two-dimensional "out of plane" cylindrical voids with circular cross-section subjected to anti-plane loadings. Moreover, Han et al. [2013] and Paux et al. [2015] have recently proposed models for rate-independent single crystals containing spherical voids. However, none of these models, while being very important steps, are complete enough to account for general crystal anisotropy, general ellipsoidal microstructure and loading conditions as well as large deformations, via evolution of microstructure.

Furthermore, in Chapter 4, we have discussed the numerical evaluation of the effective behavior of porous single crystals. In order to achieve this goal, we have first recalled that a random porous material like the one presented in this study exhibits similar effective response with that of a periodic material provided that the distribution of voids is complex enough (appropriate for large porosity) or when the porosity is small enough. Consequently, it is possible to use numerical periodic homogenization technique, and precisely to analyze the problem of a periodic porous material considering a unit-cell that contains a given distribution of voids. Thus, the comparison between the "MVAR" and the FE periodic unit-cell calculations appears to be relevant in such context.

In the sequel of this thesis, Chapters 5 through 8 have dealt with the application of the above discussed methods in the context of viscoplastic porous single crystals. To be precise, Chapter 5 deals with the estimation of the effective behavior in porous single crystals consisting of cylindrical voids subjected to plane-strain loading conditions. In turn, Chapters 6 and 7 are related to the determination of the effective behavior and 8 with the evolution of microstructure in porous single crystals consisting of spherical or ellipsoidal voids subjected to general loading conditions. In what follows, we summarize the main results obtained in these chapters.

Chapter 5 deals with the estimation of the effective behavior of porous materials consisting of aligned cylindrical voids with circular or elliptical voids distributed randomly and uniformly in a single crystal matrix. The material is subjected to plane-

strain loading conditions. The MVAR model has been found to be in good agrement with the numerics for a large range of parameters including arbitrary crystal matrix, general elliptical void shape, several porosities, creep exponent and the full space of stress triaxialities. Moreover, the model has been able to predict the strong dependence of the effective response, and especially of the average hydrostatic stress upon the number and orientation of the slip systems as well as the shape and orientation of the voids. One of the major finding of this study has been that for highly anisotropic crystals (e.g., one or even two active slip systems) the porous crystal can exhibit fully incompressible response, even in the presence of voids. This of course affects the entire effective response of the porous crystal for the entire range of stress states. That is the first time such a result is presented in the literature and reveals the significance of plastic anisotropy of the underlying phases upon the macroscopic response of the material. Moreover, it has been shown that the void shape and orientation affect strongly the response of the porous crystal. In particular, the effective response becomes much softer as one goes from a circular void to an elliptical one (which is suggestive of a crack-type geometry). In the general case of elliptical voids oriented at an arbitrary angle (with respect to the laboratory axes) and arbitrary number of slip systems, we have shown that the effective response exhibits no symmetries when plotted in the purely deviatoric plane (and at finite hydrostatic stresses) thus indicating the non-trivial coupling between the anisotropy of the underlying crystal and the (morphological) anisotropy induced by the shape and orientation of the voids.

In contrast to Chapter 5, where two-dimensional model problems has been studied in order to gain insight on the behavior of viscoplastic porous single crystals, Chapters 6 and 7 have dealt with more realistic three-dimensional microstructures and loadings. More specifically, in Chapter 6, we have studied the effective behavior of viscoplastic porous single crystals when subjected to more general loading conditions. The major finding of this work, was that for highly anisotropic crystals (e.g., three basal active slip systems in certain HCP crystal structure) the porous crystal can exhibit fully incompressible response, even in the presence of voids. This of course affects the entire effective response of the porous crystal for the entire range of stress states. Moreover, the "MVAR" has been assessed to a large extent with robust periodic unit-cell calculations and for a wide range of parameters (different crystal structures i.e. FCC, BCC, HCP, void shapes and orientations, creep exponents and porosity values),

exhibiting good agrement without any calibration parameters. In addition, in the rate-independent context, a simple way of calibrating the MVAR with just two adjustable parameters is proposed in order to obtain an excellent agreement with respect to the numerical results. It is then compared with other rate-independent models (Han et al. [2013], Paux et al. [2015]) for the case of spherical voids. This calibration procedure can, in the future (if needed), be extended to the rate-dependent case in a straightforward manner. But such an attempt has not been pursued here since the difference between the MVAR estimates and the FE results did not exceed $\sim 5\%$ in the worst case studied, i.e. for creep exponent $n = 10$.

Furthermore, theoretically motivated by making use of an original approach that consists to consider the limiting case of infinite slip systems, we provide in Chapter 7 a porous Tresca model. The proposed model presented in this study has been validated by comparison with full field FE calculations of single- and multi-void periodic unit-cells. It has been found in good agreement with the FE results for a very wide range of parameters describing the porosity, the void shapes and orientations or different loading conditions. In addition, it shows strong predictive capabilities while exhibiting critical qualitative features.

Finally, in Chapter 8, we have made use of the previous effective potentials together with the equations describing the evolution of the microstructural variables to provide some preliminary predictions of the evolution of microstructure in porous single crystals consisting of spherical or ellipsoidal voids. At low stress triaxialities, the effect of the Lode angle was critical in the evolution of the porosity and the void shapes while it was of a less significant influence in the porosity evolution at high triaxiality regime. In addition the effect of the creep exponent has been found to be significant in the evolution of the porosity for both low and high stress triaxiality, whereas it has been observed to be less important in the evolution of void aspect ratios. Moreover, for highly anisotropic crystals such as the three basal active slip systems in certain HCP crystal structure, the porous crystal was fully incompressible response, even if the void aspect ratios evolve.

At this stage, it is important to address some of the future directions associated with the results presented in this thesis. First of all, the present modeling requires the evaluation of microstructural tensors which in the general case, is carried out numerically. Since this operation involves the numerical computation of surface integrals,

further optimization of this procedure is needed particularly if extreme values of the aspect ratios (e.g., $w_i < 0.05$ or $w_i > 20$ with $i = 1, 2$) are used since the kernel of the integral becomes highly oscillatory.

Moreover, it will be useful to assess the accuracy of the MVAR predictions of the evolution of the shape and the orientation of the voids through numerical simulations. Indeed, it is well known that crystallographic aspects of plastic deformation around holes significantly affect their growth rate and in general the microstructural evolution (Srivastava and Needleman [2012, 2015]). Such validation will give us ideas in order to study coalescence of voids for arbitrary loading conditions, following for instance the approach recently proposed in Morin et al. [2015].

As another remark, the "MVAR" model has been applied in the context of porous single crystals with viscoplastic and ideally-plastic matrix phase. Nevertheless, in real life applications, the mechanical behavior of the materials under consideration exhibits also elastic effects. Consequently, it would be of great importance to be able to incorporate elastic effects in the above described models, which would allow the study of "elasto-viscoplastic" porous single crystals. The variational methodology introduced by Lahellec and Suquet [2007a,b,c, 2013] to get estimates for the effective response and evolution of microstructure in elasto-plastic or elasto-viscoplastic porous media can be applied in order to achieve this goal.

In addition to the elasticity effects, one should also introduce hardening effects through the framework depicted in Chapter 2, together which the possible development of instabilities, i.e. localization to failure (see for instance Danas and Ponte Castañeda [2012]). Thus, we would be able to treat more realistic problems such as metal ductile fracture and fatigue at the level of the grains. In the case of fatigue, a non-monotonic load is applied leading to unloading and unstable behaviors in the porous single crystal. In the appendix, as a first step, an investigation of the effect of cyclic loading conditions and finite deformations upon microstructure evolution and material softening/hardening using finite element (FEM) periodic unit-cell calculations is carried out with 3D geometry at small and large number of cycles. Then, as it has been the case for isotropic materials (see Danas and Aravas [2012]), the MVAR could then be implemented to standard finite element packages for solving real life applications such as rolling or extrusion of metals, ductile fracture, necking of specimens or mechanical behavior of Lotus-type metals for biological applications.

Furthermore, it is important to precise that since the present model deals with intragranular damage, the link has to be made with other studies related to damage at grain boundaries (e.g. Pouillier et al. [2012], Bourcier et al. [2013]) in order to obtain a full model for polycrystals. At this point, it appears important to mention recent contributions that deal with either polycrystalline solids with intergranular cavities (Lebensonh et al. [2011]) or polycrystals with two populations of (intergranular and intragranular) voids (Vincent et al. [2014a,b]), typical for nuclear fuel commonly used in nuclear reactors. In the last context, i.e. two populations of voids, the authors have carried a two scale homogenization, but with an isotropic J_2 matrix for the grain. Thus, since our findings indicate strong dependence of the damage upon slip systems number and orientation, it should be interesting to use the present anisotropic ductile damage growth model in the two scale homogenization procedure. Moreover, it is well known that when the voids lie inside the grain or the cracks are in the scale of grains, the strain-gradient effects with (Niordson and Legarth [2010], Vernerey et al. [2007]) or without (Monchiet and Kondo [2013]) crystal plasticity can have a significant impact on material response (see Miehe et al. [1999], Watanabe et al. [2010]). However, in the present study, we have not used a strain gradient plasticity model (as for instance Forest et al. [2011], Danas et al. [2012], Nielsen and Niordson [2013, 2014]) and thus, the deformation state in the present study doesn't depend upon grain size.

Finally, recent industrial problems such as lost foam casting process or 3D printing constitute very interesting challenges as applications for porous single crystals and polycrystals modeling. Indeed, it is essential to be able to provide estimates for the mechanical behavior of porous materials obtained from these manufacturing process, since in most of the cases, they are subjected to complicated loading conditions leading to failure.

Appendix A

Appendix. Void shape effects of periodic elasto-plastic materials subjected to cyclic loading

Cyclic loading of metallic materials has always attracted a lot of attention in the scientific and industrial community due to its impact in the numerous low and high cycle fatigue applications. A priori, the response of a metal under cyclic loading conditions is a multi-scale problem and several mechanisms at the microscale (e.g., dislocation structures at the scale of 1-10 μm) and meso-scale (e.g., hard precipitates and pores or cracks) lead to damage at different scales and finally initiate fatigue of the material at the macroscale. This makes the analysis and modeling of cyclic loading a very tedious work in the sense that to-date it is very difficult to propose a micromechanics-based model that spans the fatigue mechanisms in all the scales. Nonetheless, a lot of studies have been made at several length scales and many of the mechanisms in cyclic loadings have been identified.

In the high cycle regime that plasticity is strongly confined, Dang Van [1971] (see also Papadopoulos [1987] and Constantinescu et al. [2003]) proposed pressure dependent fatigue criteria based on a combined homogenization and phenomenological approach. Numerical modelling of the two scale approach (Bertolino et al. [2007], Hofmann et al. [2009], Guerchais et al. [2014]) shows that the pressure is the footprint of the residual stress created by the localized plasticity at the grains scale. In turn, in the low cycle regime, where plasticity is more spread at numerous grains, only phenomenological and statistically-based fatigue criteria have been proposed (see

for example Amiable et al. [2006a,b] and Tabibian et al. [2013]). Mean stress effects on high strength steels have been discussed already by Koh and Stephens [1991] and Kondo et al. [2003]. Recently, Morel and Bastard [2003] and Maitournam et al. [2011] for high-cycle fatigue and Tabibian et al. [2012] for low-cycle fatigue have experimentally shown the effect of multi-axial loading effects, and particularly of pressure, upon the cyclic response of steels and aluminium alloys and have introduced similar parameters for taking into account the mean stress effect. The fact that fatigue criteria, which are based on strong experimental evidence, include pressure dependence, is in striking contradiction with the common modeling of such materials using pressure-independent plasticity laws, both crystal plasticity and isotropic plasticity with or without kinematic hardening.

More specifically, advances in imaging techniques (SEM and tomography) have revealed the presence of voids in metals. In a recent study, Limodin et al. [2014]and Wang et al. have obtained 3D tomographic images (see Fig. A.1) for aluminum alloys obtained by lost-foam-casting fabrication techniques. As shown in Fig. A.1c, voids of several sizes and shapes (spherical, ellipsoidal but also non-canonical) are observed. In the same figure, the different colors indicate families of voids of similar shapes (but not size or orientation), while two representative voids are pointed out by arrows. One is an almost spherical void (with aspect ratios $w_1 \approx w_2 \approx 1$ and the other is a prolate void with average shape $w_1 \approx w_2 \approx 2$ (see Fig. A.5a for a detailed definition of void aspect ratios). It is further noted that the size of the voids ranges between $50-500\,\mu m$ with grain size in the order of $50-100\,\mu m$.

A.1   Introduction

Motivated by the tomographic image in Fig. A.1, a more physics-based way to include such pressure dependence at the material level is the use of void microstructures[1] embedded in an otherwise plastically incompressible matrix phase. These voids or cracks, which could be present in the material *ab initio* or be nucleated around precipitates and particles in the course of deformation (Essmann et al. [1981]), could be smaller, equal or larger than the size of the grains. The voids therefore can have sizes from

---

[1]To avoid any misunderstanding with the different communities in mechanics and material science, we precise here that the word "microstructure" refers, henceforth, to the voids.

$D = 5.13\text{mm}$ $D \times H = 4.8\text{mm} \times 3.9\text{mm}$

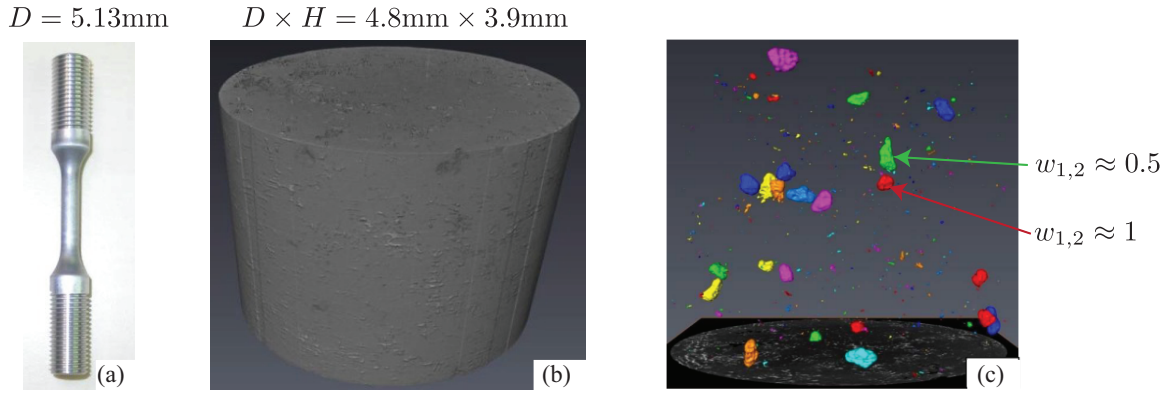$w_{1,2} \approx 0.5$

$w_{1,2} \approx 1$

Figure A.1: (a) The original uniaxial tension specimen with effective diameter $D = 5.13\text{mm}$. (b) Cylindrical volume taken from the original specimen from the effective area for X-ray tomographic observation. (c) Voids of sizes ranging between $50 - 500\,\mu m$. The two arrows show voids with average aspect ratios $w_1 \approx w_2 \approx 2$ (prolate ellipsoidal shape) and $w_1 \approx w_2 \approx 1$ (average spherical shape). Courtesy of N. Limodin and E. Charkaluk.

a few microns (e.g., 1-10 μm) to hundreds of microns (larger than 200 μm). The presence of the pore, in turn, gives rise to a compressible response of the composite material in the plastic region, and hence to pressure dependence. This is achieved by transforming the mean stress applied at the macroscale to a local shearing of the matrix material near the void surface.

As a consequence, the material is now viewed as a two-phase composite system comprising the void phase and the matrix phase. The matrix phase, depending on which scale we refer to, could be the grain or an ensemble of grains. In the first case, that the voids lie inside the grain or the cracks are in the scale of grains, it was shown that the strain-gradient effects with (Niordson and Legarth [2010], Vernerey et al. [2007] or without (Monchiet and Kondo [2013]) crystal plasticity can have a significant impact on material response Miehe et al. [1999], Watanabe et al. [2010]. In the second case, where the voids are larger than the size of the grains, standard isotropic plasticity could be used to model the response of the material, which is the case in the present study.

While the idea of using porous materials to study ductile fracture of metallic materials subjected to monotonic loading conditions has been used extensively in the literature, very few studies have been carried out in the domain of cyclic response of such materials.

Specifically, in the context of monotonic loading conditions, nonlinear homogenization models and micromechanical models (such as the well-known model of Gurson [1977]) for elasto-plastic porous materials) have been used for the prediction of pressure dependent material behavior. In the context of nonlinear homogenization techniques, Ponte Castañeda [1991a] (see also Michel and Suquet [1992] for a parallel development using a different approach) has proposed a linear comparison composite method initially applied to isotropic porous materials. In a later stage, these techniques have been extended to include in an accurate manner general ellipsoidal void shapes (see for instance the recent works of Danas and Ponte Castañeda [2009a] and Danas and Aravas [2012]). In a parallel development, extensions of the Gurson model either for isotropic void shapes (see for instance Tvergaard and Needleman [1984] and Mear and Hutchinson [1985]) or spheroidal (Gologanu and Leblond [1993], Benzerga and Besson [2001], Monchiet et al. [2006]) and ellipsoidal (Madou and Leblond [2012b]) void shapes have been proposed. Such material systems have also been analyzed very early using numerical finite element methods (see for instance the seminal work of Koplik and Needleman [1988]), and are still addressed by recent works (see for instance Tvergaard [2011], Nielsen and Tvergaard [2011], Tvergaard [2012], Tekoğlu et al. [2012]). In these works, the pressure dependence has been studied via the stress triaxiality, denoted here by X_Σ and defined as the ratio of the mean stress to the von Mises equivalent or effective deviatoric stress. More recently, the Lode angle θ, which is directly related to the third invariant of the deviatoric stress tensor, has been identified experimentally (Barsoum and Faleskog [2007a]) as an important loading parameter, especially at low stress triaxialities. Numerical simulations (Zhang et al. [2001]) and analytical micromechanical models have been proposed in this regard (Nahshon and Hutchinson [2008], Danas and Ponte Castañeda [2012]).

Nevertheless, most of the above studies have been carried out in the context of monotonic loading conditions. Even though the material is initially the same, the evolution of the void size and shape in cyclic loading conditions is markedly different than in the context of monotonic loadings. Yet, much less has been done in the context of cyclic loading conditions. Specifically, Monchiet et al. [2008b] have used a micromechanical model for porous materials to explain the mean stress effect in high cycle fatigue. Furthermore, Devaux et al. [1997], Besson and Guillemer-Neel [2003] and Rabold and Kuna [2005] have explored numerically the cyclic response of

porous materials at small and moderate number of cycles with a main emphasis on axisymmetric loading states at large strains. Their analysis has mainly focused on the prediction of porosity ratcheting, whereby the underlying void shape changes have not been studied in detail. In a similar study, Ristinmaa [1997] has carried out finite-strain unit-cell computations, but for a small number of cycles, concluding that void shape effects have very little effect on porosity ratcheting.

In a slightly different context, Pirondi et al. [2006] and Hommel and Meschke [2010] have used the Gurson [1977] and the Leblond et al. [1995] models, respectively, to investigate the low cycle fatigue response of metallic structures. Rather interestingly, the later found that by including void shape effects (contrary to the first who used Gurson model that includes no void shape effects) could dramatically improve their predictions, even though a large number of additional fitting parameters had to be used. Similar observations regarding the importance of void shape effects upon the cyclic response of porous materials have also been made recently by Carpiuc [2012] who used the model of Danas and Aravas [2012], which includes general ellipsoidal void shapes and orientations. In that study, it was found that void shape changes tend to accumulate in each cycle thus leading to ellipsoidal void shapes and consequently to porosity ratcheting, contrary to the Gurson model that predicts no porosity ratcheting (see Devaux et al. [1997] for more details). Nonetheless, all these homogenization and micromechanical models contain only partial information about the void shape changes (up to a perfect ellipsoidal shape) and as we will see in the following they need to be re-assessed first via numerical calculations such as the present study and ultimately be used to compare with experiments.

A.1.1 Scope of this study

The scope of the present study is to investigate the effect of cyclic loading conditions and finite deformations upon microstructure evolution and material softening/hardening using finite element (FEM) periodic unit-cell calculations with 3D geometry at small and large number of cycles. The matrix material is described by isotropic J_2 plasticity considering the case, described previously, of the voids being much larger than the grain size but smaller than the specimen size. Nonetheless, the results obtained in the present study could still be valid, at least in a qualitative man-

ner, in the case of materials with large, but not strongly anisotropic (e.g., FCC) grains comprising intragranular voids that are not of a nanometer size (Monchiet and Kondo [2013]).

Furthermore, it is worth to impress upon the fact that in the fatigue community, a large majority of studies in the context of cyclic loadings is done using small strain calculations, in order to increase numerical efficiency, and therefore neglect any changes of the underlying microstructure (including void shape effects). As we will see in this work, however, the local strains can be in excess of 50% due to strong localization of the deformation around voids, even if the overall applied strains are small (in the order of a few percent). For that reason and in agreement with the aforementioned micromechanical studies (Devaux et al. [1997], Besson and Guillemer-Neel [2003], Rabold and Kuna [2005]), it is also critical that a finite deformation analysis is carried out in the present work.

Specifically, in section A.2, we describe the unit-cell geometry and the applied loading states at the scale of the microstructure, defined here by the presence of a void in an homogeneous elasto-plastic matrix. Furthermore, we identify the variables used to analyze the cyclic response of the periodic porous medium and the void geometry changes. Next, in section A.3, we present the cyclic response of the unit-cell at small and large number of cycles where we identify the principal micro-deformation mechanisms that lead to an overall softening of the porous material. In the following, in section A.4, we carry out a parametric study in order to investigate the effect of the loading and the initial void shape, respectively, upon the cyclic response of the unit-cell. It should be mentioned here that the above described sections are devoted to a plastically incompressible matrix phase with purely isotropic hardening. However, in Section A.5 preliminary calculations with coupled nonlinear isotropic-kinematic hardening will also be considered showing similar qualitative characteristics with the purely isotropic hardening case. Finally, we conclude with a brief discussion of the main results and perspectives of this study.

A.2   Problem formulation

In this section, we define a periodic porous medium with cubic unit-cell geometry as well as the loading conditions used in this study. The interest in this work is the

analysis of a cubic periodic unit-cell comprising a spherical void positioned at the center. The unit-cell is subjected to periodic average cyclic loading conditions with a constant amplitude of average stress triaxiality and average Lode angle. A critical aspect of the present study is the use of a finite strain analysis contrary to the more common small strain analysis used when studying cyclic loading conditions. This will allow for the evolution of the void geometry due to the local large strains at the current configuration. In this regard, one needs to identify the relevant parameters that are necessary to describe the evolution of the void geometry, in general.

A.2.1 Geometry of the unit-cell

In order to set the stage of the following analysis we first attempt to separate the relevant length-scales of the problem at hand. In this regard, let us consider a three-dimensional specimen as shown in Fig. A.2a. It is common practice to consider that the material is homogeneous and is described by phenomenological constitutive laws (e.g., J_2 plasticity, anisotropic plasticity, etc). In reality, however, this specimen is heterogenous and in several cases of practical interest comprises defects, e.g., impurities, cracks and/or pores at the micron scale (see Fig. A.1) at a scale which is bigger than the scale of the size of the grains but much smaller than the size of the specimen and the scale of variation of the externally applied loading conditions. Furthermore, such a specimen is usually subjected to general loading conditions (such as traction, torsion or a combination of both, etc), whereas at the local level, one finds a rather complicated stress and strain loading state due to the nonlinear macroscopic geometry, which involves both shears and hydrostatic stress states. As already stated in the previous section, it has long been acknowledged that the effect of pressure is primordial in cyclic loading conditions, yet such materials are modeled very often as plastically incompressible. In this work, in order to include (physically) this pressure dependence, we consider that the underlying material that makes up the notched specimen is a periodic medium comprising initially spherical voids distributed with cubic symmetry as shown in Fig. A.2b, whereas the two scales–specimen scale and material scale–are well separated. Even though the choice of a cubic symmetry is an idealized choice, the use of a small initial void volume fraction (i.e., 1%) together with overall low strains (i.e., $< 5\%$) allows for a sufficiently general qualitative analysis without any significant

interactions between neighboring voids, as we will see in the following, at least until very late where void shapes evolve significantly and mesh distortion is prohibitive for further numerical analysis. In addition, the use of a periodic medium allows for a full-field numerical analysis of the material response due to the fact that only one cubic unit-cell (Fig. A.2c) with appropriately defined periodic boundary conditions is needed (Michel et al. [1999]). This single unit-cell can then generate by periodic repetition the entire microstructure of the composite (Fig. A.2b).

More specifically, the presence of voids will immediately give rise to an average hydrostatic stress dependence of the periodic medium at the plastic range since the voids are compressible and hence the average (plastic) strain in the unit-cell will have a non-zero hydrostatic component (i.e., it exhibits compressible plasticity). In order to keep the analysis tractable as well as to simplify our numerical calculations, we will further restrict attention to only triaxial loading states aligned with the symmetries of the unit-cell, thus analyzing only one-eighth of the cube, as shown in Fig. A.2d. This implies that the underlying void will evolve in volume and in shape when finite strains are applied at the level of the unit-cell, but not in orientation [2].

Finally, in this study, we attempt to make no direct coupling between the several scales, i.e., the specimen scale (Fig. A.2a) and the material scale (Fig. A.2b) but mainly to understand the effect of a triaxial stress state upon the cyclic response of a periodic porous material. This, of course, implies further that we cannot carry out any direct comparison with experiments since these require the use of a geometry, such as the one in Fig. A.2a.

On the other hand, this analysis has as a focus to analyze and understand the basic microstructural deformation mechanisms so that (less time-consuming) analytical homogenization models for porous materials (Monchiet et al. [2008a], Danas and Aravas [2012], Madou and Leblond [2012b]) and phenomenological pressure-dependent criteria (Dang Van [1971], Constantinescu et al. [2003], Monchiet et al. [2008b]) can be re-assessed.

---

[2]Orientation effects can readily be included by considering the entire unit-cell but this is left for a future study since this would introduce a large number of additional set of parameters to be investigated and would make the present work too lengthy
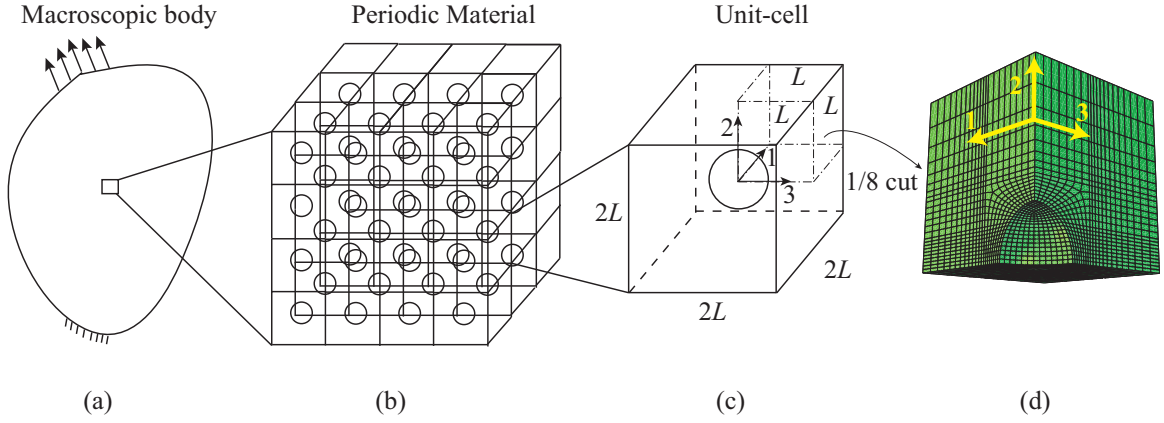
Figure A.2: (a) A three-dimensional specimen at the macroscopic scale made-up of a periodic porous material. (b) A periodic porous material with cubic symmetry at the micron scale. (c) Geometry of a single cubic unit-cell with a void at the center and (d) mesh of the 1/8 cut of the unit-cell geometry.

A.2.2 Periodic boundary conditions and cyclic loads

We consider a cubic unit-cell occupying a volume V with side length of $2L$ and boundary ∂V that comprises a spherical void at the center, as shown in Fig. A.2c. The matrix phase is described by an isotropic elasto-plastic constitutive law as described later in this section.

The unit-cell is subjected to triaxial periodic boundary conditions, so that the velocity field $\dot{\mathbf{u}}$ (the superposed dot denotes time derivative) can be split into an affine part $\boldsymbol{D} \cdot \mathbf{x}$ and a correction $\dot{\mathbf{u}}^*$, i.e., (Michel et al. [1999], Miehe et al. [1999])

$$\dot{\mathbf{u}}(\mathbf{x}) = \boldsymbol{D} \cdot \mathbf{x} + \dot{\mathbf{u}}^*(\mathbf{x}), \ \dot{\mathbf{u}}^* \text{ periodic.} \tag{A.1}$$

The second-order tensor $\boldsymbol{D}$, characterising the affine part, corresponds to the average strain-rate field in the periodic medium (i.e., the actual strain-rate field of the unit-cell if it were homogeneous) and is defined via the local field $\tilde{\boldsymbol{D}}$ which admits the following decomposition

$$\tilde{\boldsymbol{D}}(\mathbf{x}) = \boldsymbol{D} + \boldsymbol{D}^*(\mathbf{x}), \qquad \boldsymbol{D} = \frac{1}{V} \int_V \tilde{\boldsymbol{D}}(\mathbf{x}) \mathrm{d}V, \qquad \frac{1}{V} \int_V \boldsymbol{D}^*(\mathbf{x}) \mathrm{d}V = 0. \tag{A.2}$$

The average strain $\dot{\boldsymbol{\varepsilon}}$ at a given time t in the unit-cell is expressed by

$$\dot{\boldsymbol{\varepsilon}}(t) = \int_0^t \boldsymbol{D}(\tau) \, \mathrm{d}\tau. \tag{A.3}$$

In turn, the average stress $\boldsymbol{\sigma}$ (i.e., the actual stress field of the unit-cell if it were homogeneous) is defined formally in terms of the local stress field $\tilde{\boldsymbol{\sigma}}$ via
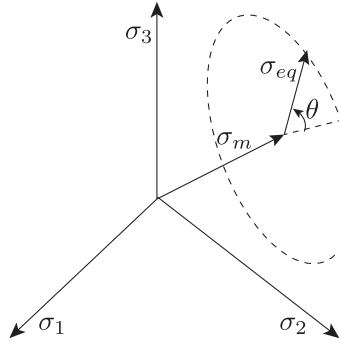
$$\boldsymbol{\sigma} = \frac{1}{V} \int_V \tilde{\boldsymbol{\sigma}}(\mathbf{x}) \mathrm{d}V, \tag{A.4}$$

where $\tilde{\boldsymbol{\sigma}}$ satisfies the following equilibrium equations and periodic boundary conditions, i.e.,

$$\mathrm{div}\,\tilde{\boldsymbol{\sigma}} = 0 \ \text{ in } \ V, \qquad \tilde{\boldsymbol{\sigma}} \cdot \mathbf{n} - \# \ \text{ on } \partial V. \tag{A.5}$$

In this expression, $\mathbf{n}$ denotes the normal to the exterior faces of the unit cell and $-\#$ is used to denote that the traction is opposite on opposite sides of the unit-cell. Henceforth, the use of the quantities $\boldsymbol{\sigma}$, $\boldsymbol{D}$ and $\dot{\boldsymbol{\varepsilon}}$ (and of any other quantity resulting from those) refers unambiguously to the average (or macroscopic) stress, strain-rate and strain fields in the unit-cell.

a)   b)
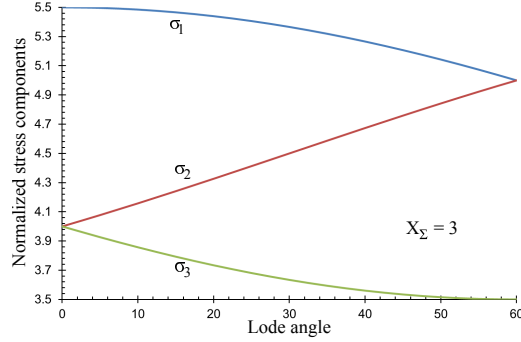

Figure A.3: (a) Schematic representation of the principal stress $(\sigma_1, \sigma_2, \sigma_3)$ cartesian system and the $(\sigma_m, \sigma_{eq}, \theta)$ cylindrical system. (b) Components of the normalized stress $3\sigma_i/2\sigma_{eq}$, $i = 1, 2, 3$ as a function of the Lode angle θ in the case of $X_\Sigma = 3$.

Table A.1: Ordering of the principal stresses for different Lode angles. The relevant directions are shown in Fig. A.2d while their relevant magnitude and graphical representation is shown in

Fig. A.3b.

$\theta = 0^o$	$\theta = 30^o$	$\theta = 60^o$
$\lvert\sigma_1\rvert > \lvert\sigma_2\rvert = \lvert\sigma_3\rvert$	$\lvert\sigma_1\rvert > \lvert\sigma_2\rvert > \lvert\sigma_3\rvert$	$\lvert\sigma_1\rvert = \lvert\sigma_2\rvert > \lvert\sigma_3\rvert$

As a consequence of the presence of the void, the average response of the unit-cell depends upon the average hydrostatic pressure (or mean average stress) as well as the

deviatoric part of the average stress tensor. Thus, it is useful to define at this point the average stress triaxiality, X_Σ, and average Lode angle, θ, in the unit-cell as measures of the average stress state in the unit-cell, such that

$$X_\Sigma = \frac{\sigma_m}{\sigma_{eq}}, \quad \cos(3\theta) = \frac{27}{2} \det\left(\frac{\boldsymbol{\sigma}'}{\sigma_{eq}}\right), \quad \sigma_m = \frac{1}{3}\sigma_{kk}, \quad \sigma_{eq} = \sqrt{\frac{3}{2}\boldsymbol{\sigma}' : \boldsymbol{\sigma}'}, \quad \text{(A.6)}$$

with $\boldsymbol{\sigma}' = \boldsymbol{\sigma} - \sigma_m\mathbf{I}$ denoting the stress deviator and $\mathbf{I}$ the second-order identity tensor. Using the definitions in equation (A.6), one can write the principal components of the stress field as a function of X_Σ and θ, via

$$\frac{3}{2\sigma_{eq}}\{\sigma_1, \sigma_2, \sigma_3\} = \left\{\cos\theta, -\cos\left(\theta + \frac{\pi}{3}\right), -\cos\left(\theta - \frac{\pi}{3}\right)\right\} + \frac{3}{2}X_\Sigma\{1, 1, 1\}. \quad \text{(A.7)}$$

The graphical illustration of the above relations is shown in Figure A.3. The $(\sigma_m, \sigma_{eq}, \theta)$ coordinates define a cylindrical coordinate system oriented along the hydrostatic axis σ_m, as shown in Fig. A.3a. In Fig. A.3b the normalized stress components, $3\sigma_i/2\sigma_{eq}$ are depicted as a function of the Lode angle θ for a stress triaxiality $X_\Sigma = 3$. Note that due to the $\pi/3$ periodicity of the functions used in relation (A.7), the three principal stresses exhibit similar periodicity. For later use, we also show explicitly in Table 1 the order of the stress components for three representative Lode angles that will be used in the following sections. Note that in the case of an initially non-spherical shape a larger range of Lode angles (i.e., $\theta > 60^o$) could be considered. However, for the sake of brevity, we will restrict attention only to the aforementioned Lode angles.

In the following, we focus on purely triaxial loading conditions aligned with the symmetry planes of the cubic unit-cell and the underlying void microstructure. This allows for numerical simplicity while keeping essential features of the void geometry changes. This leads to the following Dirichlet-type boundary conditions

$$\begin{cases} u_1(0, x_2, x_3) = 0, & u_1(L, x_2, x_3) = U_1(t), \\ u_2(x_1, 0, x_3) = 0, & u_2(x_1, L, x_3) = U_2(t), \\ u_3(x_1, x_2, 0) = 0, & u_3(x_1, x_2, L) = U_3(t). \end{cases} \quad \text{(A.8)}$$

with $\mathbf{u}^* = 0$ on ∂V. This implies that the external faces of the unit-cell remain straight (Michel and Suquet [1994], Garajeu et al. [2000]) and hence only 1/8 of the unit cell may be considered, as shown in Fig. A.2d. In turn, the void surface is traction free.

Before we define the cyclic loading in terms of the displacements $U_i(t)$ ($i = 1, 2, 3$), we first have to apply of a constant stress triaxiality and Lode angle during a given deformation process, following the methodology described in chapter 4.
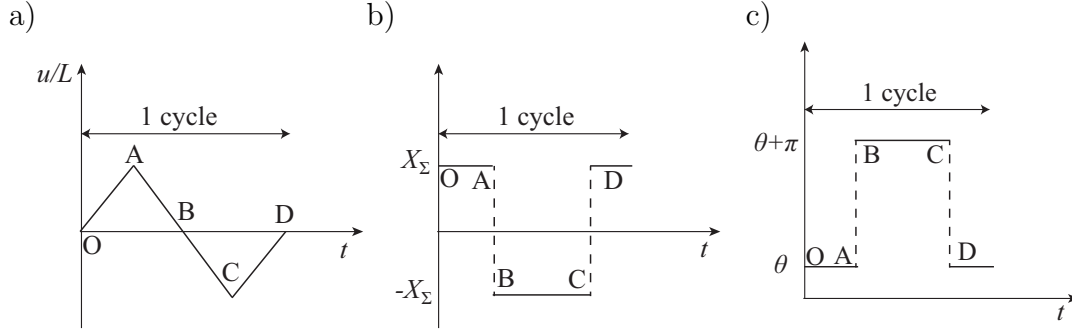
a)   b)   c)

Figure A.4: Schematic explanation of the application of the cyclic loading and the corresponding qualitative values of (a) the applied displacement u, (b) the applied stress triaxiality X_Σ and (c) the applied Lode angle θ as a function of time for one cycle.

Using the above definitions, we divide each cycle in four steps. In each step of each cycle, as shown in Fig. A.4a, we control the average strain in the unit-cell, by setting $u(t)/L \equiv p_1^G(t)$[3]. This quantity, u/L, initially increases from O to A (step 1), unloads from A to B (step 2), reversely loads from B to C (step 3) and unloads from C to D (step 4) defining thus an entire cycle. Then, the average strain-rate $\boldsymbol{D}$ is evaluated such that the stress triaxiality X_Σ and Lode angle θ remain constant in each step as discussed previously and as shown in Fig. A.4b and Fig. A.4c. Note in these figures that in order to obtain full stress reversibility during the cycle, X_Σ has to change sign and θ has to jump to $\theta + \pi$ between A-D. For convenience, hereafter, the notations X_Σ and θ are used to denote unambiguously the absolute value of the stress triaxiality (i.e., $X_\Sigma \equiv |X_\Sigma|$) and the minimum value of the Lode angle (i.e., $\theta \equiv \cos^{-1} |\cos \theta|$) in each cycle A-D.

In the following calculations, the matrix phase is described by an elasto-plastic constitutive relation. The elastic part is defined via the Young's modulus E and the Poisson ratio ν. In turn, standard J_2 plasticity theory is used to describe the plastic behavior of the matrix together with an isotropic strain hardening law (except in Section A.5 where a nonlinear kinematic hardening law is also added) given by a power-law form, which reads

$$\sigma_y = \sigma_0 \left(1 + \frac{\varepsilon^p}{\varepsilon_0} \right)^{1/N}, \qquad \varepsilon_0 = \sigma_0/E. \tag{A.9}$$

Here, σ_0 and ε_0 denote the initial yield stress and yield strain of the matrix material,

---

[3]Note that the functional form of $p_1^G(t)$ is irrelevant since the problem is time-independent.

N is the hardening exponent and ε^p is the accumulated plastic strain in the matrix phase defined in the usual way. In this study, we focus on realistic values of the elastic moduli, e.g., Young's modulus, $E \sim 1000\sigma_0$ (for instance $\sigma_0 \sim 200\text{MPa}$ corresponding to steel), Poisson's ratio, $\nu = 0.3$ and hardening exponent, $N = 10$. Nonetheless, one should point out that particularly in cyclic loading conditions, the effect of elasticity and hardening could be important as already discussed in Devaux et al. [1997], and such an analysis is detailed in Appendix A.7.

A.2.3 Evolution of void geometry

In this section, we introduce the variables used to characterize the evolution of the change in volume and shape of the void. More specifically, the porosity (i.e., the volume fraction of the void in the unit-cell) is defined as

$$f = V_v/V = 1 - V_m/V, \qquad V = V_m + V_v, \tag{A.10}$$

where V_v, V_m and V are the volume of the void, the matrix and the total volume of the unit-cell, respectively. Here V_m is calculated as the sum of each volume element, while the unit-cell volume V is evaluated using the coordinates of the corner nodes of the cubic unit-cell since due to symmetry of the void and the purely triaxial loading conditions the external faces of the cell remain straight. As a consequence of the
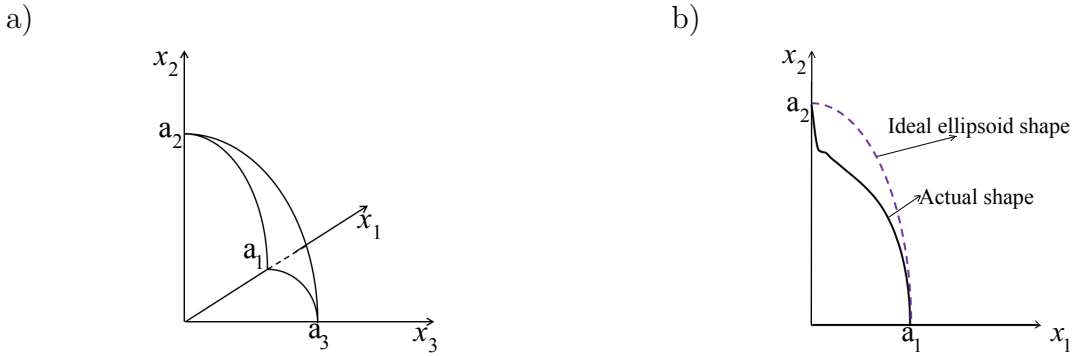
a)   b)

Figure A.5: (a) Schematic representation of 1/8 of the surface of a perfect ellipsoidal void defined by three semi-axes a_i ($i = 1, 2, 3$). (b) Cross-section of the void surface in the $x_1 - x_2$ plane where a representative difference between the actual void shape and an ideal ellipsoid shape having the same aspect ratios.

finite deformations considered in this study, significant changes in the pore shape are

also observed. Therefore, appropriate geometrical quantities need to be introduced in order to evaluate such pore shape changes. As a first-order measure, the void shape is characterized by two aspect ratios

$$w_1 = a_3/a_1, \qquad w_2 = a_3/a_2 \tag{A.11}$$

where $2a_i$ (with $i = 1, 2, 3$) denote the current lengths of the axes of the void that intersect with the coordinate axes x_i (with $i = 1, 2, 3$), respectively, as shown on Fig. A.5a. However, such a measure will be shown in the following to be insufficient since the void obtains markedly non-ellipsoidal shapes due to the cyclic loadings as opposed to the purely monotonic loadings where almost ellipsoidal shapes are observed (Srivastava and Needleman [2012]). In this regard then, as an additional measure of the pore geometry change, we have also defined the *ellipsoidicity* ratio. This ratio has been introduced as a measure of the divergence of the void geometry from an equivalent perfect ellipsoid, as depicted in Fig. A.5b. While a large number of options can be used to identify this difference, use is made here of a simple measure. First, we set the axes of the ideal ellipsoid equal to the length of the actual void axes. Then, the volume of the ideal ellipsoid, V_e, will in general be different from that of the actual void V_v due to the nonlinearity of the matrix phase, the interactions of the neighboring voids of the periodic composite and more importantly due to the cyclic loading conditions. Therefore, the ellipsoidicity ratio, $\mathcal{E}_l$ defined via

$$\mathcal{E}_l = V_e/V_v \tag{A.12}$$

gives the difference of the actual void shape from that of a perfect ellipsoid. Consequently, when the ellipsoidicity ratio takes values close to unity, the void shape remains almost an ellipsoid.

The above microstructural variables will be used in the following to analyze the micromechanisms that lead to an the material softening / hardening due to the applied cyclic loading conditions. It should be noted here that due to the cubic symmetry of the unit-cell and the purely triaxial loading conditions no void rotations are obtained.

A.3 Cyclic response and microstructure evolution

In this section, we discuss the results obtained by the previously described loading conditions. The cyclic loading conditions are parametrized by the use of two different

values of the stress triaxiality $X_\Sigma = 2/3, 3$ and three different values of the Lode angle $\theta = 0^o, 30^o, 60^o$ are used [4]. For the low triaxiality $X_\Sigma = 2/3$, we set the average strain amplitude $u/L = 5\%$ and for the high triaxiality $X_\Sigma = 3$, we set the average strain amplitude $u/L = 1\%$. The difference in amplitudes has been introduced for convenience with the calculation time needed to observe significant void geometry changes and/or localization of the strain at certain region of the unit-cell. Two sets of computations have been carried out: (i) for a small number of cycles, e.g., 5 cycles and (ii) for a large number of cycles, e.g., ≈ 50 cycles.

Moreover, for convenience with the meshing, we use an initial porosity $f = 1\%$, which corresponds to a void radius $a/L = 0.2673$, and a maximum of 32×10^4 degrees of freedom, which leads to an average of 2.5 hours computational time per cycle on a 12-cpu parallel computation. A detailed discussion of dependency of the results upon the mesh size is carried out in the Appendix A.8.
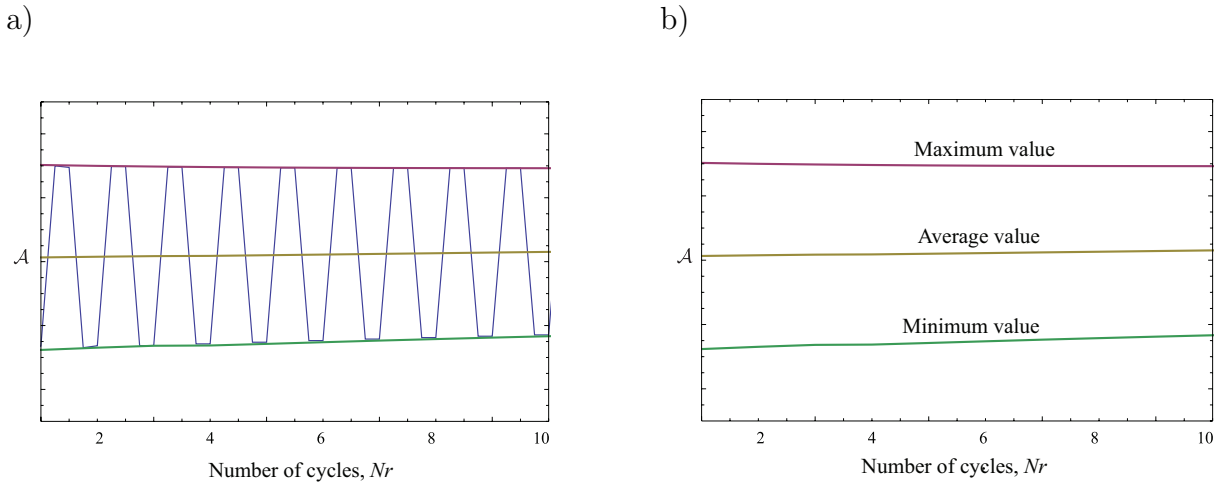
a)

b)

Figure A.6: Qualitative description of the cyclic response of a variable $\mathcal{A}$ (e.g., plastic strain, porosity, void shape change) as a function of the number of cycles Nr. The minimum, maximum and average values of $\mathcal{A}$ are extracted by the corresponding cyclic response.

In order to clarify further the results in the following sections, we include Fig. A.6, where for a given variable $\mathcal{A}$ (e.g., porosity, aspect ratios, ellipsoidicity, etc), an average quantity per cycle is defined as the arithmetic mean of the maximum and the minimum value per cycle. In the same figure, the flat, horizontal part of the curves corresponds

---

[4]Recall that the notation $X_\Sigma = 2/3$ and $\theta = 0^o$, for instance, corresponds to $|X_\Sigma| = 2/3$ and $\theta = \cos^{-1}|\cos\theta|$ according to the discussion made in the context of Fig. A.4.

to elastic unloading. On the other hand, the average von Mises stress per cycle is evaluated at the end of the first step of each cycle, as those are defined in the context of Fig. A.4.

A.3.1   Small number of cycles

In Fig. A.7, we consider stress-strain results for 5 cycles, a low stress triaxiality $X_\Sigma = 2/3$ and Lode angle $\theta = 0^o$ (with $u/L = 5\%$). Specifically, we show two normalized average principal stresses, (a) σ_1/σ_0 and (b) σ_2/σ_0, in the unit-cell as functions of the average components of the strains, ε_1 and ε_2, respectively. We focus on these two stress components since Lode angle $\theta = 0^o$ corresponds to an axisymmetric stress state case (see Table 1) and hence the third stress component is equal to the second one. In Fig. A.7a, we observe a common stress-strain cyclic response where in the first cycle a hardening is obtained in both tension and compression. This hardening tends to saturate rather fast due to the low hardening exponent used in this case, as observed by the use of the notation $C1$, $C2$, $C3$, $C4$, $C5$ which serve to identify each of the 5 cycles. In Fig. A.7b, the second average stress-strain response is similar to the first one but with a different sign of the strain due to the plastic incompressibility of the matrix. Note however that the average plastic response of the unit-cell is not incompressible due to the presence of the void, however, due to the low stress triaxiality in this example, this is only slightly visible by noting the small asymmetry of the curve in Fig. A.7b with respect to the average strain ε_2.

In Fig. A.8, we consider stress-strain results for 5 cycles, a low stress triaxiality $X_\Sigma = 3$ and Lode angle $\theta = 0^o$ (with $u/L = 1\%$). Similarly, we show two normalized average principal stresses, (a) σ_1/σ_0 and (b) σ_2/σ_0, in the unit-cell as functions of the average components of the strains, ε_1 and ε_2, respectively. As observed in Fig. A.8a, the material significantly softens during the cycle when ε_1 is (positive) tensile while it hardens when ε_1 is (negative) compressive. As will be seen next, this is due to the evolution of the porosity (i.e., void volume fraction), which increases for $\varepsilon_1 > 0$ and decreases for $\varepsilon_1 < 0$. This leads, in turn, to a significant asymmetry of the stress-strain response between positive and negative stress triaxialities (i.e., between tension and compression) which is markedly different than the corresponding stress-strain response at the lower stress triaxiality of $X_\Sigma = 2/3$ of the previous figure. Note
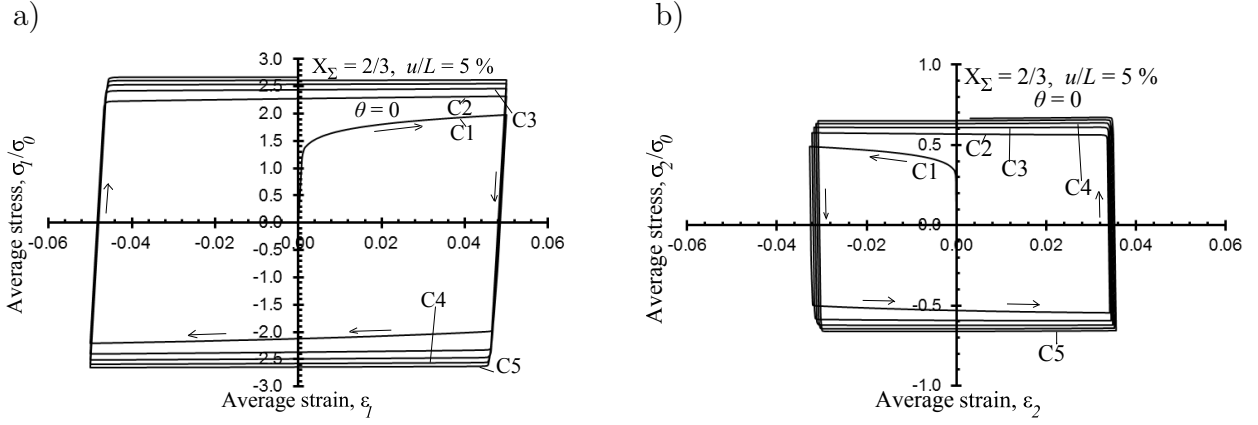
a)

b)

Figure A.7: (a) Normalized average stress σ_1/σ_0 as a function of the average strain ε_1 and (b) normalized average stress σ_2/σ_0 as a function of the average strain ε_2 at 5 cycles in the case of $u/L = 5\%$, $X_\Sigma = 2/3$, $\theta = 0^o$. The notation $C1$, $C2$, $C3$, $C4$, $C5$ represents the first, second, third, fourth and fifth cycle, respectively.
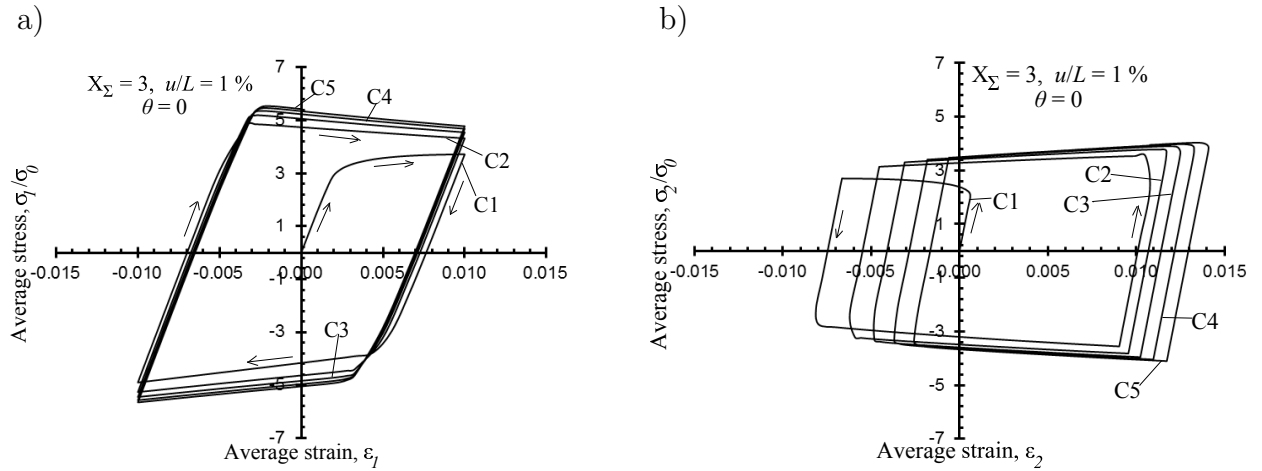
a)

b)

Figure A.8: (a) Normalized average stress σ_1/σ_0 as a function of the average strain ε_1 and (b) normalized average stress σ_2/σ_0 as a function of the average strain ε_2 at 5 cycles in the case of $u/L = 1\%$, $X_\Sigma = 3$, $\theta = 0^o$. The notation $C1$, $C2$, $C3$, $C4$, $C5$ represents the first, second, third, fourth and fifth cycle, respectively.

that the observed asymmetry is not due to a Bauschinger effect but is strongly related to the evolution of the void geometry as will be seen in the following. This asymmetry has also been identified in the context of uniaxial yielding by Cazacu et al. [2014a] as a possible cause of swift effect Swift [1947] i.e. the occurrence of inelastic axial effects. On the other hand, in Fig. A.8b, we observe a strong asymmetry in the strain axis.

This is due to the high triaxiality loading used in this case ($X_\Sigma = 3$), resulting to a highly compressible plastic response of the unit-cell.
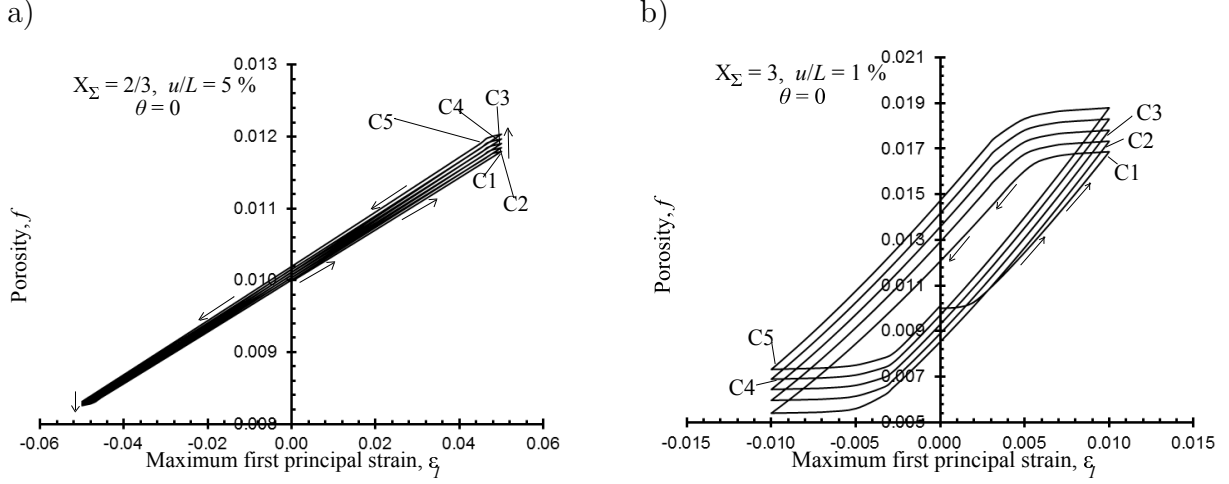
a)

b)

Figure A.9: Evolution of porosity f as a function of the average first principal strain at 5 cycles in the cases of (a) $u/L = 5\%$, $X_\Sigma = 2/3$, $\theta = 0^o$ and (b) $u/L = 1\%$, $X_\Sigma = 3$, $\theta = 0^o$. The notation $C1$, $C2$, $C3$, $C4$, $C5$ represents the first, second, third, fourth and fifth cycle, respectively.

In Fig. A.9, we discuss the evolution of the porosity f for the two afore-mentioned stress triaxialities, i.e., for (a) $X_\Sigma = 2/3$ and (b) $X_\Sigma = 3$ with $\theta = 0^o$ as a function of the average strain ε_1. As shown in Fig. A.9a, only a minor porosity ratcheting is observed if one observes the extremities of the cyclic curves at positive strains. In addition, as already stated previously, f increases for $\varepsilon_1 > 0$ and decreases for $\varepsilon_1 < 0$, as intuitively expected. On the contrary, porosity evolution is much more significant for $X_\Sigma = 3$, as observed in Fig. A.9b, where porosity grows by almost 50% (note the crossing of the f curves at $\varepsilon_1 = 0$) after only 5 cycles. This can explain the observed asymmetry of the stress-strain curve with respect to the strain ε_2 in Fig. A.8b.

At this point, it is worth noting that the observed effect of stress triaxiality upon the above-discussed stress-strain responses and porosity ratcheting, for a matrix with purely isotropic hardening, is in full qualitative agreement with the results presented by Rabold and Kuna [2005] in the context of combined isotropic and kinematic hardening. This, further, implies that the hardening characteristics of the matrix phase affect only quantitatively, but not qualitatively, the evolution of the void volume and shape. This observation is further confirmed in Section A.5.
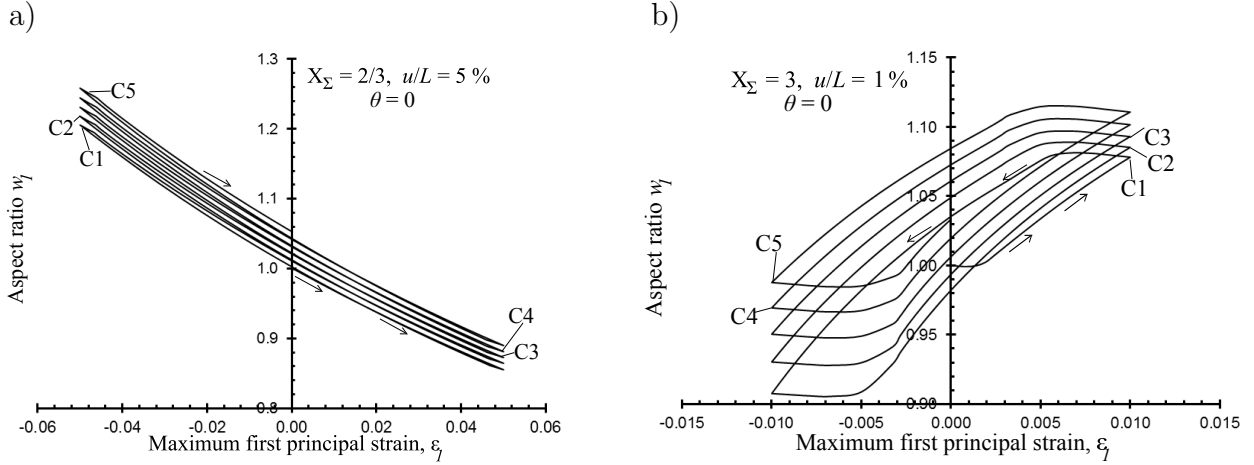
a)

b)

Figure A.10: Evolution of the aspect ratio w_1 as a function of the average strain ε_1 at 5 cycles in the cases of (a) $X_\Sigma = 2/3$ ($u/L = 5\%$) and (b) $X_\Sigma = 3$ ($u/L = 1\%$) with $\theta = 0^o$. The notation $C1$, $C2$, $C3$, $C4$, $C5$ represents the first, second, third, fourth and fifth cycle, respectively. Due to the axisymmetric loading ($\theta = 0^o$) $w_2 = 1$ during the entire deformation process.

Figure A.10 shows the evolution of the void shape via the evolution of the aspect ratio w_1 for the two stress triaxialities (a) $X_\Sigma = 2/3$ and (b) $X_\Sigma = 3$ with $\theta = 0^o$ as a function of the average strain ε_1. Note that the second aspect ratio $w_2 = 1$, since for $\theta = 0^o$ the loading is axisymmetric along x_1 (i.e., $|\sigma_2| = |\sigma_3|$). More specifically, in Fig. A.10a, we observe that for the lower stress triaxiality $X_\Sigma = 2/3$, the void aspect ratio exhibits only a small ratcheting. Interestingly, as the number of cycles increases, the void shape tends to become oblate (i.e., $w_1 > 1$, $a_1 < a_3 = a_2$) even though $|\sigma_1| > |\sigma_2| = |\sigma_3|$ and the aspect ratio decreases in the first step of $C1$, as intuitively expected. However, the very small porosity and aspect ratio ratcheting in this low triaxiality case leads to an almost symmetric stress-strain curve in Fig. A.7. On the other hand, in Fig. A.10b, a significantly asymmetric void shape change with respect to ε_1 is observed. Moreover, as a result of the high stress triaxiality, the void tends to become oblate ($w_1 > 1$, $a_1 < a_3 = a_2$) from the very first loading step even though $|\sigma_1| > |\sigma_2| = |\sigma_3|$. This counterintuitive effect has been attributed to the strong nonlinearity of the matrix and the high triaxiality loading (see Budiansky and Hutchinson [1980] and Fleck and Hutchinson [1986]). More importantly, the oblate shape persists as the number of cycles increases. This is due to the asymmetric response of the unit-cell between $\varepsilon_1 > 0$ and $\varepsilon_1 < 0$. More specifically, we find that

the rate of the void shape change is more significant in the $\varepsilon_1 < 0$ (i.e., in compressive loads) rather than in the $\varepsilon_1 > 0$ (i.e., in tensile loads). This asymmetry can be qualitatively observed by the difference in the slopes of the w_1-ε_1 curves in the $\varepsilon_1 > 0$ and $\varepsilon_1 < 0$ regimes. In turn, this asymmetry in the void shape evolution leads to a permanent irreversible void shape change from the very first cycle (i.e., after the first cycle the void is not spherical), which in turns produces the porosity ratcheting and the asymmetric average stress-strain response in Fig. A.8. At this point it is worth mentioning that the void shape irreversibility and consequently porosity ratcheting are present also for different hardening exponents (including $N \to \infty$ which corresponds to an ideally-plastic response) not shown here for the sake of a reasonable set of parameters investigated.

A.3.2   Large number of cycles

In the previous section, it has been shown that the cyclic behavior of the material, and especially the porosity ratcheting as well as the asymmetric void shape evolution have a strong effect upon the average stress-strain response of the unit-cell. Thus, in order to isolate the effect of porosity evolution and the influence of the void shape change in the cyclic response of the material, a unit-cell geometry with a spherically constrained void shape is further added in our study. It is further clarified here that the spherically constraint void does allow the evolution of the void volume (i.e., void growth) and porosity change but constraints the change of the void shape to remain spherical. This is achieved by imposing a nonlinear kinematic constraint in spherical coordinates allowing a uniform radial displacement of the nodes at the void surface, $u_r = cst$ and arbitrary displacement in the orthoradial directions (i.e. u_{ϕ_1} and u_{ϕ_2} are arbitrary where r, ϕ_1 and ϕ_2 denote the spherical coordinates).

The cases of a spherically "constrained" and a totally "unconstrained" void geometry are compared in the following for a large number of cycles. In the results that are shown subsequently, we stop the calculations at 50 cycles since after this point we observe strong localization of the deformation and the numerical solution diverges significantly. A more detailed discussion about this point is carried out in the Appendix A.8.

In Fig. A.11, we show (a) the normalized average equivalent von Mises stress per

cycle σ_{eq}/σ_0 and (b) the porosity f per cycle as a function of the number of cycles N_r for triaxiality $X_\Sigma = 3$, amplitude $u/L = 1\%$ and Lode angle $\theta = 0^o$ for the unconstrained void shape and the spherically constrained void shape cases. As we can observe in Fig. A.11a, σ_{eq}/σ_0 exhibits a maximum value for the unconstrained void shape (filled square on the curve indicated the position of this maximum) whereas the spherically constrained void calculation exhibits a continuous hardening as a function of N_r. In order to explain this rather interesting difference between the unconstrained and the constrained void shape calculations, we look into the porosity evolution in Fig. A.11b. In this figure, we observe that the increase of porosity, albeit significant, cannot (by itself) explain the softening response observed in the unconstraint void shape calculation in Fig. A.11a, since both the unconstrained void case as well as the spherically constrained void case predict almost the same evolution of the porosity as a function of the number of cycles N_r, but only the first exhibits a maximum in the σ_{eq}/σ_0. (The point where the maximum in σ_{eq}/σ_0 curve is observed is denoted with a filled square in Fig. A.11b.) The fact that the spherically constrained case exhibits also porosity ratcheting can be partially explained by the presence of elasticity and the loading-unloading response of the unit-cell, as discussed in detail in Devaux et al. [1997]. In fact, in the spherically constrained void shape case porosity ratcheting is even more pronounced than in the unconstrained void shape case.
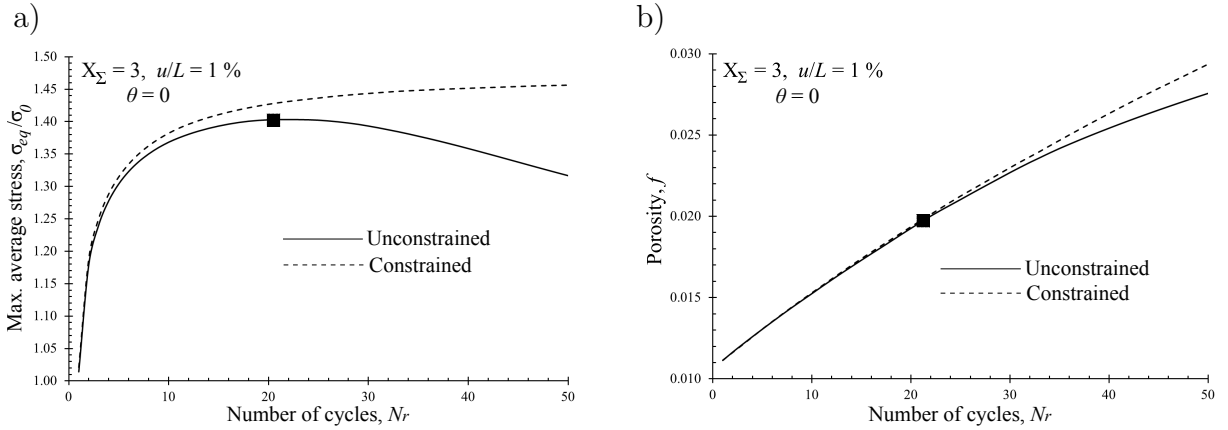
a)

b)

Figure A.11: (a) Normalized average von Mises stress σ_{eq}/σ_0 and (b) porosity f as a function of the number of cycles N_r for an unconstrained void (continuous line) and a spherically constrained void (dashed line) in the case of $X_\Sigma = 3$ and $\theta = 0^o$ ($u/L = 1\%$). The filled square (■) on the graphs indicate the points where maximum equivalent stress is observed.
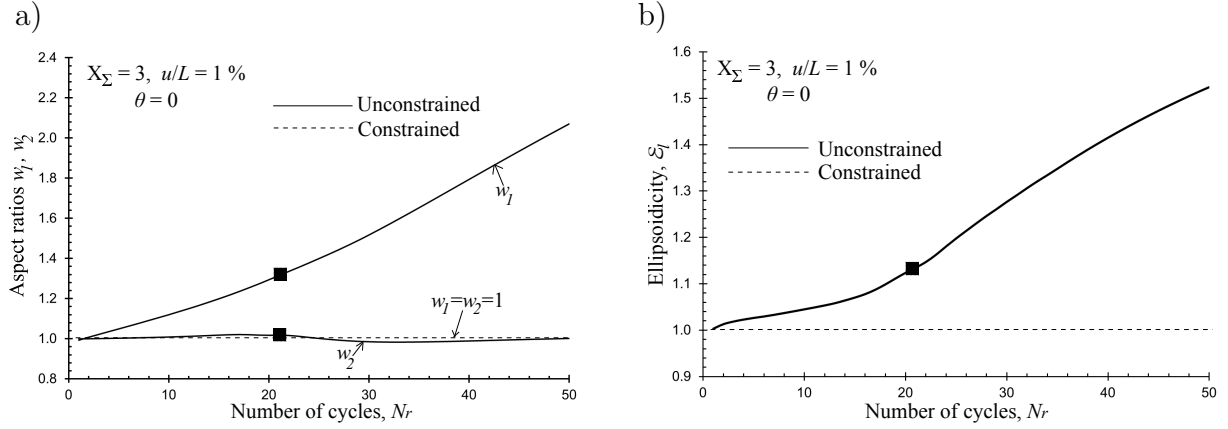
a)

b)

Figure A.12: Evolution of (a) the aspect ratios w_1 and w_2 and (b) the ellipsoidicity ratio $\mathcal{E}_l$ as a function of the number of cycles Nr for an unconstrained void and a spherically constrained void in the case of $X_\Sigma = 3$ and $\theta = 0^o$ ($u/L = 1\%$). The filled square ($\blacksquare$) on the graphs indicate the points where maximum equivalent stress is observed.

This obviously indicates that void shape effects are critical for the understanding of the cyclic response of such unit-cells. In this regard, in Fig. A.12, we show the evolution (a) of the void aspect ratios w_1 and w_2 and (b) of the ellipsoidicity ratio $\mathcal{E}_l$. While $w_2 \simeq 1$ due to the axisymmetric loading along direction 1 (see Table 1 for $\theta = 0^o$), w_1 evolves significantly as a function of the number of cycles N_r. The constrained void shape curve is also shown for clarity (i.e., $w_1 = w_2 = 1$ during the deformation process). Perhaps more importantly, the ellipsoidicity ratio $\mathcal{E}_l$—which serves to measure the deviation of the void shape from an ideal ellipsoidal shape— increases significantly as a function of N_r, in Fig. A.12b. This indicates that not only the void becomes non-spherical but also deviates significantly from an ellipsoidal shape. Detailed contours of the underlying void geometry will be shown in the following. Thus, void geometry appears to be of crucial importance in the cyclic response of such unit-cells. This further suggests that small strains calculations may be insufficient for the analysis of cyclic loadings, at least in the present context where we attempt to analyze the effect of the underlying microstructure upon the average cyclic response of the unit-cell.

A.4 Effect of the loading and the initial void shape

In this section, we carry out a parametric study in order to investigate the influence of the loading conditions, i.e. the stress triaxiality and the Lode angle, as well as the effect of the initial void shape on the cyclic behavior of the periodic porous material. In the following results, the hardening exponent is set to $N = 10$, the Young's modulus $E = 1000\sigma_0$ and the Poisson ratio $\nu = 0.3$.

A.4.1 Effect of the stress triaxiality and the Lode angle

Figure A.13 shows the normalized average equivalent von Mises stress per cycle σ_{eq} as a function of the number of cycles N_r for triaxiality (a) $X_\Sigma = 2/3$ (and amplitude $u/L = 5\%$) and (b) $X_\Sigma = 3$ (and $u/L = 1\%$) as well as for three Lode angles $\theta = 0, 30, 60^o$. The two cases of an unconstrained void and a spherically constrained void are also considered here. The main observation in the context of Fig. A.13 is that the effect of stress triaxiality X_Σ upon the σ_{eq}/σ_0 response is very significant, whereas the effect of the Lode angle is less important (at least at the range of cycles considered here) but still non-negligible. In particular, the average stress σ_{eq}/σ_0 exhibits no softening for the lower stress triaxiality $X_\Sigma = 2/3$ (Fig. A.13a) contrary to the high stress triaxiality $X_\Sigma = 3$ (Fig. A.13b). In addition, in Fig. A.13b, for $X_\Sigma = 3$ and an unconstrained void shape (continuous line), we find that the σ_{eq}/σ_0 response for $\theta = 0^o$ depicts a more pronounced decrease than the two other cases, i.e., $\theta = 30^o$ and $\theta = 60^o$. Again the spherically constrained void case shows no softening for any of the Lode angles considered here. These results indicate that primarily the stress triaxiality and secondary the Lode angle affect critically the average stress-strain response of the unit-cell.

In order to address the role of the stress triaxiality and Lode angle upon the evaluation of σ_{eq}/σ_0, we show in Fig. A.14 the porosity f as a function of the number of cycles N_r for the same set of stress triaxialities and Lode angles for both the unconstrained void and the spherically constrained void shape. In Fig. A.14a, for $X_\Sigma = 2/3$, we observe that even though the porosity evolves weakly (quantitatively) as a function of N_r for all Lode angles considered, it tends to increase for the unconstrained void while decrease for the spherically constrained void, exhibiting a markedly different qualitative response in these two cases. On the other hand, for $X_\Sigma = 3$ in Fig. A.14b
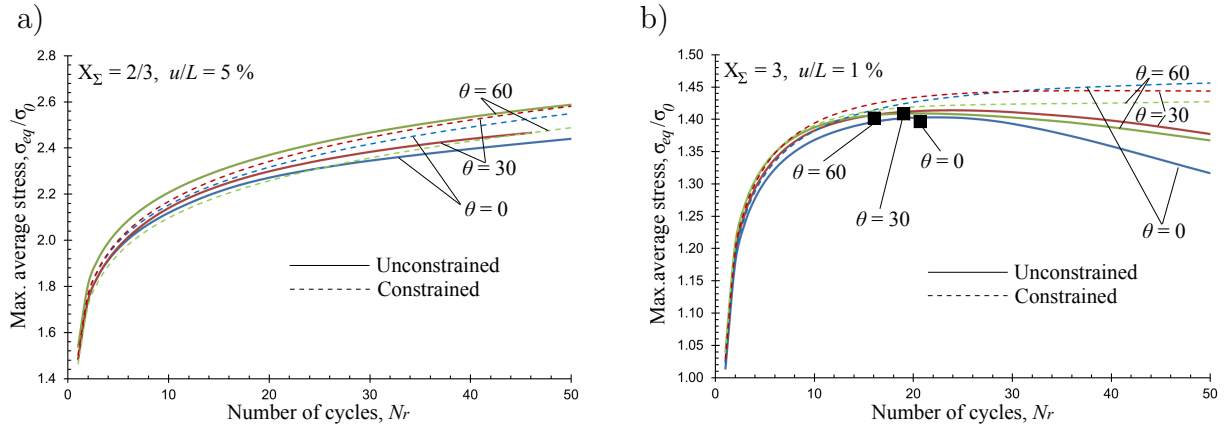
a)

b)

Figure A.13: Normalized maximum average equivalent von Mises stress evolution for unconstrained void / spherically constrained void in the case of (a) $u/L = 5\%$, $X_\Sigma = 2/3$ and (b) $u/L = 1\%$, $X_\Sigma = 3$ as a function of the number of cycles Nr. The filled square ($\blacksquare$) on the graphs indicate the point where maximum stress is observed.
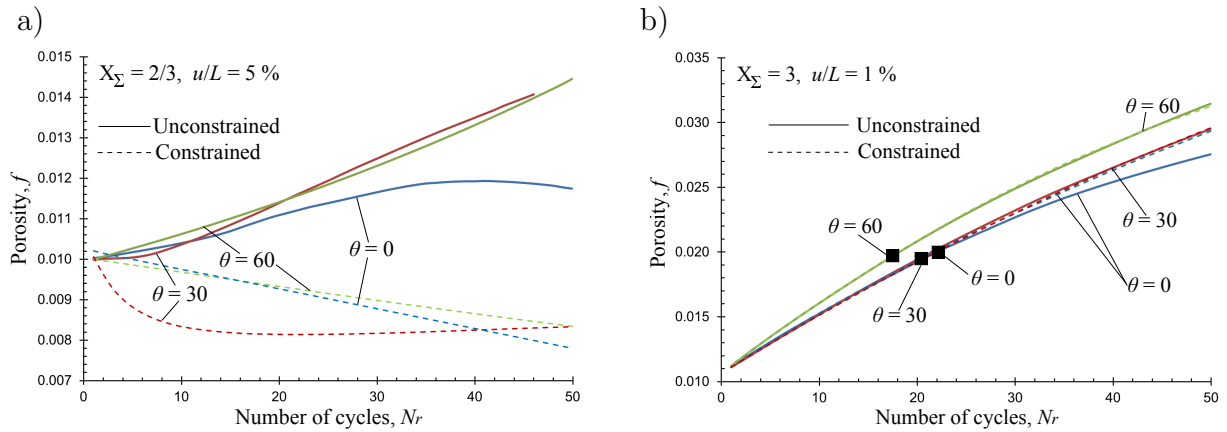
a)

b)

Figure A.14: Porosity evolution for unconstrained void / spherically constrained void in the case of (a) $u/L = 5\%$, $X_\Sigma = 2/3$ and (b) $u/L = 1\%$, $X_\Sigma = 3$ as a function of the number of cycles Nr. The filled square ($\blacksquare$) on the graphs indicate the point where maximum stress σ_{eq}/σ_0 is observed.

we observe a very important increase of f (almost three times more that its initial value) but a less pronounced dependence on the Lode angle θ. Moreover, due to the fact that the porosity evolution for $X_\Sigma = 3$ is quite similar for both unconstrained and constrained void shapes, we deduce again that the increase of porosity is not the only reason for the softening response observed in the unconstrained void shape calculation in Fig. A.13b.
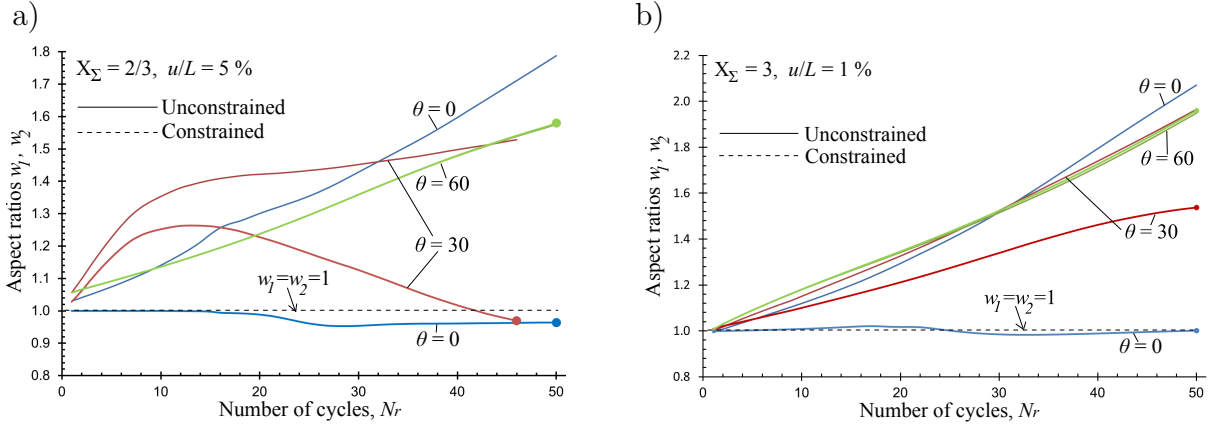
a)

b)

Figure A.15: Evolution of the aspect ratios w_1 ($-$), w_2 ($-\bullet$) for unconstrained void / spherically constrained void in the case of (a) $u/L = 5\%$, $X_\Sigma = 2/3$ and (b) $u/L = 1\%$, $X_\Sigma = 3$ as a function of the number of cycles Nr. The filled square ($\blacksquare$) on the graphs indicate the point where maximum stress σ_{eq}/σ_0 is observed.

Next we examine the void geometry changes as a function of the stress triaxiality X_Σ and the Lode angle θ. More specifically, Fig. A.15 shows the evolution of the aspect ratios w_1 and w_2, as a function of the number of cycles N_r for the same set of stress triaxialities and Lode angles considered previously. Obviously, there is no evolution of these quantities for spherically constrained void. The main observation in the context of Fig. A.15 is that the evolution of the aspect ratios w_1 and w_2 becomes significant with increasing number of cycles. It is, in fact, observed that due to the applied finite deformations, the shape of the void changes from the very first cycle and it tends to grow further as the number of cycles increases. Even more interestingly, the largest change in the void shape occurs for higher stress triaxialities, i.e., $X_\Sigma = 3$, as shown in Fig. A.15b, contrary to the case of $X_\Sigma = 2/3$ where both aspect ratios increase but in weaker manner. This result is not intuitive if one extrapolates the knowledge obtained in the context of monotonic loadings (see for instance Danas and Ponte Castañeda [2009a],Danas and Aravas [2012] and Srivastava and Needleman [2012]), where the largest void shape changes occur for lower stress triaxialities.

At this point, we note that the evolution of the void shape does not describe adequately the deformation mechanisms near the void surface. In fact, for most of the computations presented here (except for the case of $\theta = 60^o$) significant localization of the deformation occurs at the surface of the void. To illustrate this, we show, in

Fig. A.16 contours of the deformed unit-cell at 40 cycles for Lode angles $\theta = 0, 30, 60^o$ and stress triaxiality (a-c) $X_\Sigma = 2/3$ and (d-f) $X_\Sigma = 3$. To emphasize further the relative magnitude of each of the stress components $|\sigma_i|$ $(i = 1, 2, 3)$, we explicitly show them at the top corner of the displayed unit-cell. In particular, we observe a strong localization of the deformation (strains exceeding 60%) in a small zone of the void surface whose size depends upon the mesh size. While for $\theta = 0^o$, the localization strains lie in the plane $2 - 3$ since the applied stress is axisymmetric along the 1-direction, for $\theta = 30^o$ the localization zone is smaller (see for instance Fig. A.16e) but still lying mainly in the plane $2 - 3$. We should mention at this point that even though we have observed no maximum equivalent stress for the lower stress triaxiality $X_\Sigma = 2/3$ (see A.13a), the deformation localization is more than present (Fig. A.16a,b) and a critical event is expected to occur in these cases. Unfortunately, due to this strong localization of deformation the numerical calculation had to be stopped due to convergence issues as discussed further in the Appendix A.8, while a more appropriate formulation perhaps using non-local constitutive models (e.g., strain gradient plasticity models Forest et al. [2011], Danas et al. [2012], Nielsen and Niordson [2013, 2014] or even more general non-local criteria Feld-Payet et al. [2011]) are needed in this case (see for instance Feld-Payet et al. [2011]). Those models should then to be combined with appropriate remeshing techniques but such a study is beyond the scope of the present work.

This same type of localization has been observed in all computations, i.e. for $X_\Sigma = 2/3$ and $X_\Sigma = 3$ except for $\theta = 60^o$. In this last case, Fig. A.16c and Fig. A.16f show that the void elongates significantly along the x_3 axis, i.e., along the direction of the minimum absolute stress component (since for $\theta = 60^o$, $|\sigma_1| = |\sigma_2| > |\sigma_3|$). It should be noted here that the observed localization affects only a small region of the void surface and inevitably leads to strong mesh dependence at the local level after localization occurs. As is detailed in the Appendix A.8, however, this mesh dependence affects local quantities (such as the aspect ratio and ellipsoidicity) and not average quantities such as the average stress and strain in the unit-cell, as well as the porosity evolution.

It is worth noting at this point that recent experiments by continuous X-ray tomography (Hosokawa et al. [2012, 2013]) have revealed the effect of stress triaxiality upon void shape and growth, albeit in monotonic loading conditions. As suggested by
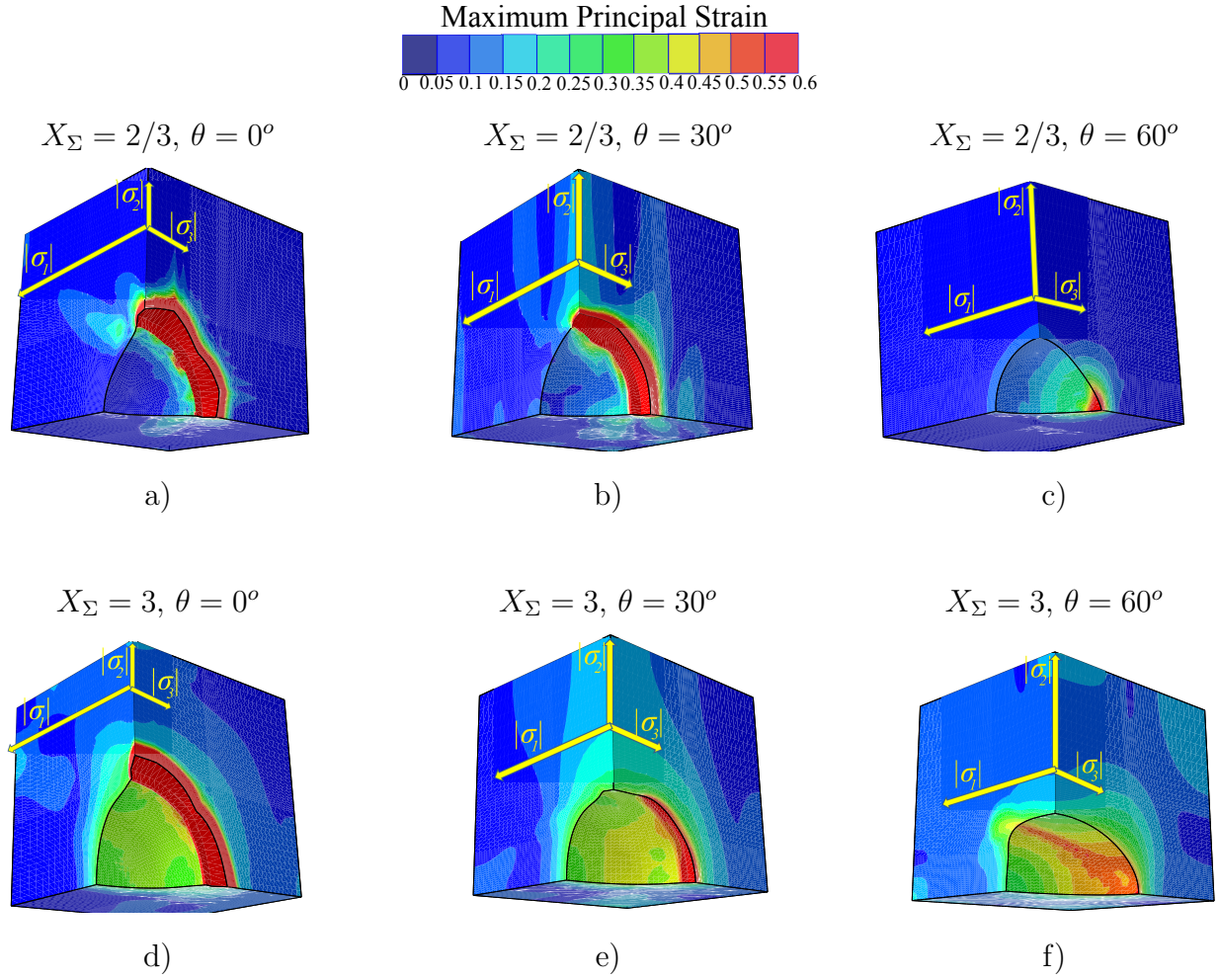
Figure A.16: Contours of the maximum principal logarithmic strain at 40 cycles in the case of $X_\Sigma = 2/3$ ($u/L = 5\%$) for (a) $\theta = 0^o$ and (b) $\theta = 30^o$ and (c) $\theta = 60^o$ and in the case of $X_\Sigma = 3$ ($u/L = 1\%$) for (d) $\theta = 0^o$ and (e) $\theta = 30^o$ and (f) $\theta = 60^o$.

the present numerical calculations, the void shape changes under cyclic loadings are very different when compared to those obtained for monotonic loadings (Danas and Ponte Castañeda [2009b], Srivastava and Needleman [2012]). Hence, a study similar to that of Hosokawa et al. [2012], but in cyclic loading conditions, could in fact shed light to the observed void shape effects.

To assess further the effects of the localization upon the void shape changes, we show in Fig. A.17, the ellipsoidicity ratio $\mathcal{E}_l$ as a function of the number of cycles N_r. We recall here that as $\mathcal{E}_l$ deviates from unity the void tends to diverge from an ideal ellipsoidal shape. In these graphs, the ellipsoidicity ratio reaches high values ($\mathcal{E}_l \gtrsim 1.5$) for the cases $X_\Sigma = 2/3$, $\theta = 0$ and $X_\Sigma = 3$, $\theta = 0$, respectively, as a result of the

corresponding deformation localization around the pore surface. The same remark can be made for $X_\Sigma = 2/3$ and $\theta = 30^o$ but with somewhat lower values of the ellipsoidicity, in the order of $\mathcal{E}_l \lesssim 1.3$. In contrast, the ellipsoidicity is the smallest (and less than 1.2) for the combination $\theta = 30^o$ and $X_\Sigma = 2/3$ as well as for $\theta = 30, 60$ and $X_\Sigma = 3$. This is in agreement with the contours of Fig. A.16c,e,f, where the void shape does not deviate significantly from an ellipsoidal shape.
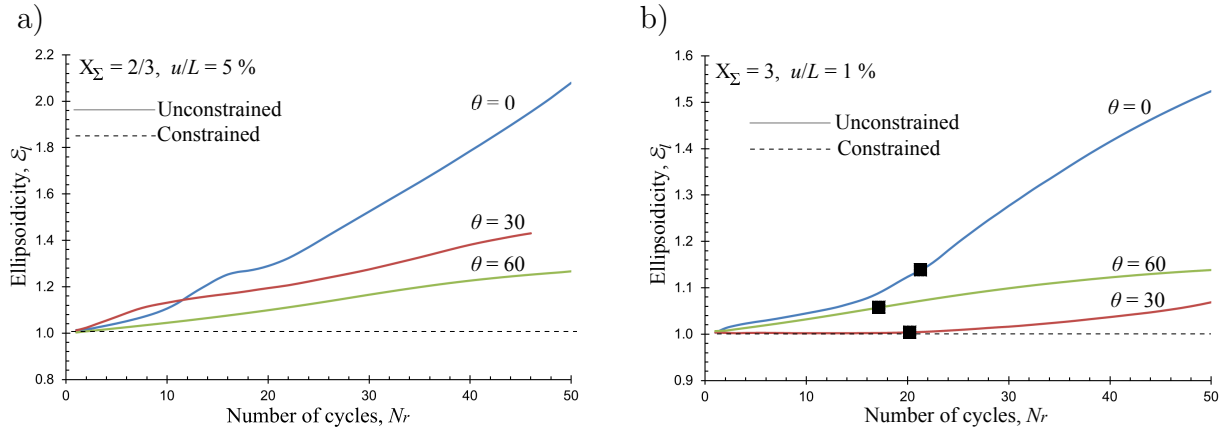

Figure A.17: Ellipsoidicity ratio $\mathcal{E}_l$ for an unconstrained void and a spherically constrained void in the case of (a) $X_\Sigma = 2/3$ ($u/L = 5\%$) and (b) $X_\Sigma = 3$ ($u/L = 1\%$) as a function of the number of cycles Nr. The filled square (■) on the graphs indicate the point where maximum equivalent stress is observed.

A.4.2   Effect of initial void shape

In this section, we investigate the effect of the initial void shape on the material cyclic response for initial porosity $f_0 = 0.01$, triaxiality $X_\Sigma = 3$, amplitude $u/L = 1\%$, Lode angle $\theta = 0^o, 60^o$ and $N = 10$. In the following, only calculations with unconstrained void shapes will be shown.

Figure A.18 shows evolution curves of (a) the average equivalent stress σ_{eq}/σ_0 and (b) the porosity f as a function of the number of cycles for three different void geometries, i.e. $w_1^0 = w_2^0 = 1, w_1^0 = 1/3 < w_2^0 = 1, w_1^0 = 3 > w_2^0 = 1$ [5]. The initial void shapes that are different than a sphere have been chosen such that they remain axisymmetric during the deformation process, i.e., $w_1^0 = 1/3, w_2^0 = 1$ is a prolate void

---

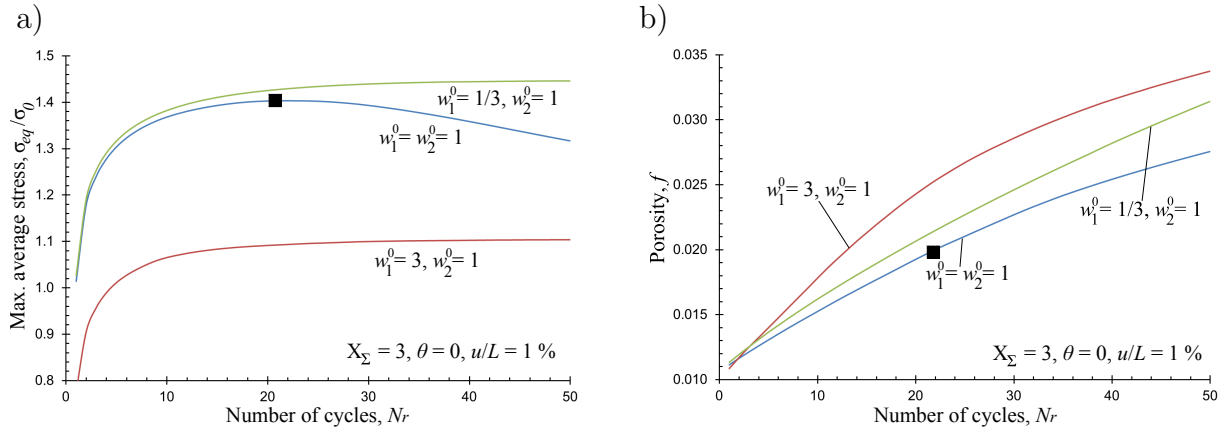[5]Hereafter, the superscript "0" in w_i^0 is used to denote initial values

a)

b)

Figure A.18: (a) Normalized average equivalent von Mises stress σ_{eq}/σ_0 and (b) porosity f for several initial values of void shapes ($w_1^0 = w_2^0 = 1$, $w_1^0 = 1/3$ and $w_2^0 = 1$, $w_1^0 = 3$ and $w_2^0 = 1$) in the case of $X_\Sigma = 3$ ($u/L = 1\%$) and $\theta = 0^o$ as a function of the number of cycles Nr. The filled square (■) on the graphs indicate the point where maximum equivalent stress is observed.
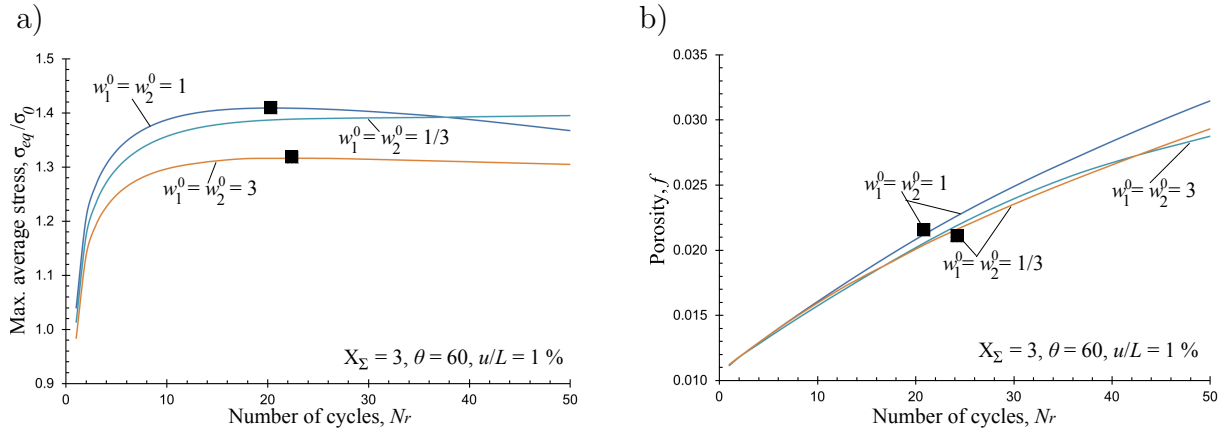
a)

b)

Figure A.19: (a) Normalized maximum average equivalent von Mises stress evolution for several initial void shapes ($w_1^0 = w_2^0 = 1, w_1^0 = w_2^0 = 1/3, w_1^0 = w_2^0 = 3$) in the case of $u/L = 1\%$, $X_\Sigma = 3$, $\theta = 60^o$ and (b) Porosity evolution for several initial void shape ($w_1^0 = w_2^0 = 1, w_1^0 = w_2^0 = 1/3, w_1^0 = w_2^0 = 3$) in the case of $u/L = 1\%$, $X_\Sigma = 3$, $\theta = 60^o$ as a function of the number of cycles Nr. The filled square (■) on the graphs indicate the point where maximum stress is observed.

and $w_1^0 = 3, w_2^0 = 1$ is an oblate void, whose symmetry axis remains aligned with the maximum principal stress σ_1 in this case. As observed in Fig. A.18a, the average σ_{eq}/σ_0 of the unit-cell exhibits a maximum only for the initially spherical void ($w_1^0 = w_2^0 = 1$)

but not for the two other cases. Moreover, the unit-cell with $w_1^0 = 1/3, w_2^0 = 1$ is the stiffest of all three cases considered here. In Fig. A.18b, the effect of the initial void shape upon the porosity evolution is also significant. It is worth emphasizing that the initially spherical void case ($w_1^0 = w_2^0 = 1$) shows the weaker porosity growth as a function of N_r even though it is the only case that exhibits a maximum in the σ_{eq}/σ_0 curve.

Similarly, Fig. A.19 shows evolution curves of (a) the average equivalent stress σ_{eq}/σ_0 and (b) the porosity f as a function of the number of cycles for three different values of the initial shape, i.e., $w_1^0 = w_2^0 = 1, w_1^0 = w_2^0 = 1/3, w_1^0 = w_2^0 = 3$ and for $X_\Sigma = 3$ and $\theta = 60^o$. The initial void shapes have also been chosen to remain axisymmetric during the entire deformation process, such as their symmetry axis remains aligned with the minimum principal stress σ_3 in this case. For this configuration, in Fig. A.19a, a maximum σ_{eq}/σ_0 is observed for two out of three cases, i.e. for the initially spherical case ($w_1^0 = w_2^0 = 1$) and the initially prolate case ($w_1^0 = w_2^0 = 3$). In Fig. A.19b the evolution of porosity f is less sensitive upon the initial void shape with that for $w_1^0 = w_2^0 = 1$ being the strongest among the three cases considered here contrary to the previous case of $\theta = 0^o$ in Fig. A.18.

In order to assess in a more visual and comprehensive way the evolution of the void shape geometry, Fig. A.20 shows initial and final (at 50 cycles) void shapes for the same set of initial void geometries used in the previous figures of this section. The main observation in the context of this figure is that for stress triaxiality $X_\Sigma = 3$, the void tends to elongate in the direction of the minimum applied principal stress, i.e. $|\sigma_2| = |\sigma_3|$ for $\theta = 0^o$ and $|\sigma_3|$ for $\theta = 60^o$, except in the case of $\theta = 60^o$ and $w_1^0 = w_2^0 = 1/3$ (initially prolate case) where the void elongates along the direction of the maximum applied stress $|\sigma_1| = |\sigma_2|$. This effect should not be confused with the the similar effect observed for monotonic loadings and high stress triaxialities, since it is attributed to the fact that, in each cycle, the void shape evolves faster during the compressive step ($X_\Sigma \leq 0$) than the tensile step ($X_\Sigma \geq 0$), as already discussed in the context of Fig. A.10 and is present also in lower stress triaxialities. At this point, it is worth noting that the direction of the void elongation is consistent (except for $\theta = 60^o$ and $w_1^0 = w_2^0 = 1/3$) with a mode I loading of a crack. In other words, the voids tend to give a crack-type shape, as observed more clearly, in Fig. A.20a,c and e, where a rather sharp crack tip starts to form in a direction perpendicular to the maximum

$$X_\Sigma = 3, \theta = 0^o$$

a)   b)   c)

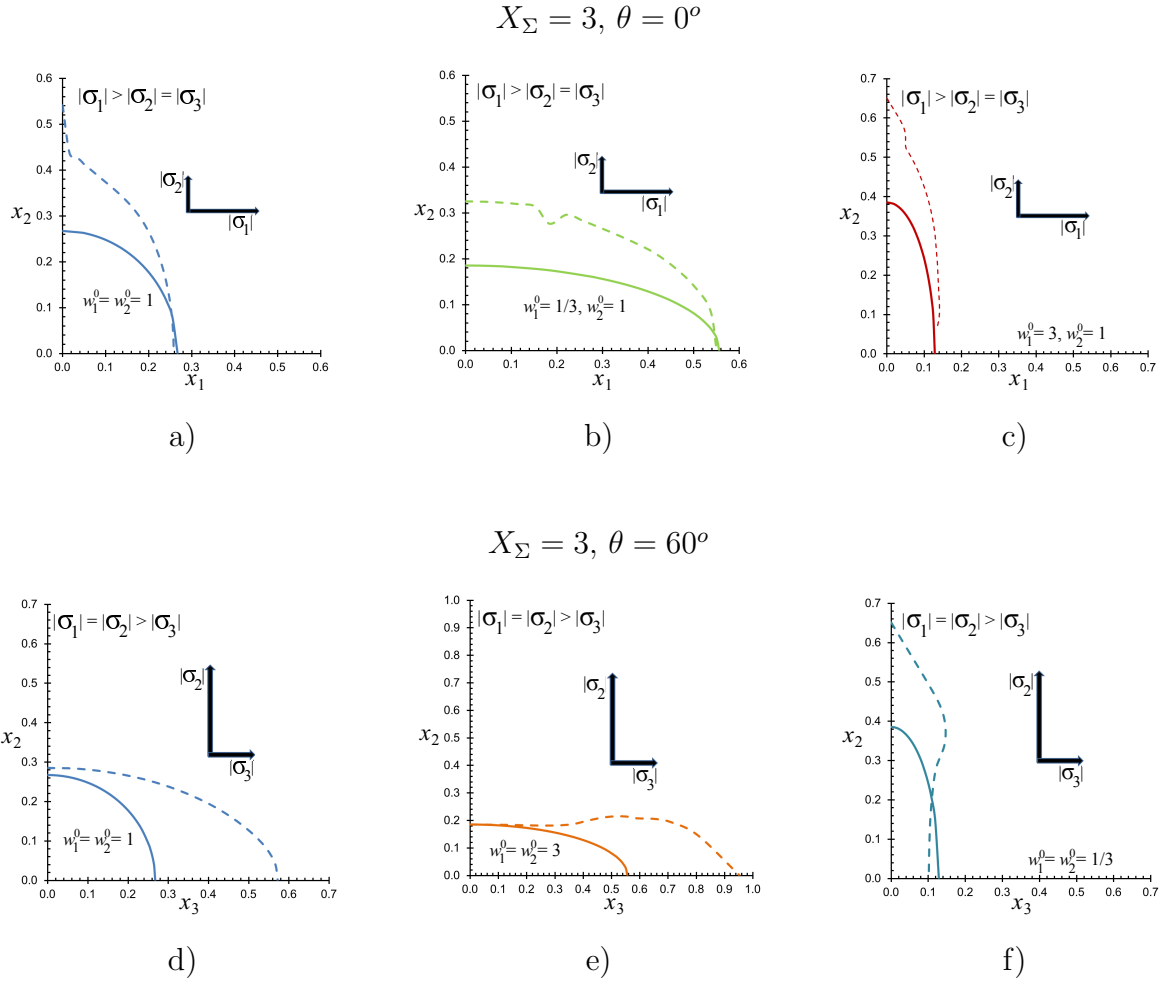$$X_\Sigma = 3, \theta = 60^o$$

d)   e)   f)

Figure A.20: Cross-sections of undeformed (continuous line) and deformed (dashed lines) void geometries at 50 cycles and stress triaxiality $X_\Sigma = 3$ in the case of $\theta = 0^o$ with initial void shape (a) $w_1^0 = w_2^0 = 1$ and (b) $w_1^0 = 1/3, w_2^0 = 1$ and (c) $w_1^0 = 3, w_2^0 = 1$ in the case of $\theta = 60^o$ with initial void shape (d) $w_1^0 = w_2^0 = 1$ and (e) $w_1^0 = w_2^0 = 3$ and (f) $w_1^0 = w_2^0 = 1/3$.

applied average stress in the unit-cell, i.e., as if they voids were under a mode I loading state. This observation simply indicates that the introduction of a pressure dependent defect (such as a pore) even if this defect is initially smooth (spherical or ellipsoidal), tends to diverge rapidly to a crack-type geometry and is expected to lead to the more common fatigue crack growth at larger number of cycles. Unfortunately at this level, severe mesh distortion did not allow us to continue further our calculation due to the strong localization of deformation. Remeshing of the final geometry together with non-local constitutive laws (Feld-Payet et al. [2011]) might be required to proceed to higher number of cycles, however, such a calculation is beyond the scope of this work

and is not pursued here.

At this point it is worth mentioning that while in monotonic loadings and under large triaxialities, the voids tend to grow rather uniformly and finally coalesce (see for instance Thomason [1985], Pardoen and Hutchinson [2000], Gologanu et al. [2001], Benzerga [2002]), in the present case of cyclic loading conditions coalescence of neighboring pores is not really due to void growth but rather due to crack initiation and propagation, which is also present at lower stress triaxialities. As observed in Fig. A.16 and Fig. A.20, the voids do not grow uniformly but rather a crack is created in a very thin localized zone for both stress triaxialities analyzed in this work. This crack is then expected to propagate and coalesce with the neighboring pores but such an analysis is highly mesh dependent and not pursued further here as discussed previously. As a result in the context of cyclic loadings, the localization of plastic strain does not take place within horizontal ligaments spanning the size of the pore and the spacing of the neighboring pores as in the usual studies of coalescence in monotonic loadings (Pardoen and Hutchinson [2000]) but rather in a confined thin region around a small portion of the void surface.

A.5   Preliminary results on combined isotropic-kinematic hardening

At this point, it would be constructive to for a matrix material following combined isotropic and nonlinear kinematic hardening. The range of parameters needed to investigate in a full extent the effect of kinematic hardening upon the cyclic response of the unit-cell is large and thus prohibitive for the present work and will be presented elsewhere in a subsequent study. Nonetheless, as we will see below the introduction of nonlinear kinematic hardening in the matrix phase does not alter the qualitative character of the deformation zone and localization around the void but only the quantitative aspects.

More specifically, let us consider the same isotropic hardening presented in equation (A.9) together with a nonlinear kinematic hardening with two-backstresses $\boldsymbol{X}^{(1)}$ and

$\boldsymbol{X}^{(2)}$ (*c.f.* Nouailhas et al. [1985]), i.e.,

$$\dot{\boldsymbol{X}}^{(1)} = q_h C_1 \boldsymbol{D}_M^p, \quad \dot{\boldsymbol{X}}^{(2)} = q_h C_2 \boldsymbol{D}_M^p - \gamma_2 \Delta\varepsilon^p \boldsymbol{X}^{(2)}, \quad \boldsymbol{X}^{(1)} = \boldsymbol{X}^{(2)} = 0 \quad \text{at} \quad t = 0. \tag{A.13}$$

In this expression, $\boldsymbol{D}_M^p$ is the second-order plastic strain-rate tensor in the matrix phase (the subscript M has been used to explicitly distinguish between strain-rate in the matrix phase and the average strain-rate in the unit-cell) and ε^p is the accumulated plastic strain defined in the context of equation (A.9). Furthermore, motivated by the choices made in Besson and Guillemer-Neel [2003], we set the values $C_1 = 2.5 \times 10^{-2}\sigma_0$, $C_2 = 10C_1$ and $\gamma_2 = 10$. These values correspond to a rather week kinematic hardening at the level of the matrix phase but as will be shown next they already lead to a strong quantitative (but not qualitative) effect upon the cyclic response of the unit-cell. The q_h serves to parameterize the relative effect of kinematic hardening with respect to the isotropic hardening and takes here three values $q_h = 0, 0.5, 1$ (with $q_h = 0$ corresponding to the case of no kinematic hardening).
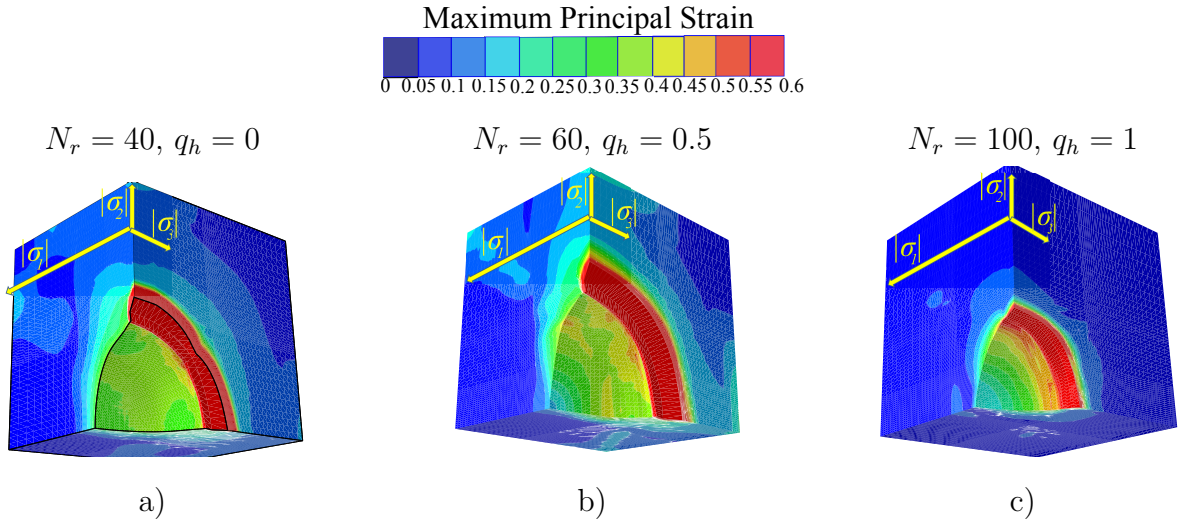

Figure A.21: Contours of the maximum principal logarithmic strain in the case of $X_\Sigma = 3$ ($u/L = 1\%$) and $\theta = 0^o$ for (a) $q_h = 0$ at $N_r = 40$cycles (no kinematic hardening), (b) $q_h = 0.5$ at $N_r = 60$cycles and (c) $q_h = 1$ at $N_r = 100$cycles.

As a representative result in the context of combined isotropic/kinematic hardening, we have chosen the case of high stress triaxiality $X_\Sigma = 3$ ($u/L = 1\%$) and Lode angle $\theta = 0^o$. In Fig. A.21, we show contours of the maximum principal strain for (a)

$q_h = 0$ at $N_r = 40$ cycles (no kinematic hardening), (b) $q_h = 0.5$ at $N_r = 60$ cycles and (c) $q_h = 1$ at $N_r = 100$cycles. The main observation in the context of this figure is that the deformation localization locus is the same with or without kinematic hardening, i.e., the strain localizes in the same position at the void surface in an attempt to create a mode-I crack-type geometry, as discussed in the previous sections. The difference however is quantitative, i.e., with the addition of kinematic hardening this deformation localization occurs at much larger number of cycles as shown in Fig. A.21. In other words, the addition of a rather small value of kinematic hardening does not alter the character of the deformation localization in the zone around the void, but rather changes the number of cycles needed to reach this localized state. In a sense, it "decelerates" the localization procedure, thus having a beneficiary effect upon the cyclic response of the material.

It should be further pointed out that similar effects have been found for other values of the stress triaxiality and the Lode parameter but are not shown here for brevity. These preliminary results call for an in-depth quantitative analysis of the effect of kinematic hardening upon the cyclic response of such unit-cells and will be presented in a future work.

A.6   Concluding remarks

In this chapter we have investigated the effects of cyclic loading conditions upon microstructure evolution and material softening/hardening using a cubic periodic unit-cell comprising a single spherical (or ellipsoidal) void at the center with volume fraction 1% that is subjected to triaxial finite deformations such that the stress triaxiality and the Lode angle are kept constant during each step of the cycle. It has been found that the void shape changes are asymmetric when subjected to positive and negative stress triaxialities. This is exhibited by a permanent irreversible void shape change from the very first cycle, which in turn leads to porosity ratcheting and an asymmetric average stress-strain response. It should be noted that this asymmetry does not lead to a Bauschinger effect but is strongly related to the evolution of the underlying void volume and shape. Furthermore, we have observed that both the stress triaxiality and the Lode angle can have strong effects upon the cyclic response of the unit cell. It has been found that for initially spherical voids the average stress in the unit-cell exhibits

a maximum as a result of the critical void shape changes at high stress triaxialities, but not due to porosity ratcheting alone. To establish this conclusion, we have carried out additional calculations on the same unit-cell but constraining the shape of the void to remain spherical during the entire deformation process. In this case, we have also obtained significant porosity ratcheting (very similar and even larger than that of the unconstraint void), but no maximum was observed in the average stress response of the unit-cell. This suggests that void shape changes are critical in the cyclic response of the unit-cell.

In addition, the observed void shape changes have led to significant localization of the deformation near the void surface. Strains larger than 50% have been observed near the void surface even when the average strain amplitude in the unit-cell has been of the order of 1%. This result further revealed the importance of carrying out the cyclic analysis under a finite deformation framework. Moreover, we have investigated the effect of initially non-spherical (i.e., ellipsoidal) voids on the cyclic response of the unit-cell. The main outcome of this parametric analysis has been that the void tends to elongate in the direction of the minimum absolute applied stress. This observation has been different only in a few distinct cases where the void shape was positioned in a significantly non-optimal direction with respect to a mode I loading direction. This void elongation, in turn, leads to a crack-shape microstructure subjected to mode I cyclic loading state and to eventual coalescence for both lower and higher stress triaxialities. Nevertheless, the strain fields in that late stage of coalescence are very different from those observed in the context of monotonic loading states and high triaxialities. In the context of cyclic loads, the localization zone is confined in a very thin region around a small portion of the void surface.

Finally, as discussed before, the cyclic behavior of materials exhibits different stages where isotropic and/or kinematic hardening (Nouailhas et al. [1985], Chaboche [2008]) are the main cyclic mechanisms. The present study provides a partial perspective upon the cyclic response of a periodic porous material by considering mainly isotropic hardening and only a test case with combined nonlinear isotropic and kinematic hardening. A complete study that analyzes the relative importance of isotropic and kinematic hardening upon the cyclic response of the unit-cell should be considered further. One should also mention that anisotropy of the matrix phase (e.g., crystal plasticity) is also expected to have an effect upon the cyclic response of such porous unit-cells.

Nonetheless, the above-presented preliminary calculations show that, for instance, the presence of kinematic hardening exhibits similar qualitative behavior with the case of no kinematic hardening but tends to decelerate the initiation of localization of deformation around the void surface. Such study is currently in progress and will be reported elsewhere.

A.7   Appendix I. Effect of the matrix hardening exponent

In this section, we discuss the effect of the hardening exponent N on the cyclic response of the material as defined in equation (A.9). For convenience and brevity, we restrict attention to stress triaxiality $X_\Sigma = 3$, amplitude $u/L = 1\%$, Lode angle $\theta = 60^o$, and a set of hardening exponents $N = 5, 10, \infty$ (where the last one corresponds to the perfect plasticity case). Initially, we discuss the effect of the hardening exponent for a realistic value of the elastic moduli, e.g., Young's modulus, $E \sim 1000\sigma_0$ (for instance $\sigma_0 \sim 200$MPa corresponding to steel) and then we also present a brief result of porosity ratcheting for $E/\sigma_0 = 50000$ in order to address the observations made by Devaux et al. [1997] in the limit of vanishing elasticity (i.e., $E/\sigma_0 \to \infty$).

As we can observe in Fig. A.22a, the average equivalent von Mises stress per cycle σ_{eq}/σ_0 decreases monotonically with respect to N. In particular, for the case of the unconstrained void shape, it exhibits a maximum value for σ_{eq}/σ_0 for $N = 10$ but not for $N = 5$, at least up to 50 cycles where the calculations are terminated. On the other hand, as expected, σ_{eq}/σ_0 shows no maximum for the $N = 5$ and $N = 10$ for the spherically constrained shape. For the case of perfect plasticity, i.e. $N \to \infty$, both the unconstrained and the constrained void shape exhibit a softening from the very first cycle.

In Fig. A.22b, however, the evolution of the porosity exhibits non-monotonic dependence upon N as a function of the number of cycles N_r. The evolution of f is higher for $N = 10$ and lower for $N = 5$, with the one corresponding to $N = \infty$ intersecting the other two curves at about 10 cycles. As we will see below this intersection could be attributed to the localization of deformation which is more pronounced in the case of $N = \infty$, but this point should further be studied in the future.

In Fig. A.23, we show evolution curves for (a) the aspect ratios $w_1 = w_2$ (for $\theta = 60^o$) and (b) for the ellipsoidicity as a function of the number of cycles N_r for the same set of hardening exponents used before ($N = 5, 10, \infty$). The evolution of the aspect ratios in Fig. A.23a are shown to be almost independent of N as $N \geq 10$, while they tend to evolve slower for larger $N = 5$. In contrast the evolution of ellipsoidicity in Fig. A.23b exhibits a non-monotonic dependence on N especially at large number of cycles taking the largest values for $N = 10$.

Finally, in Fig. A.24, we consider the case of vanishing elasticity, i.e., $E/\sigma_0 = 50000$ and record porosity ratcheting under the same loading state and the same set of hardening exponents ($N = 5, 10, \infty$). One observes that all results confirm (up to a given numerical accuracy since the Young's modulus is not infinity) the results by Devaux et al. [1997], i.e., there is no porosity ratcheting effect in the absence of elasticity. Rather interestingly, porosity ratcheting also becomes negligible for $N = 5, 10$. But this is related to the rather small macroscopic strain amplitude considered here as well as to the specific cyclic loading conditions, i.e., cyclic loads around zero average straining. Thus, if one compares these results with the previous ones (which correspond to $E = 1000\sigma_0$) then the effect of elasticity is critical for porosity ratcheting.
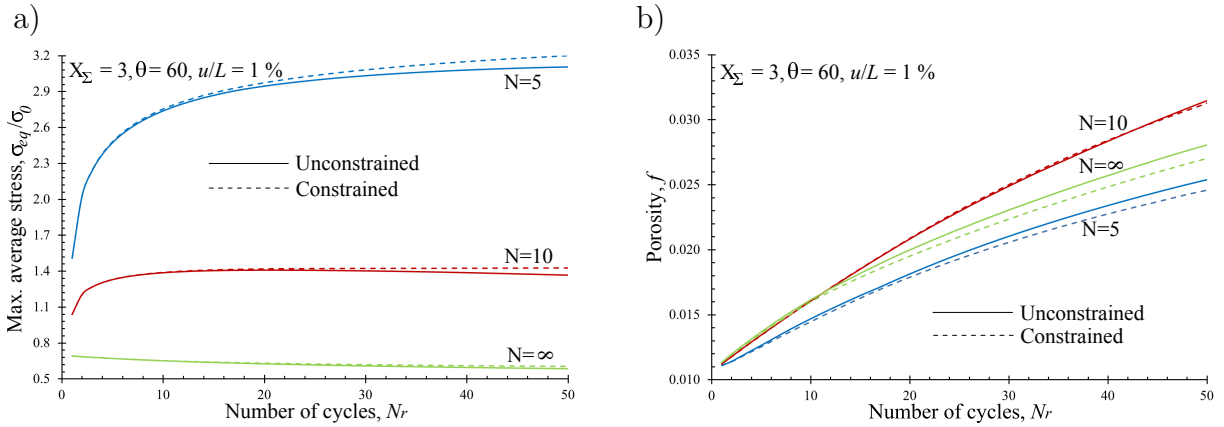

Figure A.22: (a) Normalized maximum average equivalent von Mises stress evolution for several values of hardening exponent ($N = 5, 10, \infty$) in the case of $u/L = 1\%$, $X_\Sigma = 3$, $\theta = 60^o$ and (b) Porosity evolution for several values of hardening exponent ($N = 5, 10, \infty$) in the case of $u/L = 1\%$, $X_\Sigma = 3$, $\theta = 60^o$ as a function of the number of cycles Nr.

a)

b)

Figure A.23: (a) Evolution of the aspect ratios w_1 ($-$), w_2 ($-\bullet$) for several values of hardening exponent ($N = 5, 10, \infty$) in the case of $u/L = 1\%$, $X_\Sigma = 3$, $\theta = 60^o$ and (b) Ellipsoidicity ratio for several values of hardening exponent ($N = 5, 10, \infty$) in the case of $u/L = 1\%$, $X_\Sigma = 3$, $\theta = 60^o$ as a function of the number of cycles Nr.
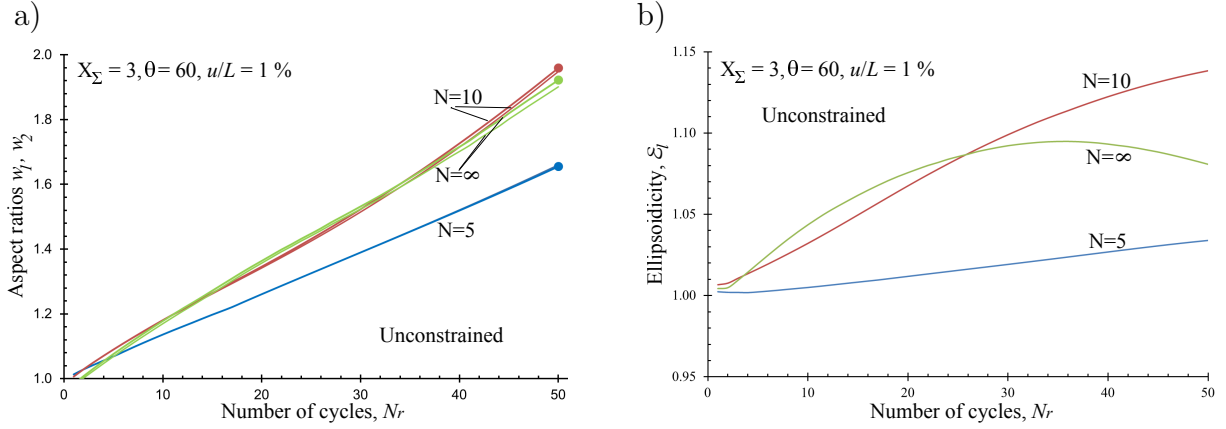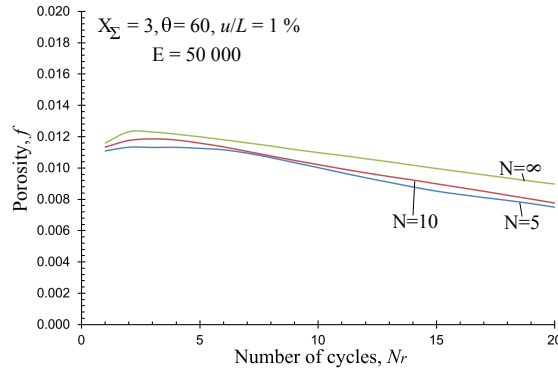

Figure A.24: Porosity evolution for several values of hardening exponent ($N = 5, 10, \infty$) in the case of $E = 50000\sigma_0$, $u/L = 1\%$, $X_\Sigma = 3$, $\theta = 60^o$ as a function of the number of cycles Nr.

A.8   Appendix II. Mesh dependence

In this section, we discuss the dependence of mesh size upon the cyclic response of the periodic unit-cell. As we have observed on several calculations with $\theta = 0, 30^o$ (see Fig. A.16), a localization of deformation appears in a small region of the void surface and thus, leads to strong mesh dependence at this zone. This led to non-convergence of the elasto-plastic computations beyond 50 cycles. In Fig. A.25, we show representative results for a loading $u/L = 1\%$, $X_\Sigma = 3$, $\theta = 30^o$ and for three different mesh sizes at the pore surface, i.e., $0.052a$, $0.037a$ and $0.026a$ (where a is the radius of the initially

spherical pore), corresponding to 5×10^4, 15×10^4 and 32×10^4 degrees of freedom (dof), respectively. Figure A.25a shows the evolution of the maximum average equivalent
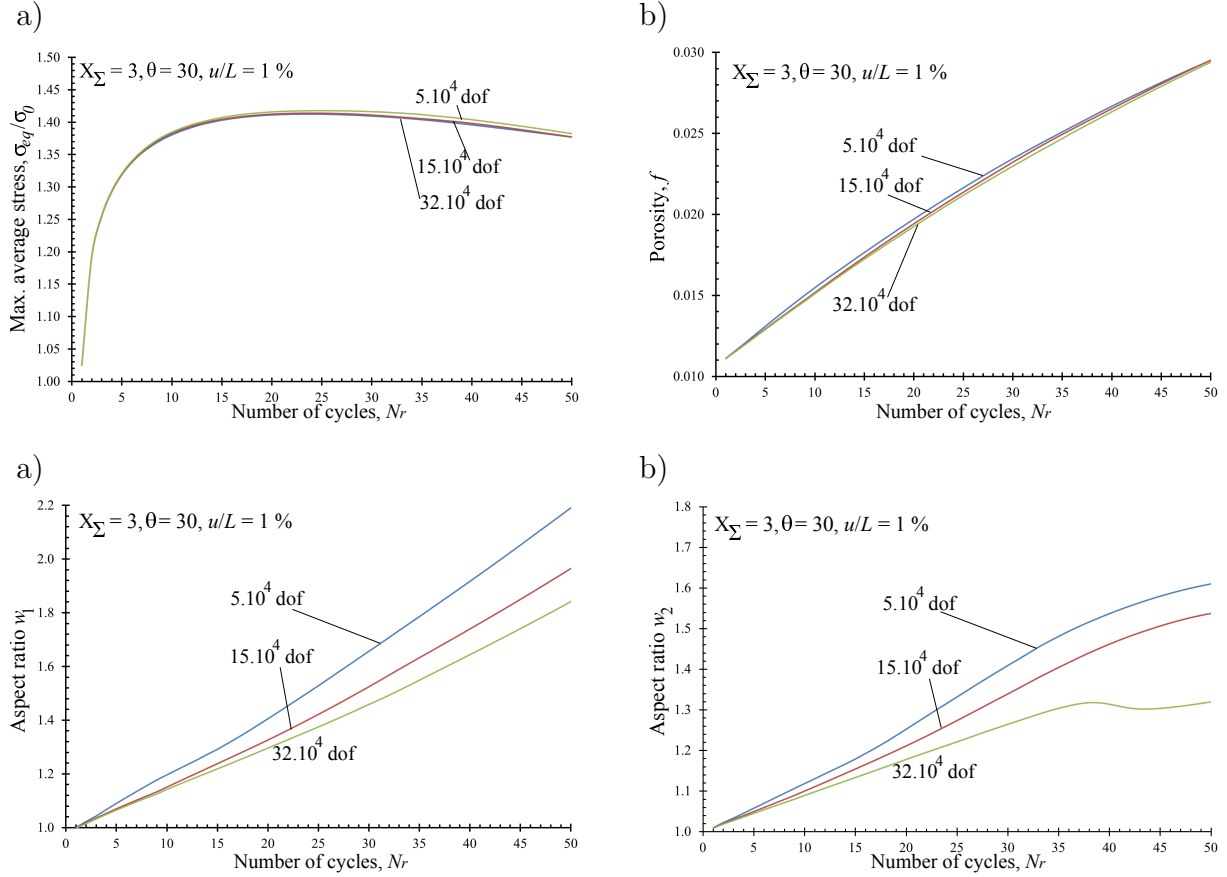
a)

b)

a)

b)

Figure A.25: (a) Normalized average equivalent von Mises stress σ_{eq}/σ_0, (b) porosity f, (c) aspect ratio w_1 and (d) aspect ratio w_2 for 5×10^4, 10^5 and 3×10^5 degrees of freedom (dof) in the case of $X_\Sigma = 3$ and $\theta = 30^o$ as a function of the number of cycles Nr.

von Mises stress as a function of the number of cycles N_r for the same loading and the aforementioned three different mesh sizes. It is evident from Figs. A.25a,b that the evolution of the average stress σ_{eq}/σ_0 (as well as the position where maximum is attained) and the porosity f (which is a direct measure of the hydrostatic average plastic strain) as a function of N_r is not sensitive to the mesh size. On the other hand, in Fig. A.25c,d we observe that the aspect ratios w_1 and w_2 are much more sensitive to the mesh size. In particular, even though the evolution of w_1 and w_2 tend to converge for $N_r < 20$, the curves diverge after this point as a result of the strong deformation localization observed in those cases. In addition, it is interesting to note that there is a monotonic decrease of the aspect ratios with increasing mesh size. Consequently, we

can conclude that the mesh dependence affects more the local quantities (such as the aspect ratio) but not average quantities such as the average stress or strain, and the porosity evolution, which depends on the hydrostatic part of the average strain in the unit-cell.

Bibliography

Abaqus. *ABAQUS/Standard Version 6.9, user manual.* Simulia Corp., 2009.

M. Agoras and P. Ponte Castañeda. Iterated linear comparison bounds for viscoplastic porous materials with ellipsoidal microstructures. *J. Mech. Phys. Solids*, 61:701–725, 2013.

S. Amiable, S. Chapuliot, A. Constantinescu, and A. Fissolo. A computational lifetime prediction for a thermal shock experiment part ii : discussion on different fatigue criteria. *Fatigue and Fracture of Engineering Materials and Structures*, 29:219–227, 2006a.

S. Amiable, S. Chapuliot, A. Constantinescu, and A. Fissolo. A comparison of lifetime prediction methods for a thermal fatigue experiment. *Int. J. Fatigue*, 28:692–706, 2006b.

N. Aravas. Finite elastoplastic transformations of transversely isotropic metals. *Int. J. Solids Struct.*, 29:2137–2157, 1992.

N. Aravas and P. Ponte Castañeda. Numerical methods for porous metals with deformation-induced anisotropy. *Comput. Methods Appl. Mech. Engrg.*, 193:3767–3805, 2004.

R.J. Asaro. Micromechanics of crystals and polycrystals. *Adv Appl Mech*, 23:1, 1983.

I. Barsoum and J. Faleskog. Rupture mechanisms in combined tension and shear – experiments. *Int. J. Solids Struct.*, 44:1768–1786, 2007a.

I. Barsoum and J. Faleskog. Rupture mechanisms in combined tension and shear – micromechanics. *Int. J. Solids Struct.*, 44:5481–5498, 2007b.

A. Benallal. On some features of the effective behavior of porous solids with general incompressible matrix behavior (submitted). *C.R. Mecanique*, 2015.

A. Bensoussan, J.L. Lions, and G.C. Papanicolaou. Asymptotic analysis for periodic structures. *North-Holland*, 1978.

A. Benzerga, J. Besson, and A. Pineau. Anisotropic ductile fracture. part ii: Theory. *Acta Metall.*, 52:4639–4650, 2004.

A.A. Benzerga. Micromechanics of coalescence in ductile fracture. *J. Mech. Phys. Solids*, 50:1331–1362, 2002.

A.A. Benzerga and J. Besson. Plastic potentials for anisotropic porous solids. *Eur. J. Mech./A*, 20:397–434, 2001.

M. Beran. Use of the variational approach to determine bounds for the effective permittivity of random media. *Nuovo Cimento*, 38:771–782, 1965.

G. Bertolino, A. Constantinescu, M. Ferjani, and P. Treiber. A multiscale discussion of fatigue and shakedown for notched structures. *Theoretical and Applied Fracture Mechanics*, 48:140–151, 2007.

M. Berveiller and A. Zaoui. An extensions of the self-consistent scheme to plastically-flowing polycrystals. *J. Mech. Phys. Solids*, 26:325–344, 1979.

J. Besson and C. Guillemer-Neel. An extension of the green and gurson models to kinematic hardening. *Mechanics of Materials*, 35:1–18, 2003.

M. Bornert, C. Stolz, and A. Zaoui. Morphologically representative pattern-based bounding in elasticity. *J. Mech. Phys. Solids*, 44:307–331, 1996.

M. Bourcier, M. Bornert, A. Dimanov, E. Heripre, and J. L. Raphanel. Multiscale experimental investigation of crystal plasticity and grain boundary sliding in synthetic halite using digital image correlation. *Journal of Geophysical Research: Solid Earth*, 118:511–526, 2013.

A. Braides and D. Lukkassen. Reiterated homogenization of integral functionals. *Math. Models Methods Appl. Sci.*, 10:47–71, 2000.

B. Budiansky. On the elastic moduli of some heterogeneous materials. *J. Mech. Phys. Solids*, 13:223–227, 1965.

B. Budiansky and J.W. Hutchinson. Self-similar shapes and asymptotic dilatation-rates for void in viscous solids. *Proceedings of the XVth International Congress of Theoretical and Applied Mechanics*, 1980.

B. Budiansky, J. W. Hutchinson, and S. Slutsky. Void growth and collapse in viscous solids. *Mechanics of Solids, The Rodney Hill 60th aniversary Volume, Hopkins, H. G. and Sewell, M. J. eds. Pergamon Press Oxford*, pages 13–45, 1982.

T.S. Cao, M. Maziere, K. Danas, and J. Besson. A model for ductile damage prediction at low stress triaxialities incorporating void shape change and void rotation. *Int. J. Solids Struct.*, 63:240–263, 2015.

A. Carpiuc. Prediction of fatigue in metals by using finite element analysis and novel pressure dependent-plasticity models. Master's thesis, Ecole Polytechnique, Paris, 2012.

O. Cazacu, B. Revil-Baudard, and Barlat. New interpretation of cyclic swift effects. *Eur. J. Mech. A/Solids*, 44:82–90, 2014a.

O. Cazacu, B. Revil-Baudard, N. Chandola, and D. Kondo. New analytical criterion for porous solids with tresca matrix under axisymmetric loadings. *Int. J. Solids Struct.*, 51:861–874, 2014b.

J.L. Chaboche. A review of some plasticity and viscoplasticity constitutive theories. *Int. J. Plasticity*, 24:1642–1693, 2008.

E. Combaz, C. Bacciarini, R. Charvet, W. Dufour, and A. Mortensen. Multiaxial yield behaviour of al replicated foam. *J. Mech. Phys. Solids*, 59:1777–1793, 2011.

A. Constantinescu, K. Dang Van, and M. H. Maitournam. A unified approach for high and low cycle fatigue based on shakedown concepts. *Fatigue Fract. Eng Mater. Struct.*, 26:561–568, 2003.

Y.F. Dafalias. *J. App. Mech.*, 52:865–871, 1985.

K. Danas. *Porous materials with evolving microstructure: constitutive modeling, numerical implementation and applications.* PhD thesis, Ecole Polytechnique de Paris, 2008.

K. Danas and N. Aravas. Numerical modeling of elasto-plastic porous materials with void shape effects at finite deformations. *Composites: Part B*, 43:2544–2559, 2012.

K. Danas and P. Ponte Castañeda. A finite-strain model for anisotropic viscoplastic porous media: I-theory. *Eur. J. Mech. A/Solids*, 28:387–401, 2009a.

K. Danas and P. Ponte Castañeda. A finite-strain model for anisotropic viscoplastic porous media: Ii-applications. *Eur. J. Mech. A/Solids*, 28:402–416, 2009b.

K. Danas and P. Ponte Castañeda. Influence of the lode parameter and the stress triaxiality on the failure of elasto-plastic porous materials. *Int. J. Solids Struct.*, 49: 1325–1342, 2012.

K. Danas, M. Idiart, and P. Ponte Castañeda. A homogenization-based constitutive model for two-dimensional viscoplastic porous media. *C. R. Mecanique*, 336:79–90, 2008a.

K. Danas, M.I. Idiart, and P. Ponte Castañeda. A homogenization-based constitutive model for isotropic viscoplastic porous media. *International Journal of Solids and Structures*, 45:3392 – 3409, 2008b.

K. Danas, V.S. Deshpande, and N.A. Fleck. Size effects in the conical indentation of an elasto-plastic solid. *J. Mech. Phys. Solids*, 60:1605–1625, 2012.

K. Dang Van. *Sur la résistance à la fatigue des métaux.* PhD thesis, University Paris 6, 1971.

G. deBotton and P. Ponte Castañeda. Variational estimates for the creep behaviour of polycrystals. *Proc. R. Soc. A*, 448:121–142, 1995.

G. DeBotton and P. Ponte Castañeda. Variational estimates for the creep behaviour of polycrystals. *Proceedings of the Royal Society of London A: Mathematical, Physical and Engineering Sciences*, 448:121–142, 1995.

J. Devaux, M. Gologanu, J.B. Leblond, and G. Perrin. On continued voids growth in ductile metals subjected to cyclic loadings. *Symposium on Nonlinear Analysis of Fracture, J.R. Willis ed.*, pages 299–310, 1997.

D. Drucker. Relation of experiments to mathematical theories of plasticity. *J. App. Mech.*, 16:349–357, 1949.

J.D. Eshelby. The determination of the elastic field of an ellipsoidal inclusion and related problems. *Proc. R. Soc. Lond. A*, 241:376–396, 1957.

U. Essmann, U. Gosele, and H. Mughrabi. A model of extrusions and intrusions in fatigued metals. i: Pointdefects production and the growth of extrusions. *Phil. Mag. A*, 44:405–426, 1981.

S. Feld-Payet, J. Besson, and F. Feyel. Finite element analysis of damage in ductile structures using a nonlocal model combined with a three-field formulation. *Int. J. Damage Mech.*, 20:655–680, 2011.

L. Flandi and J.-B. Leblond. A new model for porous nonlinear viscous solids incorporating void shape effects. i: Theory. *Eur. J. Mech. A/Solids*, 24:537–551, 2005a.

L. Flandi and J.-B. Leblond. A new model for porous nonlinear viscous solids incorporating void shape effects-i: Numerical validation. *Eur. J. Mech. A/Solids*, 24: 552–571, 2005b.

N.A. Fleck and J.W. Hutchinson. Void growth in shear. *Proc. R. Soc. Lond. A*, 407: 435–458, 1986.

S. Forest, R. Sievert, and E.C. Aifantis. Strain gradient crystal plasticity: Thermomechanical formulations and applications. *Journal of the Mechanical Behavior of Materials*, 13:219–232, 2011.

F. Fritzen, S. Forest, T. Bhlke, D. Kondo, and T. Kanit. Computational homogenization of elasto-plastic porous metals. *International Journal of Plasticity*, 29:102–119, 2012.

Y. Gan and J. Kysar. Cylindrical void in a rigid-ideally plastic single crystal iii: hexagonal close-packed crystal. *Int. J. Plasticity*, 23:592–619, 2007.

Y. Gan, J. Kysar, and T. Morse. Cylindrical void in a rigid-ideally plastic single crystal ii: experiments and simulations. *Int. J. Plasticity*, 22:39–72, 2006.

M. Garajeu, J.C. Michel, and P. Suquet. A micromechanical approach of damage in viscoplastic materials by evolution in size, shape and distribution of voids. *Comput. Methods Appl. Mech. Eng.*, 183:223–246, 2000.

P. Gilormini and J.-C Michel. Finite element solution of the problem of a spherical inhomogeneity in an infinite power-law viscous matrix. *Eur. J. Mech. A/Solids*, 17: 725–740, 1998.

M. Gologanu and J.B. Leblond. Approximate models for ductile metals containing non-spherical voids - case of axisymmetric prolate ellipsoidal cavities. *J. Mech. Phys. Solids*, 41:1723–1754, 1993.

M. Gologanu, J.-B. Leblond, G. Perrin, and J. Devaux. Theoretical models for void coalescence in porous ductile solids. i. coalescence in layers. *Int. J. Solids Struct.*, 38:5581–5594, 2001.

R. Guerchais, C. Robert, F. Morel, and N. Saintier. Micromechanical study of the loading path effect in high cycle fatigue. *Int. J. Fatigue*, 59:64–75, 2014.

A.L. Gurson. Continuum theory of ductile rupture by void nucleation and growth. *J. Eng. Mater. Tech.*, 99:2–15, 1977.

S. Ha and K. Kim. Void growth and coalescence in f.c.c. single crystals. *Int. J. Solids Struct.*, 52:863–873, 2010.

X. Han, J. Besson, S. Forest, B. Tanguy, and S. Bugat. A yield function for single crystals containing voids. *International Journal of Solids and Structures*, 50:2115–2131, 2013.

Z. Hashin. The elastic moduli of heterogeneous materials. *J. Appl. Mech.*, pages 143–150, 1962.

Z. Hashin and S. Shtrikman. On some variational principles in anisotropic and non-homogeneous elasticity. *J. Mech. Phys. Solids*, 10:335–342, 1962a.

Z. Hashin and S. Shtrikman. A variational approach to the theory of the elastic behavior of polycrystals. *J. Mech. Phys. Solids*, 10:343–352, 1962b.

Z. Hashin and S. Shtrikman. A variational approach to the theory of the elastic behaviour of multiphase materials. *J. Mech. Phys. Solids*, 11:127–140, 1963.

A. V. Hershey. The elasticity of an isotropic aggregate of anisotropic cubic crystals. *ASME J. Appl. Mech.*, 21:236–240, 1954.

E. Herve and A. Zaoui. n-layered inclusion-based micromechanical modelling. *Int. J. Engng Sci.*, 31:1–10, 1993.

R. Hill. Elastic properties of reinforced solids: Some theoritical principles. *J. Mech. Phys. Solids*, 11:357–372, 1963.

R. Hill. Continuum micro-mechanics of elastoplastic polycrystals. *J. Mech. Phys. Solids*, 13:89–101, 1965.

R. Hill. Aspects of invariance in solids mechanics. *Advances in applied mechanics*, 18: 1978, 1978.

F. Hofmann, G. Bertolino, A. Constantinescu, and M. Ferjani. A discussion at the mesoscopic scale of the stress-gradient effects in high cycle fatigue based on the dang van criterion. *Journal of the Mechanics of Materials and Structures*, pages 293–308, 2009.

J.H. Hommel and G. Meschke. A hybrid modeling concept for ultra low cycle fatigue of metallic structures based on micropore damage and unit cell models. *Int. J. Fatigue*, 32:1885–1894, 2010.

A. Hosokawa, D.S. Wilkinson, J. Kang, and E. Maire. Effect of triaxiality on void growth and coalescence in model materials investigated by x-ray tomography. *Acta Materialia*, 60:2829–2839, 2012.

A. Hosokawa, D.S. Wilkinson, J. Kang, and E. Maire. Onset of void coalescence in uniaxial tension studied by continuous x-ray tomography. *Acta Materialia*, 61: 1021–1036, 2013.

M. Huang, Z. Li, and C. Wang. Discrete dislocation dynamics modelling of microvoid growth and its intrinsic mechanism in single crystals. *Acta Mater.*, 55:1387–1396, 2007.

M. Huang, L. Zhao, and J. Tong. Discrete dislocation dynamics modelling of mechanical deformation of nickel-based single crystal superalloys. *Int. J. Plasticity*, 28: 141–158, 2012.

Y. Huang. A user material subroutine incorporating single crystal plasticity in the abaqus finite element program. *Mech Report, Division of Engineering and Aplied Sciences, Harvard University*, 178, 1991.

M. Hussein, U. Borg, C. Niordson, and V. Deshpande. Plasticity size effects in voided crystals. *J. Mech. Phys. Solids*, 56:114–131, 2008.

J.W. Hutchinson. Bounds and self-consistent estimates for creep of polycrystalline materials. *Proceedings of the Royal Society of London. Series A, Mathematical and Physical Sciences*, 348:101–127, 1976.

M. Idiart and P. Ponte Castañeda. Variational linear comparison bounds for nonlinear composites with anisotropic phases. ii. crystalline materials. *Proc. R. Soc. A*, 463: 925–943, 2007.

M.I. Idiart. Non linear sequential laminates reproducing hollow sphere assemblages. *C. R. Mecanique*, 335:363–368, 2007.

M.I. Idiart and P. Ponte Castañeda. Field statistics in nonlinear composites. i: theory. *Proc. R. Soc. Lond. A*, 463:183–202, 2006.

M.I. Idiart, H. Moulinec, P. Ponte Castañeda, and P. Suquet. Macroscopic behavior and field fluctuations in viscoplastic composites: Second-order estimates versus full-field simulations. *J. Mech. Phys. Solids*, 54:1029–1063, 2006.

F.P Jimenez and S. Pellegrino. Constitutive modeling of fiber composites with a soft hyperelastic matrix. *International Journal of Solids and Structures*, 49:635–647, 2012.

M. Kailasam and P. Ponte Castañeda. A general constitutive theory for linear and nonlinear particulate media with microstructure evolution. *J. Mech. Phys. Solids*, 46:427–465, 1998.

S.M. Keralavarma and A.A. Benzerga. A constitutive model for plastically anisotropic solids with non-spherical voids. *J. Mech. Phys. Solids*, 58:874–901, 2010.

S.M. Keralavarma, S. Hoelscher, and A.A. Benzerga. Void growth and coalescence in anisotropic plastic solids. *Int. J. Solids Struct.*, 48:1696–1710, 2011.

S.K. Koh and R.I. Stephens. Mean stress effects on low cycle fatigue for a high strength steel. *Fatigue & Fracture of Engineering Materials & Structures*, 14:413–428, 1991.

Y. Kondo, C. Sakae, M. Kubota, and T. Kudou. The effect of material hardness and mean stress on the fatigue limit of steels containing small defects. *Fatigue & Fracture of Engineering Materials & Structures*, 26:675–682, 2003.

J. Koplik and A. Needleman. Void growth and coalescence in porous plastic solids. *Int. J. Solids Structures*, 24:835–853, 1988.

E. Kroner. Berechnung der elastischen konstanten des vielkristalls aus den konstanten des einkristalls. *Z. Physik*, 151:504–518, 1958.

E. Kroner. Bounds for eective elastic moduli of disordered materials. *J. Mech. Phys. Solids*, 25:137–155, 1977.

J. Kysar, Y. Gan, and G. Mendez-Arzuza. Cylindrical void in a rigid-ideally plastic single crystal. part i: Anisotropic slip line theory solution for face-centered cubic crystals. *Int. J. Plasticity*, 21:1481–1520, 2005.

J.W. Kysar. Addendum to 'a user material subroutine incorporating single crystal plasticity in the abaqus finite element program'. *Mech Report, Division of Engineering and Aplied Sciences, Harvard University*, 178, 1997.

N. Lahellec and P. Suquet. Effective behavior of linear vicoelastic composites: a time-integration approach. *Int. J. Solids Struct.*, 44:507–529, 2007a.

N. Lahellec and P. Suquet. On the effective behavior of nonlinear inelastic composites: I. incremental variational principles. *J. Mech. Phys. Solids*, 55:1932–1963, 2007b.

N. Lahellec and P. Suquet. On the effective behavior of nonlinear inelastic composites: Ii. a second-order procedure. *J. Mech. Phys. Solids*, 55:1964–1992, 2007c.

N. Lahellec and P. Suquet. Effective response and field statistics in elasto-plastic and elasto-viscoplastic composites under radial and non-radial loadings. *Int. J. Plasticity*, 42:1–30, 2013.

R.A. Lebensonh, M.I. Idiart, P. Ponte Castañeda, and P. Vincent. Dilatational viscoplasticity of polycrystalline solids with intergranular cavities. *Philosophical Magazine*, 91:22:3038–3067, 2011.

J. Leblond, G. Perrin, and P. Suquet. Exact results and approximate models for porous viscoplastic solids. *Int. J. Plasticity*, 10:213–235, 1994.

J.-B. Leblond, G. Perrin, and J. Devaux. An improved gurson-type model for hardenable ductile metals. *Eur. J. Mech. A/Solids*, 14:499–527, 1995.

N. Limodin, A. El Bartali, L. Wang, J. Lachambre, and E. Charkaluk. Application of x-ray microtomography to study the influence of the casting microstructure upon the tensile behaviour of an al si alloy. *Nucl. Instrum. Phys. Res. Sect. B Beam Interact. Mater. Atoms*, 324:57–62, 2014.

F. López Jiménez. Modeling of soft composites under three-dimensional loading. *Composites: Part B*, 59:173–180, 2014.

O. Lopez-Pamies, T. Goudarzi, and K. Danas. The nonlinear elastic response of suspensions of rigid inclusions in rubber: Iia simple explicit approximation for finite-concentration suspensions. *Journal of the Mechanics and Physics of Solids*, 61:19–37, 2013.

K. Madou and J.B. Leblond. A gurson-type criterion for porous ductile solids containing arbitrary ellipsoidal voids-i: Limit-analysis of some representative cell. *Journal of the Mechanics and Physics of Solids*, 60:1020–1036, 2012a.

K. Madou and J.B. Leblond. A gurson-type criterion for porous ductile solids containing arbitrary ellipsoidal voids-ii: Determination of yield criterion parameters. *Journal of the Mechanics and Physics of Solids*, 60:1037–1058, 2012b.

K. Madou and J.B. Leblond. Numerical studies of porous ductile materials containing arbitrary ellipsoidal voids - ii: Evolution of the length and orientation of the void axes. *European Journal of Mechanics A/Solids*, 42:490–507, 2013.

M.H. Maitournam, C. Krebs, and A. Galtier. A multiscale fatigue life model for complex cyclic multiaxial loading. *Int. J. Fatigue*, 33:232–240, 2011.

A. Mbiakop, A. Constantinescu, and K. Danas. On void shape effects of periodic elasto-plastic materials subjected to cyclic loading. *European Journal of Mechanics and Solids*, 49:481–499, 2015.

F. Mc Clintock. A criterion for ductile fracture by the growth of holes. *J. App. Mech.*, 35:363–371, 1968.

M. Mear and J. Hutchinson. Influence of yield surface curvature on flow localization in dilatant plasticity. *Mech. Mater.*, 4:395–407, 1985.

J.-C. Michel, H. Moulinec, and P. Suquet. Effective properties of composite material with periodic microstructure: a computational approach. *Comput. Methods Appl. Mech. Engrg.*, 172:109–143, 1999.

J.C. Michel and P. Suquet. The constitutive law of nonlinear viscous and porous materials. *J. Mech. Phys. Solids*, 40:783–812, 1992.

J.C. Michel and P. Suquet. An analytical and numerical study of the overall behaviour of metal-matrix composites. *Modelling Simul. Mater. Sci. Eng.*, 2:637–658, 1994.

C. Miehe, J. Schroder, and J. Schotte. Computational homogenization analysis in finite plasticity simulation of texture development in polycrystalline materials. *Computer Methods in Applied Mechanics and Engineering*, 171:387–418, 1999.

G.W. Milton. Bounds on the elastic and transport properties of two-component composites. *J. Mech. Phys. Solids*, 30:177–191, 1982.

V. Monchiet and D. Kondo. Combined voids size and shape effects on the macroscopic criterion of ductile nanoporous materials. *International Journal of Plasticity*, 43: 20–41, 2013.

V. Monchiet, C. Gruescu, and D. Kondo. Approximate yield criteria for anisotropic metals with prolate or oblate voids. *C. R. Mecanique*, 2006.

V. Monchiet, E. Charkaluk, and D. Kondo. An improvement of gurson-type models of porous materials by using eshelby-like trial velocity fields. *C.R. Acad. Sci. Paris*, 335:32–41, 2007.

V. Monchiet, O. Cazacu, E. Charkaluk, and D. Kondo. Macroscopic yield criteria for plastic anisotropic materials containing spheroidal voids. *Int. J. Plasticity*, 24: 1158–1189, 2008a.

V. Monchiet, E. Charkaluk, and D. Kondo. A micromechanical explanation of the mean stress effect in high cycle fatigue. *Mechanics Research Communications*, 35: 383–391, 2008b.

V. Monchiet, E. Charkaluk, and D. Kondo. Macroscopic yield criteria for ductile materials containing spheroidal voids: An eshelby-like velocity fields approach. *Mechanics of Materials*, 72:1–18, 2014.

F. Morel and M. Bastard. A multiaxial life prediction method applied to a sequence of non similar loading in high cycle fatigue. *International Journal of Fatigue*, 25: 1007–1012, 2003.

T. Mori and K. Tanaka. Average stress in matrix and average elastic energy of materials with misfitting inclusions. *Acta Metall.*, 21:571–574, 1973.

L. Morin, J.B. Leblond, and A.A Benzerga. Coalescence of voids by internal necking: Theoretical estimates and numerical results. *J. Mech. Phys. Solids*, 75:140–158, 2015.

K. Nahshon and J.W. Hutchinson. Modification of the gurson model for shear failure. *Eur. J. Mech. A/Solids*, 27:1–17, 2008.

A Needleman and J.R Rice. Limits to ductility set by plastic flow localization. *Mechanics of sheet metal forming*, pages 237–267, 1978.

K.L. Nielsen and C.F. Niordson. A 2d finite element implementation of the fleck-willis strain-gradient flow theory. *Eur. J. Mech. A/Solids*, 41:134–142, 2013.

K.L. Nielsen and C.F. Niordson. A numerical basis for strain-gradient plasticity theory: Rate-independent and rate-dependent formulations. *J. Mech. Phys. Solids*, 63:113–127, 2014.

K.L. Nielsen and V. Tvergaard. Failure by void coalescence in metallic materials containing primary and secondary voids subject to intense shearing. *Int. J. Solids Struct.*, 48:1255–1267, 2011.

C.F. Niordson and J.W. Kysar. Computational strain gradient crystal plasticity. *Journal of the Mechanics and Physics of Solids*, 62:31–47, 2014.

C.F. Niordson and B.N. Legarth. Strain gradient effects on cyclic plasticity. *J. Mech. Phys. Solids*, 58:542–557, 2010.

D. Nouailhas, J.L. Chaboche, S. Savalle, and G. Cailletaud. On the constitutive equations for cyclic plasticity under nonproportional loading. *Int. J. Plasticity*, 1: 317–330, 1985.

R. Ogden. *Nonlinear elastic Deformations*. Halsted Press, New York, 1984.

I.V. Papadopoulos. *Fatigue polycyclique des mètaux : une nouvelle approche*. PhD thesis, ENPC, 1987.

T. Pardoen and J.W. Hutchinson. An extended model for void growth and coalescence. *J. Mech. Phys. Solids*, 48:2467–2512, 2000.

J. Paux, L. Morin, R. Brenner, and D. Kondo. An approximate yield criterion for porous single crystals. *Eur. J. Mech. A/Solids*, 51:1–10, 2015.

A. Pirondi, N. Bonora, D. Steglich, W. Brocks, and D. Hellmann. Simulation of failure under cyclic plastic loading by damage models. *Int. J. Plasticity*, 22:2146–2170, 2006.

P. Ponte Castañeda. The effective mechanical properties of nonlinear isotropic composites. *J. Mech. Phys. Solids*, 35:45–71, 1991a.

P. Ponte Castañeda. Effective properties in power-law creep. *Mechanics of creep brittle materials*, 2:218–229, 1991b.

P. Ponte Castañeda. Nonlinear composite materials: Effective constitutive behavior and microstructure evolution. *Suquet, P. (Ed.), Continuum micromechanics. In: CISM lectures series. Springer, New York*, pages 61–130, 1997.

P. Ponte Castañeda. Second-order homogenization estimates for nonlinear composites incorporating field fluctuations: I-theory. *Journal of the Mechanics and Physics of Solids*, 50:737–757, 2002a.

P. Ponte Castañeda. Second-order homogenization estimates for nonlinear composites incorporating field fluctuations: Ii-applications. *Journal of the Mechanics and Physics of Solids*, 50:759–782, 2002b.

P. Ponte Castañeda. Bounds for non linear composites via iterated homogenization. *J. Mech. Phys. Solids*, 60:1583–1604, 2012.

P. Ponte Castañeda and J.R. Willis. The effect of spatial distribution on the effective behavior of composite materials and cracked media. *J. Mech. Phys. Solids*, 43: 1919–1951, 1995.

P. Ponte Castañeda and M. Zaidman. Constitutive models for porous materials with evolving microstructure. *J. Mech. Phys. Solids*, 42:1459–1497, 1994.

P. Ponte Castañeda and M. Zaidman. The finite deformation of nonlinear composite materials. i. instantaneous constitutive relations. *Int. J. Solids Structures*, 33:1271–1286, 1996.

E. Pouillier, A.F. A.-F. Gourgues, D. Tanguy, and E.P. Busso. A study of intergranular fracture in an aluminium alloy due to hydrogen embrittlement. *International Journal of Plasticity*, 34:139–154, 2012.

F. Rabold and M. Kuna. Cell model simulation of void growth in nodular cast iron under cyclic loading. *Computational Materials Science*, 32:489–497, 2005.

G. Requena, E. Maire, C. Leguen, and S. Thuillier. Separation of nucleation and growth of voids during tensile deformation of a dual phase steel using synchrotron microtomography. *Materials Science and Engineering A*, 589:242–251, 2014.

A. Reus. Calculation of the flow limits of mixed crystals on the basis of the plasticity of the monocrystals. *Z. Angew. Math. Mech.*, 9:49–58, 1929.

B. Revil-Baudard and O. Cazacu. New three-dimensional strain-rate potentials for isotropic porous metals: Role of the plastic flow of the matrix. *Int. J. Plasticity*, 60: 101–117, 2014.

J.R. Rice. Tensile crack tip fields in elastic-ideally plastic crystals. *Mechanics of Materials*, 6:317–335, 1987.

J.R. Rice and D.M. Tracey. On the ductile enlargement of voids in triaxial stress fields. *J. Mech. Phys. Solids*, 17:201–217, 1969.

M.D. Rintoul and S. Torquato. Reconstruction of the structure of dispersions. *J. Colloid Interface Sci.*, 186:467–476, 1997.

M. Ristinmaa. Void growth in cyclic loaded porous plastic solid. *Mech. Mat.*, 26: 227–245, 1997.

J. Segurado and J. Llorca. A numerical approximation to the elastic properties of sphere-reinforced composites. *Journal of the Mechanics and Physics of Solids*, 50: 2107–2121, 2002.

J. Segurado and J. Llorca. Discrete dislocation dynamics analysis of the effect of lattice orientation on void growth in single crystals. *Int. J. Plasticity*, 26:806–819, 2010.

A. Srivastava and A. Needleman. Porosity evolution in a creeping single crystal. *Model. Simul. Mater. Sci. Eng.*, 20, 2012.

A. Srivastava and A. Needleman. Effect of crystal orientation on porosity evolution in a creeping single crystal. *Mechanics of Materials*, 2015.

A. Srivastava, S. Gopagoni, A. Needleman, V. Seetharaman, A. Staroselsky, and R. Banerjee. Effect of specimen thickness on the creep response of a ni-based single-crystal superalloy. *Acta Materialia*, 60:5697–5711, 2012.

P. Suquet. Overall properties of nonlinear composites: a modified secant moduli theory and its link with ponte castañeda's nonlinear variational procedure. *C. R. Acad. Sci. Paris II*, 320:563–571, 1995.

H. Swift. Length changes in metals under torsional overstrain. *Engineering*, 163: 253–257, 1947.

S. Tabibian, E. Charkaluk, A. Contantinescu, F. Szmytka, and A. Oudin. Tmf-lcf life assessment of a lost foam casting aluminum alloy. *Int. J. Fatigue doi:10.1016/j.ijfatigue.2012.01.012.*, 2012.

S. Tabibian, E. Charkaluk, A. Constantinescu, F. Szmytka, and A. Oudin. Tmf-tmf criteria for lost foam casting aluminum alloys. *Fatigue and Fracture of Engineering Materials and Structures*, 36:281–374, 2013.

D.R.S Talbot and J.R. Willis. Variational principles for inhomogeneous non-linear media. *Journal of Applied Mathematics*, 35:39–54, 1985.

T. Tang, S. Kim, and M. Horstemeyer. Fatigue crack growth in magnesium single crystals under cyclic loading: molecular dynamics simulation. *Comput. Mater. Sci.*, 48:426–439, 2010a.

T. Tang, S. Kim, and M. Horstemeyer. Molecular dynamics simulations of void growth and coalescence in single crystal magnesium. *Acta Mater.*, 58:4742–4759, 2010b.

G. I. Taylor. Plastic strains in metals. *J. Inst. Metals*, 62:307–324, 1938.

C. Tekoğlu, J.B. Leblond, and T. Pardoen. A criterion for the onset of void coalescence under combined tension and shear. *J. Mech. Phys. Solids*, 60:1363–1381, 2012.

P.F. Thomason. A three-dimensional model for ductile fracture by the growth and coalescence of microvoids. *Acta Metall.*, 33:1087–1095, 1985.

S. Torquato. Random heterogeneous materials: Micorstructures and macroscopic properties. *Springer*, 2002.

S. Traiviratana, E. Bringa, D. Benson, and Meyers. Void growth in metals: atomistic calculations. *Acta Mater.*, 56:3874–3886, 2008.

V. Tvergaard. Material failure by void growth. *Adv Appl Mech*, 27:83–151, 1990.

V. Tvergaard. Void shape effects and voids starting from cracked. *Int. J. Solids Struct.*, 48:1101–1108, 2011.

V. Tvergaard. On cavitation instabilities with interacting voids. *Eur. J. Mech. A/Solids*, 32:52–58, 2012.

V. Tvergaard and A. Needleman. Analysis of the cup-cone fracture in a round tensile bar. *Acta Metall.*, 32:157–169, 1984.

V. Tvergaard and K.L. Nielsen. Relations between a micro-mechanical model and a damage model for ductile failure in shear. *J. Mech. Phys. Solids*, 58:1243–1252, 2010.

F. Vernerey, W.K. Liu, and B. Moran. Multi-scale micromorphic theory for hierarchical materials. *J. Mech. Phys. Solids*, 55:2603–2651, 2007.

P. Vincent, P. Suquet, Y. Monerie, and H. Moulinec. Effective flow surface of porous materials with two populations of voids under internal pressure: I. a gtn model. *Int. Journal. Plasticity*, 56:45–73, 2014a.

P. Vincent, P. Suquet, Y. Monerie, and H. Moulinec. Effective flow surface of porous materials with two populations of voids under internal pressure: Ii. full-field simulations. *Int. Journal. Plasticity*, 56:74–98, 2014b.

W. Voigt. Ueber die bezienhung zwischen den beiden elastitats-constanten isotroper. *Ann. Physik*, 38:573–588, 1889.

J. Wallis. *Arithmetica Infinitorum*. 1656.

L. Wang, N. Limodin, A. El. Bartali, and E. Charkaluk. X-ray tomography observation of a al si alloy, personal communication.

I. Watanabe, D. Setoyama, N. Iwata, and K. Nakanishi. Characterization of yielding behavior of polycrystalline metals with single crystal plasticity based on representative characteristic length. *Int. J. Plasticity*, 26:570–585, 2010.

J.R. Willis. Bounds and self-consistent estimates for the overall properties of anisotropic composites. *J. Mech. Phys. Solids*, 25:185–202, 1977.

J.R. Willis. Variational principles and bounds for the overall properties of composites. *Continuum Models and Discrete Systems*, 2:185–212, 1978.

J.R. Willis. On methods for bounding the overall properties of nonlinear composites. *J. Mech. Phys. Solids*, 39:73–86, 1991.

F. Willot, Y. Pellegrini, M.I. Idiart, and P.P. Castañeda. Effective-medium theory for infinite-contrast two-dimensionally periodic linear composites with strongly anisotropic matrix behavior: Dilute limit and crossover behavior. *Physical Review B.*, 78, 104111, 2008.

T.Y. Wu, J.L. Bassani, and C. Laird. Latent hardening in single crystals i. theory and experiments. *Proc. Phys. Soc. Lond. A*, 435:1–19, 1991.

S.K. Yerra, C. Tekoglu, F. Scheyvaerts, L. Delannay, P. Van Houtte, and T. Pardoen. Void growth and coalescence in single crystals. *Int. J. Solids Struct.*, 47:1016–1029, 2010.

K.S. Zhang, J.B. Bai, and D. Francois. Numerical analysis of the influence of the lode parameter on the void growth. *Int. J. Solids Struct.*, 38:5847–5856, 2001.

K. Zhao, C. Chen, Y. Shen, and T. Lu. Molecular dynamics study on the nanovoid growth in face-centered cubic single crystal copper. *Comput. Mater. Sci.*, 46: 749–754, 2009.